TU Delft

Delft University of Technology

Coastal Science for Sea Turtle Conservation

Christiaanse, Jakob

DOI
10.4233/uuid:66088341-44a0-4752-9c9e-258d467e0cb3

Publication date
2025

Document Version
Final published version

Citation (APA)
Christiaanse, J. (2025). *Coastal Science for Sea Turtle Conservation*. [Dissertation (TU Delft), Delft University of Technology]. https://doi.org/10.4233/uuid:66088341-44a0-4752-9c9e-258d467e0cb3

Important note
To cite this publication, please use the final published version (if applicable).
Please check the document version above.

Copyright
Other than for strictly personal use, it is not permitted to download, forward or distribute the text or part of it, without the consent of the author(s) and/or copyright holder(s), unless the work is under an open content license such as Creative Commons.

Takedown policy
Please contact us and provide details if you believe this document breaches copyrights.
We will remove access to the work immediately and investigate your claim.

This work is downloaded from Delft University of Technology.
For technical reasons the number of authors shown on this cover page is limited to a maximum of 10.

Coastal Science for Sea Turtle Conservation

Jakob C. Christiaanse

Coastal Science for Sea Turtle Conservation

Coastal Science for Sea Turtle Conservation

Dissertation

for the purpose of obtaining the degree of doctor
at Delft University of Technology,
by the authority of the Rector Magnificus, Prof. dr. ir. T. H. J. J. van der Hagen,
chair of the Board for Doctorates,
to be defended publicly on
Monday 15 December 2025 at 15:00 o'clock

by

Jakob Cornelis CHRISTIAANSE

Master of Science in Civil Engineering,
Delft University of Technology, Netherlands,
born in Rotterdam, Netherlands.

This dissertation has been approved by the promotors.

Composition of the doctoral committee:

Rector Magnificus	chairman
Prof. dr. ir. A. J. H. M. Reniers	Delft University of Technology, *promotor*
Prof. dr. ir. S. G. J. Aarninkhof	Delft University of Technology, *promotor*
Dr. ing. J. A. Á. Antolínez	Delft University of Technology, *copromotor*
Independent members:	
Prof. dr. J. H. Slinger	Delft University of Technology
Prof. dr. ir. S. N. Jonkman	Delft University of Technology
Prof. dr. I. L. Turner	University of New South Wales, Australia
Dr. T. S. Agardy	Sound Seas and Baird & Associates, USA
Reserve member:	
Dr. ir. M. A. de Schipper	Delft University of Technology

This dissertation was partly financed by the TURTLE research project (T-DEL/2023/095), funded by TKI Deltatechnologie with support from TU Delft, Texas A&M University, Deltares, Boskalis, King Abdullah University of Science and Technology (KAUST), and University of Exeter.

Keywords: Sandy beaches; sea turtles; nest flooding; erosion; beach groundwater; nature-based solutions; field observations; remote sensing; machine learning, shoreline modeling.

Printed by: Ridderprint

Cover by: Annekee Groeninx van Zoelen

Copyright © 2025 by Jakob C. Christiaanse

ISBN 978-94-6518-189-9

An electronic version of this dissertation is available at: https://repository.tudelft.nl/

Contents

Summary vii

Samenvatting ix

1 Introduction 1

2 Field site, instrumentation, and collected data 11

3 Drivers of nest flooding 41

4 Uncertain future for global nesting beaches 71

5 New horizons for nesting sea turtles 99

6 Aiding sea turtle conservation through coastal management 123

7 Conclusion 139

References 145

A Supporting information for Chapter 3 165

B Supporting information for Chapter 4 171

C Supporting information for Chapter 5 189

Acknowledgments 195

About the author 199

List of publications 201

Summary

Sandy beaches provide a wide range of ecosystem services, including flood protection, sediment and water storage, recreational values, and habitat for diverse flora and fauna. Over the past centuries, humans have increasingly developed settlements and infrastructure on the landward side, while waves, storm surges, and sea level rise encroach from the ocean side. These stressors may lead to ecological impacts across varying temporal and spatial scales, threatening the ecosystem services for humans and animals alike.

Among the species particularly vulnerable to the degradation of sandy beaches are sea turtles, who rely on these habitats for nesting. These endangered reptiles play key ecological roles in coastal and marine ecosystems worldwide, for instance by maintaining healthy coral reefs and sea grass meadows. Unfortunately, climate change and human activity severely threaten their populations. Among the challenges they face are the flooding and erosion of their nesting beaches. Incubating nests require a narrow temperature and moisture window to develop, making them susceptible to inundation. Episodic erosion can destroy nests and change beach morphology over several seasons. Long-term, chronic erosion and coastal squeeze may gradually diminish suitable nesting beaches worldwide. Although both flooding and erosion are recognized as significant threats, they remain under-represented in conservation management and research. Nature-based solutions—such as turtle-friendly sand nourishments or restoration of coastal vegetation and reefs—may offer promising opportunities to preserve existing nesting habitats, and potentially enable sea turtles to expand to currently unused beaches. However, we first need to understand the coastal processes that enable and threaten sea turtle nesting to effectively design such solutions.

This thesis identifies coastal processes that govern the vulnerability of sea turtle nesting beaches, and assesses their implications for global habitat suitability and conservation. Specifically, it investigates processes related to nest flooding and long-term erosion, while also examining how regional coastal characteristics influence global nesting habitat suitability. Employing detailed local case studies and global analyses, this thesis integrates diverse methods—including field experiments, numerical modeling, remote sensing, statistical analyses, global datasets, and machine learning—to illustrate the broad potential of coastal science tools for sea turtle conservation, which are essential for developing an integrative approach to assess nesting beach vulnerability and inform targeted interventions.

To study the drivers of nest flooding, an extensive field campaign was carried out on Galveston Island, Texas, USA—a mild-sloping, fine-grained barrier island—in the fall of 2023. Two beach transects were monitored over a period of 1.5 months to measure the beach groundwater table, nearshore hydrodynamics, and sediment characteristics (Chapter 2). Analysis of these data using advanced spectral methods revealed storm surges and rain as the dominant drivers of short-term fluctuations in the beach groundwater table and, by extension, the flooding of turtle nests (Chapter 3). Due to the high risk of flooding, Galveston Island is currently unsuitable for turtle nesting, highlighting the necessity of continuing the ongoing nest relocation program. These findings underscore the importance of consid-

ering beach groundwater in nest flooding assessments and encourage comparative studies across diverse coastal settings, where different processes may predominate (e.g., on steeper, coarser-grained beaches).

The vulnerability of nine globally significant nesting sites to future erosion and sea level rise was explored by combining coastal remote sensing, numerical modeling, and global datasets (Chapter 4). Analysis of satellite-derived shorelines revealed significant variability in seasonal and long-term shoreline change across the sites. Using the shoreline model CoSMoS-COAST, future shoreline change was projected until 2100 under various sea level rise scenarios, complemented by estimates of beach width and potential accommodation space, based on global datasets. These projections also showed substantial variability—three sites were particularly vulnerable to future erosion and sea level rise, while others showed continued accretion. Despite significant uncertainties in the long-term projections, these results provide important insights into seasonal and long-term morphodynamics, identify vulnerable nesting beaches, and present a replicable framework for assessing shoreline change at nesting beaches worldwide, including data-limited regions.

Lastly, the relationship between regional coastal characteristics and the global distribution of nesting sites was examined by applying machine learning techniques on global datasets. These global data spanned hydrodynamic, atmospheric, geophysical, habitat, and human processes and were mapped to a novel 50-km-resolution hexagonal coastline grid (Coastgons; Chapter 5). Results suggested that sea surface temperature, tidal range, extreme surges, and proximity to coral and seagrass habitats significantly influence global nesting distribution. Low tidal ranges and low storm surge exposure emerged as particularly favorable for individual species, likely due to reduced risk of nest flooding. Furthermore, this analysis identified new regions potentially suitable for nesting, revealing that approximately 23% of global coastal regions between $-39°$ and $48°$ latitude could host suitable nesting beaches, while only 7% are currently used by turtles. This implies that there is potential for sea turtles to expand their nesting habitat. Although sea turtle behavior remains difficult to predict, these results help quantify suitable nesting conditions and can inform future studies into the potential colonization of new nesting habitats.

The analyses presented in this thesis show how state-of-the-art coastal monitoring and modeling approaches can be used to observe, understand, and predict coastal processes at nesting beaches—critical steps for informing when and how to intervene using nature-based solutions. Therefore, Chapter 6 argues that existing methods and tools from coastal science and management hold significant, yet underused, potential for sea turtle conservation. A stepwise framework is introduced for integrating sea turtle ecology and coastal management. The framework follows an Observe–Understand–Predict–Intervene cycle and links ecological thresholds, coastal processes, and management interventions across scales, from Regional Management Units (RMUs) to individual beaches. It is illustrated how state-of-the-art monitoring, modeling, and nature-based solutions (NBS) can be embedded within this framework to inform when and how to intervene. Increased in-situ data collection and interdisciplinary collaboration will be critical to apply and refine this approach, thereby enhancing the long-term resilience of nesting habitats.

Samenvatting

Zandstranden bieden een breed scala aan ecosysteemdiensten, waaronder bescherming tegen overstromingen, bufferen van sediment en water, recreatieve waarden en leefgebieden voor diverse flora en fauna. In de afgelopen eeuwen zijn ze echter steeds intensiever gebruikt en ontwikkeld door mensen aan de landzijde, terwijl golven, stormvloeden en zeespiegelstijging hen vanaf de zeezijde bedreigen. Deze stressfactoren veroorzaken ecologische effecten op uiteenlopende temporele en ruimtelijke schalen, waardoor ecosysteemdiensten voor mens en dier onder druk komen te staan.

Onder de soorten die bijzonder kwetsbaar zijn voor de aantasting van zandstranden behoren zeeschildpadden, die afhankelijk zijn van strandgebieden om te nestelen. Deze bedreigde reptielen spelen cruciale ecologische rollen in kust- en mariene ecosystemen over de hele wereld, bijvoorbeeld door koraalriffen en zeegrasvelden te onderhouden. Helaas worden hun populaties ernstig bedreigd door klimaatverandering en menselijke activiteit—onder andere door het overstromen en eroderen van nesten tijdens het broedseizoen, evenals het verlies van geschikte neststranden door langdurige erosie. Hoewel beide problemen erkend worden in de wetenschap, krijgen ze onvoldoende aandacht in natuurbeheer en onderzoek. Natuurgebaseerde oplossingen—zoals schildpad-vriendelijke zandsuppleties of het herstellen van kustvegetatie en riffen—bieden kansrijke mogelijkheden om neststranden te behouden en wellicht zelfs uit te breiden. Om dergelijke oplossingen effectief te kunnen ontwerpen is het echter noodzakelijk om eerst inzicht te krijgen in de kustprocessen die nestelgebieden van zeeschildpadden ondersteunen of juist bedreigen.

Dit proefschrift identificeert kustprocessen die de kwetsbaarheid van neststranden van zeeschildpadden bepalen en beoordeelt hun implicaties voor de geschiktheid van habitats en het conservatie op mondiale schaal. In het bijzonder worden processen onderzocht die verband houden met overstroming van nesten en langdurige erosie, evenals de wijze waarop regionale kustkenmerken de geschiktheid van nesthabitats wereldwijd beïnvloeden. Aan de hand van gedetailleerde lokale casestudy's en globale analyses integreert deze dissertatie uiteenlopende methoden—waaronder veldexperimenten, numeriek modelleren, remote sensing, statistische analyses, globale datasets en machine learning—om het brede potentieel van kustwetenschappelijke methodes voor het behoud van zeeschildpadden te illustreren. Deze zijn van essentieel belang voor het ontwikkelen van een integratieve benadering om de kwetsbaarheid van neststranden te beoordelen en gerichte interventies te ondersteunen.

Om de oorzaken van nestoverstromingen te onderzoeken werd in het najaar van 2023 een uitgebreide veldcampagne uitgevoerd op Galveston Island, Texas, VS—een barrière-eiland met een milde helling en fijn sediment. Twee strandtransecten werden gedurende anderhalve maand gemonitord om het grondwaterniveau in het strand, de hydrodynamica van het kustgebied en sedimentkenmerken te meten (Hoofdstuk 2). Analyse van deze data met geavanceerde spectrale methoden toonde aan dat stormvloeden en regenval dominante factoren zijn in kortetermijnfluctuaties van het grondwaterniveau, en daarmee bepalend voor het overstromen van schildpadnesten (Hoofdstuk 3). Vanwege het hoge risico op overstro-

ming is Galveston Island momenteel ongeschikt voor het nestelen van zeeschildpadden, wat het belang onderstreept van het voortzetten van het lopende nestverplaatsingsprogramma. Deze bevindingen benadrukken bovendien het belang van grondwaterstudies bij het beoordelen van nestoverstromingen, en stimuleren vergelijkende studies op stranden met andere kenmerken (bijvoorbeeld steilere, grof-korrelige stranden), waar andere processen mogelijk domineren.

De kwetsbaarheid van negen wereldwijd belangrijke neststranden voor toekomstige erosie en zeespiegelstijging werd onderzocht door satellietbeelden, numeriek modelleren en mondiale datasets te combineren (Hoofdstuk 4). Analyse van satelliet-afgeleide kustlijnen liet aanzienlijke variabiliteit zien in seizoensgebonden en lange termijn kustlijnevolutie. Met het kustlijnmodel CoSMoS-COAST werd vervolgens de kustlijnverandering tot 2100 voorspeld onder diverse scenario's van zeespiegelstijging, aangevuld met schattingen van strandbreedte en potentiële accommodatieruimte. Ook deze prognoses lieten grote variabiliteit zien: drie locaties bleken bijzonder kwetsbaar voor toekomstige erosie en zeespiegelstijging, terwijl andere locaties juist kustaangroei toonden. Ondanks de aanzienlijke onzekerheden in lange termijn-prognoses bieden deze resultaten belangrijke inzichten in seizoensgebonden en lange termijn kustdynamiek, identificeren ze kwetsbare neststranden, en vormen ze een reproduceerbaar raamwerk om kustlijnverandering op neststranden wereldwijd te beoordelen, zelfs in regio's met beperkte data.

Ten slotte werd de relatie tussen regionale kustkenmerken en de mondiale verspreiding van neststranden onderzocht met behulp van wereldwijde datasets, een nieuw hexagonaal kustlijnraster met een resolutie van 50 km (Coastgons), en machine learning technieken (Hoofdstuk 5). Resultaten toonden aan dat zeewatertemperatuur, getijverschillen, extreme stormvloeden en nabijheid van koraal- en zeegrasgebieden significant van invloed zijn op de wereldwijde verspreiding van nestgebieden. Vooral lage getijverschillen en beperkte blootstelling aan extreme stormvloeden bleken gunstig voor verschillende soorten, waarschijnlijk vanwege het verminderde risico op nestoverstroming. Verder werden nieuwe potentieel geschikte nestgebieden geïdentificeerd. Uit deze analyse blijkt dat ongeveer 23% van de kustgebieden wereldwijd tussen $-39°$ en $48°$ breedtegraad geschikt zou kunnen zijn, terwijl momenteel slechts 7% daadwerkelijk door zeeschildpadden wordt benut. Dit impliceert dat zeeschildpadden potentieel hun nestgebied zouden kunnen uitbreiden. Hoewel het gedrag van zeeschildpadden lastig voorspelbaar blijft, helpen deze resultaten om geschikte nestcondities te kwantificeren en bieden ze aanknopingspunten voor onderzoek naar de kolonisatie van nieuwe nestgebieden.

De analyses in dit proefschrift laten zien hoe geavanceerde methoden voor kustmonitoring en -modellering kunnen worden gebruikt om kustprocessen op neststranden te observeren, te begrijpen en te voorspellen—cruciale stappen om te bepalen wanneer en hoe natuurgebaseerde oplossingen moeten worden ingezet. Hoofdstuk 6 stelt daarom dat bestaande methoden en instrumenten uit de kustwetenschap en het kustbeheer aanzienlijke, maar nog onderbenutte, mogelijkheden bieden voor de bescherming van zeeschildpadden. Er wordt een stapsgewijs raamwerk geïntroduceerd om ecologie en kustbeheer te integreren en zo de bedreigingen aan te pakken. Dit raamwerk volgt een Observeren–Begrijpen–Voorspellen–Ingrijpen cyclus en verbindt ecologische drempelwaarden, kustprocessen en interventies op verschillende schalen, van RMU's tot individuele stranden. Er wordt geïllustreerd hoe geavanceerde monitoring, modellering en natuurgebaseerde oplossingen binnen dit raam-

werk kunnen worden ingebed om te bepalen wanneer en hoe moet worden ingegrepen. Een meer observaties en interdisciplinaire samenwerking zal cruciaal zijn om dit raamwerk toe te passen en verder te verfijnen, en daarmee de langetermijnveerkracht van neststranden te versterken.

Cover photo by Adhith Swaminathan ©: Leatherback sea turtle (*Dermochelys coriacea*) returning to the sea on Little Andaman Island, India.

1 Introduction

1.1. Sea turtle nesting beaches under pressure

Sandy beaches form a soft, dynamic interface between marine and terrestrial forces and cover around a third of the global, ice-free coast (Hulskamp et al., 2023; Luijendijk et al., 2018). In the past, the sandy coastal zone has mostly been studied in relation to its function as flood protection and recreational use (e.g., Leaman et al., 2021; McLachlan et al., 2013). Yet, sandy beaches provide a wide range of additional ecosystem services, such as sediment and water storage, nutrient cycling, and habitat for a multitude of flora and fauna, including nesting sea turtles and shorebirds (Defeo et al., 2009; Nel et al., 2014). They are complex ecosystems that react to a range of dynamic stressors. Over the past centuries, they have become increasingly used and developed by humans on the landward side (Neumann et al., 2015), while waves, storm surges, and sea level rise encroach from the ocean side. These stressors may lead to ecological impacts across varying temporal and spatial scales, deteriorating the many ecosystem services that sandy beaches provide for humans and animals alike (Barbier et al., 2011; Defeo et al., 2009).

Sea turtles rely on sandy beaches for nesting (Figure 1.1) and are key species in many coastal and marine ecosystems worldwide (Heithaus, 2013). For instance, green turtles (*Chelonia mydas*) are vital grazers of Earth's widely distributed seagrass beds (Christianen et al., 2023), which themselves sequester large amounts of carbon but are deteriorating at an alarming rate (Waycott et al., 2009). Hawksbill turtles (*Eretmochelys imbricata*), on the other hand, are among the few animals that feed on sponges, making them a key species in maintaining healthy coral reef ecosystems (Meylan, 1988). Despite their ecological significance, six of the seven species are listed on the IUCN Red List as *Vulnerable*, *Endangered*, or *Critically Endangered* (IUCN, 2022)—the sole exception being the flatback sea turtle (*Natator depressus*), currently classified as *Data Deficient*. The long-term survival of sea turtles is intrinsically linked to the continued availability of suitable nesting beaches worldwide.

Although sea turtles have successfully evolved and adapted to habitat changes over millions of years, their populations have decreased strongly over the past centuries (McClenachan et al., 2006). This has been mainly attributed to excessive human exploitation, which peaked in the late 1960's (Humber et al., 2014). In the past decades, policy changes have resulted in better protection from exploitation and illegal trade. However, current population numbers are still far below historic estimates (McClenachan et al., 2006) and sea turtles remain under serious threat from fishery by-catch, plastic pollution, and climate change impacts—including the flooding and erosion of their nesting beaches (Hawkes et al., 2009;

Figure 1.1: Photographs showing an adult green sea turtle nesting on Ascension Island (left) and a clutch of hawksbill hatchlings leaving their nest and crawling towards the sea on Hawai'i (right). Photo credit S. Weber/Ascension Island Government and John Rodarte/Hawai'i Wildlife Fund, respectively.

Patrício et al., 2021). Due to their slow population growth rates, sea turtles are unable to recover quickly from population declines. In fact, recovery rates may range from several decades to a century (Duarte et al., 2020). This makes them highly vulnerable to relatively fast-paced changes to their nesting habitats (Mortimer, 1995; Pike & Stiner, 2007), particularly for species with limited nesting ranges, such as the critically endangered Kemp's ridley sea turtle (*Lepidochelys kempii;* Milton et al., 1994).

An imminent threat is the inundation and erosion of nesting beaches during episodic events with high water levels and/or waves (Figure 1.2a). Incubating turtle nests are highly susceptible to sea- and freshwater inundation, which may disrupt the temperature and moisture conditions that facilitate the gas, water, and heat exchange between the eggs and surrounding sand (Ackerman, 1997; Mortimer, 1990). Nest flooding has been reported in the literature as a major threat to sea turtle populations (e.g., Gammon et al., 2023; Patrício et al., 2021; Van Houtan & Bass, 2007; Ware et al., 2021) and has motivated various management efforts, including the relocation of freshly laid nests to higher elevations, safer beaches, or tailored hatcheries (Pintus et al., 2009). Although the species-specific tolerance of nests to inundation is not yet fully understood, recent studies suggest both the duration and frequency of flooding events are critical factors affecting egg viability (Foley et al., 2006; Limpus et al., 2021; Pike et al., 2015). Therefore, while flooding itself may mostly occur overland (due to wave runup, storm surges, or even tidal overwash; Caut et al., 2010; Martins et al., 2022), beach groundwater dynamics may also be critical in determining the impact on individual nests (Foley et al., 2006; Ware & Fuentes, 2018).

Aside from flooding, storm erosion can significantly alter beach morphology (Coco et al., 2014; Gomes da Silva et al., 2020), which may impact nesting on a time-scale of several seasons, for example by exposing a larger part of the beach to frequent inundation (Long et al., 2011). Beaches generally recover from storm erosion over time (e.g., Castelle et al., 2017), but individual events can still have a strong impact on local sea turtle populations. This is particularly true for severe storms, including tropical cyclones. Many nesting beaches lie in areas prone to tropical cyclones and are therefore vulnerable to extreme inundation and erosion (Dewald & Pike, 2014; Fuentes et al., 2011; 2019). Some of the World's largest green turtle populations nest almost exclusively on small, remote atoll islands (e.g., Raine Island, Australia and East Island, Hawai'i). In extreme cases, these islands can be

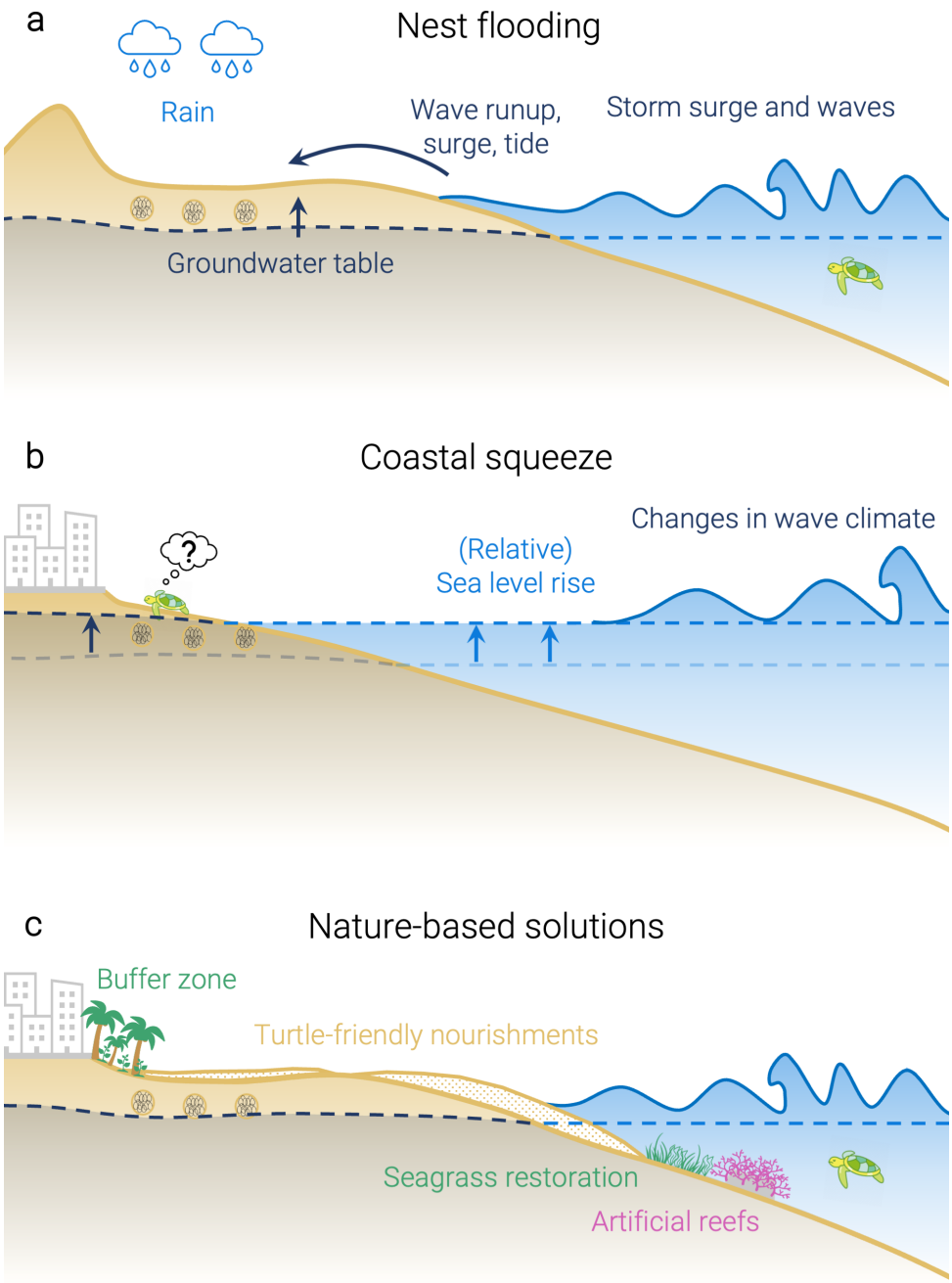

Figure 1.2: Schematic cross-shore profile of a nesting beach (not to scale), showing: a) processes related to nest flooding and erosion; b) processes related to coastal squeeze; and c) examples of potential NBS that could help mitigate flooding and erosion on nesting beaches. Though we show a cross-shore schematic here for simplicity, the shown processes are not exhaustive and also have alongshore drivers and variability.

completely washed away, as happened to East Island during Hurricane *Walaka* in 2018 (Baker et al., 2020).

On longer time-scales, structural erosion and coastal squeeze may gradually diminish the amount of nesting habitat available to sea turtles (Figure 1.2b; e.g., Fish et al., 2005; Fuentes et al., 2010; Katselidis et al., 2014). Structural erosion can have several causes, including sea level rise (SLR), longshore sediment transport disruption, river damming, or climate-induced shifts in sediment supply. Moreover, beaches also respond to interannual to decadal climate oscillations (e.g., El Niño/Southern Oscillation, ENSO; Barnard et al., 2015; Castelle et al., 2024). Hence, long-term changes in these signals may also lead to erosion at nesting beaches (e.g., intensifying ENSO episodes; Cai et al., 2014; Vos et al., 2023b). Coastal squeeze occurs when the eroding coastline cannot migrate landward due to a fixed barrier, either human-made (e.g., sea wall) or natural (e.g., cliff), leading to a narrowing or even disappearing beach (Pontee, 2013). Even where migration space exists, it remains unclear whether sediment supply and beach morphology can keep up with accelerating SLR (Rosati et al., 2013; Vitousek et al., 2017b).

These threats to global nesting beaches are likely to intensify in the future along with projected human and climate change-induced impacts: Storms and seasonal to interannual climate signals (e.g., ENSO) are expected to become more frequent and severe (Cai et al., 2014; Knutson et al., 2021; Reguero et al., 2019), raising the risk of nest flooding and erosion. Sea level rise will increase the frequency of flooding events and elevate coastal groundwater levels (Rotzoll & Fletcher, 2013; Taherkhani et al., 2020). Nearly 90% of globally identified nesting sites are located in the tropics (Figure 1.3; Mazaris et al., 2014), which is the geographical zone most vulnerable to increased coastal flooding from sea level rise (Vitousek et al., 2017a). Finally, only a quarter of global nesting sites are located in protected areas, and many lie in developing countries (Mazaris et al., 2014), where the coastal zone will become more and more developed (Neumann et al., 2015), increasing the risk of structural erosion and coastal squeeze.

Figure 1.3: Overview of global sea turtle nesting sites (all species, indicated in dark green) documented by SWOT (Halpin et al., 2009; Kot et al., 2021) and WIDECAST (Eckert & Eckert, 2019).

1.2. Toward nature-based solutions that enable sea turtle nesting

Within coastal science and engineering, there has been an increasing shift towards nature-based solutions over the past decade, whereby the focus is shifting from *building in nature* to *building with nature* (de Vriend et al., 2015). This has led to more research on how coastal processes and engineering interventions affect the local ecology, biodiversity, and ecosystem services. Coastal nature-based solutions may offer promising opportunities to preserve global sea turtle nesting habitats. For instance, the design of turtle friendly beach nourishments or the restoration/addition of coastal vegetation and reefs may help mitigate flooding and erosion (Figure 1.2c).

Several sea turtle species appear to be capable of the (assisted) colonization of new nesting grounds (e.g., Barbanti et al., 2022; Shaver & Caillouet Jr., 2015). The most prominent example of this is the emergence of a new Kemp's ridley nesting population at Padre Island National Seashore in Texas (Gulf of Mexico), through a long-term nest relocation and head-starting program (Shaver & Caillouet Jr., 2015). But also in the Mediterranean, for example, green and loggerhead turtles are increasingly colonizing new beaches in the cooler, western part of the basin (e.g., Italy and Spain), likely as a response to warming temperatures (Hochscheid et al., 2022; Mancino et al., 2023). These phenological shifts indicate that, as global temperatures rise, sea turtles may increasingly be forced to venture beyond their current nesting and foraging habitats (Fuentes et al., 2024; Laloë & Hays, 2023; Patel et al., 2021). Therefore, nature-based solutions that enable nesting on sandy beaches may potentially even help expand global turtle nesting habitats to new beaches.

Effectively designing and implementing such solutions requires a comprehensive understanding of the beach ecosystem, including biotic (e.g., nesting characteristics) and abiotic (e.g., longshore/cross-shore processes) factors at play (Slinger & Vreugdenhil, 2020). Yet, despite the clear need for an interdisciplinary approach (Nel et al., 2014), collaboration between the (scientific) sea turtle and coastal communities remains limited. As a result, past assessments of coastal threats to nesting beaches have mostly relied on ecological knowledge, without expertise on coastal morphology and hydrodynamics. For example, most studies assessing impacts of SLR on nesting beaches have simply added an elevated water level to a static beach topography, without considering any morphological changes (the so-called *bathtub* approach, e.g., Fish et al., 2005; Fuentes et al., 2010; Rivas et al., 2023). At the same time, while many of the driving processes behind coastal threats to nesting beaches are studied by coastal scientists and managers (e.g., flooding and erosion during storms), sea turtle habitat is not commonly considered in coastal engineering projects. Hence, there is a need to study the coastal processes that threaten (or enable) sea turtle nesting on sandy beaches.

1.3. Research objective

To address the growing coastal threats to sea turtle nesting habitats and the current disconnect between coastal and ecological sciences, the overarching aim of this thesis is to:

> Identify coastal processes that govern the vulnerability of sea turtle nesting beaches, and assess their implications for global habitat suitability and conservation.

Herein, coastal processes encompass the hydrodynamic and eco-morphological processes related to the short- and long-term evolution of the beach. For example, episodic flooding of the beach through storm surges or the long-term evolution of the shoreline. These processes can be seen as either enablers or threats to sea turtle nesting (e.g., prolonged flooding of turtle nests is a threat, whereas the lack thereof is an enabler). The overarching aim is divided into three specific research questions (RQ), forming the basis for this thesis:

RQ1 What are the driving processes behind sea turtle nest flooding on sandy beaches?

RQ2 How vulnerable are key global nesting beaches to erosion and sea level rise?

RQ3 How do regional coastal characteristics influence global habitat suitability for sea turtle nesting?

While RQ1 and RQ2 assess physical threats to existing nesting sites (flooding and erosion), RQ3 shifts to a global perspective, seeking to understand how coastal characteristics shape the spatial distribution of suitable nesting habitats. Answering these different research questions requires integrating multiple lines of evidence. Therefore, this thesis uses a mix of methods and tools—including field experiments, numerical modeling, remote sensing, global datasets, statistical analyses, and machine learning—to illustrate the broad potential of coastal science tools for sea turtle conservation, which are essential for developing an integrative approach to assess nesting beach vulnerability and guide targeted interventions.

To assess the driving processes behind nest flooding (RQ1), an extensive field campaign was carried out on Galveston Island, Texas, USA, to gather in-situ data of local hydrodynamics, groundwater, temperature, sediment characteristics, and beach morphology. These field data were analyzed using statistical and spectral techniques. The vulnerability of nesting beaches to erosion (RQ2) is analyzed through a combination of satellite-derived shorelines, numerical modeling, and global datasets. Finally, the global distribution of sea turtle nesting (RQ3) is assessed using global datasets and machine learning algorithms. The following section outlines the thesis structure and how these methods are applied in the different chapters.

1.4. Outline

This thesis consists of seven chapters. This first chapter has provided an introduction to the coastal threats facing sea turtle nesting beaches and the challenges in finding solutions, along with the objective and approach of this thesis. The remainder of this thesis is structured as follows:

Chapter 2 describes the field campaign on Galveston Island, providing detailed information on the field site, instrumentation, and collected data. This includes a technical validation of the measurements along with practical guidelines on how to use the openly accessible dataset.

In **Chapter 3**, the field observations are analyzed to assess the drivers of nest flooding on Galveston Island, providing an answer to RQ1. Through advanced spectral methods we analyze how waves, tides, storm surge, and rain drive fluctuations in the beach groundwater, resulting in the flooding of turtle nests.

Chapter 4 combines satellite-derived shorelines, shoreline modeling, and global datasets to analyze the shoreline evolution, characteristics, and future vulnerability at nine globally important sea turtle nesting sites, thereby answering RQ2. The analysis identifies seasonal and long-term shoreline change patterns, forecasts the future shoreline position under various SLR scenarios, and quantifies available accommodation space based on backbeach elevation and infrastructure.

Chapter 5 addresses RQ3 by combining global datasets with machine learning algorithms to establish patterns in the coastal characteristics of global nesting regions. First, the influence of 22 variables (e.g., wave height, tidal range, sea surface temperature) on the distribution of nesting sites for each species is assessed. A clustering method is then used to identify new, potentially suitable nesting regions around the world, based on the most influential variables.

In **Chapter 6**, the results of chapters 2–5 are discussed within a broader perspective of how coastal monitoring and modeling can aid global sea turtle conservation. We introduce a stepwise framework linking ecological thresholds, coastal processes, and management interventions across scales to integrate sea turtle ecology and coastal management. We call for increased interdisciplinary collaboration and outline potential future research directions to move toward nature-based solutions that enable sea turtle nesting.

Finally, **Chapter 7** presents the main conclusions of this thesis by providing an answer to the three research questions, along with a list of specific recommendations for follow-up research.

Chapters 2–6 are written as standalone journal papers, meaning there is some repetition of concepts throughout the thesis, particularly in the introductions of the individual chapters.

Cover photo by Lauren Owens Lambert ©: Kemp's ridley sea turtle (*Lepidochelys kempii*) nesting on Padre Island, Texas, USA.

2

Field site, instrumentation, and collected data

Abstract
Beach groundwater and nearshore hydrodynamic data were collected during a field experiment along two dissipative beach transects on Galveston Island, Texas, in the fall of 2023. The monitored beaches serve as nesting habitat for the critically endangered Kemp's ridley sea turtle. Conditions ranged from calm to stormy, with two storms occurring during the experiment, inundating the entire beach up to the dune toe. Collected hydrodynamic data include readings from pressure loggers submerged in the foreshore and mounted in groundwater wells in the backshore, data from two wave buoys about 1.5 km offshore, and GoPro timestacks of the instantaneous waterline (wave runup). Other collected data include bathymetry and topography surveys, subsurface temperature and moisture content readings, and sediment characteristics. This comprehensive dataset can be used to (1) study relevant beach inundation and groundwater processes, including their effect on the local ecosystem (e.g., repeated flooding of sea turtle nests), (2) study the propagation of nearshore hydrodynamic processes into the beach matrix and groundwater table, and (3) validate existing beach groundwater models.

This chapter has been published in *Scientific Data* as:

Christiaanse, J. C., Antolínez, J. A. A., van der Grinten, M. J., Taal, F., Figlus, J., Dellapenna, T. M., Ritt, B., Marshall, C. D., Tereszkiewicz, P. A., Cohn, N., Majzlik, E. J., & Reniers, A. J. H. M. (2025). Measurements of groundwater, hydrodynamics, morphology, and sand temperature at a dissipative sea turtle nesting beach. *Scientific Data*, 12, 123. [Link]

2.1. Background & Summary

Sandy beaches serve important societal and ecological functions, not only as natural barriers protecting the inhabited coastal zone from ocean hazards, but also as habitats for a diverse range of species (e.g., nesting sea turtles and marine birds; Nel et al., 2014). However, beaches are under increasing pressure due to climate change and human activity (Ranasinghe, 2016). Rising sea levels and more frequent and intense extreme weather events not only lead to increased overland flooding (Cayan et al., 2008; Ranasinghe, 2016; Vitousek et al., 2017a) but also alter groundwater dynamics (Befus et al., 2020; Bjerklie et al., 2012; Housego et al., 2021).

Groundwater dynamics play a pivotal role in coastal ecosystem functions, as they influence habitat health (Masterson et al., 2014), salt intrusion (Bear et al., 1999), coastal flooding (Rotzoll & Fletcher, 2013), and sediment transport dynamics (Bauer et al., 2009; Masselink et al., 2009). The groundwater table is expected to follow sea level rise rates (Bjerklie et al., 2012; Michael et al., 2013) and is above mean sea level under normal circumstances (overheight; Turner et al., 1997). There can be considerable short-term variability in the groundwater table (> 1 m) due to high water level events, wave runup, and precipitation (Housego et al., 2021). A higher mean groundwater table may compound the effects of these short term events. For example, higher beach groundwater levels have been reported to increase wave runup (Delisle et al., 2023). These challenges are especially critical in low-lying habitats like barrier island systems (Housego et al., 2021; Masterson et al., 2014) and for endangered species like sea turtles, who depend on sandy beaches for nesting: turtle nests, buried in the sand, require a relatively narrow temperature and moisture window during their 6–8 week incubation period (Ackerman, 1997), and are therefore vulnerable to inundation from overland flooding and groundwater (Patrício et al., 2021; Van Houtan & Bass, 2007).

To continuously assess these risks and evaluate potential solutions, researchers and engineers rely on existing knowledge and numerical models to predict beach groundwater dynamics. However, groundwater dynamics are influenced by a complex interplay of factors, including beach slope (Sous et al., 2013; Turner et al., 1997), sediment size and permeability (Gourlay, 1992; Raubenheimer et al., 1999; Turner et al., 1997), and hydrodynamic forcing (Delisle et al., 2023; Turner et al., 1997). Not all of these processes are fully understood, and many existing beach groundwater models (e.g., Delisle et al., 2023; Nielsen, 1990; Raubenheimer et al., 1999) have not been validated against extensive field data across a variety of beach environments. While multiple studies report field data, relatively few combine observations of groundwater and swash (Horn, 2006), and the data are often not readily accessible (e.g., Raubenheimer et al., 1999; Turner, 1998). Therefore, enhancing our understanding of these processes through field observations is crucial for reducing uncertainty in model predictions and developing strategies to restore and preserve beach habitats effectively.

Here, we present data collected during a field campaign in the fall of 2023 at two beach transects on Galveston Island, Texas (Gulf of Mexico, Figure 2.1a). These dissipative, fine-grained beaches (Wright & Short, 1984) serve as nesting habitat for many marine species, among which the critically endangered Kemp's ridley sea turtle (*Lepidochelys kempii*; Valverde & Holzwart, 2017). We measured hydrodynamic processes in the foreshore and groundwater dynamics in the backshore over a period of 1.5 months, using an array of eight pressure loggers per transect—two submerged in the foreshore and six mounted in

groundwater wells between the high tide line and the dune toe (Figure 2.1b). Offshore wave conditions were recorded with two directional wave buoys. These observations were accompanied on several days by GoPro video footage of the instantaneous shoreline (wave runup). We also recorded the sand temperature at a moderate potential turtle nest depth (≈ 40 cm) next to each groundwater well and a vertical profile of sand temperature and moisture content near the dune toe (where most turtles nest). Finally, we carried out multiple bathymetric and topographic surveys and derived sediment characteristics from extracted cores.

All data were collected between 16 October 2023 and 29 January 2024 (Figure 2.2) and covered a range of different conditions. Two storms occurred, with high waves and water levels inundating the backshore and wave runup reaching up to the dune toe. During these storms, the groundwater head at the dune toe reached the sand surface for several hours. We also observed calm conditions and low water levels during consistent offshore winds. Significant wave heights at the wave buoys ranged from 0.1 to 1.8 m and the total mean water level in the foreshore from −0.4 to 1.2 m NAVD88. This comprehensive dataset can be used to (1) study relevant groundwater and inundation processes, including their effect on the beach ecosystem (e.g., repeated flooding of sea turtle nests), (2) study the propagation of nearshore hydrodynamic processes into the beach matrix and groundwater level, and (3) validate existing beach groundwater models.

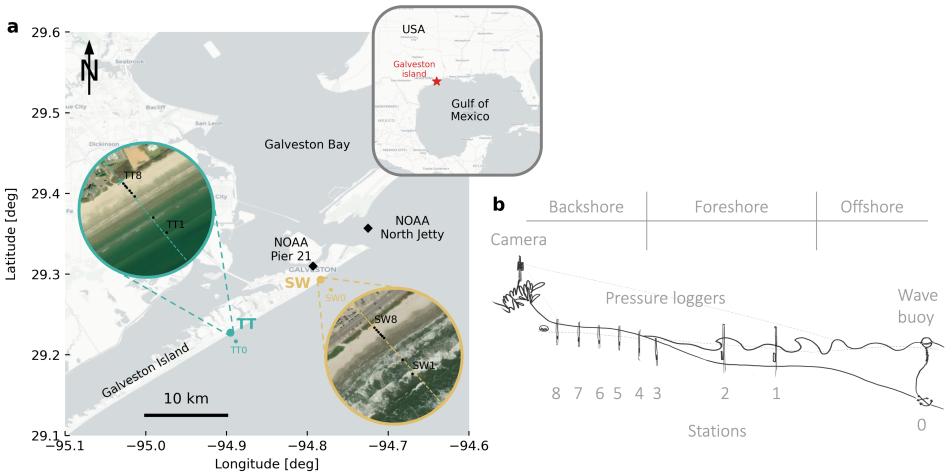

Figure 2.1: Overview of the field experiments. a) Geographical overview of the area around Galveston Island, including the two field sites and NOAA stations. Satellite snapshots show the two field site transects with stations 1–8. Station 0 (offshore) is shown on the large map. b) conceptual illustration of the experimental setup at each transect (not to scale). At offshore station 0 a wave buoy measures the incoming wave conditions. Foreshore stations 1 and 2 are equipped with submerged PLs. Backshore stations 3 to 8 are equipped with PLs in groundwater wells and TLs. Basemaps are from OpenStreetMap (www.openstreetmap.org/copyright) and satellite snapshots from ESRI World Imagery (ESRI, 2024).

2.2. Methods

2.2.1. Study area

Galveston Island, situated along the upper Texas Gulf coast, is a sandy barrier island which shelters Galveston Bay from the Gulf of Mexico. This large bay connects the Houston metropolitan area to the ocean. Galveston Island stretches southwest for about 45 km from the bay entrance and is fronted by sandy beaches across its entire length, with dunes of about 1–3 m height. It serves as an important habitat for many plants and animals, including two species of sea turtles—Kemp's ridley and loggerhead (*Caretta caretta*, only sporadically; Seney & Landry, 2008; Valverde & Holzwart, 2017). The Kemp's is critically endangered and typically only nests along the Gulf of Mexico and southeast US coasts. In the southwest, a naturally stable tidal inlet (San Luis Pass) separates Galveston Island from Follet's Island. At the northeastern end of Galveston Island, a 3.5-km-long jetty protects the shipping channel into the bay. The city of Galveston is located on the northern part of the island and is protected from the sea by a 17-km-long concrete seawall, constructed in the early 1900s, which has essentially replaced the dunes behind the beach (Davis, 1951).

General circulation patterns along the upper Texas coast are strongly related to the larger-scale current patterns in the Gulf of Mexico and exhibit a seasonal variation, with a mean northeast bound alongshore current in summer and southwest bound for the remainder of the year (Zavala Hidalgo et al., 2003). This coincides with the predominant seasonal wave directions (south in spring/summer and southeast in fall/winter), although wave heights are generally low (mean $H_s < 1$ m; NOAA, 2024a). Though Galveston Island has a micro-tidal, mixed-diurnal tide (mean spring tidal range $\approx$ 0.8 m; NOAA, 2024b), local water levels are very dynamic and regularly differ from the astronomical tide by a factor of two. This is expected to be (partly) caused by atmospheric pressure variations and wind- and wave-induced setup (Huff et al., 2020). Furthermore, the region has experienced high sea-level rise rates in the past century (6.5 mm/year since 1904) and is prone to hurricanes during the Atlantic hurricane season (June–November; Paine et al., 2021).

Galveston Island's beaches are mild-sloping and fine-grained ($D_{50} \approx$ 100–160 μm; Maglio et al., 2020; USACE, 2022). In front of the city, they are interrupted by groins every 300–500 m and are regularly nourished, most recently in 2017 and 2019 with dredged material from the bay entrance channel, which is significantly coarser than the native sediment (Elko et al., 2021; Maglio et al., 2020). South of the city, there have not been regular nourishments. The combination of the seawall and groins has starved the southwest-bound sediment supply and led to significant erosion southwest of the city in the past decades (up to several meters per year; Feagin et al., 2005; Paine et al., 2021). The coastline in front of the city is generally stable or extending seaward, though mainly due to the nourishments (Paine et al., 2021).

2.2.2. Experimental setup

The experiments were conducted at two field sites along Galveston Island's gulf coast: Tipsy Turtle (TT) located about 10 km southwest of Galveston (in front of the Tipsy Turtle Sea Bar & Grill, hence the name); and Sea Wall (SW) located in Galveston, in front of the sea wall between 18th and 19th Street. Location TT represents a more natural beach system, with no recent nourishments, whereas location SW is in front of the city, where nourishments have

been more frequent.

The field campaign consisted of three deployments (Figure 2.2): one pre-deployment at TT from 20 to 30 October 2023 (D1, 10 days) and two main deployments from 2 November to 4 December 2023 at TT (D2, 32 days) and from 7 November to 4 December 2023 at SW (D3, 27 days). The two main deployments (D2 and D3) had the same experimental base design, consisting of nine measurement stations spread over the cross-shore profile, with the most seaward station ≈ 1.5 km offshore and the other eight stations in the fore- and backshore (Figure 2.1). The stations were named by their field site abbreviation, followed by their number, starting from 0 at the offshore station to 8 at the landward end (dune toe). The pre-deployment (D1) had no offshore station, and its stations were distinguished from D2 by adding an extra 0. So, the stations range from TT10 to TT80 (D1), TT0 to TT8 (D2) and SW0 to SW8 (D3).

At station 0 (offshore) a directional wave buoy recorded the incoming wave conditions (only D2 and D3). Stations 1 and 2, located in the foreshore, were equipped with submerged pressure loggers (PL) to measure incoming waves and water levels. Stations 3 to 8 were spread over the (normally) emerged backshore, roughly between the high tide line and the dune toe, and equipped with PLs, mounted inside 1.5-m-deep groundwater wells, and temperature loggers (TL) buried in the sand at a typical turtle nesting depth (≈ 40 cm). At station 8 (dune toe) we also installed a vertical array of six buried moisture, temperature, and electrical conductivity loggers, spaced at ≈ 10-cm depth intervals, as well as a barometer recording air pressure and temperature (only D2 and D3). At stations 3 (high tide line) and 8 (dune toe) we extracted 1.5-m-deep sediment cores for analysis in the lab. On filming days, the GoPro camera was mounted on a pole near the dune, overlooking the transect and focused on the instantaneous waterline.

We conducted a total of 24 morphological surveys over both field sites (Figure 2.2). These included a pre-deployment topographic drone survey (16 October 2023) and a post-deployment bathymetric echo-sounder survey (29 January 2024) of both sites. The remaining 20 were standard walking RTK-GPS beach profile surveys.

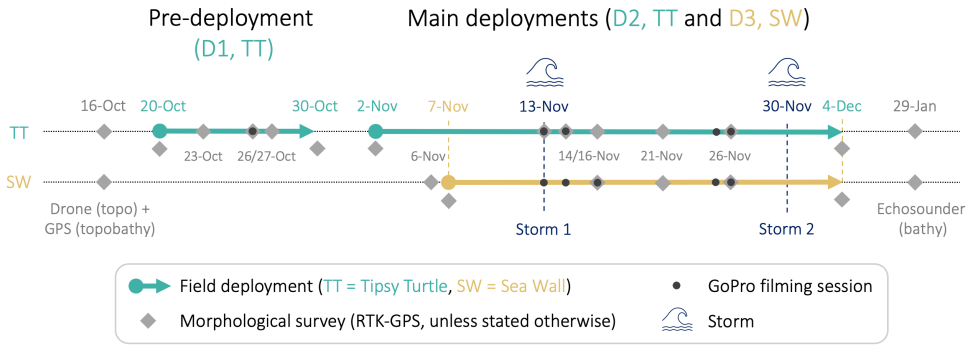

Figure 2.2: Timeline of the field campaign. The two dotted backround lines represent the timelines at the two field sites. Each deployment period is represented by an arrow. Important dates or surveys are highlighted with labels: morphological surveys (grey diamonds), GoPro sessions (black dots), and the two storms (wave icon). The timeline is not to scale.

2.2.3. Deployment and instrumentation

This section describes the instruments used during the experiments and how, when, and where they were deployed. This is done per instrument/data type. The instrumentation of deployments D2 and D3 is visualized in detail in Figure 2.3, along with timeseries of the measured nearshore water level, backshore groundwater table, and wave heights.

GPS and morphological surveys

Transect elevation profiles and instrument positions were recorded with handheld RTK-GPS equipment—*Leica CS15 controller* (Leica Geosystems AG, 2016a) and *GS08 rover* (Leica Geosystems AG, 2016b)—hereafter GPS for brevity. Horizontal coordinates were recorded in meters referenced to the North American Datum of 1983 (NAD83) Texas South Central (EPSG:6587), as easting (x-coordinate) and northing (y-coordinate). Elevations (z-coordinate) were recorded in meters relative to the North American Vertical Datum of 1988 (NAVD88). The GPS estimated the 3D accuracy of each point measurement and only recorded a position once the potential error was below 3.5 cm.

The GPS was used to record a total of 20 cross-shore elevation profiles across the deployments and field sites (13 at TT and 7 at SW, see dates in Figure 2.2). Starting from the first foredune, we took point measurements every few meters, depending on the slope. The GPS rover was mounted to a 2-m-long survey pole; hence profile measurements were limited to a water depth of roughly 1.5 to 1.9 m, depending on wave conditions. We timed profile surveys with low water levels as much as possible, but given the variable conditions, the extent of the profiles ranged from 40 to 170 m.

On 16 October, we conducted an aerial topographic survey using a *DJI Phantom 4 RTK* drone equipped with a *1-inch 20MP CMOS* camera (FOV 84° 8.8 mm/24 mm f/2.8-f/11 lens; DJI, 2023). The drone was combined with a *DJI D-RTK 2 High Precision GNSS Mobile Station* for accurate georeferencing. The GNSS mobile station was referenced at the National Geodetic Survey AW0617 (TT, approximately 2145 m from the field site) and AW1703 (SW, approximately 65 m from the field site) control benchmarks. The drone images were processed using *Pix4Dmapper* photogrammetry software to create a digital elevation model (DEM) and a 3D polygonal model, which includes texture and color data of the terrain. Next, a photogrammetric point cloud was built, based on the estimated drone positions and aligned images, providing detailed 3D data of the area's physical features. Additionally, we created an orthomosaic, a georeferenced and seamless image, which offers a comprehensive and accurate visual representation of the surveyed area. The individual photogrammetric techniques applied in this process are not explained in detail here, but for an overview of methods we refer to Colomina and Molina (2014). Post-processing quality assurance and accuracy testing was done using known horizontal and elevation measurements of other National Geodetic Survey or Galveston City reference markers found in the surveyed area. For both locations a horizontal accuracy of 3.26 cm +/- 1.2 cm and a vertical accuracy of 5.31 cm +/- 1.06 cm were found.

Finally, on January 29, when oceanographic conditions and vessel availability finally allowed, we conducted a bathymetric survey along the two transects with a vessel-mounted echo sounder. The survey covered an $\approx$ 80-m-wide area around each transect from the nearshore ($\approx$ 1 m depth) to about 1 km offshore through nine survey transects (spaced at roughly 10 m alongshore). The middle transect survey was extended to about 2.5 km

offshore, well beyond the location of the Spotters. This was done with a *Teledyne Odom Echotrac CV100* single-beam echo sounder (Teledyne Odom Hydrographic, 2015) operating at 200 kHz and mounted to the side of a small vessel. The exact position of the echo sounder was calculated from a *SBG Ekinox-E* inertial navigation system (SBG Systems, 2016), which received RTK-GPS positions from a *Trimble MPS865* GPS receiver (Trimble Marine Construction, 2021). Post-processing of the depth readings included despiking, smoothing, velocity of sound adjustments, and tidal correction and was done using *HYPACK Max* software. For the velocity of sound adjustment we applied sound velocity profiles measured near the two Spotter locations using a *Valeport SWiFT SVP* (Valeport Limited, 2023). Like the GPS profiles, the final seafloor coordinates were recorded as easting (x) and northing (y), referenced to NAD83 Texas South Central (EPSG:6587), and elevation (z), referenced to NAVD88.

Pressure loggers (PL)

We used a combination of *RBR Solo* (RBR Global, 2022) and *HOBO U20L* (HOBO Data Loggers, 2024) loggers to record pressure. The Solos recorded at 16 Hz, except for three which had a maximum sampling rate of 2 Hz. The Hobos measured at 1/15 Hz (every 15 seconds). We used the higher frequency loggers further seaward, where the water level can vary at smaller timescales than further landward. The distribution of the PLs over the eight fore- and backshore stations of each deployment is summarized in Table 2.1 and visualized in Figure 2.3d, e.

	1	2	3	4	5	6	7	8
D1	Solo 16	Solo 16	Solo 16	Solo 16	Solo 16	Solo 16	Solo 2	Solo 2
D2	Solo 16	Solo 16	Solo 16	Solo 16	Solo 2	Solo 2	Hobo	Hobo
D3	Solo 16	Solo 16	Solo 16	Solo 16	Solo 2	Hobo	Hobo	Hobo

Table 2.1: Overview of the PL distribution over the three deployments. The columns represent the eight stations in the fore- and backshore and the rows are the three deployments. The number behind 'Solo' indicates the sampling rate (16 or 2 Hz). All Hobos measured at 1/15 Hz.

In the foreshore (stations 1 and 2) we installed 16-Hz-Solos, roughly 50 cm above the bed, in a porous PVC casing, mounted to vertical galvanized steel poles, which were driven into the sand using a handheld post driver. Conditions during the deployment of D3 on 7 November were quite energetic, which made it difficult to position the PLs at SW1 and SW2. Therefore, they were mounted slightly higher above the bed. As a consequence, the PL at SW1 emerged during several low tides and did not record the lowest water levels.

Along the backshore (stations 3–8) the PLs were mounted inside 1.5-m-long slotted PVC wells with an interior diameter of 5 cm and 250 μm horizontal slots along the entire length. Since the slot size was larger than the relatively fine sediment at the beach ($D_{50} \approx 150\,\mu m$), we used filter cloth to limit the infiltration of fine sediment into the well. For D1 and D2 we tightened polyester filter felt (filtration rating 75 μm) around the wells with tie-wraps every 5 cm and covered the overlap with duct tape. For D3 we used an elastic polyester filter sock (filtration rating 88 μm), which could simply be pulled over the well (Figure 2.4a). The wells were sealed with pointed caps at the bottom and flat caps, with a 2-mm-hole for

pressure equalization, at the top.

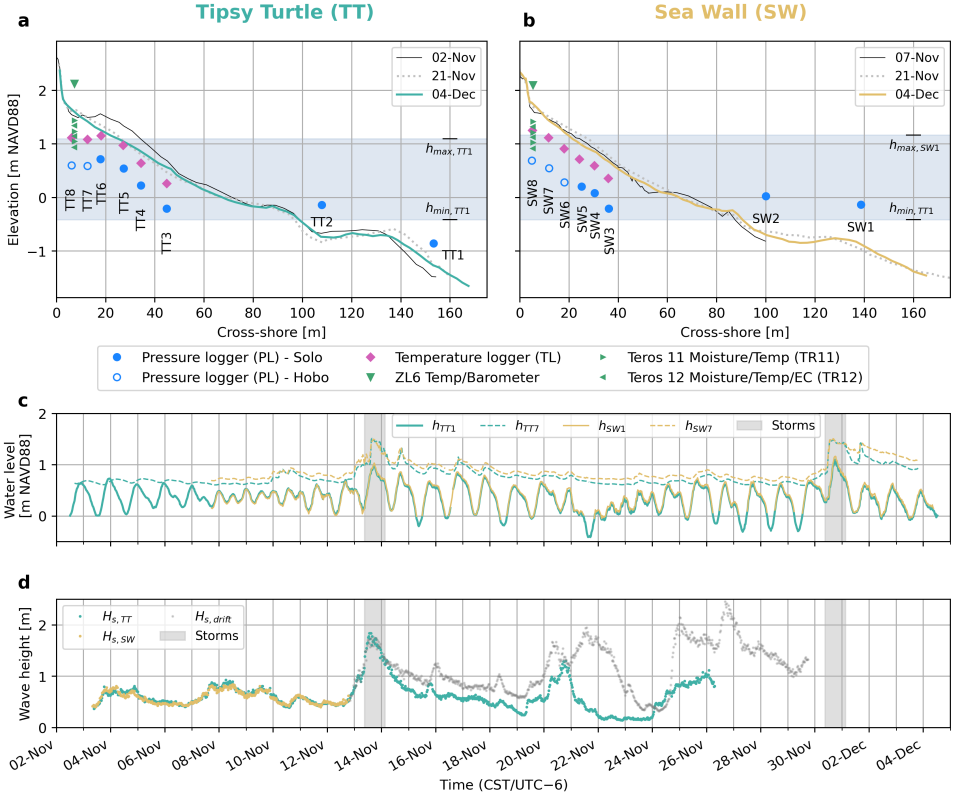

Figure 2.3: Experimental setup for the two main deployments (D2 and D3). D2 at TT is represented in teal and D3 at SW in beige. a, b) Cross-shore profiles and instrumentation; c) 30-minute averaged water level recorded in the foreshore (h_{TT1}/h_{SW1}) and near the dune toe (h_{TT7}/h_{SW7}); d) 30-minute significant spectral wave height recorded by the two wave buoys. Data from the SW buoy after it started drifting is shown in grey.

The wells were installed by water-jetting them into the beach surface (Figure 2.4e): we sawed off the tip of the pointed bottom cap to create a $\approx$ 3-cm-hole, through which we pumped water at high speed using a garden hose and a *Honda WX10T* water pump. This water stream liquefied the surrounding sediment, allowing the well to be pushed into the surface. We stopped when the top of the well was just above the sand surface and pushed a foam plug inside to seal the jetting hole in the bottom cap and prevent sediment from entering the well. The Solo PLs were tie-wrapped to a threaded metal rod which was fixed to the inside of the top well cap (Figure 2.4b). To bring them into position we inserted the rod into the well and tightly screwed on the top cap. The Hobos were thicker and not suitable to fix to the metal rod, so we connected them to the well cap through a cord, and installed them by carefully lowering them into the well and screwing on the cap.

Converting the pressure data to a referenced water level required the elevation of each PL. We measured their position with the GPS multiple times during the deployment. Be-

cause they were mounted inside wells (backshore) and PVC casings (foreshore) the GPS recordings were indirect, as we measured the position of the top of the well cap and PVC casing respectively. Therefore, we also measured the vertical distance between the sensor of each PL and the GPS measurement point. For the pre-deployment at TT (D1) the PL positions were recorded on 20, 23, 26, 27, and 30 October; for the main deployment at TT (D2) on 2, 13, 16, 21, 25, 26 November and 4 December; and at SW (D3) on 7, 14, 16, 21, 25, 26 November, and 2 and 4 December. However, depending on field conditions, not all loggers could be GPS positioned on every occasion, especially at the foreshore stations.

Temperature loggers (TL)

We recorded the sand temperature next to each monitoring well with *HOBO TidbiT MX Temp 400* temperature loggers (HOBO Data Loggers, 2022), measuring at 5-min intervals (1/300 Hz). The TLs were buried in the sand approximately 40 cm below the surface (at deployment). This depth corresponds to the typical nest depth of loggerhead turtles in this region, and was chosen as a representative sea turtle nesting depth since it is deeper than Kemp's ridley nests, but shallower than green turtle nests. For D1 we simply buried the TLs and attached them to the wells with a yellow cord to easily retrieve them again. For D2 and D3, we fixed each TL to the bottom of an 80-cm-long wooden stake. The stakes were then buried up to half their length ($\approx$ 40 cm). This way, the TLs could easily be retrieved, while we marked the stakes with safety tape to serve as visual signals at the field site (as the wells themselves were not easily recognizable).

ZL6 and Teros loggers

A vertical array of three *METER TEROS 11 Soil Moisture and Temperature* (TR11) and three *METER TEROS 12 Soil Moisture, Temperature, and Electrical Conductivity* (TR12) loggers (METER Group Inc., 2024) was used to record vertical variations in soil characteristics at station 8 (dune toe). We only had one set available for D2 and D3, so it was deployed at TT8 (D2) from 2 to 21 November and at SW8 (D3) from 21 November to 4 December (Figure 2.6). The individual TR11/12 loggers were mounted to a wooden pole in alternating order at 10-cm depth intervals, starting with a TR11 (Figure 2.4d). They were connected to a *METER ZL6* data logger (METER Group Inc., 2023), mounted above the ground on the same pole. The ZL6 stored the TR11/12 data and recorded local air pressure and temperature, all at 5-min intervals (1/300 Hz). At TT, the array was installed with the first TR11 approximately 10 cm below the surface, the lowest TR12 therefore reaching about 70 cm deep. At SW we installed the array a little bit deeper, reaching from about 30 to 90 cm depth.

Wave buoys

At the offshore stations (TT0/SW0) we deployed two *SOFAR Spotter* wave buoys (Spotters; Sofar Ocean Technologies Inc., 2023) to record the incident wave conditions during D2 and D3. The Spotter uses satellite GPS to measure its local displacement in three dimensions (XYZ) at a 2.5-Hz sampling rate. From the resulting displacement timeseries it computes directional wave spectra at 30-min intervals (Sofar Ocean Technologies Inc., n.d.). Spotters also record their geographical position (latitude/longitude), the sea surface temperature, relative humidity, and estimated wind velocity and direction every 30 min (the wind parameters are derived from the computed wave spectra; Voermans et al., 2020). The Spotters were deployed from a vessel on 3 November in a water depth of $\approx$ 8 m (low-tide)—for TT0

this was ≈ 1.3 km offshore and for SW0 ≈ 1.8 km. They were moored to a floating buoy (11.2-liter volume), which in turn was anchored to the seabed through an anchor-chain with five 25-pound weights (total ≈ 65 kg for weights plus chain). This indirect mooring setup is recommended by SOFAR, giving the Spotters more freedom of movement compared to direct mooring.

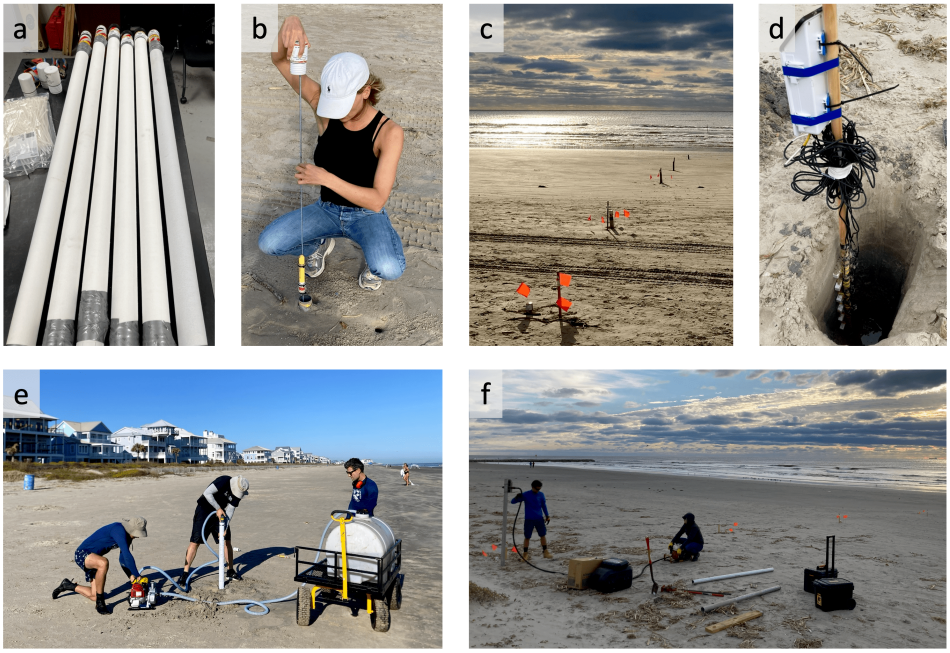

Figure 2.4: Photo impressions of the field campaign: a) Prepared PVC groundwater wells, wrapped in white filter cloth to limit fine sediment infiltration; b) Mounting of an RBR Solo PL in an installed well. The PL (yellow) is fixed to a metal rod, which is attached to the cap of the well; c) Overview of deployed instruments at TT. Each station is marked with orange warning flags; d) Installation of the Teros and ZL6 loggers at SW; e) jetting installation of one of the wells at TT; f) Extraction of sediment cores at SW using a vibracorer. All photos are courtesy of the authors.

GoPro footage

The transects were monitored with *GoPro Hero 10 Black* cameras (*23MP CMOS* camera sensor, 16 mm f2.8 lens; GoPro Inc., 2021) on 26 October (only TT), and 13, 14, 16 (only SW), 25, and 26 November (Figure 2.2). The goal was to use the camera footage to extract runup timeseries. Therefore, the cameras were positioned to capture a comprehensive view of the transect, focused on the instantaneous shoreline, while spanning from the distant horizon to the base of the dune. They were securely enclosed within a protective PVC box which was mounted to a pole, approximately 2 m above the ground (Figure 2.5). The *GoPro Quick* smartphone app was used for real-time stream access to ensure a satisfactory field view every time they were deployed. To maximize spatial and temporal resolution, the GoPros recorded at 4K with a rate of two frames per second. An external battery was used

to prolong the recording time, allowing up to twelve hours of filming. Both cameras were equipped with a 128 GB SD memory card (7–9 hours of filming required approximately 30 GB of local storage).

Intrinsic camera calibration was performed individually for each camera and filming mode to tailor the calibration parameters to specific settings. This involved capturing a short video of a flat checkerboard pattern with known dimensions, under several angles and distances. Radial and tangential distortions were corrected using the OpenCV Python toolbox (Bradski, 2000) along with the camera- and setting-specific calibration matrix, encompassing focal lengths and optical center location. The root mean square reprojection error, which should remain sub-pixel, served as a criterion for the quality of the intrinsic calibration.

Extrinsic camera calibration—georeferencing the two-dimensional undistorted images to real-world coordinates—was done by solving a photogrammetric equation with six unknowns: the real-world coordinates of the camera and the three camera rotation angles (azimuth, tilt, and swing). To approximate the solution we used the CIRN Quantitative Coastal Imaging Toolbox in Matlab (Bruder & Brodie, 2020). In theory, three ground control points (GCPs) with known real-world coordinates along with an educated guess of the camera position and angles are sufficient to solve the equation. However, in practice, more GCPs are needed for improved accuracy and reliability. We deployed six GCPs during each filming day, strategically positioned above the waterline to cover the entire area of interest and prevent colinearity as much as possible (Figure 2.5). During each GoPro deployment, the position of the camera and GCPs was recorded with the GPS.

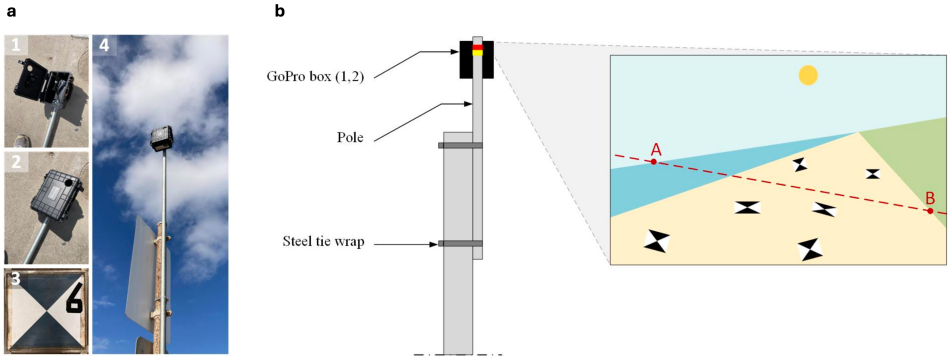

Figure 2.5: Photos (a) and conceptual setup (b) of the GoPro cameras to record the instantaneous shoreline. Panel a shows photos of the open (1) and closed (2) protective box, a ground control point (3), and the fully mounted system (4).

Sediment cores

To analyze the soil characteristics, we extracted two sediment cores from each field site using an *Oztec* vibracorer (Figure 2.4f). The cores were extracted at stations TT3/SW3 and TT8/SW8, representing the high-water line and the dune toe, respectively. The cores had a length of approximately 1.5 m and were extracted on 20 October (TT) and 21 November (SW), due to limited availability of the vibracorer. Hence, the SW cores were extracted after

the first storm on 13 November, which eroded some of the surface, although the erosion at SW was significantly less than at TT (Figure 2.3d,e). After extraction, the cores were sealed and stored in a cool room at 3°C. Between 1 and 4 December, we split the cores in the laboratory and carried out three separate analyses:

- **Grainsize distribution**: We used a *Malvern Mastersizer 2000* (Malvern Instruments Ltd., 2007) to determine the grain size at 10-cm intervals over the length of each core. At each interval, we extracted a small sediment sample from a 1-cm-thick layer of the core (i.e., between the top and 1 cm from the top, between 10 and 11 cm from the top, and so on). The sample was suspended in water in a small plastic centrifuge tube and then analyzed by the Malvern. To get a more reliable grain size estimate, the Malvern ran each sample three separate times and returned all three measurements, as well as the average.

- **Line-scan imaging**: We created high-resolution line-scan TIFF images of the entire length of the split cores. We used a *Geoscan V* line-scan camera (exposure time 10 ms, calibration aperture 14.12, image aperture 11.39) integrated in a *Geotek Multi-Sensor Core Logger (MSCL)* system (Geotek, 2021). Each core was scanned with a resolution of 200 pixels per centimeter (i.e., 1 pixel = 50 μm).

- **XRF spectrometry**: We conducted X-ray fluorescence (XRF) spectrometry using an *Olympus Vanta XRF* integrated into the same *Geotek MSCL* system as the line-scan (Geotek, 2021). The XRF measured the elemental abundances of a range of elements between Magnesium (Mg) and Uranium (U) every 5 cm.

2.2.4. Maintenance and disruptions

Several instruments needed some form of maintenance during the fieldwork, causing gaps in the recorded data. Furthermore there were some unforeseen incidents during the deployments, also causing disruptions. In the processed timeseries, these gaps were filled with *Not a Number (NaN)* values. These disruptions are summarized here and an overview of the activity of each instrument, including gaps, is presented in Figure 2.6.

Pressure loggers

During all deployments we carried out (irregular) inspections of the monitoring wells, quickly unscrewing the cap to check the logger. These quick inspections usually took no more than 1–2 min. Additionally, the Hobo PLs, measuring at 1/15 Hz, reached their internal storage capacity after about six days. Hence, they had to be removed from the well to offload the data at least every six days, which normally took about 15 min. The Solos had enough capacity to record continuously for the entire deployment duration. Nonetheless, on 16 November, we retrieved all deployed PLs (D2 and D3, foreshore and backshore) to offload data. This was done as a precaution to check if anything went wrong and to safely back up the first part of the data. This means that no data were recorded at SW (D3) between 08:45 and 11:30, and at TT (D2) between 13:45 and 16:20 Central Standard Time (CST/UTC–6). Next to these regular maintenance breaks, there were several incidents that led to gaps in the data and/or changes in the vertical position of the PL:

- After the retrieval of the instruments of D1, the PL from TT20 (*solo02*) was unresponsive and could not be read out. No exterior damage was discovered so it was sent to RBR Global for assessment and repair. Unfortunately, no data could be recovered from the logger, so there is no recorded pressure data for D1 at TT20.

- The monitoring well at TT60 (D1) was hit by a truck on 27 October at 12:27 CST (time determined from spike in recorded pressure). Luckily, the PL (*solo06)* was not damaged and kept recording. We replaced the well and reinstalled the PL at 16:15 CST on the same day.

- Similarly, the well at SW5 (D3) was hit by a truck on 9 November at 13:09 CST, however, we only discovered this on 13 November. The PL (*solo09*) was not damaged and kept recording, although during the hit it moved downward by 11 cm. The time and vertical movement were determined from a clear step in the recorded pressure. We removed the PL on 13 November 13:15 CST and replaced the well and reinstalled the PL on 14 November 10:30 CST, which moved the logger upward again by 6 cm.

- On 13 November, during a quick check, we discovered that the plug in the well at SW8 was not weighted correctly and had moved upward around 13:20 CST (time determined from step in pressure data), also pushing the installed PL (*hobo05*) upward (unlike the Solos, which were fixed to a metal rod, the Hobos were hanging on a cord from the well cap). We pushed the plug down again and put extra weight on top and the PL was in position again on 13 November 20:35 CST.

- After the storm on 13 November the steel poles at TT1 and TT2 (D2) were visibly tilted, moving the PLs (*solo03* and *solo04*) slightly downward (more so at TT1). Unfortunately the only pre-storm recording of the PL positions was on 2 November, directly after deployment. After the storm, the positions were recorded on 16 and 21 November and 4 December. The difference between the pre-storm position and the average of the three post-storm ones gives a downward vertical movement of 9.3 cm at TT1 (*solo03)* and 3.7 cm at TT2 (*solo04*), although it is not entirely clear how accurate the pre-storm positions were and if the entire movement was due to the storm. We could not identify a significant step in the recorded pressure series so the movements likely happened gradually during the storm.

- During the data offload on 16 November, we discovered some sand in the lower part of the well at TT3 (D2), which probably entered the well during the storm on 13 November. There were no problems retrieving the PL (*solo05*), however as a precaution we reinstalled it about 16 cm higher up on the metal rod.

- During the data offload of the Hobos at TT (D2) on 27 November we discovered that *hobo01* at TT8 had malfunctioned after the previous offload on 21 November. No data could be recovered for this period, and we replaced it with a spare Hobo for which we kept the same ID (*hobo01*) from 27 November 9:03 CST. We used the same cord so the logger elevation did not change.

- Finally, the PL elevations at TT2, TT6, SW1, and SW2 led the loggers to be emerged during several periods with low water levels. In the foreshore (TT2, SW1, and SW2)

this was the case during some of the low tides. In general the PL elevations were chosen based on a trade-off between having enough depth and minimizing the risk of the logger getting buried if it were installed to close to the bed. At SW1 and SW2 the loggers were also installed slightly higher because of the difficult and energetic conditions during deployment, and were not changed afterwards. At TT6 the logger was installed a few cm too high for the lowest water levels on 28 and 29 November, due to the presence of the berm at deployment, resulting in gaps of six and four hours, respectively.

Temperature loggers

There was no regular maintenance involved for the TLs, but several disruptions occurred, all of which during D2 at TT. We believe that the reason for this is that the beach at TT eroded significantly more than at SW (up to 40 cm in some places, Figure 2.3d), which destabilized the wooden stakes to which the TLs were mounted.

- On 13 November around 17:30 CST, during the first storm, the TLs at TT5 (*TL113*) and TT6 (*TL114*) were washed away (as they were mounted to wooden stakes protruding from the sand surface). The loggers were not damaged and were recovered and reinstalled on 14 November 12:30 CST.

- On 14 November around 11:00 CST the TL at TT3 (*TL111*) disappeared from its position (the reason is unclear). It was found and recovered undamaged in the foredune later in November but not reinstalled.

- On 30 November around 17:00 CST, during the second storm, the TL at TT4 (*TL112*) was washed away. It was recovered undamaged on 1 December but not reinstalled.

Wave buoys

Unfortunately, neither Spotter completed the full deployment period. The SW0 Spotter started drifting from its deployment position on 12 November, nine days after its deployment. It is unclear what exactly happened, but it was most likely caught or hit by a vessel or trawling net, as it briefly moved upwind. It then started drifting southward freely on 14 November and kept recording for the next 17 days. It finally stranded on 29 November in Mexico, about 490 km southwest of Galveston, and was recovered, still connected to the secondary floating buoy (but not the anchor chain and weights). The TT0 Spotter stayed in position until 26 November, when it was collected in the net of a local fishing vessel (confirmed by the captain of the vessel). Unfortunately, the crew released the buoy from the vessel a few days later and it ultimately stranded on Matagorda Beach on 30 November, roughly 120 km southwest of Galveston, where it was recovered. During its trip, it lacked the ballast chain (likely removed on the vessel) and therefore the required stability for reliable measurements. Fortunately, both Spotters were recovered intact and with undamaged memory cards. There is no Spotter data from either TT0 or SW0 after 26 November, which includes the second storm on November 30th. However, the data from the SW0 Spotter during its entire trip to Mexico is available (Figure 2.3g).

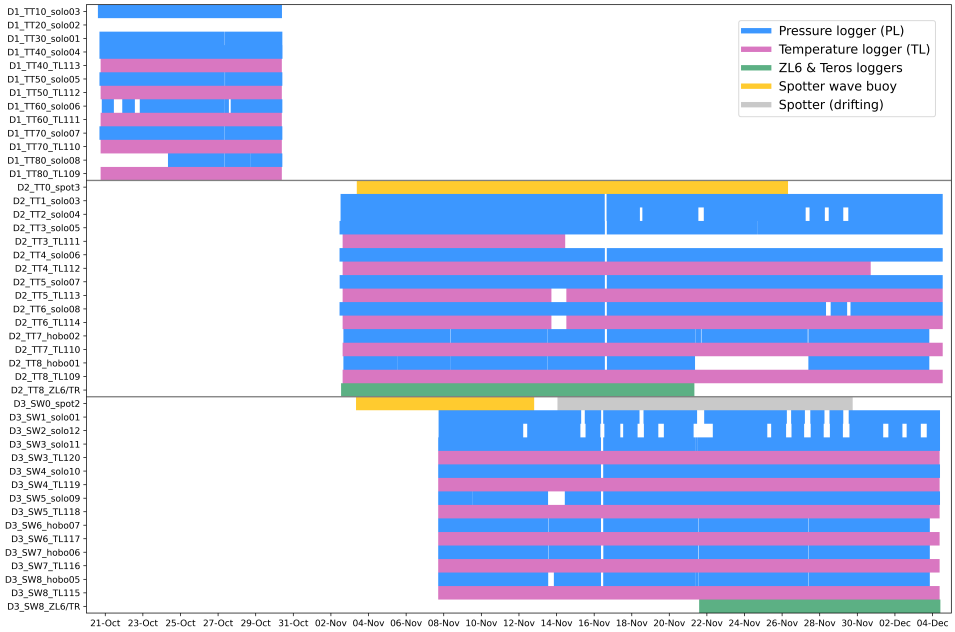

Figure 2.6: Instrument activity for all three deployments (separated by the grey horizontal lines) of the pressure loggers (blue), temperature loggers (pink), ZL6/Teros loggers (green), and wave buoys (yellow). The ZL6/TR row represents the ZL6 logger as well as all six TR11/12 loggers connected to it.

2.3. Data Records

All data are stored open access on the 4TU.ResearchData repository, as a data collection called *TURTLE: Measurements of groundwater, hydrodynamics, sand temperature, and sediment characteristics at two beach transects on Galveston Island, Texas, USA* (Christiaanse et al., 2024a), accessible through the following link: https://doi.org/10.4121/93256801-ed01-4627-9e49-8607967a0853. The collection includes seven datasets (the peer reviewed version numbers corresponding to this publication are denoted by the v-numbers at the end):

- TURTLE - Main data - deployment D1 - location TT (20 – 30 Oct 2023), v3, [Link]
- TURTLE - Main data - deployment D2 - location TT (2 Nov – 4 Dec 2023), v3, [Link]
- TURTLE - Main data - deployment D3 - location SW (7 Nov – 4 Dec 2023), v3, [Link]
- TURTLE - GoPro Timestacks (26 Oct – 26 Nov 2023), v2, [Link]
- TURTLE - Beach profiles and bathymetry (16 Oct 2023 – 29 Jan 2024), v2, [Link]
- TURTLE - Topographic drone survey (16 Oct 2023), v2, [Link]
- TURTLE - Supplementary data, v2, [Link]

Each deployment has its own main dataset, which includes the PL, TL, Spotter, ZL6/TEROS, and sediment core data. The morphological GPS and echo sounder surveys are gathered in the 'Beach profiles and bathymetry' dataset. The drone survey data and GoPro timestacks are stored as separate datasets because of their relatively large file sizes. Finally, the supplementary data contain external data that were used in the processing of the observations (i.e., air pressure and water level from NOAA, 2024b).

2.3.1. Deployment datasets

Each deployment dataset contains all data gathered as part of that specific deployment, except the morphological surveys and GoPro footage. For D1 this is only PL and TL data, for D2 and D3 it also includes the, ZL6/TEROS, Spotter, and sediment core data (even though the cores at TT were extracted on 20 October, the data are gathered in the main data of D2). Each instrument/data type has its own directory within the dataset, where all data files are located, and which also contains a folder called 'raw' with the unaltered logger output files (if applicable). Additionally, each folder contains a *README.txt* file with detailed explanations and instructions.

All processed deployment data files follow the same naming convention (except the sediment core data, see below): *YYYYMMDD_YYYYMMDD_AA_SSS_dataname.ext*, where the two *YYYYMMDD* represent the start and end date of the data record, *AA* is the deployment ID (D1/D2/D3), *SSS* is the field site ID (TT/SW) or station ID (TTX/SWX), *dataname* is the data identifier, and *ext* is the file extension. For example, the data from *solo03* at TT1 of D2 are gathered in the NetCDF file *20231102_20231204_D2_TT1_solo03.nc*. Furthermore, for all time series data, the timestamps have been converted to Unix epoch time (seconds since 1 January 1970, UTC).

The first directory, '0_Meta', contains relevant meta data for the instruments of the corresponding deployment. This includes CSV files with the measured GPS positions of each instrument, the pressure offsets for each PL used to correct the raw data (see Technical Validation section), an overview of the bucket tests carried out to validate the PLs, and a matrix containing the instrument activity shown in Figure 2.6.

The processed PL time series are gathered in the directory '1_PL', in one NetCDF (*.nc*) file per PL. Each NetCDF file includes five variables: raw pressure (pr), processed pressure (pp), water depth (d), logger elevation (z), and water level relative to NAVD88 (h). For storage efficiency, the data have been converted to Pascal (pressure) and mm (depth/elevation) and stored as integers, with invalid data points given a value of -9999. Raw pressure, pr, are the raw pressure readings from the logger. The processed pressure, pp, is pr corrected for the atmospheric pressure at NOAA's Pier 21 station (ID 8771450, included in supplementary dataset) and, if required, a logger specific pressure offset (see Technical Validation section). Additionally, values at inactive timestamps (e.g., data offload, emergence during low-tide, disruptions) have been filtered and replaced with -9999. The water depth above the logger, d, was computed hydrostatically by dividing pp by the gravitational acceleration ($g = 9.81\ m/s^2$) and the density of sea water ($\rho = 1023.6\ kg/m^3$). The logger elevation, z, was derived from the GPS recordings (see Technical Validation section) and the final water level relative to NAVD88, h, is the sum of d and z. Due to their large file sizes, the raw output files of the PLs are gathered in a separate directory, '9_PL_raw', so they can be downloaded separately if desired. These are *.rsk* files for all Solos, which can

be read using the *Ruskin* software by RBR; and *.hproj* files for all Hobos, which can be read using the *HOBOware* software from HOBO.

The TL data are gathered in the directory '2_TL'. The 'raw' folder contains the raw CSV files extracted from each individual TL. The processed time series (converted to Unix epoch time and filtered for inactive timestamps) are gathered in a single CSV file. Its columns represent the measured sand temperature at each corresponding station and are named as *SSS_LOGID*, where *SSS* is the station ID and *LOGID* is the logger ID (e.g., *TT3_TL109* represents the sand temperature at station TT3, which was measured with logger TL109).

The ZL6/TEROS data are gathered in the directory '3_ZL6TEROS'. The 'raw' folder contains the raw Excel file (.xlsx) extracted from the ZL6 logger. The processed 5-min-interval time series of air temperature (at, ZL6), air pressure (ap, ZL6), volumetric water content (wc, TR11/12), sand temperature (st, TR11/12), and electric conductivity (ec, TR12) are gathered in one CSV file. The variables are named as *Z_LLLL_vv*, where *Z* is the vertical position (starting from 0 for the ZL6 down to 6 for the lowest TR12), *LLLL* is the logger type (ZL6/TR11/TR12), and *vv* is the variable abbreviation (at/ap/wc/st/ec). For instance, *4_TR12_wc* represents the volumetric water content measured by the TR12 at the fourth position from the surface.

The Spotter data are gathered in the directory '4_Spotter'. The 'raw' folder contains the 15 raw CSV files extracted and compiled from the Spotter SD card, including the full 2.5-Hz displacement time series. For an overview of the data in each raw file we refer to the Spotter GitHub repository (Smit, 2021). The folder 'bulk' contains the 30-min-interval bulk parameters that were transmitted live during the Spotter deployment, including spectral wave parameters, estimated wind velocity and direction, relative humidity, sea surface temperature, and geographic position (latitude/longitude). The folder contains one CSV file each for the raw and processed bulk data. The latter were manually filtered for outliers in the significant wave height and mean wave period (Figure 2.3g). All wave parameters at a timestamp with an outlier in either the significant wave height or mean wave period were set to *NaN*. The wind, temperature, humidity, and geographic coordinates were not filtered for outliers, but we did filter data at invalid timestamps at the start and end of the time series for all variables. The CSV file for the SW0 Spotter contains an additional column, *drift_flag*, which was set to 0 during the normal deployment and to 1 for all records gathered when it was drifting (see teal and grey data in Figure 2.3g). Invalid data entries in-between were filtered. Due to privacy reasons we removed all location data from before the Spotters were released in the water and after they stranded on the beach (both in the raw and processed files).

The sediment core data are gathered in the directory '5_Cores' of the main datasets of D2 (TT) and D3 (SW). All files are named *YYYYMMDD_SSS_dataname.ext*, where *YYYYMMDD* represents the extraction date of the core, *SSS* the station ID, *dataname* the data identifier, and *ext* the file extension (e.g., *20231121_SW3_grainsize.csv* contains the grain size distributions for the SW3 core). Grain size data are provided in two files per core: the raw TXT file containing the tabled output of the Malvern, and a processed CSV file containing the summarized grain size distributions at each depth interval, based on the average of the three Malvern runs per sample. The line-scan images are provided in four files per core: the raw TIFF image of the entire core, an edited TIFF image with a length-scale along the left side, a raw XML file containing metadata about the core dimensions, camera setting,

and resolution, and a raw RGB file. The three raw files can be read together using *Geotek* software (Geotek, 2021). For the XRF we only provide the raw data files: an OUT file containing the tabled output data in text format, and a binary DAT file containing the data and instrument calibrations, which can be read using *Geotek* software.

2.3.2. Morphological surveys

The morphological survey data is split into two datasets, one containing the beach profile and bathymetric echo sounder data and a separate dataset for the drone survey because of its large file sizes. The first is divided into two directories: *GPS*, containing the hand-held GPS profiles, and *Echo*, containing the bathymetric echo sounder survey data. The GPS profiles are provided in one CSV file per recorded beach profile and named *YYYYMMDD_AA_SS.csv*, where *YYYYMMDD* represents the survey date, *AA* the deployment ID (D1/D2/D3), and *SS* the field site ID (TT/SW). The columns in the CSV file contain the timestamp of each point measurement and the horizontal and vertical coordinates, including coordinates in a deployment specific cross-shore coordinate system (see below). The echo sounder survey is provided in two CSV files (one per field site) containing the time and horizontal and vertical coordinates.

The horizontal coordinates of the GPS surveys are given in two official coordinate reference systems: NAD83 Texas South Central easting (e) and northing (n) in meters (EPSG:6587), and WGS84 latitude (lat) and longitude (lon) in degrees (EPSG:4326). The vertical coordinate (z) is in meters relative to NAVD88. To reference all profiles and instrument positions of one deployment to a single cross-shore axis, we created a local, deployment specific coordinate system by fitting a line through the longest and straightest profile of each deployment and defining an origin behind the dune toe (Figure 2.3a-e). We then projected all GPS profiles and instrument positions to this line resulting in a cross-shore coordinate, x, the distance to the origin, positive in seaward direction. The alongshore coordinate, y, represents the distance between the projected and measured points. The local coordinate systems are referenced to real-world coordinates through the axis angle (relative to North) and the coordinates of the origin (Table 2.2).

The topographic drone survey data are gathered in five files per field site: two TIFF files for the DEM and the orthomosaic, a LAZ file containing the point cloud, an OBJ file containing the 3D polygonal surface mesh, and an accompanying MAT file which contains material definitions for the polygonal mesh (e.g., color and texture). The latter two can be loaded into CAD software.

	Base profile	Angle $[°N]$	Origin E $[m]$	Origin N $[m]$	Origin lon $[°]$	Origin lat. $[°]$
D1	20 Oct	142.03	998954.83	4161529.28	-94.89517	29.22765
D2	2 Nov	140.61	998951.14	4161526.83	-94.89521	29.22763
D3	4 Dec	138.22	1009525.55	4169174.65	-94.78367	29.29320

Table 2.2: Local cross-shore coordinate system for each deployment, referenced to real-world coordinates through the angle relative to North and the coordinates of the origin (E/N = easting/northing, lon/lat = longitude/latitude).

2.3.3. GoPro timestacks

The GoPro timestacks are gathered in a separate dataset and all files are named *YYYYMMDD_HHMM_AA_SS_GXCODE.ext*, where *YYYYMMDD* is the date of the recording, *HHMM* is the starting time in CST, *AA* is the deployment ID, *SS* is the field site ID, and *GXCODE* is the GoPro file ID. For storage efficiency, the GoPros store a long filming session in several separate files, the order of which can be determined from the GoPro file ID. For practical reasons, we named all files with the starting time of their respective session. The timestacks are stored in NetCDF files which contain the RGB values of each pixel, as well as the time and space dimensions. The spatial coordinates are given in easting and northing NAD83 Texas South Central. Additionally, we projected the timestack transects to the deployment specific cross-shore coordinate systems (x and y coordinates). There is also a folder with plots of each timestack so they can be visually inspected without having to read all the data. Due to the enormous file sizes of the individual videos, we decided not to include them in the data repository. However, the video footage may be acquired by contacting the authors directly.

2.3.4. Supplementary data

The supplementary dataset contains records of the air pressure recorded at NOAA station *8771450* (Galveston Pier 21) and water level recorded at NOAA station *8771341* (Galveston Bay Entrance, North Jetty). Both were obtained from the NOAA Tides and Currents database (NOAA, 2024b) and are provided as CSV files.

2.4. Technical Validation

2.4.1. Pressure loggers

Atmospheric pressure is continuously recorded at 6-min intervals by NOAA's Pier 21 station in Galveston (station ID *8771450*, 2 km from SW and 14 km from TT; NOAA, 2024b). The ZL6 logger also measured air pressure at TT8 from 2 to 21 November and at SW8 from 21 November to 4 December. The recorded pressure from the ZL6 compared very well to the NOAA station at both field sites ($r = 1.00$, $RMSE = 0.21$ mbar at TT and $r = 1.00$, $RMSE = 0.16$ mbar at SW).

We let all PLs record the atmospheric pressure for at least 30 min, before and after each deployment, as well as once during the two main deployments (on 16 November). To validate the recorded pressure time series we compared them to the ZL6 and/or NOAA readings. If the mean absolute deviation over the calibration period was larger than 1 mbar ($\approx$ 1 cm of water under hydrostatic conditions) we corrected the pressure data according to the measured offset. Furthermore, we conducted bucket tests with seawater from the respective field site before and after each deployment, and again on 16 November, during the two main deployments. During these tests, the loggers were simultaneously dipped in a bucket of water. Once the water surface settled from the disturbance, we measured the water level in the bucket. The corrected pressure time series converted to within 1–2 cm of the measured bucket water levels, which we deem to be an acceptable margin. Most of the PLs did not show a significant temporal drift in the recorded offset, so a constant offset was applied to the entire time series. For some loggers the offset was more complicated:

- *solo08* at TT80 (D1) remained emerged for the first days of D1 as the groundwater

table did not reach the logger. Until late on 21 October the readings compare well to the air pressure measured by NOAA. However, from then on a negative pressure offset started to develop, growing linearly until 24 October at about 4:50 CST, when a sudden spike increased the pressure by about 5 mbar, moving it back near the recorded pressure by NOAA. During this period the groundwater table was rising (confirmed by the other loggers). The spike was likely caused by the groundwater first touching the logger. Unfortunately, it is not entirely clear whether the pressure offset was still present when the logger was fully submerged. However, after the spike, the recorded pressure was near the NOAA record again, slowly increasing as the groundwater submerged the logger. Additionally, *solo08* recorded the correct water level in both bucket tests. We therefore assumed no pressure offset when the logger was submerged. Given that the groundwater table at TT80 cannot be derived from the logger when it was emerged, we filtered all recorded pressure values until 24 October 8:00 CST (when the sensor appeared fully submerged) in the processed data.

- *solo01* showed a positive offset with a temporal drift in both of its deployments (D1 and D3). For D1 it went from $\approx$ 5.5 mbar at the start to $\approx$ 7.5 mbar at the end, and at D3 from $\approx$ 6 mbar at the start to $\approx$ 8 mbar at the end (during the offload on 16 November it was $\approx$ 7 mbar). We therefore linearly interpolated the offset between the determined values on 7 and 16 November and 4 December.

- After malfunctioning, *hobo01* was replaced by a spare logger, for which we retained *hobo01* as ID. The original *hobo01* had a constant offset of -2.5 mbar, whereas the new hobo had no offset. This was corrected in the processed time series.

- *solo09* (only deployed for D3 at SW5) appeared to be the most inconsistent logger with varying offsets, albeit always relatively small (< 2 mbar). However, in all three bucket tests it recorded the correct water level within 1 cm, so we did not apply any offset to it.

- For the Hobos of D3 (*hobo07* at SW6, *hobo06* at SW7, and *hobo05* at SW8) an offset was found at the time of deployment (7 November), when all three loggers appeared to be $2-3$ mbar off (also translating to $2-3$ cm in the bucket test). However, at the first data offload (13 November) the air pressures were not off anymore and no offset was found for the remainder of the deployment. Moreover, the difference in corrected pressures between the six groundwater stations did not seem disproportional during the first week. We figure the offset at the start may have been caused by the loggers needing to 'acclimatize' to the temperature. Given the relatively small offset and the uncertainty whether it persisted into the first deployment week, we did not correct it in the data (i.e., all three PLs had an offset of 0 over the entire deployment).

2.4.2. Logger elevations

Every point measurement with the GPS returned an estimate of its 3D accuracy, usually between 2–3.5 cm. Between multiple measurements of a fixed location, the expected range around the true position should therefore be 4–7 cm. This was tested by recording the position of five fixed points on three different days (10, 20, and 24 May 2024), resulting in a

mean elevation range of 4 cm ($std = 1.8$ cm). In theory, the more measurements are taken, the more the range should converge to its maximum value and the mean to the true position.

The first GPS recordings of the backshore PLs of D1 and D2 were taken shortly after jetting the groundwater wells into the beach and mounting the loggers. Given the rather intrusive jetting procedure, the soil around the well may have needed some time to settle back to pre-jetting conditions, potentially resulting in a slight movement of the well. This hypothesis is supported by the fact that the first recorded elevation was often at one of the limits of the measured range. We therefore excluded elevation recordings taken on the same day as the jetting when computing the elevation ranges for all backshore PLs (stations 3–8). This was only relevant for D1 and D2, as the wells for D3 were jetted on 6 November, a day before deploying the loggers and recording their positions.

The resulting elevation ranges are mostly below or near the expected 7-cm limit (Table 2.3). For four PLs, the elevation range was above this limit, namely 9.3 cm at TT40 (D1, *solo04*), 12.2 cm at TT1 (D2, *solo03*), 7.9 cm at SW7 (D3, *hobo06*), and 9.6 cm at SW8 (D3, *hobo05*). The large range at TT1 can be attributed to the tilting of the pole during the storm. However, we could not determine the exact cause for the higher ranges at TT40, SW7, and SW8. It could still be attributable to the uncertainty in the GPS measurement, however it is also plausible that the wells at these stations slightly moved at some point during the deployments. Practically the entire range at SW7 and SW8 can be attributed to a large elevation change between 14 and 16 November. It could be that the wells slightly moved due to something happening in the sand, but it seems unusual for that to happen in only two days' time and not during either of the storms. Another possibility could be interference from a bypasser, although one would then expect a relatively sudden shift, which we could not identify in either pressure time series.

	1	2	3	4	5	6	7	8	mean	std
D1	2.6	3.9	2.7	9.3	4.2	(0.7)	6.2	5.0	4.9	2.3
D2	(12.2)	4.9	4.2	4.1	4.1	5.3	3.2	5.2	4.4	0.8
D3	3.7	5.3	5.7	5.4	5.5	6.2	7.9	9.6	6.2	1.8

Table 2.3: Overview of the PL elevation ranges in cm measured with the GPS. Columns 1 to 8 represent the eight stations and the final two columns show the mean and standard deviation over the eight stations. The elevations for TT60 and TT1 (values in brackets at D1/6 and D2/1 respectively) were excluded from the mean and standard deviation. The reason is that they did not reflect appropriate conditions (the PL at TT1 moved during the storm on 13 November, and for TT60 there were only two measurements as the well had to be replaced mid-deployment).

For the final logger elevations, needed to derive the referenced water level from the pressure data, we used the mean of all valid recorded elevations (excluding the first recording directly after jetting, as mentioned above). In case the elevation of a PL changed over time, we adjusted this in the data. The sudden changes were easily corrected with a stepwise elevation profile in time. For the PLs at TT1 and TT2 we applied a linearly interpolated elevation profile to account for the elevation change over the course of the storm on 13 November. We used the only recorded pre-storm elevation (from 2 November) until 13 November at 10:00 CST and the mean post storm elevation as of 13 November at 21:00 CST. In between, we linearly interpolated the elevation.

For the foreshore PLs (stations 1 and 2) we did an additional validation step by comparing the observed water levels during calm conditions (low wind, low waves). The expected low surge and setup components mean that the water level at the two field sites and NOAA station 8771431 (Galveston Bay Entrance, North Jetty) should be similar. Small differences are still expected, especially compared to the NOAA station, which is in the inlet channel of Galveston Bay. We identified three periods of relatively calm conditions, from 17–18 November ($H_s < 0.5$ m), 21–23 November ($H_s < 0.3$ m), and 3–4 December. All three periods had generally low residual water levels (i.e., surge), shown by the small difference between the observed water level and the predicted astronomical tide at the NOAA station (Figure 2.7). Over the three periods, the difference between the observed water levels at the four field stations (TT1, TT2, SW1, SW2) and NOAA is very similar, with an RMSE around 6 cm for all four stations (Table 2.4). As expected, the RMSE between stations at the same location was significantly smaller (2.7 cm between TT1 and TT2, and 1.2 cm between SW1 and SW2). The RMSE between the same stations and different field sites (TT1 vs. SW1 and TT2 vs. SW2) was around 5 cm.

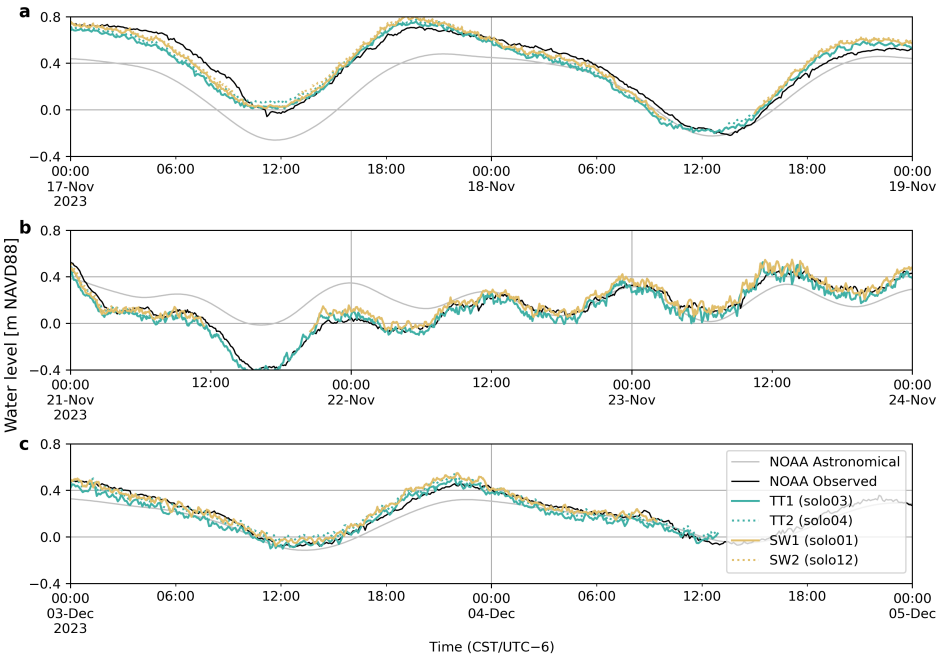

Figure 2.7: Recorded water levels at TT1 (*solo03*), TT2 (*solo04*), SW1 (*solo01*), SW2 (*solo12*), and NOAA station 8771341 (Galveston Bay Entrance, North Jetty), during three periods of relatively calm conditions (low wind and low waves): 17–18 November (a), 21–23 November (b), and 3–4 December 2023 (c).

	TT1	TT2	SW1	SW2	NOAA
TT1		1	0.99	0.99	0.97
TT2	2.7		0.98	0.98	0.96
SW1	5.3	4.5		1	0.97
SW2	6.0	4.9	1.2		0.96
NOAA	6.3	5.8	5.7	5.8	

Table 2.4: Correlation and RMSE between the recorded water levels at TT1 (*solo03*), TT2 (*solo04*), SW1 (*solo01*), SW2 (*solo12*), and NOAA station 8771341 (Galveston Bay Entrance, North Jetty), during calm conditions (low wind and low waves). The upper diagonal of the table shows the correlation coefficient (r) and the lower diagonal the RMSE in cm.

2.4.3. Sand temperature and water content

To assess the reliability of the sand temperature data we compared the readings of the TLs at the dune toe stations (TT8 and SW8) with those of the TEROS loggers at a similar depth. For TT8, this was the TR12 at position 4 (the fourth logger from above), whereas at SW8 the TL was situated roughly in between the TEROS' at positions 2 and 3. The temperatures agree well with a RMSE of $0.17°C$ at TT8 and $0.25°C$ at SW8 (Figure 2.8). The higher RMSE at SW8 makes sense as the TL elevation was in-between two TEROS loggers (we used the TR11 at position 3 to compute the RMSE as it was slightly closer). The errors may be partly caused by the horizontal distance (roughly 1–2 m) between the positions of the loggers. Moreover, at both locations the highest errors occur in the first hours after deploying the TEROS array (the TLs were deployed earlier). The installation of the TEROS array involved digging a deep hole, which stayed open for at least an hour, potentially affecting the sand temperature for several hours after.

We did not have any data to validate the measured water content. The TEROS loggers measure the dielectric permittivity of the soil, which is then converted to the volumetric water content (VWC) through a calibration equation. In the user manual it is claimed that the TEROS 11/12 factory calibration for mineral soils (Equation 2.1, where RAW is the raw data value) should derive the VWC with an accuracy of approximately 3% (METER Group Inc., 2024). However, for all six loggers, the observed VWC reaches up to $0.6 - 0.65$. Such high values seem unrealistic for sandy beaches, which generally have a porosity in the range of 0.35 to 0.5 (Atkins & McBride, 1992; Román-Sierra et al., 2014). Unfortunately, we did not calibrate the loggers to site specific soil samples due to time constraints and the mentioned accuracy claim in the user manual. We were therefore unable to correct the observations accordingly. Nonetheless, we make the data accessible, as the relative VWC values and trends thereof may still provide relevant insights into the sand moisture dynamics. Furthermore, the VWC values can be reconverted to the raw dielectric permittivity output using Equation 2.1. The raw values can then be converted to VWC again with a different calibration equation. However, the provided VWC should be used with care, taking the above into account.

$$VWC = 3.879 \cdot 10^{-4} \cdot RAW - 0.6956 \tag{2.1}$$

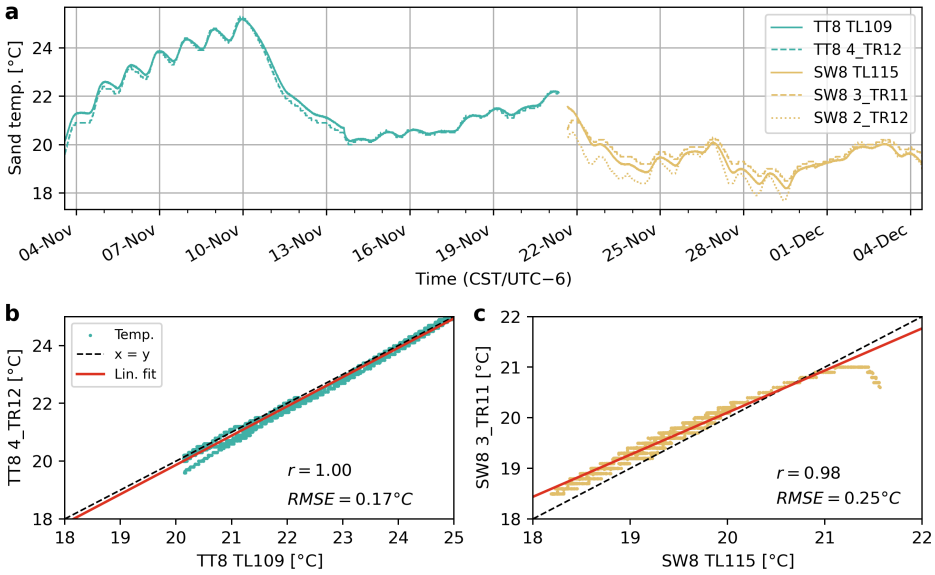

Figure 2.8: Comparison of the sand temperature readings between the Hobo TLs and the TEROS loggers at the two dune toe stations (TT8 and SW8). a) Time series of sand temperature at TT8 (teal) and SW8 (beige). Panels b and c show scatter plots of the Hobo TL versus the TEROS temperature data at the two stations, including the RMSE and correlation (r).

2.4.4. Wave buoys

The National Data Buoy Center (NDBC) operated by NOAA has a buoy (ID *42035*) that records half-hourly offshore wave and wind conditions approximately 37 km east of Galveston (NOAA, 2024a). Originally, the plan was to compare the Spotter data to the wave data from NOAA for validation. Unfortunately, buoy *42035* started drifting and stranded on Galveston Island on 25 October 2023, roughly one week before the deployment of the two Spotters. It remained out of service for the entire deployment duration and was only repaired and deployed again in May 2024. This means that there is no verified wave data near the deployed Spotter locations for validation, as the two next closest stations with wave data are NDBC buoy *42019* ($\approx$ 160 km southwest of Galveston) and NDBC buoy *42091* ($\approx$ 220 km east of Galveston), both of which are much further offshore than *42035*.

Given the simultaneous deployment of the two Spotter buoys in relative proximity to each other ($\approx$ 13.5 km), we compared the data of the Spotters as a simple validation step. This was only possible for the period between 3 and 12 November, however, before the SW0 Spotter (*spot2*) started drifting. For that validation period, the two Spotters compare well, showing high correlations for significant wave height ($r = 0.94$, $RMSE = 0.05$ m) and mean wave period ($r = 0.93$, $RMSE = 0.24$ s, Figure 2.9). Given the lack of further data, we refer to other, more comprehensive validation studies of Spotter wave and wind data (Beckman & Long, 2022; Kinsela et al., 2024; Raghukumar et al., 2019; Voermans et al., 2020).

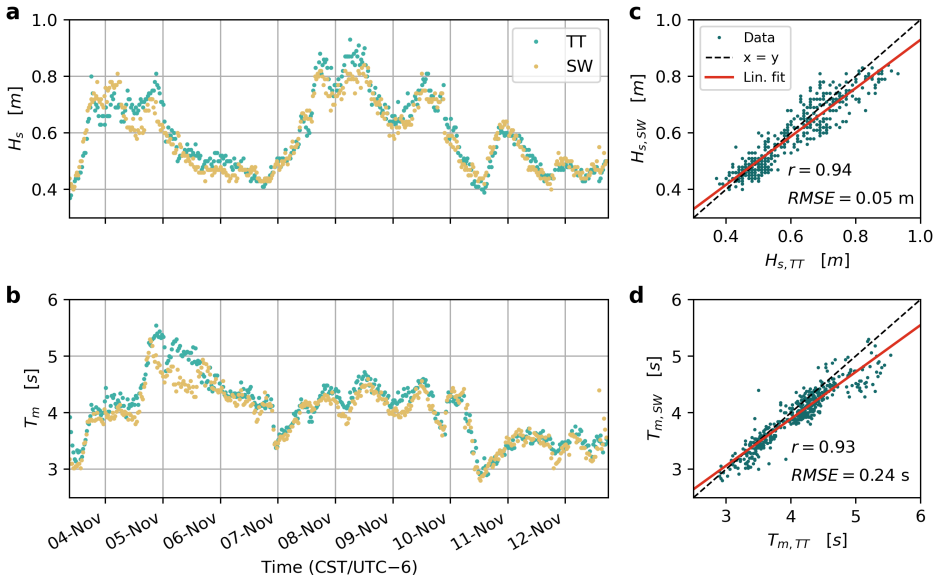

Figure 2.9: Comparison of the spectral wave data of the two Spotters between 3 and 13 November, showing timeseries of significant wave height (H_s, panel a) and mean wave period (T_m, panel b). Panels c and d show scatter plots with correlations and RMSE for H_s ($r = 0.94$, $RMSE = 0.05$ m) and T_m ($r = 0.93$, $RMSE = 0.24$ s) at TT0 and SW0.

2.4.5. Sediment grain size

The measured grain sizes at the beach surface showed a mean D_{50} of approximately 153 μm at TT and 172 μm at SW (Figure 2.10a-d). These results generally lie within the ranges reported in literature (Maglio et al., 2020; USACE, 2022). The Malvern Mastersizer 2000 is suitable for grain sizes up to 2 mm. While most of the sediment at the two field sites is much finer than that, certain soil layers contained a significant amount of shells/shell fragments larger than 2 mm, especially at SW. These are likely remnants of past nourishments, which were coarser than the native sand and contained shelly material (Maglio et al., 2020)—this also explains the coarser D_{50} at SW and most shelly material being found there, as it is much closer to the nourished areas. When preparing the samples for the Malvern we avoided large shell fragments as much as possible, meaning these were not adequately represented in the obtained grain size distributions. However, the core from SW3 contained so much shelly material between 62 and 98 cm from the top (Figure 2.10e, marked in red) that we could not prepare completely shell-less samples. Therefore, the derived grain size distribution for these layers may not be well represented by the Malvern results.

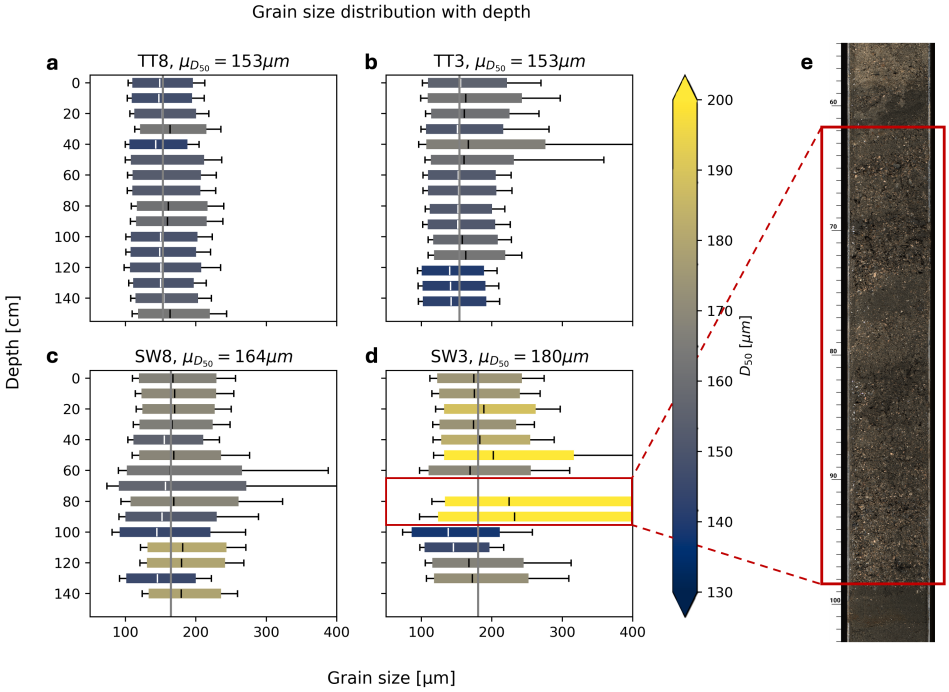

Figure 2.10: Overview of obtained grainsize distributions for the four cores. The boxplots show the obtained grain-size distributions over the depth of the cores at TT8 (a), TT3 (b), SW8 (c), and SW3 (d). The boxplot dimensions show the D_{50} (middle line and box color), the range between D_{20} and D_{80} (extent of the box), and D_{10} and D_{90} (whiskers). Panel (e) shows a snapshot of the linescan from the SW3 core, with the red boxes highlighting the section with predominantly shelly material.

Usage Notes—Usage notes for the specific data files are included in all data folders as *README.txt* files. Most of the data are either stored in NetCDF format (*.nc files) or CSV format (*.csv files). Both file types can be opened and read using most major coding languages. We used Python 3.12 for the processing of all data. If using Python, we recommend *Xarray* for reading NetCDF files and *pandas* for CSV files. The NetCDF files follow CF-1.8 conventions, so when reading them with *Xarray*, the unix time values are automatically converted to datetime objects and missing values (-9999) replaced by NaN (*Not a Number*). For any unanswered questions concerning the data or field experiments please contact the authors.

Acknowledgements—The field campaign and data collection described in this paper are part of the TURTLE project, which is funded by TKI Delta Technology with support from TU Delft, Texas A&M University, Deltares, and Boskalis (grant number T-DEL/2023/095). We would like to express our sincere gratitude to everyone who helped us in some form during the field experiments in Galveston, in particular: Annekee Groeninx van Zoelen, Julius Prins, Josh Joubert, Fangzhou Tong, Jaclynn Turnbaugh, Nicholas Diaz, Miranda Sauceda, Avery Franklin, Thomas Doe, Justin Cerv, and Thomas Muskwinsky. We also want to thank Pablo Ruiz Salcines and Herman Ramsden for helping with the recovery of the Spotter buoy in Mexico. We further express our thanks to the following experts for discussing the field campaign with us and sharing their thoughts and ideas: Prof. dr. Ian Turner, Dr. Britt Raubenheimer, Dr. Orencio Duran, Dr. ir. Paul van Wiechen, and Prof. dr. Carlos Duarte. Further, thanks to Dr. ir. Matthieu de Schipper and Pieter van der Gaag for their help in facilitating instrumentation from the TU Delft Waterlab. Finally, many thanks to Prof. dr. ir. Bas Jonkman for facilitating the connection between TU Delft and TAMUG from which this field campaign emerged, and to Prof. dr. ir. Stefan Aarninkhof for his help with the funding acquisition.

Author contributions—J.C., J.A., and J.F. acquired funding, J.C. conceived and coordinated the field experiments, J.C., J.A., M.G., F.T, J.F., and P.T. carried out the field deployments, J.C., J.A., J.F., T.D., C.M, N.C., and P.T. provided instrumentation for the field experiments, J.C. processed the pressure, temperature, wave, and sediment core data, J.C. and F.T. processed the GPS data, M.G. processed the GoPro footage, B.R. conducted and processed the drone surveys, E.M. conducted and processed the echo sounder survey, J.C. performed the technical validation, packaged the data, and wrote the original manuscript, all authors reviewed the manuscript.

Cover photo Florida Fish and Wildlife Conservation Commission ©: Loggerhead sea turtle (*Caretta caretta*) hatchling on a beach in Florida.

3

Drivers of nest flooding

Abstract
Beach groundwater dynamics play a critical role in coastal ecosystem functions, particularly in low-lying beach habitats used for nesting by endangered species like sea turtles. Incubating nests are susceptible to prolonged inundation below the groundwater table (GWT), as flooding duration critically affects egg viability. Understanding how oceanic processes and rain drive GWT fluctuations in the nesting area is essential for evaluating nest relocation strategies and designing nature-based solutions that mitigate nest flooding. Here, we analyze how infragravity waves, tides, storm surge, and rainfall drive short-term fluctuations (hourly to weekly) in the beach GWT on Galveston Island, Texas—a dissipative, mild-sloping barrier island system along the northwestern Gulf of Mexico coast. Applying tailored spectral analyses to field observations collected in 2023, we show that surge and rainfall dominate short-term GWT response in the nesting area, while higher-frequency wave and tidal signals are increasingly damped landward. To facilitate this analysis, we classify observed water levels into *groundwater*, *mixed*, and *submerged* regimes based on estimated wave runup. A flooding threshold analysis reveals multiple, prolonged nest inundation events (exceeding 12 hours) across the backshore, even for the shallowest nests. This strongly suggests that Galveston Island's beaches are currently unsuitable for turtle nesting, underscoring the need to continue the ongoing nest relocation program and further research nature-based solutions that enable sea turtle nesting (e.g., turtle-friendly nourishments).

This chapter has been published in *Coastal Engineering* as:

Christiaanse, J. C., Antolínez, J. A. A., Marshall, C. D., Figlus, J., Dellapenna, T. M., & Reniers, A. J. H. M. (2025). Beach groundwater response to ocean processes and rain on a mild-sloping barrier island: implications for sea turtle nest flooding. *Coastal Engineering*, 201, 104795. [Link]

3.1. Introduction

The increasing shift towards nature-based solutions in coastal engineering has led to a need for more research on how coastal processes and engineering interventions affect the local ecology, biodiversity, and ecosystem services (de Vriend et al., 2015; Nel et al., 2014). In this context, beach groundwater dynamics—the spatial and temporal variation of groundwater and moisture within the beach matrix—play a pivotal role in coastal ecosystem functions (Richardson et al., 2024), as they influence habitat health (Masterson et al., 2014), freshwater resources and salt intrusion (Bear et al., 1999; Holding et al., 2016), coastal flooding (Delisle et al., 2023; Rotzoll & Fletcher, 2013), and sediment transport dynamics (Bauer et al., 2009; Masselink et al., 2009). They are particularly important in low-lying habitats like barrier island systems (Holding et al., 2016; Housego et al., 2021; Masterson et al., 2014) and for endangered species like sea turtles, who depend on sandy beaches for nesting. Yet, despite its significance, groundwater is often overlooked in the design and analysis of coastal interventions (Rotzoll & Fletcher, 2013).

Sea turtles—key species in many coastal ecosystems worldwide (e.g., Christianen et al., 2023; Meylan, 1988)—bury their eggs in beach sand, where they incubate for 6–8 weeks. Successful incubation requires a relatively narrow range of temperature and moisture conditions that facilitates the exchange of gases, water, and heat between the eggs and surrounding sand (Ackerman, 1997; Mortimer, 1990). Consequently, turtle nests are highly susceptible to sea- and freshwater inundation, which has been reported as a major threat to sea turtle populations (e.g., Gammon et al., 2023; Patrício et al., 2021; Van Houtan & Bass, 2007; Ware et al., 2021) and has motivated various management efforts, including nest relocation (Pintus et al., 2009). Although the species-specific tolerance of nests to inundation is not yet fully understood, recent studies suggest that both the duration and frequency of flooding events are critical factors affecting egg viability (Foley et al., 2006; Limpus et al., 2021; Pike et al., 2015). Flooding itself mainly occurs overland through wave runup, storm surges, high tides, rainfall, or a combination thereof. These driving processes can raise the groundwater table (GWT) in the nesting area of the beach. Given the significance of inundation duration, the response of the GWT to these processes plays a large role in determining the fate of individual nests (McGehee, 1990; Patino-Martinez et al., 2014). While studies that investigate the implications and drivers of nest inundation are increasing (e.g., Carpio Camargo et al., 2020; Caut et al., 2010; Gammon et al., 2023; Lyons et al., 2022), very few actively include the GWT in their analyses (Foley et al., 2006; Guard et al., 2008; Ware & Fuentes, 2018). Therefore, understanding what drives groundwater fluctuations in the nesting area of the beach is critical to evaluate the need for management practices like nest relocation and to design nature-based solutions that can help mitigate the flooding of turtle nests (Limpus et al., 2021; Ware & Fuentes, 2018).

Numerous studies have analyzed the influence of coastal hydrodynamics on beach groundwater. In general, both field studies (e.g., Nielsen, 1990; Raubenheimer et al., 1999; Turner et al., 1997) and laboratory experiments (e.g., Cartwright et al., 2004) have demonstrated that the beach matrix functions as a low-pass filter, resulting in the attenuation of oceanic fluctuations (e.g., tidal signal) in the GWT as they propagate inland, accompanied by increasing phase lag and asymmetry. Analytical and field observations have shown storm-driven pulses (due to surge and wave effects) in the GWT to propagate further and faster inland than tidal oscillations (Housego et al., 2021; Li et al., 2004). These oceanic forcings,

along with rainfall, can drive considerable short-term variability (> 1 m) in the beach GWT (Housego et al., 2021). Above the GWT lies the capillary fringe (CF), an additional saturated zone where negative pore pressures draw water upward from below (Gillham, 1984; Turner, 1993). On longer time-scales, the combination of tides and waves drives a super-elevation of the beach GWT, as it rises more quickly than it drops (Nielsen, 1989; Turner et al., 1997)—i.e., the mean GWT is above mean sea level. Furthermore, the GWT is expected to follow sea level rise (Bjerklie et al., 2012; Michael et al., 2013), which could compound short-term fluctuations, for example by increasing wave runup (Delisle et al., 2023).

Short-term variations in the GWT and the CF are influenced by a complex interplay of factors, including beach slope (Sous et al., 2013; Turner et al., 1997), sediment size and permeability (Gourlay, 1992; Raubenheimer et al., 1999; Turner et al., 1997), hydrological factors (Holding et al., 2016; Turner et al., 1997), and hydrodynamic forcing (Delisle et al., 2023; Turner et al., 1997). For instance, the relative super-elevation and CF width are expected to be higher in fine-grained, mild-sloping beach systems, which have lower permeability and therefore slower drainage (Turner & Nielsen, 1997). However, not all of these processes are fully understood and their interactions vary across different coastal environments, so it remains challenging to generalize findings between different environmental settings (Horn, 2006; Turner et al., 1997).

Here, we analyze how ocean processes and rainfall drive short-term (hourly to weekly) fluctuations in the beach GWT, specifically focusing on events that cause sea turtle nest inundation. We use data collected during an extensive field campaign in the fall of 2023 on Galveston Island, Texas, USA (Christiaanse et al., 2025b)—a dissipative, mild-sloping barrier island beach system along the northwestern Gulf of Mexico coast. The observations enable us to assess the influence of infragravity waves, tides, storm surge, and rainfall on measured water levels between the shoreline and the dune toe. However, because the extent of the swash zone varied over time, the observed water levels did not always represent the pure beach GWT. To facilitate interpretation, we categorize the observed water levels into three regimes based on estimated wave runup: *groundwater*, *mixed*, and *submerged*. While we use the term GWT throughout this paper, our analysis explicitly focuses on ocean processes and rainfall acting directly on the beach system, and does not include inland groundwater processes (e.g., aquifer recharge or regional groundwater flow). Our results (1) provide new observations on the interplay of coastal hydrodynamics and the beach GWT on mild-sloping beaches (to our knowledge, the first such observations in the Gulf of Mexico); (2) aid local coastal managers in evaluating nest relocation strategies; and (3) support research toward nature-based solutions that enable sea turtle nesting on Galveston Island (e.g., turtle-friendly beach nourishments).

3.2. Methods

3.2.1. Study area

Galveston Island is one of many low-lying barrier islands along the northwestern Gulf of Mexico coastline. It is located along the upper Texas coast, roughly 45 km southeast of Houston (Figure 3.1a), and forms an important part of the Texas coastal protection system, as it shelters Galveston Bay from the Gulf of Mexico (USACE, 2021). Similar to other Texas barrier islands, Galveston Island began forming approximately 4500 years ago as submerged sandbars. These gradually evolved with an accumulation of fine sand deposits

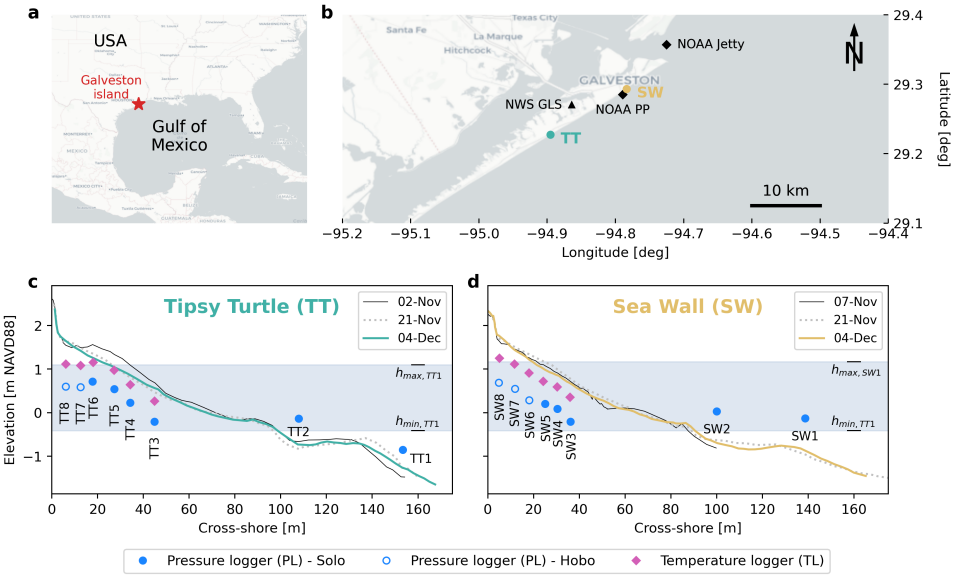

Figure 3.1: a) Location of the study area in North America. b) Geographic overview of the study area. The two field sites are marked in their respective colors, and external observation stations (NOAA & NWS) in black. c), d) Cross-shore profiles and instrumentation at the two field sites.

on top of older Pleistocene-era sediments (Garner, 1997). The island's surficial aquifer consists of a 10–15-m sand stratum, underlain by the confining *Beaumont Formation*—a Pleistocene unit primarily composed of clay with interbedded sand and silt (Capuano & Jones, 2022; Kreitler et al., 1977; Petitt & Winslow, 1957). The GWT is generally within a few feet of the surface (Garner, 1997). The surficial aquifer depth is comparable to those reported for other US barrier islands (e.g., the North Carolina Outer Banks; Housego et al., 2021). Following past studies, the regional aquifer structure is therefore approximated as homogeneous, despite small-scale heterogeneity (e.g., Befus et al., 2020; Housego et al., 2021; Rotzoll & Fletcher, 2013).

Galveston Island's beaches are mild-sloping and fine-grained ($D_{50} \approx 100$–$160\ \mu$m; see Christiaanse et al., 2025b; Maglio et al., 2020; USACE, 2022, for full grain size distributions) and are backed by about 1–3 m-high dunes. In front of the city of Galveston—located on the northeastern part of the island—the beach is interrupted by groins every 300–500 m and backed by a 17 km-long concrete seawall, which essentially replaces the dune. Although situated in a mixed-diurnal micro-tidal setting (mean spring tidal range ±0.8 m), local water levels show considerable variability, often deviating from the astronomical tide by a factor of two (NOAA, 2024b). This variability is likely caused by a complex interplay of barotropic and baroclinic processes, such as atmospheric pressure variations and wind- and wave-induced setup (Huff et al., 2020). In addition, the region has experienced high sea level rise over the past century (around 6.5 mm/year since 1904) and is prone to hurricanes during the Atlantic hurricane season from June to November (Paine et al., 2021).

The Kemp's ridley (*Lepidochelys kempii*) is the main sea turtle species to nest on Galveston Island, with sporadic nesting by loggerhead sea turtles (*Caretta caretta*; Seney &

Landry, 2008; Valverde & Holzwart, 2017). The Kemp's ridley is the most critically endangered sea turtle in the world and is endemic to the western Gulf of Mexico, although more recently nesting is occurring in the northern Gulf of Mexico and southeast US coasts. The nesting season occurs from April to July for Kemp's, and from May to October for loggerheads (Marquez, 1994). Galveston Island is outside the historic Kemp's ridley nesting range (which lies further south in Mexico), but the species was introduced to Texas through a large-scale head-starting program over the past decades (Marquez et al., 2005; Shaver & Caillouet Jr., 2015). As a result, the number of nesting females in Texas is steadily increasing. Moreover, Galveston Island's geographic position may enable it to become an important future climate refuge for the species. However, the continuous erosion and frequent inundation of Galveston's beaches combined with their low-elevation setting make it uncertain whether they can function as a suitable long-term nesting habitat for sea turtles. Due to the critically endangered status of the Kemp's ridley sea turtle, the current policy is to relocate all sea turtle nests in Texas to an incubation facility or corrals at Padre Island National Seashore, with a few exceptions (Shaver & Caillouet Jr., 2015).

3.2.2. Field measurements and data

Measurements of groundwater, hydrodynamics, and sand characteristics were collected during the TURTLE field experiments on Galveston Island in the fall of 2023. Here, we give a summary of the part that is relevant for this study. For a detailed description of the complete field site, experimental setup, instrumentation, collected data, and technical validation, see Christiaanse et al. (2025b). The local cross-shore coordinate systems and station numbers defined in Christiaanse et al. (2025b) have been adopted here for consistency.

The data were collected at two field sites: *Tipsy Turtle* (TT), located about 10 km southwest of Galveston (in front of the Tipsy Turtle Sea Bar & Grill); and *Sea Wall* (SW), located in front of the sea wall between Galveston's 18th and 19th Street (Figure 3.1b). At TT the beach system is more natural with no recent nourishments, whereas nourishments have been carried out occasionally at the SW site. The main difference in the cross-shore profiles of the two locations was the initial presence of a berm on the backshore at TT, whereas the SW profile showed a fairly constant backshore slope (see black lines in Figure 3.1c, d). This berm however eroded during storm conditions on 13/14 November, after which the two profiles were more similar.

For this study, we used the data from the two main deployments: 2 November to 4 December 2023 at TT (32 days) and 7 November to 4 December 2023 at SW (27 days). Both deployments had the same experimental setup, consisting of nine measurement stations along the cross-shore profile: At station 0, located about 1.5 km offshore, a directional wave buoy recorded the incoming wave conditions. At stations 1 and 2, submerged pressure loggers (PL) measured the incoming waves and water levels in the foreshore. Stations 3 to 8 were spread over the backshore, roughly between the high tide line and the dune toe. At each of these six stations a PL measured the GWT inside a 1.5-m-deep slotted PVC well, and a buried temperature logger (TL) recorded the sand temperature at a typical turtle nesting depth ($\pm$40 cm). Additionally, at station 8 (dune toe), a vertical array of six buried moisture, temperature, and electrical conductivity loggers (spaced at 10-cm depth intervals) was installed. Due to the berm at TT, the logger at station TT6 was deployed slightly higher than the ones at TT7 and TT8 (Figure 3.1c), whereas the logger elevations at SW increased

monotonically between SW3 and SW8.

Next to the field observations, we used astronomical tide predictions from NOAA station 8771510 (Pleasure Pier, PP) and observed water levels from station 8771341 (North Jetty; NOAA, 2024b). We also used hourly precipitation totals from a weather station at Galveston Scholes Field Airport (GLS), accessible through the National Weather Service database (NWS, 2024). Finally, 30-year monthly precipitation statistics for Galveston were collected from the NCEI U.S. Climate Normals data base (NCEI, 2023).

3.2.3. Data processing

While most of the processing steps are described in detail in Christiaanse et al. (2025b), we did a few additional processing steps here. The time series were recorded at varying sample rates, depending on the PL type (RBR Solo and Hobo U20L) that was used. At the upper well stations (TT7 and TT8 and SW6 to SW8) the Hobo loggers recorded at 1/15 Hz. At TT5, TT6, and SW5 we used 2-Hz RBR Solo's and at all other stations 16-Hz RBR Solo's. For the analyses presented in this study, we resampled the original time series to different time intervals depending on the analyzed process (Section 3.2.5).

Most time series contained short gaps caused by data offloads or other maintenance activities. These were generally in the order of minutes and were interpolated linearly to yield continuous time series. On 16 November all loggers were retrieved for 2–3 hours for a data offload and maintenance check. This was done on the rising (falling) tide at TT (SW), so the resulting gaps did not include high or low water. Therefore, they were linearly interpolated as well. However, some time series contained longer gaps that could not be interpolated. Specifically, there is no data at TT8 from 21 November 16:25 to 27 November 9:03, at SW5 from 13 November 13:15 to 14 November 10:30, and at SW8 on 13 November from 13:20 to 20:35 (all times in CST/UTC-6). In Appendix A.1, we explain the data gaps and how we handled them in this study in more detail.

3.2.4. Water level regimes and wave runup

The observed water levels at the backshore stations did not always represent the pure GWT, as some of the stations (particularly the lower ones) were regularly submerged, during high tide and surge events. When fully submerged, the observed water level represents the free surface elevation. Even when the beach at a given station was not fully submerged, water level observations may be affected by wave runup (wave setup + swash). Therefore, we classified the observed time series of the backshore stations (3–8) into three different water level regimes, based on the horizontal excursion of the mean water level at station 2 and the estimated 2%-exceedance value of the wave runup ($R_{2\%}$). These values were computed at 30-minute intervals to classify the observed water levels as:

1. *Groundwater*: onshore of the $R_{2\%}$ position,
2. *Mixed*: between $R_{2\%}$ and the shoreline based on the water level at station 2,
3. *Submerged*: seaward of the shoreline.

We estimated the vertical elevation of $R_{2\%}$ based on Stockdon et al. (2006), who provide empirical formulations to compute $R_{2\%}$ from offshore wave conditions based on two components: wave setup and swash. They give a general formulation, which also includes the

beach slope (β) and a formulation for very dissipative conditions, recommended for a surf similarity parameter $\zeta < 0.3$ (Iribarren number, after Iribarren & Nogales, 1949). Video-based observations of the wave runup at SW on 13 and 14 November 2023 showed that the dissipative formulation provided the most accurate $R_{2\%}$ estimate (RMSE = 0.08 m; van der Grinten et al., 2025), whereas the general formulation overestimated $R_{2\%}$, even for a mild beach slope ($\beta = 0.016$). The estimated wave runup must be added to a reference water level to compute the total elevation. Given that the observed water levels at stations 1 and 2 already include part of the wave setup, we used the dissipative $R_{2\%}$ formulation added to the observed water level at the NOAA Jetty station:

$$R_{2\%} = 0.043\sqrt{H_0 L_0} + h_{NOAA}, \tag{3.1}$$

where H_0 and L_0 are the deep-water significant wave height and wave length, and h_{NOAA} is the 30-minute observed water level at the NOAA Jetty. The offshore wave conditions were derived from wave conditions measured by the wave buoy at TT0, located at a water depth of about 8 m, approximately 1.5 km offshore of TT. We did not use the buoy at SW0 because it only recorded reliable data between 3 and 12 November 2023. However, the conditions measured at SW0 correlated very well with those at TT0 over this period ($r = 0.94$; Christiaanse et al., 2025b). We used linear wave theory to convert the measured significant wave height, H_s, and peak period, T_p, to H_0 and L_0 (Holthuijsen, 2007). The deep-water wave length was computed as $L_0 = gT_p^2/2\pi$, while H_0 was derived from the linear shoaling coefficient ($H_0 = H_s/K_s$). The computation and formulae are explained in detail in Appendix A.2.1.

The wave buoy at TT0 was active between 3–26 November, after which it started drifting away (Christiaanse et al., 2025b). Unfortunately, there was no alternative wave data available in the region, because the offshore NOAA wave buoy (ID *42035*) was down during the entire deployment. However, the computed wave runup correlated well with $\sqrt{H_s L_0}$ at TT1 ($r = 0.88$) and SW1 ($r = 0.86$). We therefore used a linear regression based on $\sqrt{H_s L_0}$ to derive the wave runup for the conditions outside the operational buoy window (mostly beyond 26 November). A detailed explanation of this interpolation and the final estimated R2% are presented in Appendix A.2.

3.2.5. Spectral analysis

We used spectral analysis to quantify the influence of four driving processes on the observed groundwater fluctuations across the backshore (stations 3–8): infragravity (IG) waves, astronomical tide, rainfall, and storm surge. We excluded the water level on the bay side from this analysis, as it closely followed the sea level fluctuations and there was no significant change in the water level due to a residual sink or source (e.g., river inflow). We used the Fast Fourier Transform (FFT) to convert the observed time series from the time domain to the frequency domain. To ensure stationarity, we tailored the spectral analyses specifically to each driving process, explained in detail in the following sections.

Infragravity waves

To quantify the propagation of IG waves into the beach matrix we applied the FFT on the time-scale of sea states, assuming a stationarity window of 30 minutes. We used (resampled) 2-Hz time series where available (TT1 to TT6 and SW1 to SW5) and 1/15-Hz time series

at the upper well stations (TT7 and TT8 and SW6 to SW8, see Figure 3.1c, d for the instrument locations). The Nyquist frequency at the upper wells was therefore 1/30 Hz, giving a shortest resolvable wave period of 30 s. A common definition for the IG frequency band is from 1/250 to 1/25 Hz (Bertin et al., 2018), however that would have included waves with periods between 25 and 30 s, which could not be resolved from the 1/15-Hz time series. We therefore applied a bandwidth of 1/250 to 1/30 Hz in our analysis.

We used FFT to compute the power spectral density (PSD) over 30-minute windows along each time series (except for the gaps). Following Welch's method, we divided each 30-minute window into four blocks of 7.5 minutes (Welch, 1967). The final PSD was obtained by averaging the spectra computed over the four blocks. The choice of four blocks was based on a trade-off between reducing noise and retaining enough resolution to accurately resolve the longest periods in the considered IG bandwidth (250 s). We then used the n^{th}-order spectral moment (m_n) of the PSD to compute the significant IG wave height ($H_{m0,IG}$) and mean IG wave period ($T_{m-10,IG}$; Hofland et al., 2017; Holthuijsen, 2007):

$$m_n = \int_{1/250}^{1/30} f^n PSD(f) df, \qquad H_{m0,IG} = 4\sqrt{m_0}, \qquad T_{m-10,IG} = \frac{m_{-1}}{m_0} \tag{3.2}$$

Tide

Given that the astronomical tide is characterized by a sum of multiple constant harmonics, it is inherently stationary. In principle, spectral analysis through FFT is therefore well suited to analyze the propagation of the tide into the GWT. However, FFT does not directly provide information about the phase lag between the two time series, which is needed to understand how the ocean tidal signal is delayed in the GWT.

To analyze the propagation and relative phase shift of the tide, we computed the cross-spectral density (CSD), which is the Fourier Transform of the cross-correlation function between two time series. The magnitude and phase of the CSD represent the shared power and relative phase shift between the two signals at each frequency band, respectively. Combined with the PSDs of the individual signals, the CSD was used to compute the *coherence*, which quantifies the consistency of the relationship between the signals at each frequency band from 0 (no coherence) to 1 (perfect coherence). Robust estimation of the CSD and coherence generally requires averaging over blocks to reduce noise and spectral leakage, as in Welch (1967). However, given our time series were relatively short compared to the dominant diurnal tidal periods, this would have led to poor frequency resolution.

We therefore used the multitaper method (MTM) introduced by Thomson (1982), a statistically robust alternative that enables spectral estimation over the entire time series using several orthogonal data windows (tapers). MTM is widely used in neuroscience but has also successfully been applied in hydrology (e.g., Van Hoek et al., 2016) and ocean sciences (e.g., Anarde et al., 2020; Jeyaseelan & Balaji, 2015; Percival & Walden, 1993). In short, the original time series is tapered (= multiplied) by k members of the Slepian functions (Slepian, 1978), which are orthogonal and thus statistically independent. From the resulting tapered versions of the original time series, k statistically independent *eigenspectra* are computed through FFT. The final spectrum is obtained by the (weighted) average of the k eigenspectra. Compared to conventional spectral analysis, MTM reduces bias and spectral

leakage (Babadi & Brown, 2014; Bronez, 1992; Percival & Walden, 1993). Moreover, it is possible to derive an internal estimate of the variance through *jackknifing* (Thomson, 2007).

To reduce high-frequency noise, we resampled the time series to 10-minute intervals. We then used the *multi_taper_csd()* function from the *Nitime* python library (Nitime, 2019) to estimate the PSD at each station and the CSD between station 1 and every other station. We used a time half-bandwidth of $NW = 3$, yielding $k = 5$ tapers. The tapers were adaptively weighted and filtered for low bias using the *adaptive_weights* and *low_bias* options in Nitime. The phase difference was computed as the argument (angle) of the complex CSD estimate, resulting in a value between $-\pi$ and π (radians) at each frequency. A positive (negative) phase difference translated to a lag (lead) in the signal compared to station 1. Hereby, the phase wraps around the two limits $[-\pi, \pi]$, which represent a fully out-of-phase signal. The time lag/lead at each frequency (f) was computed by dividing the phase difference by $2\pi f$. The coherence, $C_{x,y}(f)$, between each pair of time series (x and y) was computed as:

$$C_{x,y}(f) = \frac{|CSD_{x,y}(f)|^2}{PSD_x(f) \cdot PSD_y(f)}, \tag{3.3}$$

where $CSD_{x,y}(f)$ is the cross-spectral density and $PSD_{x(y)}(f)$ is the power spectral density of x (y). We quantified an uncertainty estimate for the coherence and the phase difference using a *jackknifing* technique, as outlined in Thomson (2007). This involved creating k separate estimates using a "leave-one-out" approach—i.e., estimating the coherence and phase k times by excluding one of the k tapers every time. The internal variance of the coherence was then derived from the error between each separate estimate and the average estimate. For the circular phase, we used a simple uncertainty estimate based on the maximum and minimum of the $k - 1$ jackknife estimates. For a detailed explanation of the coherence and phase uncertainty estimation, we refer to Appendix A.3.

We quantified the amplitude decay and phase lag of the tidal signal across the stations over two frequency bands based on the dominant diurnal and semi-diurnal constituents at Galveston Island. At NOAA's Pleasure Pier Station (NOAA PP in Figure 3.1b), the diurnal tide is dominated by the K_1, O_1, P_1, and Q_1 coefficients, with a combined amplitude of ± 42 cm. The semi-diurnal tide is dominated by the M_2, S_2, and N_2 coefficients, with a combined amplitude of ± 21 cm. Based on the frequencies of these harmonics and the frequency resolution and width of the tidal spectral peaks in the the computed PSDs, we defined:

- The diurnal frequency band between $1 \cdot 10^{-5}$ and $1.25 \cdot 10^{-5}$ Hz (22.2 to 27.8 hour periods).
- The semi-diurnal frequency band between $2.12 \cdot 10^{-5}$ and $2.35 \cdot 10^{-5}$ Hz (11.8 to 13.1 hour periods).

To quantify the tidal amplitudes at each station, we took the square root of the integrated PSD over the corresponding frequency band:

$$A_{t,i} = \sqrt{\int_{f_{low}}^{f_{hi}} PSD_i(f) df}, \tag{3.4}$$

where $A_{t,i}$ is the total diurnal or semi-diurnal amplitude at station i, $PSD_i(f)$ is the PSD at station i, and f_{low} and f_{hi} represent the limits of the frequency band. We then quantified the phase lag (in hours) of the (semi-)diurnal tide at each station relative to station 1. The phase lag was computed as the average of all CSD phase values within the respective frequency band, retaining only frequencies with coherence $C \geq 0.5$. This threshold ensured that the estimated phase lag was based on coherent frequency components only.

This analysis required full continuous time series without missing data. Therefore, we interpolated the data gaps at TT8, SW5, and SW8 (see Section 3.2.3) linearly, even though this may have introduced artifacts. The results were interpreted with this caveat in mind. At SW5 (±21 hours) and SW8 (±7 hours) the gaps were relatively short, so we do not expect the results to be affected significantly.

Surge and rainfall

The stationarity assumption does not hold for the surge component of the total water level. As the corresponding frequencies are not known a priori and may vary over time, isolating the meteorological surge signal from the rest of the time series was difficult. We applied a low-pass FFT filter to reconstruct the low-frequency signal at each station. We used the same 10-minute resampled time series as for the tidal analysis and a cut-off period of 36 hours ($\approx 7.7 \cdot 10^{-6}$ Hz) for the FFT filter, to prevent potential spectral leakage of the diurnal tide (±25-hour period) from influencing the surge signal.

Next to the meteorological surge, the low-passed time series also included residual components, such as low-frequency tidal variations and the smoothed GWT response to rainfall. Based on the tidal predictions at NOAA PP, there are two relevant low-frequency tidal constituents that we could not isolate from the signal: solar semi-annual (*SSA*) and solar annual (*SA*; NOAA, 2024b). However, both have amplitudes below 10 cm, so on the time-scale of our observations (±30 days), we assumed these to be negligible relative to the surge component. Moreover, the foreshore water levels should not be affected by rainfall. We therefore assumed the low-passed signal to be an acceptable proxy for the meteorological surge at stations 1 and 2. At the groundwater stations (3–8), however, the response to rainfall was significant in the low-passed signal. Due to the lack of local high-resolution rain data and the difficulty of separating the surge and rain responses in the groundwater, we decided to include the rainfall in this part of the analysis. It should be noted, however, that the actual response of the GWT to rainfall occurs on shorter timescales (minutes to hours). We discuss this further in Section 3.4.1.

We selected five separate events to analyze the groundwater response to the surge and rainfall from the low-passed signals (Table 3.1). We used hourly precipitation rates from the GLS weather station (NWS GLS in Figure 3.1b) and two-hour averaged wind speed and direction data from NOAA's North Jetty station (NOAA Jetty in Figure 3.1b), to determine whether each of the five events was influenced by surge, rain, or both. One event was rain-only, two events surge-only (one with a reverse surge), and two storm events with both surge and rain. For each event we analyzed the corresponding maxima (minimum for the reverse surge) in the low-passed signals across the stations. The amplitude at each station was computed as the difference between the maximum and the preceding minimum (vice-versa for reverse surge) and the time lag was quantified relative to the maximum (minimum) at the most seaward station. Data gaps that could not be interpolated (see section 3.2.3) were excluded from the analysis, meaning that TT8 was excluded from the reverse surge and

surge, and SW5 and SW8 were excluded from storm 1.

Event name	Date	Surge influence	Rain influence
Rain	9/10 Nov	No	Yes
Storm 1	13/14 Nov	Yes	Yes
Reverse surge	21/22 Nov	Yes (negative)	No
Surge	25/25 Nov	Yes	No
Storm 2	30 Nov/1 Dec	Yes	Yes

Table 3.1: Overview of events considered in the low-pass FFT analysis of groundwater response to the meteorological surge and rainfall.

3.2.6. Nest flooding analysis

Kemp's ridley turtles typically nest between the high tide line and the first dune, with most nests near the vegetation line in front of the first dune, and their nests are typically 30–40 cm deep (Culver et al., 2020; Marquez, 1994). That mainly corresponded to the area covered by the upper three stations (6–8) at each site. For each of these stations, we quantified the number and duration of nest inundation events. An inundation event was defined as the GWT exceeding the nest depth threshold and lasted until the GWT dropped below the threshold again. We used a threshold of 30 cm below the sand surface at the start of the deployment, representing the shallowest nests.

Given the data used in this study was mostly gathered in November 2023, outside the nesting season, our results were not directly transferable to actual nests, which are in the sand from April to potentially late September. Therefore, we performed a statistical comparison of historical water levels and rainfall rates between the nesting season and November to assess if similar conditions could be expected. We used 23 years of historical hourly water levels at the North Jetty station (2001–2023) which we detrended using simple linear regression to account for sea level rise. For rainfall, we used 30 years of monthly precipitation normals from the GLS weather station (1991–2020).

3.3. Results

3.3.1. Observed water levels

There was considerable variability in the observed water levels, both at the foreshore stations (1 and 2) as well as the backshore stations (3–8, Figure 3.2). In the foreshore the mean water level was around 0.35 m + NAVD88 (North American Vertical Datum of 1988) and the total range was about 1.6 m (double the mean spring tidal range in the area of ±0.8 m). The mean water level at the backshore stations steadily increased towards the dune to 0.83 m (0.95 m) at TT8 (SW8), resulting in a super-elevation of about 0.5–0.6 m at the dune toe. The observed water levels also became increasingly positively skewed towards the dune. Notably, the lowest observed GWT at the six upper backshore stations (6–8) was above the mean water level in the foreshore. The total range varied but was in the region of 1 m at most backshore stations, roughly two-thirds of the water level range in the foreshore. Note that the time series at TT6, TT8, SW5, and SW8 contained some gaps which may have slightly influenced the results presented in Figure 3.2 (see also Section 3.2.3).

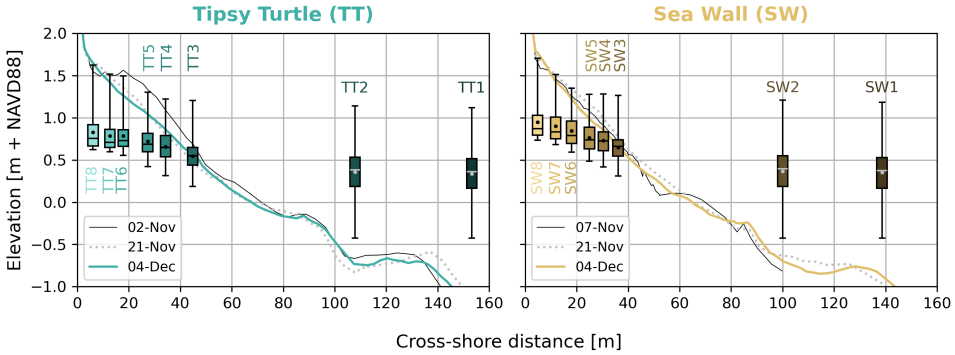

Figure 3.2: Summary of observed (ground)water levels across the field stations. Boxes show the inter-quartile range, whiskers the entire observed range, bars the median, and dots the mean. The corresponding bed profiles are shown for reference.

Based on the water level regimes, the lowest groundwater stations (TT3/SW3) were submerged several times during high tides, particularly TT3 (Figure 3.3). TT4, SW4, TT5, and SW5 were mainly submerged during the two storm events. All lower backshore stations (3–5) had significant periods of mixed water level regimes, when the station was between the $R_{2\%}$ and waterline. Particularly TT3, which had the lowest elevation of all backshore stations, was in mixed or submerged conditions roughly 50% of the time. All other stations were in the groundwater regime at least 75% of the time. At stations 6–8 the observed time series mainly reflected groundwater conditions, with only short periods of the mixed regime during the storms at stations 6 and 7.

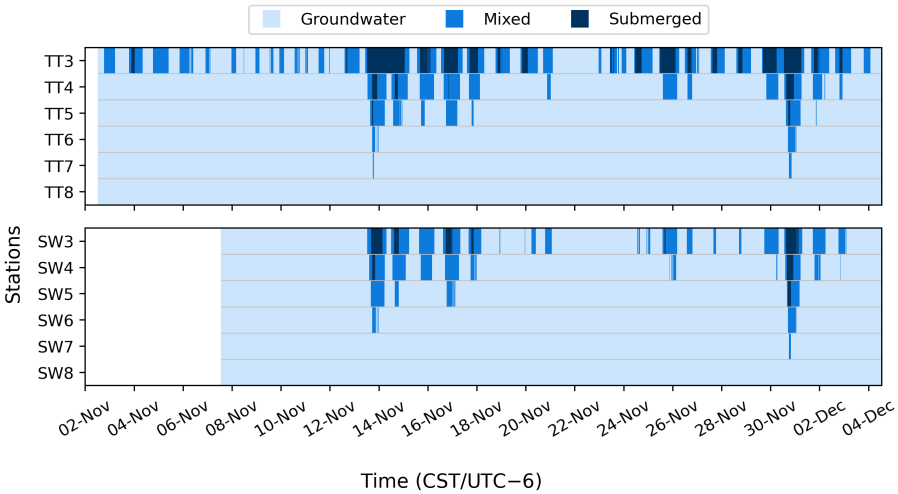

Figure 3.3: Water level regimes (every 30 minutes) at the backshore stations of TT (upper panel) and SW (lower panel): groundwater (beach surface above $R_{2\%}$), mixed (beach surface between $R_{2\%}$ and water level at station 2), and submerged (beach surface below water level at station 2).

3.3.2. Drivers of GWT fluctuations

IG waves

Most of the IG wave energy was observed during the two storms on 13 and 30 November, when the significant IG wave height, $H_{m0,IG}$, reached up to 23 cm in the foreshore (Figure 3.4). This storm IG energy generally increased at the lower backshore stations (3–5), with $H_{m0,IG}$ reaching 40+ cm. During these conditions, the water level at all three lower stations represented mixed or submerged conditions (not the GWT). The IG wave height within the inner surf and swash is a result of the balance between shoaling, dissipation by breaking, bed friction, reflections, and the non-linear transfer from the sea-swell to the IG waves leading up to it (Henderson & Bowen, 2002; Thomson et al., 2006). These processes are controlled by the beach slope, with shoaling generally stronger on milder slopes (Battjes et al., 2004; van Dongeren et al., 2007). Conservation of energy flux ($H^2\sqrt{gh} = constant$) with water depths of $h \approx 2.5$ m (TT1), 2 m (TT2), and 0.5 m (TT3) during the storms would result in shoaled wave heights of about 1.05 (TT2) and 1.5 (TT3) times higher than at TT1. This is roughly consistent with the observations in Figure 3.4, showing that the IG waves shoal before dissipating by breaking and friction.

IG energy at the backshore stations was also highly dependent on the tide, with $H_{m0,IG}$ dropping to zero during almost every low tide, suggesting that IG oscillations only have a strong influence in the swash zone. Consequently, at the upper groundwater stations (6–8), IG response was primarily limited to the two storm events, with minimal IG energy observed at the dune toe (station 8).

In the PSDs of TT1 and SW1, IG energy was mainly concentrated around three bands (see purple shaded PSDs in Figure 3.4). The main band had periods of 60–70 s. A second, lower energy band was at 30–40-s periods, and a third band at longer periods (120–200 s), mainly visible during the storms. At TT2/SW2, the first two IG bands appeared to have merged into a single band concentrated around 50–60-s periods. At the backshore stations, the IG periods showed a bimodal character, linked to the water level regimes (Table 3.2). During mixed and submerged conditions, $T_{m-10,IG}$ was similar to the period in the foreshore. During groundwater conditions, $T_{m-10,IG}$ was significantly larger, along with a smaller $H_{m0,IG}$. This pattern suggests that the shorter IG bands visible in the foreshore were damped out rapidly and only the longer-period band propagated into the GWT, consistent with earlier studies showing frequency-dependent attenuation (e.g., Nielsen, 1990; Turner et al., 1997).

	TT1	TT2	TT3	TT4	TT5	TT6	TT7	TT8
Submerged	66	68	73	81	83	-	-	-
Mixed	-	-	92	86	88	83	82	-
Groundwater	-	-	163	166	157	142	134	162

Table 3.2: Mean IG wave period $T_{m-10,IG}$ (s) across the three water level regimes and the stations at TT. Only periods with $H_{m0,IG} \geq 1$ cm were included, to filter out noise. The bimodal character $T_{m-10,IG}$ is clearly visible from the longer periods during groundwater conditions compared to mixed/submerged conditions.

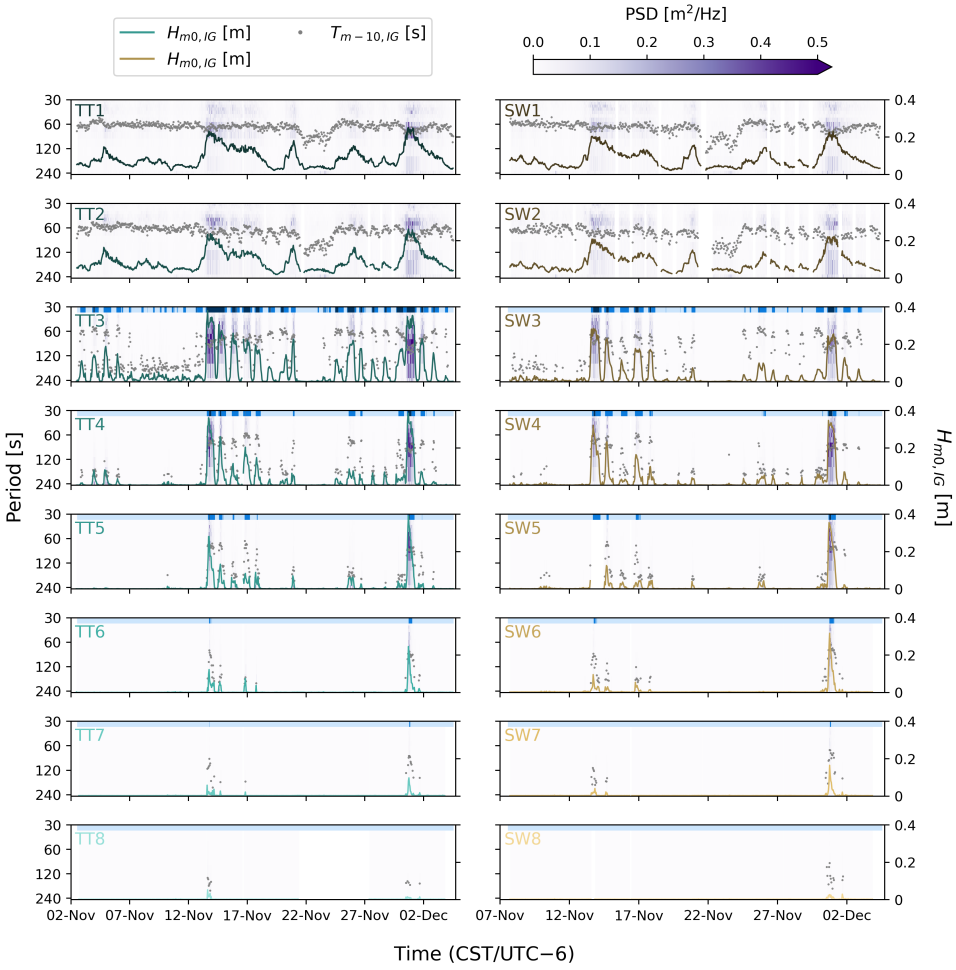

Figure 3.4: Infragravity spectrograms at TT (left column) and SW (right column), from station 1 (top) to station 8 (bottom). The solid colored lines represent $H_{m0,IG}$, while the grey dots represent $T_{m-10,IG}$ (only plotted for $H_{m0,IG} > 1$ cm, to filter noise). Frequencies were converted to periods for visualization. The blue shaded bar at the top of the subplots of stations 3–8 shows the water level regime over time: groundwater (lightest), mixed (middle), submerged (darkest), see also Figure 3.3.

Tide

The computed multitaper PSDs at each station showed clear peaks around the diurnal and semidiurnal tidal frequencies (Figure 3.5b). As expected, the spectra at the foreshore stations (TT1 and TT2) were nearly identical, confirmed by the CSD and coherence which was near 1 across the frequency range (Figure 3.5c). Towards the dune, the tidal signal decayed and the power shifted to lower frequencies. The tide already showed significant decay at stations 3–5, but the coherence remained near 1 over both tidal bandwidths, with relatively narrow 90% confidence intervals (low uncertainty). From TT6 on, most of the tidal power was damped out and the coherence dropped, with increasing uncertainty (confidence inter-

vals). Nonetheless, the diurnal peak was still clear in the CSDs at stations 6–8. At TT8 the coherence was inconsistent across the frequency range and had no clear peaks around the tidal frequencies. This may be partly caused by the missing data between 21–28 November, as the tidal coherence at SW8 was higher and less uncertain (see Appendix Figure A.3).

The total diurnal and semi-diurnal amplitudes computed from the PSDs amounted to 48 and 21 cm at TT1 and 47 and 24 cm at SW1, close to the predicted values of 42 and 21 cm at the NOAA Pleasure Pier station (Figure 3.6). As expected, the amplitudes and phases at stations 1 and 2 were approximately equal. The amplitudes then rapidly decayed to below 10 cm at station 8—a reduction of 80–85% at both TT and SW. The computed phase lags relative to station 1 were more inconsistent, but generally showed an increasing lag (nearly 2 hours) towards the dune. The diurnal tide lagged less than the semi-diurnal tide. Uncertainty

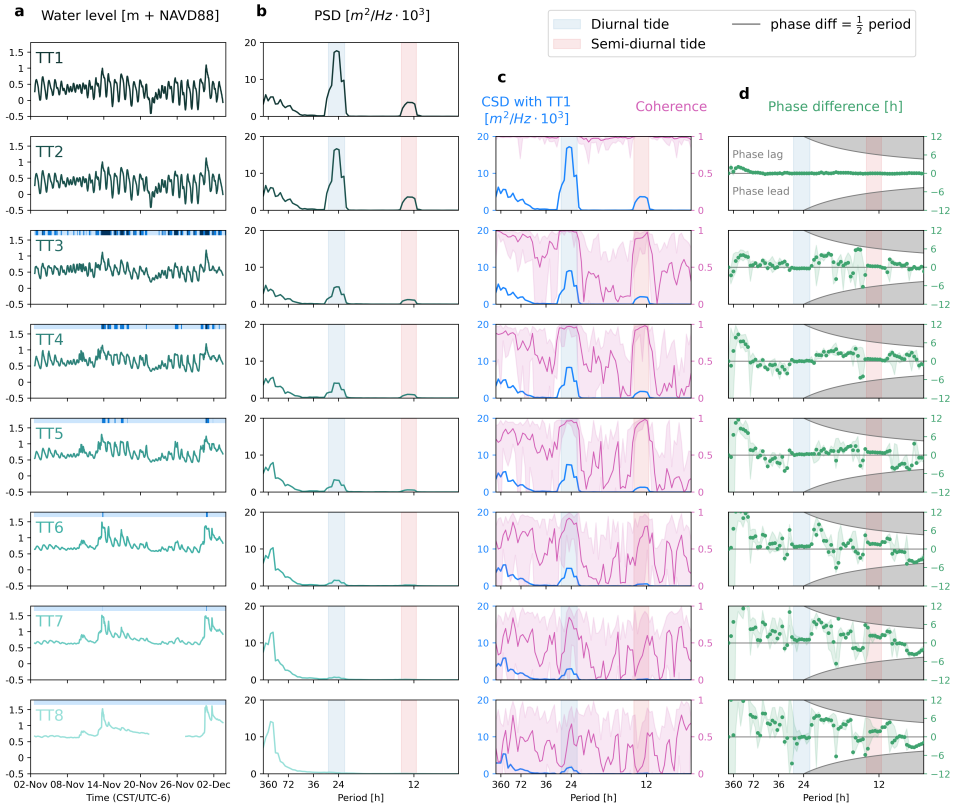

Figure 3.5: Multitaper spectral analysis of the tidal propagation along the stations at TT. a) Observed water level time series at each station, with the blue shaded bar representing the inundation regime over time (see Figure 3.3); b) Power spectral density (PSD) computed from the detrended time series; c) cross-spectral density (CSD, blue) and coherence (pink, 90% confidence interval given by shaded area) between station 1 and stations 2–8; d) estimated phase difference (green) between station 1 and stations 2–8 in hours (uncertainty given as green shaded area). A positive (negative) phase difference denotes a lag (lead) in the signal at stations 2–8. The maximum phase difference (1/2 period) is denoted by the grey borders. In columns b–d, the tidal bandwidths are shaded in blue (diurnal) and red (semidiurnal). For location SW, see Appendix Figure A.3.

in the estimated phase lags also increased towards the dune, but was generally much lower within the tidal bands than outside.

It should be noted that, particularly for stations 3–5, the time series represent different water level regimes. Therefore, the computed amplitudes and phase lags do not represent pure groundwater signals and should be seen as an estimate of the conditions at that particular location across water level regimes. We therefore mainly describe the trends seen here, rather than absolute values. For instance, the results showed an unexpected, but small phase lead (15–20 minutes) for the diurnal tide at TT3 and SW3. However, these stations had the most inconsistent water level regimes (see blue shaded bars in Figure 3.5a). This lead is likely caused by noise or interference from other processes, as it should physically not be possible for the ”groundwater” tide to lead the ocean tide (see also section 3.4.1).

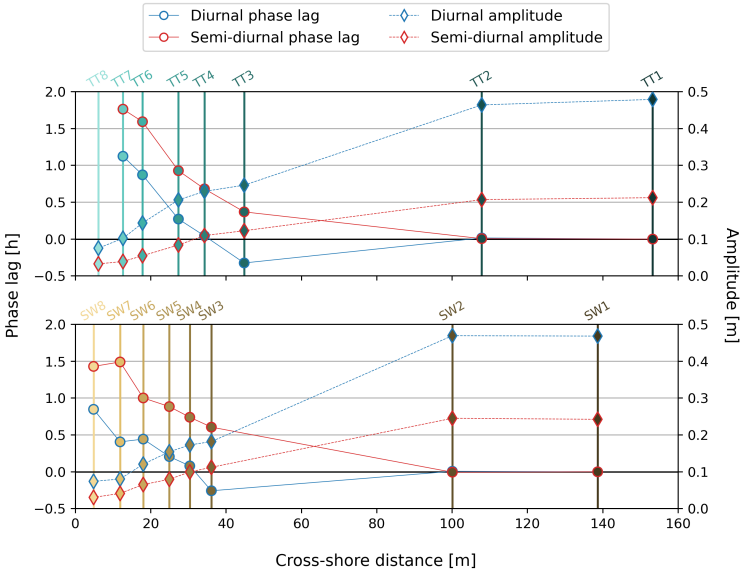

Figure 3.6: Summary of tidal amplitudes (diamonds, right y-axis) and phase lags (circles, left y-axis) across the field stations of locations TT (a) and SW (b). The phase lags are given relative to station 1.

Surge and rainfall

Figure 3.7 shows the low-passed time series along with the peaks of the five considered events. The Reverse surge (21/22 November) and Surge (25/26 November) were the only two events without rain. During the reverse surge, all backshore stations were in the groundwater regime and the amplitude quickly decayed from $\approx$ 0.55 m in the foreshore to $<$ 0.2 m near the dune toe (Figure 3.8). The smaller amplitude of the positive surge was relatively stable between stations 1–3 ($\approx$ 0.15 m), then slightly increased at stations 4 and 5. Station 5 was the first station in the groundwater regime and from there, the amplitude decreased towards the dune toe, similarly to the reverse surge. Both events showed an increasing time lag of the peaks towards the dune, with the reverse surge showing a larger lag as it propagated a longer distance through the groundwater (up to 11–13 hours, compared to 3–5 hours

for the positive surge, see Figure 3.8).

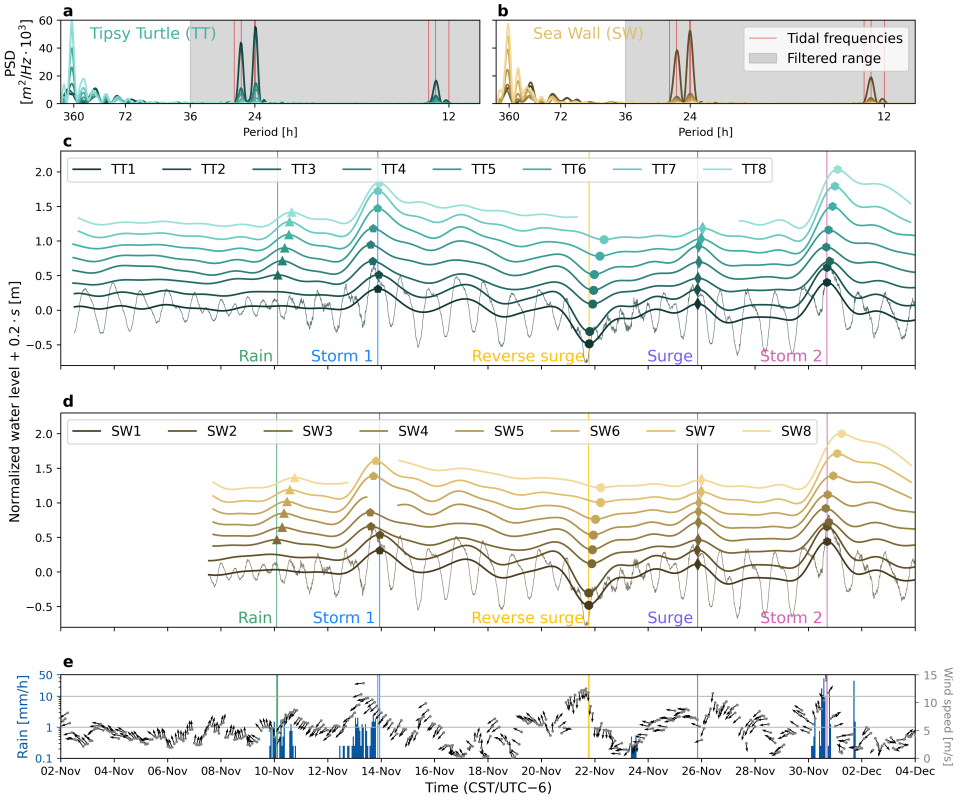

Figure 3.7: a, b) Power spectral densities (PSD) computed from single FFT's of the 10-minute time series. The low-pass FFT filter removed all periods shorter than 36 hours (grey-shaded area); c), d) Low-passed and normalized water level recorded at each station. The time series were shifted vertically in steps of 20 cm for visualization purposes. Markers track the extrema corresponding to five individual events: rain (triangles, green), storm 1 (pentagons, blue), reverse surge (circles, yellow), surge (diamonds, purple), and storm 2 (hexagons, pink). The colored vertical lines show the time of the extrema at station 1 (station 3 for rain); e) Time series of hourly precipitation rates at the GLS weather station (blue bars), and 2-hour averaged wind speeds (grey dots) and directions (black arrows) at the NOAA North Jetty station.

The rain-only event (9/10 November) shows that rainfall can lead to a significant response in the low-passed time series, with amplitudes of about 0.1–0.25 m across the stations. There is also an increasing time lag of the low-pass rain peak between stations 3 and 8 at both locations. This does not represent a landward propagating signal—rather the time for the rain to infiltrate increases with the vertical distance to the GWT, which generally increases in landward direction (see also Section 3.4.1).

The two storm events (Storm 1 and Storm 2) consisted of positive surges (approximately 0.3 and 0.55 m, respectively, at station 1), accompanied by rainfall. During both events, the lower stations were fully inundated and the GWT at the upper stations reached the sand surface. For Storm 1, rainfall was persistent over the entire day (13 November) leading up

to the surge peak, but less intense and there was no rain after the surge peak (Figure 3.7c–e). The amplitude in the low-passed signal was relatively stable across the first three stations (≈ 0.3 m), before increasing up to 0.55–0.65 m at station 7, and decreasing slightly at TT8 (there was no data for SW8, Figure 3.8). For Storm 2 the rain was very intense (up to 50 mm/h at NWS GLS) but for a shorter period and closer to the peak of the surge. About one day after the peak surge there was another heavy shower (Figure 3.7c–e). Moreover, the meteorological surge (±0.55 m) was almost double that of Storm 1, leading to a stronger surge influence compared to the rain. The amplitude decreased at station 3 and then steadily increased to > 0.8 m at station 8, although only at TT6, TT7, TT8, SW7, and SW8 was the amplitude larger than in the foreshore (Figure 3.8).

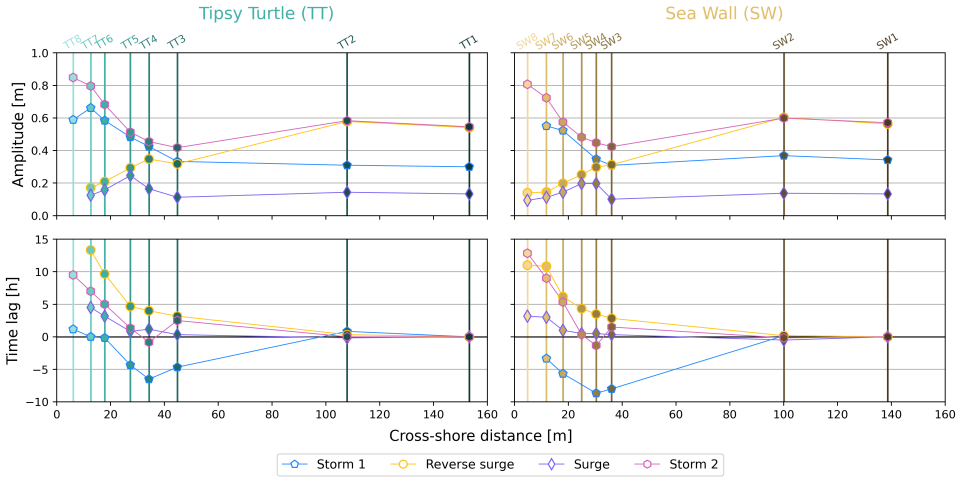

Figure 3.8: Estimated amplitudes (top row) and time lags (bottom row) of the extrema of the five considered events at TT (left column) and SW (right column).

The time lags during the two storms were more inconsistent than during the surge-only events. Storm 1 showed an apparent lead of the peak at the groundwater stations, compared to the foreshore surge. Especially the lower stations (3–5) showed large leads (up to 6 hours at TT4 and 8 hours at SW4). During Storm 2 the time lags were more in line with expectations, increasing towards the dune (up to 9–12 hours at station 8). There were still small leads at TT4/SW4 (about 1 hour), even though at TT3/SW3 there was a lag. The phase leads are likely related to the response of the GWT to multiple driving processes acting simultaneously, notably the surge and rain (see Section 3.4.1). Next to the amplitude and phase changes across the stations, the peaks of the two storms also became increasingly asymmetric towards the dune toe, with the groundwater rising faster and dropping slower.

3.3.3. Nest flooding

The nest depth threshold was exceeded by the GWT several times at all upper groundwater stations (6–8) of both TT and SW (Figure 3.9). The total number of flooding events was highest at TT6 (7) and SW6 (14) and decreased towards the dune toe, with 3 and 2 flooding events observed at TT8 and SW8, respectively (Table 3.3). At all six stations, there was at

least one inundation event that lasted between 12 and 24 hours, and all three SW stations had one event lasting more than 24 hours. At both sites, the longest inundation events happened during the storm on 30 November. Flooding events generally lasted for longer at SW than at TT. The storm on 30 November was followed by another heavy rain shower on 1 December (Figure 3.7e). At SW6 and SW7, the water level did not drop below the threshold before rising again due to the additional rainfall, leading to flooding events of about 70 and 60 hours, respectively. At TT6, about 25 cm of the beach surface was eroded after the first storm (13 November), meaning that any potential nests would have likely been washed away. At the other stations, morphological changes were milder (5–10 cm) and generally showed more accretion than erosion.

Duration [h]	TT6	TT7	TT8	SW6	SW7	SW8
< 3	4	2		6	2	
3–6		1		4	1	
6–12	2		1			
12–24	1	2	2	3	1	1
> 24				1	1	1
Total #	7	5	3	14	5	2

Table 3.3: Overview of nest flooding events at the upper groundwater stations, divided into bins depending on the flooding duration.

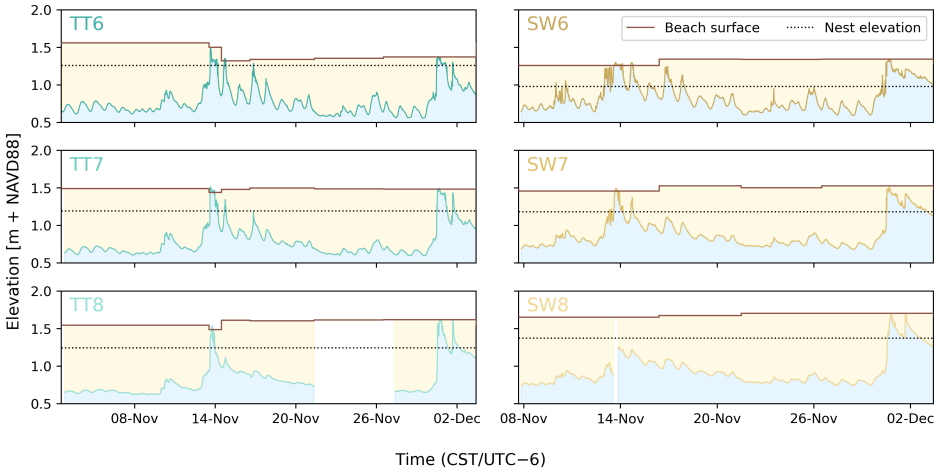

Figure 3.9: Overview of observed GWTs at stations 6–8 at TT (left) and SW (right). The beach surface and typical Kemp's Ridley nest depth are added for reference.

3.4. Discussion

3.4.1. Groundwater response to driving processes

In line with previous studies on beach groundwater (e.g., Cartwright et al., 2004; Hegge & Masselink, 1991; Nielsen, 1990; Raubenheimer et al., 1999; Turner & Nielsen, 1997), our results show that the beach matrix acts like a low-pass filter, increasingly damping out higher frequency fluctuations in the groundwater. The observed super-elevation (0.5–0.6 m) and vertical variability of GWTs (O(1 m)) are also consistent with previous observations reported in the literature (e.g., Housego et al., 2021; Nielsen, 1990; Turner et al., 1997). IG waves appear to be relevant near the swash zone, where they shoal before reaching the shore, also in line with previous studies (e.g., Henderson & Bowen, 2002; Thomson et al., 2006; van Dongeren et al., 2007). Only the lower frequency IG bands propagate into the GWT, shown by a bimodal behavior of the mean IG period across groundwater and mixed/submerged conditions. The tidal signal becomes increasingly damped, asymmetric, and phase-lagged towards the dune toe. Both IG and tidal fluctuations are damped to a degree that they have little influence on the GWT near the dune toe. Hence, of the considered processes, the surge and rainfall dominate the observed GWT fluctuations in the upper backshore, including the nesting area.

As multiple driving processes simultaneously interact with the beach matrix, their combined effects result in a conditional GWT response. During storm 1 the ocean surge peak occurred on the falling tide, whereas during storm 2 it occurred on the rising tide, much closer to the high tide. This partly explains the higher water levels observed during storm 2. Rainfall and bed level changes also contribute, particularly because they often coincide with stormy conditions (Zheng et al., 2013), as was the case during both observed storms. The GWT time series represent the combined response to all these processes, making it difficult to isolate the signals of individual drivers, in particular those acting on similar time scales. More advanced methods which work better on non-stationary data, such as wavelet analysis or empirical mode decomposition, could potentially improve the isolation of the surge, for example. Another approach could be to assess the surge component and overheight using an empirical or analytical model (e.g., Li et al., 2004; Nielsen, 1999; Nielsen, 1990). Moreover, longer-term observations (6+ months) would enable more detailed analysis as they facilitate more accurate spectral estimation and increase the chance of capturing isolated events (e.g., high waves but no significant surge, or vice versa).

This combined response to multiple simultaneous drivers may explain some of the limitations and inaccuracies in our analyses. For instance, the observed time leads of the groundwater peaks relative to the surge peaks in the foreshore during the storm events (Figure 3.8). Both storm events were accompanied by rainfall and high wave runup. Before the surge peak of storm 1 (13 Nov) there was a ±24-hour period with several rain showers, elevating the GWT ahead of the surge (Figure 3.10a). Consequently, as the surge and tide increase and wave runup reaches further up the beach, the GWT may reach the beach surface before the peak of the foreshore water level. Unless the location is fully submerged thereafter, the GWT will not rise further, resulting in an earlier low-pass peak. These hypotheses are supported by the second storm (30 Nov) showing mostly time lags, as the rain, ocean surge, and high tide are more in-sync (Figure 3.10b). Finally, bed level changes complicate things even further as they change the potential extent of the GWT. For instance, erosion can lower the beach surface and, with it, the GWT (e.g., at TT5 and TT6 during both storms 3.10a,

b). As such, the GWT can sometimes even be used to roughly track morphological changes (Anarde et al., 2020).

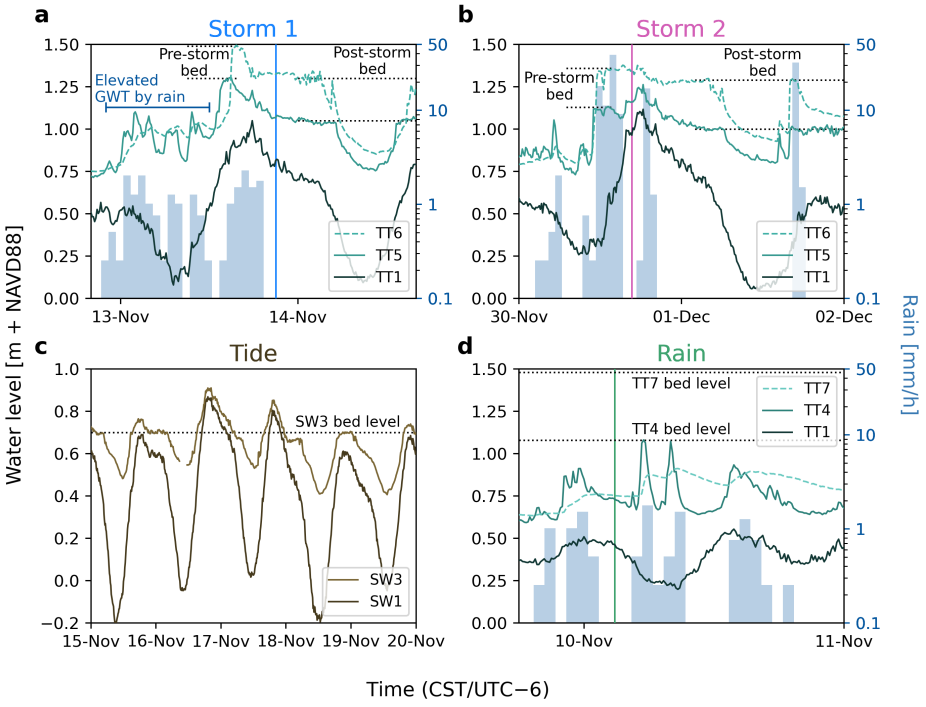

Figure 3.10: Observed (ground)water levels at various stations, showing the conditional GWT response to the driving processes and their interaction with the beach matrix. a) Water levels and bed level changes at TT during Storm 1; b) Water levels and bed level changes at TT during Storm 2; c) Tidal damping and asymmetry at SW3 compared to SW1; d) GWT response to rain at TT on 9/10 November. Black dotted lines indicate bed levels, while the blue, pink, and green vertical lines indicate the time of the low-frequency peak at TT1 (Storm 1 and Storm 2) and TT3 (Rain), see also Figure 3.7.

The anomalous phase lead of the diurnal tide at TT3 and SW3 (Figure 3.6) is likely the result of noise or interference from surface flows (e.g., during the storms). Both stations were regularly submerged (Figure 3.3). During submergence no significant time difference in the tidal signal is expected. However, once the beach re-emerges the sediment damps and slows the tidal retreat in the GWT. This creates a time-varying asymmetry in the signal, as the low tides occur during groundwater conditions (and therefore lag the ocean tide), whereas many high tides occur in mixed/submerged conditions (Figure 3.10c). In some cases, the groundwater may reach the beach surface ahead of the high tide peak and, if the location is not submerged, stop rising until the tide drops again, which might translate to a phase lead. However, this is unlikely to completely offset the observed lags in the low tide and therefore fails to explain the phase leads. These could also be an artifact of the spectral analysis being applied to the full time series with mixed regimes, essentially violating the stationarity condition, even though the ocean tidal signal itself is inherently stationary. The

computed amplitudes and phase differences shown in Figure 3.6 should therefore not be used as absolute values but rather to identify patterns (e.g., overall increasing lag towards dune).

The full response of the GWT to rain cannot be assessed from the low-passed time series because the main response occurs on shorter timescales. The rain event on 9/10 November consisted of several showers over a period of about one day, leading to multiple short peaks in the GWT (Figure 3.10d). These are smoothed into one peak in the low-passed time series, but the GWT response occurs at higher frequencies. At stations 3–5 the response was different compared to stations 6–8, with two clear spikes indicating a relatively quick uprush of the GWT, before rapidly dropping again. At stations 6–8 the response was more gradual and the GWT also dropped more slowly, failing to reach its pre-shower level before the next increase. This difference is likely due to the sediment above the GWT being more saturated at the lower stations, reducing the effective porosity, and allowing the infiltrating rain to fill the pores more rapidly. Moreover, before the first shower, the GWT is about 45 cm below the surface at TT4 compared to about 85 cm at TT7 (Figure 3.10d). Therefore, the water needs to infiltrate further down at the higher stations and will get absorbed into the pore spaces of the drier sand, smoothing the response and leading to a time delay, which ultimately shows in the low-passed peak as well. Local and more frequent measurements of rainfall at the study site could help better identify and describe the GWT response to rain.

3.4.2. Impact on nest flooding

Our results suggest that the surge and rainfall are the dominant drivers of nest flooding on Galveston's beaches and that the nest threshold was breached several times at each station. Past studies have indicated that both the frequency and duration of flooding events are critical for egg viability. For example, turtle eggs have been reported to tolerate short inundation periods (1–3 hours), but egg mortality rates start to increase quickly after six hours (Pike et al., 2015). Moreover, eggs in the first or last 20% of their incubation periods are practically intolerant to flooding of any duration, with hatching rates already decreasing drastically after inundations as short as one hour, especially for saltwater (Limpus et al., 2021). Rainfall by itself likely has less impact on turtle nests than the surge, as eggs are more tolerant to freshwater and showers often lead to high but relatively short spikes in the GWT. A high surge on the other hand is bound to elevate the GWT for at least several hours, especially in combination with wave runup. However, compound events, like the rain-elevated GWT ahead of the surge during storm 1 still make rain an important factor for nest flooding.

The observed frequency and duration of flooding events in this study make it highly unlikely that turtle nests on Galveston Island's beaches could yield viable hatchlings (Table 3.3). The GWT is relatively high, generally staying within 1 m of the sand surface, and can rise quickly and for prolonged time periods. We believe that this is due to a combination of the local sediment characteristics and the mild-sloping, low-elevation beach and dune system. Kemp's ridleys sometimes also nest on or behind the first dune (Marquez, 1994), potentially to mitigate nest flooding. We did not monitor the GWT beyond the dune toe, however, the low elevation of the first "dune" (usually below 1 m) makes it unlikely that those nests would be safe from inundation. Moreover, we used a relatively shallow nest threshold—in reality nests can be deeper (especially for other species), thus experiencing more flooding if laid in the same region of the beach. Our findings indicate that Galveston

Island's beaches currently do not provide an ideal nesting habitat for sea turtles, even for relatively shallow nests (we did not quantitatively evaluate deeper nest thresholds as these would have been inundated even longer). Therefore, we recommend continuation of the relocation practices carried out by the State of Texas, as implemented by the state sea turtle coordinator and the Padre Island National Seashore's Division of Sea Turtle Science and Recovery.

Moreover, we hypothesize that the CF could similarly disrupt egg gas exchange, leading to mortality rates comparable to GWT inundation. Here, we define the CF as the fully saturated zone above the GWT (it is sometimes also defined as the full zone of capillary action, reaching into the partially saturated zone with increased oxygen availability). Oxygen availability rapidly decreases in the fully saturated CF, suggesting that gas exchange for eggs within that zone may be insufficient (Haberer et al., 2014; Jost et al., 2011). Especially in fine sediments (< 0.1 mm), the CF width may potentially exceed 0.7 m (Turner & Nielsen, 1997). Unfortunately, our deployed moisture sensors were not calibrated properly, and we could not quantitatively estimate the CF from the measurements (Christiaanse et al., 2025b). However, a rough estimate of the CF width may be obtained from the average grain size: using $D_{50} \approx 0.15$ mm for Galveston Island (Christiaanse et al., 2025b) would result in a theoretical CF in the order of 0.5 m (Turner & Nielsen, 1997). This could drastically reduce the suitability of Galveston Island's beaches for turtle nesting. Thus, despite the absence of existing literature on how the CF might impact sea turtle nests, we believe that it could be a significant determinant for turtle nests. While gas exchange is important, sea turtle eggs also need sufficient moisture levels (Ackerman, 1997; Mortimer, 1990), suggesting they could be optimally placed in the partially saturated zone above the CF. Future research should therefore not only investigate the tolerance of turtle nests to complete inundation but also to CF exposure, for example by extending field/laboratory experiments like Limpus et al. (2021) and Pike et al. (2015). Additionally, simultaneous measurements of CF extent and nest depths could shed more light on a potential relation and optimal nest depths.

The beach groundwater dynamics during the nesting season (April–September) may differ to some degree from our observations (mainly November). For instance, the higher summer temperatures may lead to more evapotranspiration (i.e., faster drying of the beach), and therefore a lower mean GWT. However, hourly water levels at NOAA's North Jetty station from 2001–2023 indicate that extreme water levels are more common and reach significantly higher values (> 1.5 m NAVD88) during the nesting season (Figure 3.11a). This is most likely due to the peak of the hurricane season (August–October) overlapping with nesting. Major hurricanes would completely wash away any nests, but regular (tropical) storms may frequently bring similar or slightly higher water levels than those observed in November 2023. The North Jetty water levels are relatively representative of those observed at TT1, though TT1 shows higher extremes, likely owing to wind and wave setup (Figure 3.11b). Long-term rainfall data from GLS (1991–2020) suggest that while the early nesting season is drier than November, August and September are wetter (Figure 3.11c). Based on these factors, we expect the risk of nest flooding to be similar or even higher during the nesting season. Long-term observations of the GWT combined with measurements of local rainfall and evapotranspiration would help validate this hypothesis by improving our understanding of the steady state groundwater flow and seasonal GWT variations.

We chose the two field sites for this study because they facilitated comparisons between

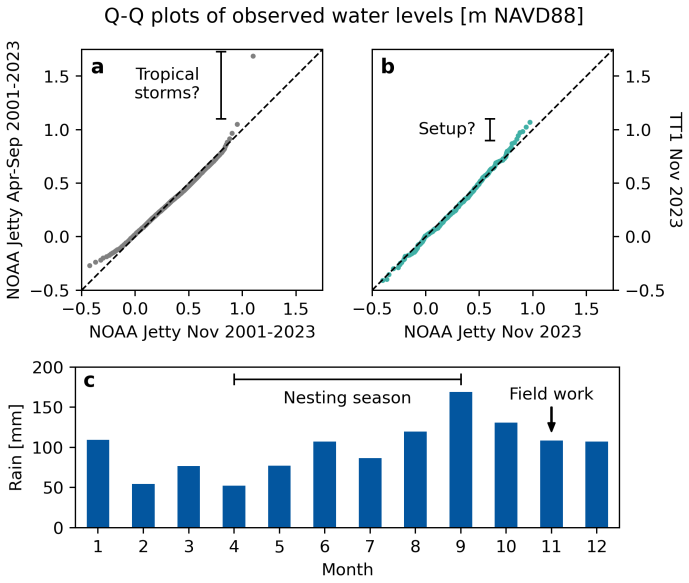

Figure 3.11: Statistical comparison of water levels and monthly rainfall during the nesting season (April–September) and November. a) Quantile-Quantile (Q-Q) plot of the observed hourly water level at the NOAA North Jetty station in November 2001–2023 (x-axis) and April–June 2001–2003 (y-axis). b) Q-Q plot of the observed water levels in November 2023 at NOAA Jetty (x-axis) and TT1 (y-axis). c) NCEI Climate Normals mean monthly precipitation totals over 1991–2020 at the GLS weather station.

a more natural (TT) and engineered (SW) beach setting. While the general results were similar, the engineered SW site typically exhibited a higher GWT, slower drainage, and longer flooding durations, even though the beach elevation at SW7 and SW8 was slightly higher than at TT7 and TT8. This is likely the result of an interplay of various factors, which may include the engineered beach setting at SW. For example, the profile at TT (including the berm that eroded during storm 1) may be more effective in preventing higher water levels from affecting the GWT in the nesting area. Varying sediment characteristics may also play a role, for instance nourished beaches can be more compacted than natural ones (Hannides et al., 2019), which would result in lower permeability and slower groundwater drainage. Although nourishments in Galveston have generally been placed south of SW, the sand was still more compacted than at TT and contained visibly more shelly material (Christiaanse et al., 2025b). The sea wall, paved street, and groins may also affect groundwater flow and rainwater runoff in the area. For example, the sea wall foundation could present a significant obstacle to groundwater drainage towards the landward side. Although both sites are currently not ideal for nesting, our observations indicate that the engineered site (SW) is less suitable than the natural one (TT). This supports previous studies that have observed reduced sea turtle nesting suitability on nourished beaches (e.g., Brock et al., 2009; Grain et al., 1995; Steinitz et al., 1998).

Given the interdependence between groundwater dynamics and beach slope, elevation, and sediment size (Turner et al., 1997), the importance of GWT fluctuations for nest flooding may vary significantly among global sea turtle nesting beaches. Specifically, steeper, higher

elevation beaches with coarser sediments typically have greater permeability and drainage (Turner et al., 1997), meaning that the mean GWT is likely deeper below the surface and the CF width is smaller (Turner & Nielsen, 1997). In such environments, we do not expect such frequent and extended periods of elevated groundwater, and therefore also less risk of prolonged nest inundation. That is, nests may still flood during high wave or surge events, but if the GWT drops below the nests more quickly the risk to egg viability will be lower. Nonetheless, continued inundation of nests is a threat on many nesting beaches worldwide, including the largest existing green turtle rookery on Raine Island, Australia (Limpus et al., 2021). Moreover, Kemp's ridleys are the smallest species of sea turtle, digging the shallowest nests. Other species can dig deeper nests (up to about 1 m below the surface), which may remain inundated for longer time periods, depending on their location in the beach profile. Therefore, while flooding is primarily driven by ocean processes (and rain), our results underscore the importance of considering the GWT in studies and assessments of nest inundation, particularly in low-elevation beach systems. In that context, future research should work towards developing a generic framework to assess nest inundation on sandy beaches, taking into account local beach morphology and aquifer properties, hydrological and hydrodynamic forcing, and groundwater dynamics.

3.4.3. Toward nature-based solutions that enable sea turtle nesting

While it remains uncertain how sea turtles select their nesting beaches (Miller et al., 2003), it has been hypothesized that they try to reduce the risk of nest flooding by nesting in regions with lower tidal ranges and lower extreme surges (Christiaanse et al., 2024b), and selecting an appropriate spot or elevation on the beach (Maurer & Johnson, 2017). Coarser grain sizes are generally correlated with steeper beach slopes (Bujan et al., 2019), and have greater permeability, resulting in faster groundwater drainage (Turner et al., 1997) and a thinner CF (Turner & Nielsen, 1997). Based on these relations and our observations in a fine-grained, low-elevation beach system, we would expect sea turtles to favor higher-elevation beaches with coarser sediment. Beach elevation has previously been identified as an important factor in determining nesting suitability for Kemp's ridleys specifically (Culver et al., 2020), but also loggerhead, hawksbill, and green turtles (e.g., Horrocks & Scott, 1991; Kikukawa et al., 1999; Yamamoto et al., 2012). Yet, to date no clear relationship between sediment size and turtle nesting has been found (e.g., Foley et al., 2006; Mortimer, 1990), except that turtles appear to avoid sites with extremely high or low grain sizes (Yamamoto et al., 2012). Mortimer (1990) hypothesized that too low water content could explain green turtles struggling on beaches with coarse sand (±1 mm), but did not conclude anything for finer grain sizes.

Beach elevation will become even more important in the light of future sea level rise, as the mean GWT is expected to follow mean sea level (Bjerklie et al., 2012; Michael et al., 2013). This will increase the risk of elevated groundwater due to ocean- and/or rain-driven inundation if the beach morphology cannot keep up with the rising water levels. This is particularly concerning in regions with high relative sea level rise rates, like the western Gulf of Mexico. However, it may also provide opportunities for nature-based solutions to improve the suitability of low-lying beach systems for turtle nesting—for instance, by increasing the beach elevation through turtle-friendly beach nourishments. Different beach nourishment strategies for Galveston Island are currently being evaluated for coastal resilience and pro-

tection (USACE, 2021) and these studies should include the impact on turtle nesting and the flooding of nests in particular. Increasing the beach elevation through re-profiling or nourishment has previously been suggested as a nature-based solution for nesting beach rehabilitation (Limpus et al., 2021; Montague, 1993) and has successfully been implemented on Raine Island, Australia, in the past decade (Smithers & Dawson, 2023). However, a lot of care must be taken to ensure that the resulting beach profile and sediment characteristics enable turtle nesting, rather than hindering it (e.g., by nourishing with native sediment and reducing sand compaction; Grain et al., 1995; Hannides et al., 2019; Montague, 1993).

3.5. Conclusion

Understanding how ocean processes and rain drive short-term beach groundwater variability in sea turtle nesting areas is critical for evaluating management practices like nest relocation and designing nature-based solutions that mitigate nest flooding. In this study, we investigated the beach GWT response to ocean processes and rain in a fine-grained, mild-sloping beach system by analyzing field data gathered on Galveston Island, Texas in the fall of 2023. We quantified the influence of IG waves, tide, surge, and rainfall on short-term GWT fluctuations between the high tide line and the dune toe by performing tailored spectral analyses on ±30-day time series of water level observations, categorized into *groundwater*, *mixed*, and *submerged* regimes.

We observed significant short-term variability in the beach GWT across the backshore ($\mathcal{O}(1\text{ m})$). Our results were generally consistent with previous studies, showing that the beach matrix acts as a low-pass filter, with higher frequency signals getting increasingly damped, lagged, and distorted landward. Surge and rainfall dominated the GWT response in the upper backshore, the primary sea turtle nesting zone. The tidal signal was increasingly damped and asymmetric towards the dune, whereas IG waves were only relevant near the swash zone. Our analysis explicitly excluded inland groundwater processes (e.g., aquifer recharge or regional groundwater flow), focusing solely on ocean and rainfall-driven groundwater fluctuations within the beach.

A flooding threshold based on a representative nest depth of 30 cm below the surface revealed multiple, prolonged nest inundation events (exceeding 12 hours), even for the shallowest nests. This suggest that Galveston Island is currently not a suitable nesting habitat for sea turtles as nests are likely to get flooded frequently and for prolonged periods. We therefore recommend continuing the current nest relocation program. Our findings underscore the importance of including the GWT in studies of nest flooding and encourage further research towards nature-based solutions that enable sea turtle nesting in low-elevation beach systems like Galveston Island, for example through the design of turtle-friendly nourishments. By integrating insights from coastal science and sea turtle biology, we can develop tailored solutions that not only mitigate flooding risks but also enhance habitat suitability under future climate scenarios.

Data availability—All field data used in this study is described in (Christiaanse et al., 2025b) and available through the 4TU.ResearchData repository at: https://doi.org/10.4121/93256801-ed01-4627-9e49-8607967a0853.

Acknowledgements—The data analyzed in this paper was collected as part of the TURTLE project, which is funded by TKI Delta Technology (grant number T-DEL/2023/095) with support from TU Delft, Texas A&M University, Deltares, Boskalis, University of Exeter, and King Abdullah University of Science and Technology (KAUST). We would like to express our gratitude to the following people who contributed significantly to the data collection: Ir. Meye van der Grinten, Ir. Falco Taal, Dr. Nick Cohn, and Dr. Pete Tereszkiewicz. Further, we want to thank Prof. dr. Ian Turner and Dr. Marie-Pierre Delisle for discussing the data with us and sharing their thoughts and ideas. Finally, many thanks to Prof. dr. ir. Stefan Aarninkhof for his help with the funding acquisition.

CRediT authorship contribution statement—Jakob C. Christiaanse: Writing – review & editing, Writing – original draft, Visualization, Validation, Software, Resources, Methodology, Investigation, Funding acquisition, Formal analysis, Data curation, Conceptualization. José A.A. Antolínez: Writing – review & editing, Supervision, Resources, Investigation, Funding acquisition, Conceptualization. Christopher D. Marshall: Writing – review & editing, Resources. Jens Figlus: Writing – review & editing, Resources, Investigation. Timothy M. Dellapenna: Writing – review & editing, Resources. Ad J.H.M. Reniers: Writing – review & editing, Supervision, Formal analysis.

Cover photo by Andrew Dunstan ©: Green sea turtles (*Chelonia mydas*) nesting and mating at Raine Island, Australia.

4

Uncertain future for global nesting beaches

Abstract

Endangered sea turtles rely on sandy beaches for nesting, linking their long-term survival to global beach availability. However, beaches worldwide are increasingly threatened by anthropogenic stressors and sea level rise (SLR). Reliable vulnerability assessments require understanding beach dynamics across multiple time scales, informed by long-term coastal change records. While many nesting beaches lie in remote, data-poor environments, recent advances in coastal remote sensing now allow us to monitor coastal change worldwide. Here, we combine satellite-derived shorelines (CoastSat), shoreline modeling (CoSMoS-COAST), and global datasets to investigate shoreline evolution and future vulnerability at nine globally important sea turtle nesting sites. We investigate seasonal and long-term shoreline change, hindcast (1980–2024) and forecast (2025–2100) shoreline positions under various SLR scenarios, and quantify available accommodation space based on backbeach elevation and infrastructure footprints. We find that shoreline evolution and vulnerability vary considerably, with three sites showing historical accretion trends and four sites showing erosion. This demonstrates that the previously widely applied *bathtub* approach—adding SLR to a static beach profile—is not suitable to assess the vulnerability of sea turtle nesting beaches. Three eroding beaches emerge as particularly vulnerable due to projected shoreline retreat coupled with limited accommodation space. Despite significant uncertainties arising from long-term shoreline projections, our results provide important insights into seasonal and long-term morphodynamics, identify vulnerable nesting sites, and offer a comprehensive, transferable framework for assessing shoreline evolution and vulnerability at other sites. Understanding these dynamics is crucial to inform conservation and management strategies to future-proof these critical nesting habitats.

This chapter is currently under review at *Earth's Future* as:

Christiaanse, J. C., Vitousek, S., Reniers, A. J. H. M., & Antolínez, J. A. A. (in review). Vulnerability of key sea turtle nesting beaches to future erosion and sea level rise.

4.1. Introduction

Sandy beaches cover approximately one-third of the world's ice-free coastline (Luijendijk et al., 2018) and provide a wide range of ecosystem services. They play a critical role in sediment and water retention, serve as buffers against elevated water levels, offer recreational opportunities, and provide essential habitats for sea turtles and shorebirds (Defeo et al., 2009; Nel et al., 2014). Sea turtles, which are key species in many marine ecosystems (e.g., Christianen et al., 2023; Meylan, 1988), rely on these sandy coasts for nesting (Ackerman, 1997). Consequently, the long-term survival of these endangered reptiles is intrinsically tied to the availability of suitable nesting sites around the world. However, sandy beaches worldwide are increasingly threatened by anthropogenic and climatic stressors, such as sea level rise (SLR; e.g., Leaman et al., 2021; Rosati et al., 2013; Vitousek et al., 2017b). Therefore, there is significant concern about the resilience of global sea turtle nesting sites in the face of ongoing and future erosion and rising sea levels (Patrício et al., 2021; Rivas et al., 2023).

Sandy beaches are dynamic environments that constantly change in response to a range of stressors such as winds, waves and tides, episodic storm events, interannual climate oscillations, and long-term climate-induced trends (e.g., Antolínez et al., 2018; Ashton et al., 2001; Castelle et al., 2015; Vitousek et al., 2017b). Beaches generally erode under stormy conditions and recover during low-energy periods, cycling through different beach states across seasons (Wright & Short, 1984). Embayed beaches often show seasonal rotations, owing to changes in wave climate (Abdulsalam et al., 2025; Harley et al., 2015). Interannual oscillations can drive beach change over multiple years (e.g., El Niño/Southern Oscillation, ENSO; Barnard et al., 2015; Vos et al., 2023b). Structural changes in sediment supply and transport (e.g., through trapping by coastal infrastructure or river damming) can drive chronic erosion/accretion over years to decades (e.g., Pianca et al., 2015). Finally, while beach survivability in response to accelerated SLR is still hotly debated and may vary greatly across different environments (e.g., Cooper et al., 2020; Vousdoukas et al., 2020), it is generally understood that accelerated SLR will cause shoreline retreat (Vitousek et al., 2017b). This may lead to significant long-term beach loss, especially when a static/hardened backbeach environment prevents landward migration of sand (i.e., *coastal squeeze*; Pontee, 2013).

Sea turtles have survived and nested in dynamic beach environments for millions of years, though over the past centuries their populations have declined drastically (McClenachan et al., 2006). Their slow population growth rates mean they are less resilient to short-term population declines (Duarte et al., 2020), making them particularly vulnerable to relatively rapid changes (within years to decades) to their nesting habitat (Mortimer, 1995; Pike & Stiner, 2007). Long-term erosion—from SLR or other causes—could reduce suitable nesting area on the beach, increase the risk of nest flooding, or even lead to the loss of entire nesting beaches. These threats are gaining significant attention in both sea turtle research and conservation efforts (Christiaanse et al., 2025d; Hawkes et al., 2009; Patrício et al., 2021). Nature-based solutions—for instance, through turtle-friendly design of sand nourishments (e.g., Smithers & Dawson, 2023) or by restoring vegetation or reefs to provide coastal protection from flooding and erosion (Barbier et al., 2011)—may offer promising opportunities to preserve current nesting beaches and potentially even enable nesting on new beaches (Christiaanse et al., 2024b).

To evaluate the need for intervention and design nature-based solutions, we first need to understand how the beach system behaves across different time scales and how vulnerable it is to (future) flooding and erosion. Numerous studies have tried to quantify the potential loss of nesting area to SLR by using a simple *bathtub* approach—adding a mean sea level increase onto a fixed digital elevation model of the beach (e.g., Fish et al., 2005; Fuentes et al., 2010; Rivas et al., 2023). Although computationally efficient, this approach does not consider any morphological response of the system and therefore does not provide reliable estimates of beach loss (Wolinsky & Murray, 2009). Understanding the vulnerability of nesting beaches to erosion requires long-term observations (e.g., of the shoreline position, which is commonly used to assess beach change across time scales; Splinter & Coco, 2021; Vitousek et al., 2023a), and information on backbeach topography and human development. Yet, many nesting beaches are located in the tropics and in developing countries (Mazaris et al., 2014), where availability of in-situ field data is generally low. Fortunately, the advent of publicly available satellite imagery and coastal remote sensing tools now allows us to extract reasonably accurate shoreline observations (order 10 m) over the past 30–40 years anywhere in the world (Bergsma et al., 2021; Vitousek et al., 2023a; Vos et al., 2019a).

Here, we combine satellite-derived shorelines, shoreline modeling, and global datasets to analyze the shoreline evolution, characteristics, and future vulnerability of nine globally important sea turtle nesting beaches. We use historical shoreline positions extracted from publicly available satellite imagery using CoastSat (Vos et al., 2019a) to identify seasonal and long-term shoreline change. We calibrate a shoreline model (CoSMoS-COAST; Vitousek et al., 2023b; 2025) with the extracted shorelines to hindcast daily shoreline positions from 1980 to 2025 and forecast them from 2025 to 2100 under various SLR scenarios. Additionally, we quantify the accommodation space at each site using a global coastal digital terrain model (DeltaDTM; Pronk et al., 2024) and global infrastructure footprints (buildings and roads). The shoreline evolution and backbeach characteristics are combined to assess the vulnerability of each site to future erosion and SLR. Our results (1) contribute to the understanding of seasonal and long-term variability of shoreline dynamics at these critical nesting beaches, (2) indicate which sites may be particularly vulnerable to future SLR, and (3) provide a comprehensive, readily applicable framework to analyze shoreline evolution and vulnerability at nesting sites around the world.

4.2. Methods

4.2.1. Study sites

We investigated shoreline evolution and accommodation space at nine key sea turtle nesting sites around the world (Figure 4.1, Table 4.1): Long Beach (Ascension Island), La Escobilla (Mexico), Dirk Hartog Island (Australia), Busca Vida (Brazil), Tortuguero (Costa Rica), Alagadi (Cyprus), Joao Barrosa (Cape Verde), Rancho Nuevo (Mexico), and Masirah Island (Oman). We selected these sites as they (i) host some of the largest nesting populations on the planet, making them important nesting sites for various species; (ii) are relatively remote; and (iii) their morphological evolution is largely unstudied. We describe the results of the first two sites (Long Beach and La Escobilla) in detail in the main text of this paper, while the other seven locations are briefly discussed and summarized. Detailed site descriptions and results figures for the seven remaining sites are provided in Appendix B.

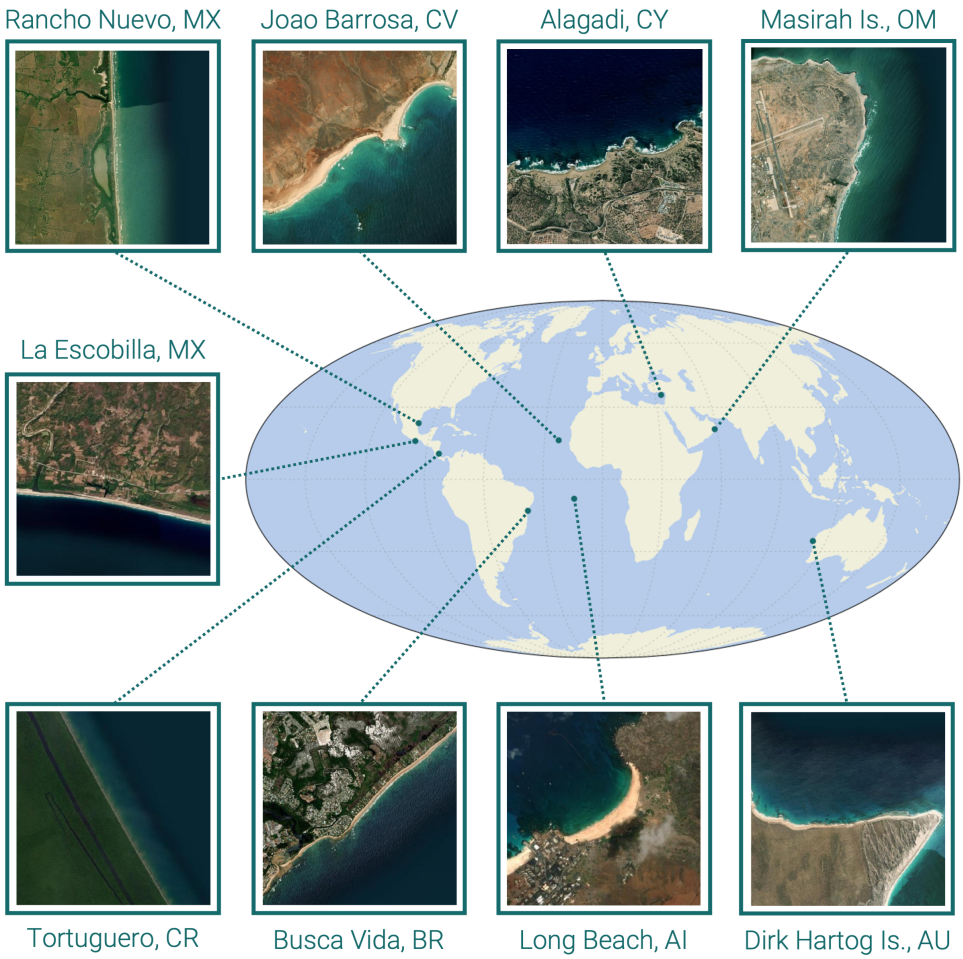

Figure 4.1: Overview map of the nine nesting sites analyzed in this study. Satellite snapshots created from ESRI World Imagery (ESRI, 2024).

Long Beach, Ascension Island

Ascension Island is an isolated volcanic peak on the mid-Atlantic ridge, which hosts one of the largest green sea turtle (*Chelonia mydas, Cm*) nesting populations in the world (Weber et al., 2014). Long beach, an embayed beach on the island's north-west side, is the largest beach and supports the highest number of nests (Godley et al., 2001). The main nesting season spans from January to June. The tidal range is relatively small (0.9 m), but the island is exposed to high wave energy (mean $H_s \approx 1.8$ m), with mostly persistent south-easterly swells from trade winds and less frequent but larger westerly swells. Being situated on the north-west side of the island, Long beach is partly sheltered from the dominant south-easterly swells.

La Escobilla, Mexico

La Escobilla covers a 7-km long stretch of open sandy beach on the southern Pacific coast of Mexico. It is one of only several olive ridley (*Lepidochelys olivacea, Lo*) mass-nesting (*arribada*) beaches worldwide, and therefore an extremely important nesting site for the species (Ocana et al., 2012). In fact, Escobilla hosts the largest sea turtle nesting aggregation in the world, with up to one million olive ridleys nesting in just a few days (Mast et al., 2025). The main nesting season ranges from August to November. Several small rivers and lagoons span the length of the beach. The tidal range (1.2 m) and wave climate (mean $H_s \approx 1.4$ m) are moderate, though the beach is fully exposed to the dominant long-period southwesterly swells.

Site	Country	Lon/Lat	Beach type	Main species	Nest season	$\overline{H}_s$	Tide
Long Beach	Ascension Is.	-14.41, -7.92	Embayed	*Cm*	1–6	1.8	0.9
La Escobilla	Mexico	-96.73, 15.72	Open	*Lo*	8–11	1.4	1.2
Dirk Hartog Is.	Australia	112.99, -25.5	Embayed	*Cc*	11–4	2	0.9
Busca Vida	Brazil	-38.27, -12.87	Open	*Ei*	10–3	1.1	1.7
Joao Barrosa	Cabo Verde	-22.71, 16.03	Open/embayed	*Cc*	6–11	1.4	0.7
Tortuguero	Costa Rica	-83.47, 10.48	Open (BI)	*Cm*	7–10	0.9	0.3
Alagadi	Cyprus	33.49, 35.34	Embayed	*Cm*, *Cc*	5–10	0.8	0.3
Rancho Nuevo	Mexico	-97.77, 23.18	Open (BI)	*Lk*	4–7	0.9	0.5
Masirah Is.	Oman	58.91, 20.66	Open/embayed	*Cc*	5–9	1	2

Table 4.1: Overview of the nine sea turtle nesting sites analyzed in this study. The abbreviation BI in the beach type stands for Barrier Island. The last two columns show the mean significant wave height ($\overline{H}_s$) and the mean tidal range, both in meters. Species abbreviations are: *Cm – Chelonia mydas*, *Cc – Caretta caretta*, *Ei – Erytmochelys imbricata*, *Lk – Lepidochelys kempii*, and *Lo – Lepidochelys olivacea*.

4.2.2. Data and indicators

Coastal transects (GCTS)

We used the Global Coastal Transect System (GCTS; Calkoen et al., 2025b) to extract roughly shore-normal transects every 100 m along each nesting beach. For nesting beaches longer than 5 km, we limited the analysis to a roughly 5-km long stretch. When spatial nesting data was available from literature we tried to select the stretch with the highest nesting density, otherwise we investigated a stretch around the center of the beach. We then selected three representative transects from the available GCTS transects, generally near the middle and the two ends of the (5-km-stretch of) beach. The analyses were carried out by intersecting the transects with the satellite-derived shorelines, elevation data, and infrastructure footprints to define relevant positions along the transects (see following sections).

Satellite-derived shorelines (CoastSat)

We used the python-based toolbox *CoastSat* to extract shorelines from publicly available satellite imagery, described in detail in Vos et al. (2019b). Briefly, CoastSat downloads satellite images (Landsat 5, 7, 8, 9, and Sentinel 2) through Google Earth Engine for a user-defined region of interest and pre-processes them (e.g., by removing cloudy pixels and

applying pan-sharpening for enhanced resolution). Each pixel is then classified into 'water', 'white-water', 'sand', or 'other', using a Neural Network classifier. This classification is used in combination with the Modified Normalized Difference Water Index (MNDWI; Xu, 2006) to extract a sub-pixel resolution shoreline contour, that best separates the 'sand' and 'water' classes (Vos et al., 2019a). The shorelines are then mapped to user-defined transects. Given that the individual satellite images capture the beach at varying tidal levels, the shoreline positions are tide-corrected using tidal data from the global FES2022 tide model (CNES, 2024). The *CoastSat.Slope* module can be used to estimate the beach-face slope by tide-correcting the shoreline time series for a range of potential slope values, and selecting the one that results in the highest damping of the tidal frequencies in the shoreline signal (Vos et al., 2020).

We used all available images from 1984 to the end of 2024 (41 years) from all available satellite missions (Landsat 5, 7, 8, 9, and Sentinel 2). We used the default parameters along with several manual settings per study site (e.g., cloud cover threshold, maximum deviation from reference shoreline, etc.), which are detailed in Appendix B.2. We could not validate the extracted shoreline positions due to a lack of in-situ beach survey data, but we carried out visual inspections of the mapped shorelines on the corresponding satellite images. Moreover, CoastSat-derived shorelines have been validated and compared to in-situ observations in several studies, across different environments and beach settings, generally resulting in a shoreline position error in the order of 10–15 m (Castelle et al., 2021; Vos et al., 2023a; Vos et al., 2019a; 2023b). They are less accurate on macro-tidal, high-energy beaches (Castelle et al., 2021), but all our study sites were micro-tidal, except Masirah Island (meso-tidal, Table 4.1). Finally, CoastSat-derived shorelines have been successfully used to study beach behavior from seasonal to decadal time scales at many locations (e.g., Castelle et al., 2022; Vos et al., 2023b; Warrick et al., 2025).

We mapped the extracted shorelines to the GCTS transects to obtain time series of the relative shoreline position at each transect. Outliers were filtered using CoastSat's built-in *SDS_transects.reject_outliers()* function. We estimated the beach slope using *CoastSat.Slope* during the tidal correction. The shorelines were not corrected for any residual water level differences (e.g., storm surge). Finally, we computed a reference shoreline position by taking the median (less sensitive to extremes/outliers than the mean) shoreline position between 2021 and 2024 (i.e., representing the current shoreline position).

Accommodation space

To quantify the current accommodation space available at each study site, we used three distance indicators, all relative to the reference shoreline position: the backbeach distance (BBD), the infrastructure-free distance (IFD), and the beach width (Figure 4.2). An elevation profile of the backbeach along each transect was extracted from *DeltaDTM*—a state-of-the-art digital terrain model that covers the global coastal regions between 0 and 30 m elevation (Pronk et al., 2024). DeltaDTM has a horizontal resolution of 1 arcsecond (≈ 30 m) and a vertical mean absolute error of 0.45 m. We computed the distance between the first point along each transect above 10 m + MSL elevation and the reference shoreline position as BBD.

To compute the IFD, we used building (Calkoen et al., 2025a) and road footprints from *Overture maps* (www.overturemaps.org). Road footprints from Overture mainly come from OpenStreetMap (www.openstreetmap.org/copyright) and are divided into hierarchical cate-

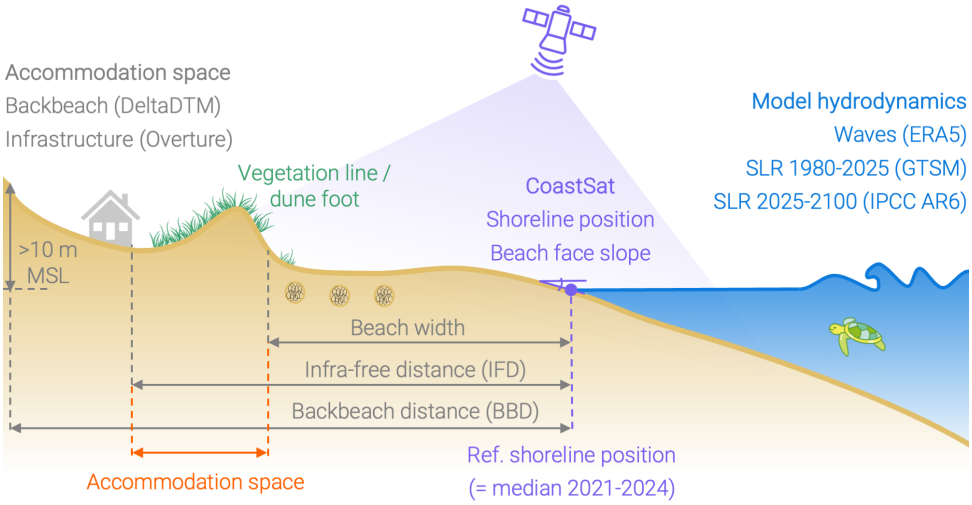

Figure 4.2: Schematic cross-shore profile of a nesting beach (not to scale), showing the various indicators and datasets used in this study. The accommodation space is computed by subtracting the beach width from the lesser of the infrastructure-free distance (IFD) and the backbeach distance (BBD).

gories, from highways to walking paths. Due to the high number of classes, we summarized them into highway (highways and trunks), major road (primary and secondary roads), minor road (tertiary and residential roads), and cycle/walking paths (all remaining roads). As IFD, we computed the distance along each transect from the reference shoreline position to the first intersection with a highway, major road, or building (i.e., the shortest distance was used as IFD, similar to Lansu et al., 2024). We excluded the minor road and foot/cycle categories as they do not necessarily represent fixed obstacles to future shoreline migration. Because the scattered building footprints often fall in-between transects, we used a 50-m buffer zone around each transect to determine intersecting buildings.

The shortest distance of the BBD and IFD represented the maximum available space for shoreline retreat. However, if the shoreline were to retreat this entire distance, there would be no beach behind. Therefore, we estimated the current beach width by intersecting each transect with a manually digitized vegetation edge/dune foot line. To draw this line, we used the most recent Google Earth image at each site and followed the first clear vegetation line behind the beach. For Joao Barrosa and Masirah Island there was no clear vegetation line, so we estimated the dune foot from high-resolution satellite imagery, Google Street View, and public images of the beach, if available. As final proxy of the available accommodation space, we subtracted the beach width from the shortest distance (IFD or BBD; Figure 4.2). Hence, this approach assumes that the beach would only start narrowing once the accommodation space is exceeded.

4.2.3. Shoreline model (CoSMoS-COAST)

The shoreline-change model used here is a recent update of CoSMoS-COAST (Vitousek et al., 2017c; 2021; 2023b), a transect-based, data-assimilated model, which integrates long- and cross-shore sediment transport processes. We calibrated the model with historical wave

conditions and satellite-derived shoreline positions over a hindcast period from 1980 to 2024. Next, we ran forecast simulations (2025–2100) to project long-term shoreline change and assess erosion vulnerability at three selected transects within each study site.

Model equation, parameters, and calibration

The governing equation of CoSMoS-COAST is based on the one-dimensional conservation of sediment volume equation:

$$\frac{\partial Y}{\partial t} = \frac{Y_{eq} - Y}{\tau} - \frac{1}{d_c}\frac{\partial Q}{\partial X} - \frac{c}{\tan\beta}\frac{\partial S}{\partial t} + \upsilon_{lt}, \tag{4.1}$$

where the left-hand term is the rate of change in the shoreline position Y with respect to time t, and the four terms on the right-hand side represent: (1) wave-driven cross-shore equilibrium shoreline change (after Vitousek et al., 2021; Yates et al., 2009), where Y_{eq} is the equilibrium shoreline position (set by instantaneous wave conditions) and τ the equilibrium timescale; (2) gradients in longshore transport, where d_c is the depth of closure, Q is the longshore transport, and X is the alongshore coordinate; (3) sea-level driven profile recession (i.e., the *Bruun rule*), where S is the sea level, $\tan\beta$ is the transgression slope, and c a recession coefficient; and (4) a linear residual trend. See Vitousek et al. (2017c, 2021, 2023b) for details on each model component and its parameters.

Although the underlying equation 4.1 and unknown model parameters (Table 4.2) of the CoSMoS-COAST model used here (and also in Mao et al., 2025) are the same as in Vitousek et al. (2023b), the numerical-solution technique and parameter-estimation method differ from the original. The current model reformulates the cross-shore and longshore-transport terms as discrete convolution operations (see Mao et al., 2025; Vitousek et al., 2025, for details), resulting in the following equation for the shoreline position Y at time t:

$$Y(t) = Y_0 + f_{cs}(t) * g_{cs}(t) + f_{ls}(t) * g_{ls}(t) - c\frac{S(t) - S_0}{\tan\beta} + \upsilon_{lt}t, \tag{4.2}$$

where Y_0 is the initial shoreline position, $*$ represents a convolution operation, $f_{cs}(t)$, $g_{cs}(t)$ and $f_{ls}(t)$ and $g_{ls}(t)$ are the cross-shore and longshore convolution functions, respectively, given by:

$$f_{cs}(t) = -\Delta Y_{cs}\frac{H_s^2(t) - \bar{H}_s^2}{\bar{H}_s^2}, \tag{4.3}$$

$$g_{cs}(t) = \left(1 - \frac{\Delta t}{\Delta T_{cs}}\right)^{t/\Delta t}, \tag{4.4}$$

$$f_{ls}(t) = \Delta Y_{ls}\sin\left(2\alpha(t)\right), \tag{4.5}$$

$$g_{ls}(t) = \left(1 - \frac{\Delta t}{\Delta T_{ls}}\right)^{t/\Delta t}, \tag{4.6}$$

where H_s is the significant wave height, Δt the model time step (1 day), and α the wave incidence angle relative to the shoreline angle.

The seven unknown model parameters resulting from equations 4.2–4.6 are summarized in Table 4.2. The current model is calibrated using a constrained optimization routine (see upper and lower parameter bounds in Table 4.2), not the ensemble Kalman filter method of the original model Vitousek et al. (2023b). The new (iterative) optimization method was tailored to simulate a smaller number of independent transects, whereas the original (sequential, non-iterative) method was designed to run over $\mathcal{O}(1.000–10.000$'s) of transects, for which an iterative optimization method would have been too costly. The parameter-estimation routine used here minimizes the loss function:

$$\mathcal{L}_i = \sqrt{RMSE_{\text{norm}}^2 + (1-\rho)^2 + (1-STD_{\text{norm}})^2} \tag{4.7}$$

for each transect i, individually, where

$$RMSE_{\text{norm}} = \frac{RMSE_{\text{pred}}}{STD_{\text{obs}}} = \frac{\sqrt{\frac{1}{N}\sum_{n=1}^{N}\left(Y_{\text{obs}_n} - Y_{\text{mod}_n}\right)^2}}{STD_{\text{obs}}}, \tag{4.8}$$

$$STD_{\text{norm}} = \frac{STD_{\text{pred}}}{STD_{\text{obs}}}, \tag{4.9}$$

and ρ are the normalized root mean square error, the normalized standard deviation, and the Pearson correlation coefficient, respectively. The subscripts $_{\text{obs}}$ and $_{\text{pred}}$ denote observed and predicted values.

Parameter	Symbol	Unit	Lower bound	Upper bound
Cross-shore equilibrium timescale	ΔT_{cs}	days	20	300
Cross-shore equilibrium excursion	ΔY_{cs}	m	2	100
Longshore equilibrium timescale	ΔT_{ls}	days	20	365
Longshore equilibrium excursion	ΔY_{ls}	m	−250	250
Bruun coefficient	c	-	0.5	1.5
Residual linear trend	v_{lt}	m/y	−1	1
Initial shoreline position	Y_0	m	−70	70

Table 4.2: Overview of the seven model parameters that need to be calibrated in the CoSMoS-COAST shoreline model. The final two columns denote the bounds of the calibration range.

Forcing and model scenarios

We first ran and calibrated the model over the hindcast period (1980–2024). To force the model, we used historical time series of parametric wave conditions from the global ERA5 reanalysis (Hersbach et al., 2018) and SLR from the Global Tide and Surge Model v3.0 (GTSM; Muis et al., 2020). For waves, we extracted the daily maximum significant wave height (H_s) and corresponding mean wave direction (θ) from the nearest ERA5 node at each study site. For historical SLR, we extracted the yearly mean sea level at the nearest GTSM

node. Thus, the wave conditions were updated at each timestep (daily), whereas the mean sea level was updated each year.

For the model calibration and validation we used the CoastSat-derived shoreline positions. Given the inherent noise and error in satellite-derived shorelines (Vitousek et al., 2023a; Vos et al., 2019a), we applied a density-based filter and smoothed the obtained shorelines before feeding them into the model: first, we removed all years with less than five observations, to decrease the chance of isolated observations disproportionally affecting the long-term trend. These were mainly years in the early part of the period (before the launch of Landsat 7 in 2000). Next, we smoothed the shorelines using the *smoothn* Matlab function (smoothing parameter $S = 30$; Garcia, 2010). Then, the optimization routine searched for the set of model parameters that minimize the multivariate loss function (Eq. 4.7) using the modeled shorelines and the smoothed shoreline time series in the hindcast period.

For the forecast period (2025–2100), we used the model with the optimized parameter values obtained during the hindcast period. We extracted decadal SLR rates from the nearest node of the regional IPCC AR6 SLR projections (Fox-Kemper et al., 2023). To account for scenario and SLR modeling uncertainty we ran the model for the 5th, 50th, and 95th percentile of the lowest (SSP1–2.6) and highest (SSP5–8.5) emission scenarios of the low confidence AR6 projections (which include both low and medium confidence processes; Garner et al., 2021; Kopp et al., 2023). The 50th percentile represented the median projections, while the 5th and 95th percentiles were used to determine a 90% confidence interval. We interpolated decadal to yearly rates and cumulatively added these to the mean sea level between 2021–2024 derived from GTSM (i.e., the final four years of the hindcast period). We did not explicitly account for projected future changes in wave climate (e.g., Morim et al., 2025; Reguero et al., 2019), but drew a random month from the 45-year ERA5 time series (1980–2024) for each month starting from January 2025 (i.e., for January 2025, we drew a random January between 1980–2024, then a random February, etc., following the method of Davidson et al., 2010). Hence, the future wave time series were shuffled versions of the ERA5 time series.

Performance verification

We evaluated the model performance with the same shoreline time series used for calibration, as there were no in-situ shoreline data available for any of the sites. As model performance is known to depend on the chosen metric (Montaño et al., 2020), we used two widely applied methods (e.g., Gomez-de la Peña et al., 2023; Montaño et al., 2020; Repina et al., 2025): (1) Mielke's index, λ, which ranges between 0 (poor) and 1 (perfect performance); and (2) Taylor diagrams (Taylor, 2001), which allow a graphical comparison of multiple models with a reference (observations) based on their normalized standard deviation (STD_{norm}), Pearson's correlation (ρ), and normalized root mean squared error ($RMSE_{\text{norm}}$)—i.e., the same metrics as used in the optimized loss function (Eq. 4.7). Mielke's index was computed as (Duveiller et al., 2016):

$$\lambda = 1 - \frac{\frac{1}{N}\sum_{n=1}^{N}\left(Y_{\text{obs}_n} - Y_{\text{pred}_n}\right)^2}{STD_{\text{obs}}^2 + STD_{\text{pred}}^2 + \left(\overline{Y}_{\text{obs}} - \overline{Y}_{\text{pred}}\right)^2}, \tag{4.10}$$

where N is the number of observed (Y_{obs}) and modeled (Y_{pred}) shoreline positions, $\overline{Y}_{\text{obs}}$ and

$\overline{Y}_{\text{pred}}$ are the mean values, and STD_{obs} and STD_{pred} the standard deviations. The numerator represents the mean squared error (MSE).

4.2.4. Shoreline evolution analysis

To assess the shoreline evolution and erosion vulnerability of the nine sites, we used the CoastSat-derived shoreline positions and the model hind- and forecasts. First, we decomposed the CoastSat-derived time series to derive seasonal and long-term components. Then, we used Empirical Orthogonal Function (EOF) analysis on the model hindcast. The full approach is visualized in Figure 4.3 and explained in more detail in the following paragraphs.

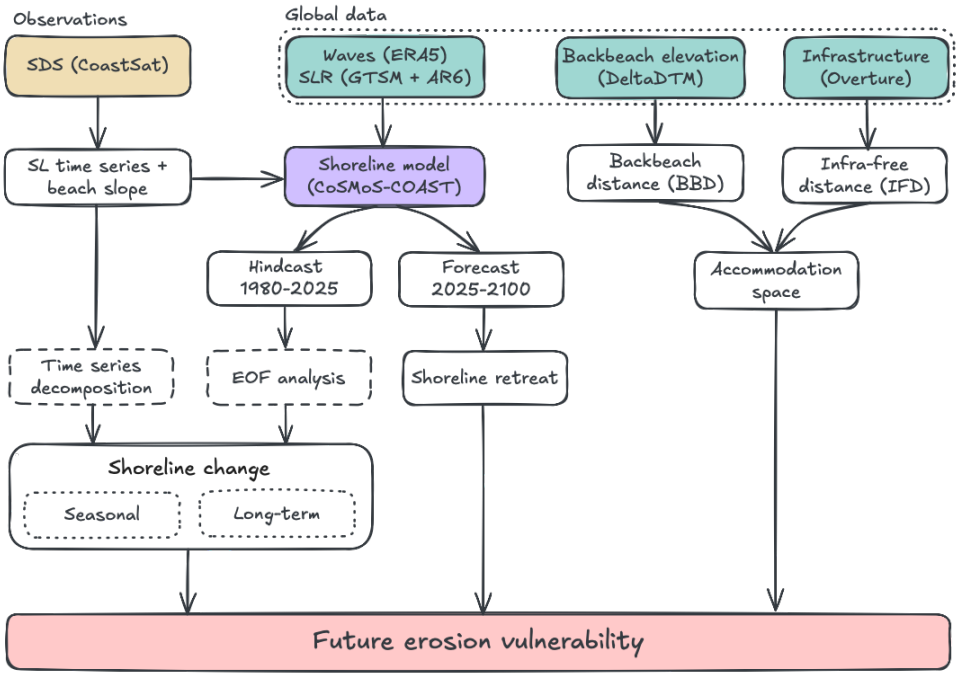

Figure 4.3: Flowchart showing the approach used in this study. The future erosion vulnerability of the nine nesting beaches is assessed by combining historical shoreline change (satellite-derived and hindcasted), modeled shoreline projections, and an estimate of the accommodation space.

Shoreline time series decomposition

To analyze seasonal to long-term trends in the satellite-derived shoreline positions, we used *Seasonal-Trend Decomposition based on LOESS* (STL; Cleveland et al., 1990), where LOESS stands for Locally Estimated Scatterplot Smoothing (Cleveland, 1979). Using STL, the CoastSat-derived shoreline position time series at each transect was decomposed into three components:

$$Y(t) = Y_{\text{lt}}(t) + Y_{\text{ss}}(t) + Y_{\text{res}}(t), \tag{4.11}$$

where Y_{lt} is the long-term trend, Y_{ss} is the recurring seasonal component, and Y_{res} is the residual shoreline position.

First, we derived Y_{lt} using LOESS (Python library *loess* by Cappellari et al., 2013) with a four-year smoothing window, in order to separate interannual to decadal variability in shoreline change from seasonal fluctuations (as in Warrick et al., 2025). LOESS requires regular sampling intervals without gaps, for which we used the median monthly shoreline position. We linearly interpolated gaps of up to nine consecutive months. In case there were larger gaps, we only used the most recent part of the time series, with gaps of nine months or less. Interpolated values were only used in the derivation of Y_{lt}, not the seasonal component. We then detrended the time series by removing Y_{lt}, leaving the seasonal and residual components. The seasonal component (Y_{ss}) was then computed from the bulk monthly median shoreline position over the remaining time series (i.e., the median position per month over all years). We estimated the seasonal shoreline excursion as the difference between the maximum and minimum position in the seasonal cycle. Finally, subtracting Y_{ss} from the detrended time series yielded the residual component ($Y_{res} = Y - Y_{lt} - Y_{ss}$). Interannual variability in the seasonal cycle is therefore included in Y_{res}.

While Y_{lt} provided some means of visually assessing long-term shoreline change, it still included inter-annual signals. Therefore, we also quantified the total long-term shoreline change rate at each site through (1) a linear regression fit to the smoothed CoastSat observations (i.e., the same data as used for the model hindcast) and (2) the long-term trend (v_{lt}) from the model, which was capped at 1 m of shoreline change per year (Table 4.2).

EOF analysis on shoreline hindcast

We performed EOF analysis on the modeled daily shoreline positions to further assess the dominant modes of shoreline change over the hindcast period (45 years, 1980–2025). For a complete technical description of EOF applied to shoreline analysis, see Miller and Dean (2007a). Briefly, the eigenvector decomposition was applied on the covariance matrix of spatio-temporal shoreline positions. Hence, EOFs describe the main spatial shoreline change modes, including their temporal amplitudes (given by the principal components, PCs). This allows quantifying how the shoreline positions at different transects change over time (Antolínez et al., 2019; Miller & Dean, 2007a; 2007b). The number of EOFs/PCs is equal to the the smallest dimension (in this case one per transect, so three EOFs).

4.3. Results

4.3.1. Long Beach, Ascension Island

Due to the remoteness of Ascension Island, there were no images from Landsat 5 and only very few from Landsat 7. From 2013/14 (post-Landsat 8 launch), image frequency increased, leaving twelve years of data for the shoreline decomposition ($n = 400$ shorelines after outlier removal, Figure 4.4f–h). As can be seen from the seasonal cycles at the three transects, Long Beach is a perfect example of a rotating pocket beach: transect T3 erodes during the austral winter (higher wave energy), while the more sheltered T1 accretes during the same period (Figure 4.4b, e–h). The nesting season overlaps with the austral summer and a wider beach at T3. At both transects, the total seasonal shoreline excursion was around 45 m. At T2 the seasonal excursion was less (19 m), being closer to the pivot point of the beach rotation. The nesting season mostly overlapped with the widest beach at T3 (austral

summer) though extending well into the rotation of the beach. Over the past twelve years, the long-term trend appeared relatively stable, with some interannual variability and a weak erosive trend at T2 and T3.

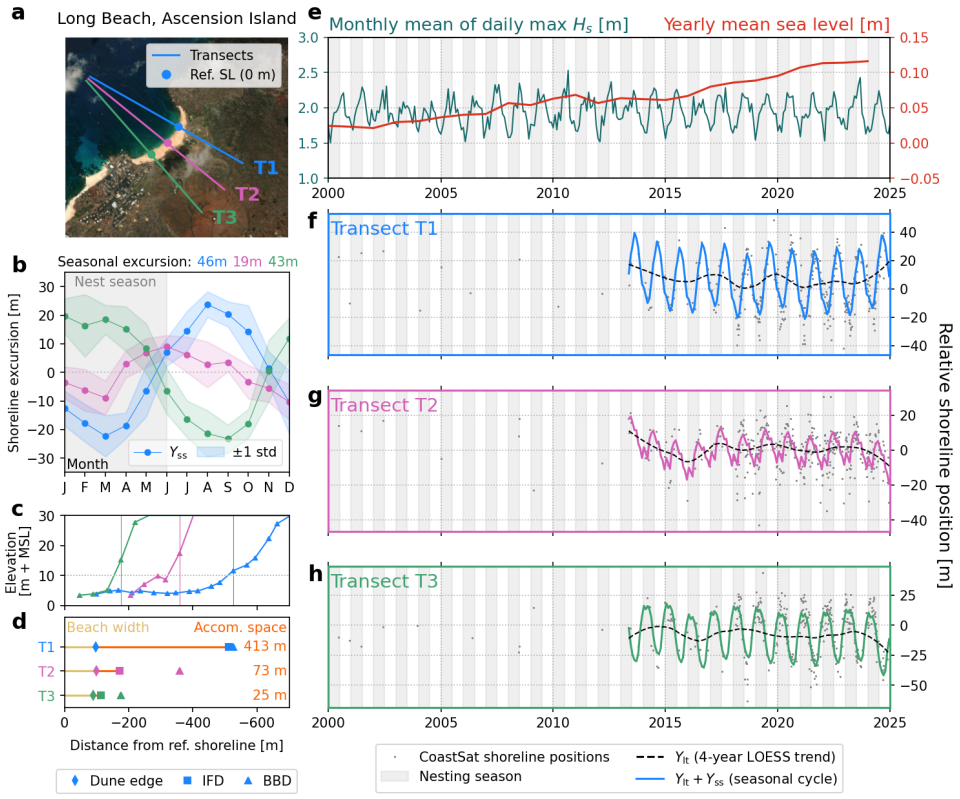

Figure 4.4: Shoreline and accommodation space analysis for Long Beach, Ascension Island: a) Satellite image showing the transects and reference shoreline position; b) Seasonal shoreline component, Y_{SS}, at each transect; c) Backbeach elevation profiles, with vertical lines denoting the first point above 10 m + MSL; d) Beach width and accommodation space at each transect; e) Historical wave and water level time series; f-g) Observed and decomposed (long-term and seasonal) shoreline position time series at each transect.

The backbeach elevation and accommodation space varied significantly in alongshore direction (i.e., across the transects; Figure 4.4c). At the northern end (T1) the backbeach was flatter and only started steepening about 400–500 m from the reference shoreline. Moving south, the backbeach profile became increasingly steep with a sharp increase in the slope around 150 m from the shoreline at T3, owing to a hill behind the southern part of the beach. The median beach width was about 100 m at T1 and T2 and 90 m at T3. Though the backbeach is not highly developed, the accommodation space at all three transects was determined by buildings behind the beach, with the least space at T3 (25 m) and T2 (73 m) and significantly more space at T1 (413 m, Figure 4.4d). Considering the backbeach elevation only, the accommodation space would have increased to about 350 m and 80 m at

T2 and T3, respectively.

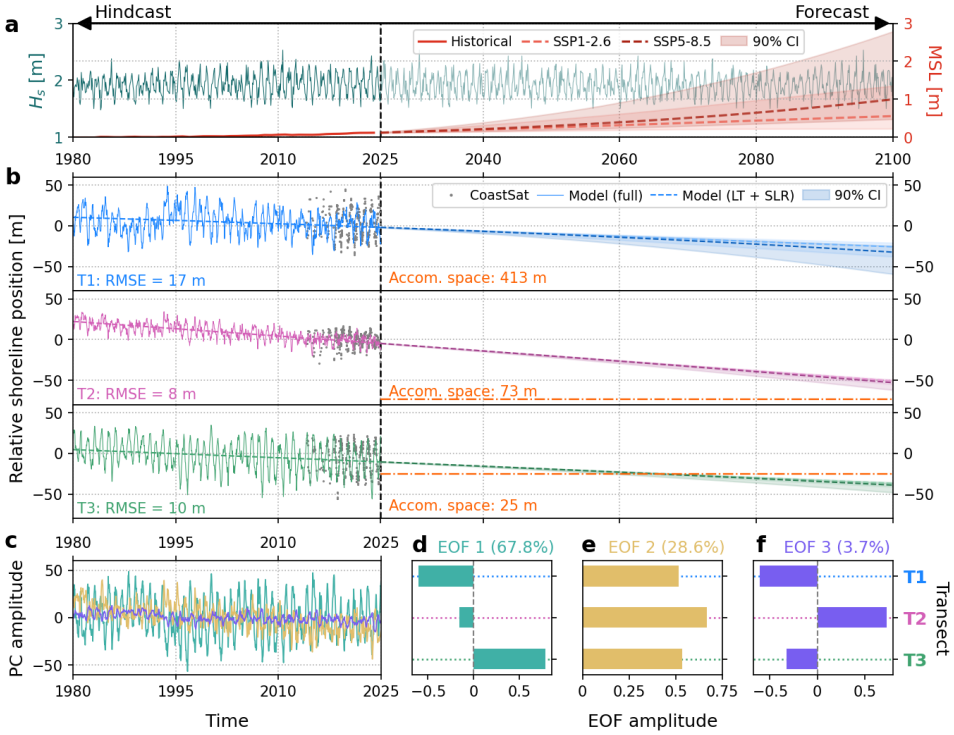

Figure 4.5: Shoreline modeling results at Long Beach, Ascension Island. a) Wave and sea level time series used to force the model; b) Modeled shoreline position at each transect for the hindcast (1980–2025) and forecast (2025–2100) periods. Grey dots are the CoastSat shorelines, solid lines represent the full model results, and dashed lines only include the long-term trend (v_{lt}) and SLR components. In the forecasts, the two dashed lines represent the median SSP1–2.6 (lighter color) and SSP5–8.5 (darker color) SLR projections, while the shading indicates the area between the 5th and 95th percentile; c) Amplitude of the three PCs over the hindcast period; d–f) Amplitudes of the three EOFs at each transect and percentage of explained variance.

The model performed differently across the three transects, but generally matched the observed seasonal cycles (Figure 4.5b). Especially at T3 the model aligned well with the observations and had a relatively low root-mean-square-error ($RMSE = 10$ m) compared to the fluctuations in the signal ($\mathcal{O}(50$ m$)$). At T1 and T2 the model still achieved reasonable RMSE values, though especially at T1 it struggled to fully capture the seasonal and interannual variability. At T2 the RMSE was smaller than at T3, but the signal fluctuations were also significantly smaller (i.e., the relative RMSE was larger at T2). Over the past 45 years, the hindcast showed long-term erosion at all transects, though strongest at T2 (≈ 0.5 m/year). This suggests the beach was less curved in the past, with the shoreline at T2 further seaward relative to T1 and T3.

The EOF analysis confirmed the beach rotation as the dominant mode of change, represented by EOF 1 (68% of the variance). It clearly showed the seasonal oscillation in the PC amplitude over time and the corresponding opposite EOF coefficients at T1 and T3 (Figure

4.5c, d). EOF 2 (≈ 29%) represented a combination of a seasonal to interannual cross-shore mode in which all transects erode/accrete simultaneously, and the long-term erosive trend, strongest at T2 (highest EOF amplitude; Figure 4.5c, e). Although EOF 3 only explained about 4% of the variance, it represented part of the reorientation of the beach (from straighter to more curved), with T2 eroding and T1 and T3 accreting (Figure 4.5c, f; no net accretion as in EOF 2 both T1 and T3 eroded).

The model predicted future erosion at all three transects, but to differing degrees. T2 was the most erosive with at least 50 m of shoreline retreat projected by 2100, under both median SLR scenarios, significantly reducing the available accommodation space (Figure 4.5a, b). The median projections were slightly less erosive at T1 and T3, though at T1 the 90% confidence intervals covered a larger spread, with the SSP5–8.5 95th percentile also predicting more than 50 m shoreline retreat. At T3 the difference between SLR scenarios was relatively small, with around 35–50 m of shoreline retreat by 2100. More importantly, shoreline retreat at T3 was projected to exceed the available accommodation space of 25 m around 2060/70.

4.3.2. La Escobilla, Mexico

At La Escobilla there was sufficient data for the STL shoreline decomposition from 1993 onward (32 years and $n = 1016$ shorelines after outlier removal, Figure 4.6f–h). Again, there was a clear seasonal pattern in the shoreline position, with the excursion around 25 m at all transects (Figure 4.6c). Instead of a rotating beach, La Escobilla showed a dominant cross-shore mode, with all transects accreting and eroding in phase with each other. The entire beach narrowed in the austral winters, during the peak of the southern hemisphere swell, and widened in the austral summers. This means the beach is relatively narrow when turtle nesting starts in August, but widens as the nesting season progresses.

Although mean sea level at La Escobilla increased by about 10 cm since 1985 (Figure 4.6e), the shoreline data showed a long-term accretion trend—strongest at T1 since about 2000 (≈ 1 m/year), and at T2 and T3 mostly over the past decade (Figure 4.6f–h). Between 1993 to about 2010–15, the long-term shoreline position was relatively stable at T2 and T3, with some interannual oscillations. Since then the beach has generally accreted. There have been no beach nourishments near this site, but one explanation for the accretion could be that the river to the west of T1 has been supplying the beach with sediment (Figure 4.6a). This hypothesis was supported by the eastward movement of the river channel on the beach, apparent in historical satellite images. This suggests alongshore sediment transport is eastward, which could also explain the lag in the start of the long-term accretion from T1 (closest to the river) to T3 (furthest, Figure 4.6f–h).

The beach width at La Escobilla decreased from 85 m at T1 to 61 m at T3. The backbeach was relatively flat and low at all three transects and only at T1 the slope started to increase some 500 m from the shoreline. The accommodation space at T1 was determined by the backbeach elevation reaching above 10 m + MSL 546 m behind the beach, although using the IFD would have resulted in similar accommodation space (≈ 600 m). At T2 and T3 the backbeach profile remained low and the accommodation space was set by the IFD, resulting in 476 m at T2 and only 23 m at T3. This shows the sensitivity of the accommodation space to individual buildings: the backbeach was not highly developed but there are a few houses behind T3, leading to the much lower accommodation space. Moreover,

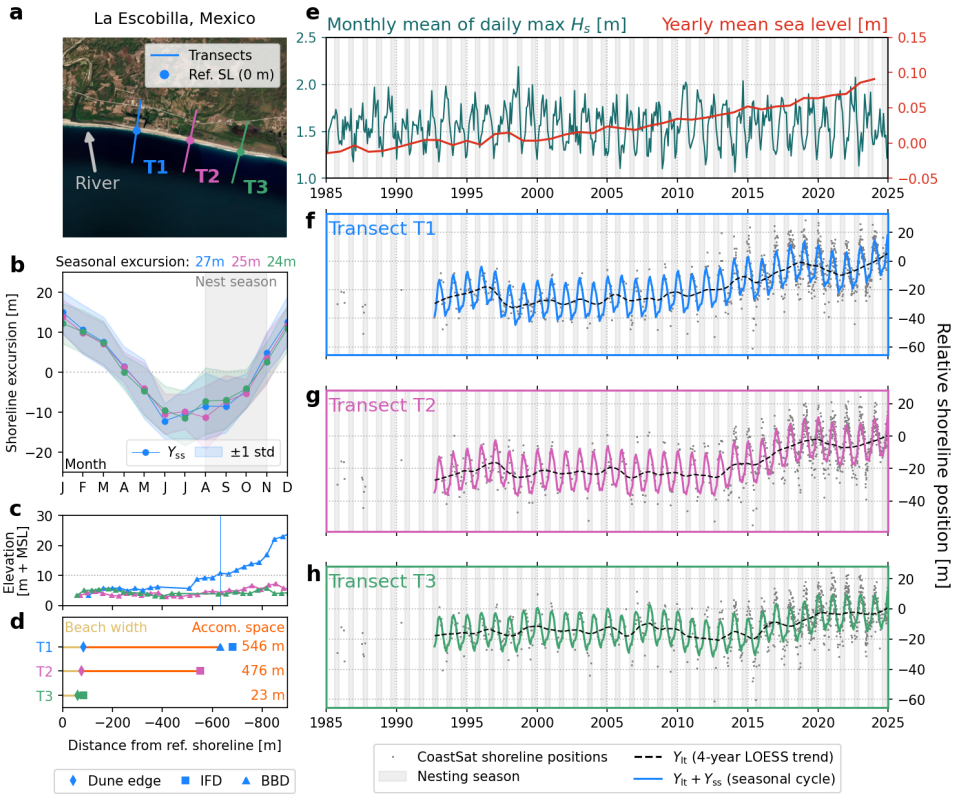

Figure 4.6: Shoreline and accommodation space analysis for La Escobilla, Mexico: a) Satellite image showing the transects and reference shoreline position; b) Seasonal shoreline component, Y_{SS}, at each transect; c) Backbeach elevation profiles, with vertical lines denoting the first point above 10 m + MSL; d) Beach width and accommodation space at each transect; e) Historical wave and water level time series; f-g) Observed and decomposed (long-term and seasonal) shoreline position time series at each transect.

while the accommodation space was higher at T1 and T2, there is a village behind the beach in-between these two transects, leading to significantly less accommodation space there.

The model showed similar results for the three transects and generally matched the observations well, replicating the seasonal behavior and long-term accretion with relatively low RMSE values (8–9 m, Figure 4.7a). However, it struggled with simulating the amplitude of interannual oscillations, which it underestimated, most evidently at T3. The observed accretion over the past decades was simulated by the model through a linear trend, contrasting with the observed stability in shoreline position between 1990–2010 and increased accretion afterward. The synchronous behavior among the transects was also reflected in the EOF analysis: EOF 1 explained virtually all variance in the signal, representing a cross-shore mode (including the seasonal cycle) as well as the long-term accretion trend, strongest at T1 and weakening slightly to T3 (Figure 4.7b, c). The other two EOF modes were negligible compared to EOF 1. The future projections all showed continued accretion, again strongest at T1 (50+ m by 2100) and weakening toward T3 (15–30 m), even under nearly 3 m of SLR.

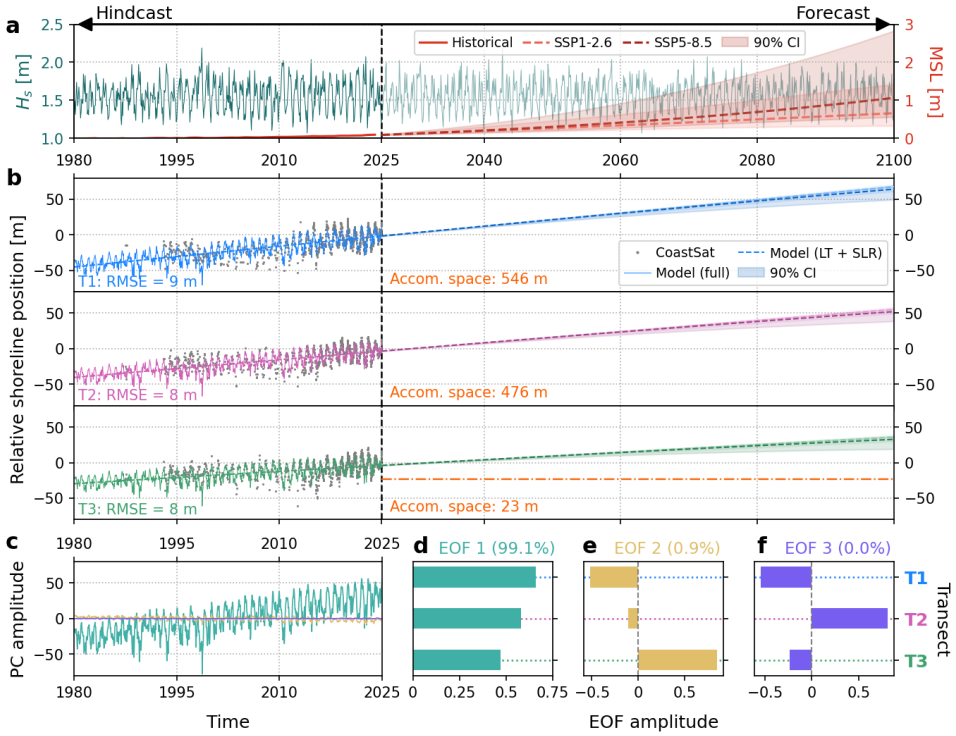

Figure 4.7: Shoreline modeling results at La Escobilla, Mexico. a) Wave and sea level time series used to force the model; b) Modeled shoreline position at each transect for the hindcast (1980–2025) and forecast (2025–2100) periods. Grey dots are the CoastSat shorelines, solid lines represent the full model results, and dashed lines only include the long-term trend (v_{lt}) and SLR components. In the forecasts, the two dashed lines represent the median SSP1–2.6 (lighter color) and SSP5–8.5 (darker color) SLR projections, while the shading indicates the area between the 5th and 95th percentile; c) Amplitude of the three PCs over the hindcast period; d–f) Amplitudes of the three EOFs at each transect and percentage of explained variance.

Differences between the SLR scenarios were small.

4.3.3. Global results

Observed shoreline change and accommodation space varied significantly across the seven other locations (see overview in Table 4.3; figures analogous to 4.4–4.7 are given in Appendix B.4). Strong and clear seasonal cycles were apparent at Joao Barrosa (up to 36 m) and Masirah Island (up to 27 m). At Alagadi, Busca Vida, Dirk Hartog Island, Tortuguero, and Rancho Nuevo, some seasonality was visible, but interannual or long-term signals generally dominated shoreline change over the past decades.

Several sites showed a long-term historical erosion trend, both in the linear fit based on the CoastSat-derived shoreline positions, as well as in the model trend (v_{lt}). Rancho Nuevo showed the strongest erosion (0.8–0.9 m/year at T3), followed by erosion rates below 0.5 m/year at Long Beach, Dirk Hartog Island, and Alagadi (Figure 4.8). Busca Vida and Masirah Island had relatively stable shorelines, while Tortuguero, La Escobilla, and

particularly Joao Barrosa (up to 2 m/year) showed accretion trends.

Over the forecast period, the model projected significant shoreline retreat at Long Beach, Dirk Hartog Island, Alagadi, and Rancho Nuevo by 2100. At Rancho Nuevo this was well below the available accommodation space, but at Dirk Hartog and Alagadi accommodation space was limited at two of the three transects, suggesting that shoreline retreat at these sites could lead to a reduction in beach width, especially under the SSP5–8.5 scenario. The model generally projected continued accretion at Joao Barrosa and La Escobilla until 2100. Moreover, Joao Barrosa, Tortuguero, Rancho Nuevo, and Masirah Island had large accommodation space at all three transects.

The difference in shoreline change between the SLR scenarios varied significantly across the nine sites, with higher Bruun coefficients (c) in the model (i.e., more SLR impact) leading to larger differences. The median projections were generally quite close together, but the 90% confidence intervals spanned wide ranges at some locations. At Masirah Island, for instance, the 2100 projection ranged from no change or even slight accretion (SSP1–2.6 5th percentile) to over 50 m of shoreline retreat (SSP5–8.5 95th percentile). For some locations the range covered accretion as well as erosion. At other locations, like La Escobilla or Rancho Nuevo, the difference between the scenarios was small compared to the projected change.

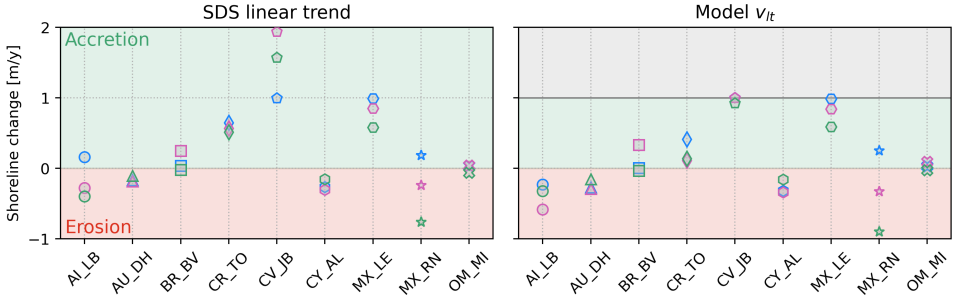

Figure 4.8: Long-term shoreline position trends at each location and transect based on a linear regression of the smoothed observations (left) and the long-term trend (v_{lt}) in the model (right, bounded between -1 and 1 m/y). Marker shapes denote the site (see x-axis) and marker edge color the transect (T1 blue, T2 pink, T3 green).

4.4. Discussion

4.4.1. Vulnerability of global nesting sites to erosion and SLR

Our results suggest that vulnerability to future erosion and SLR varies significantly across the nine sites, and in alongshore direction at some sites (Figure 4.9). At seven of the nine sites (all except La Escobilla and Joao Barrosa), potential future shoreline retreat is projected at one or more of the three transects. At some of these, the projections also include accretion, depending on the SLR scenario (e.g., Tortuguero, Masirah Is.). La Escobilla and Joao Barrosa are clearly projected to continue accreting in the future, suggesting these sites are the least vulnerable to SLR. Long Beach, Dirk Hartog Is., and Alagadi have limited accommodation space, which is exceeded for several scenarios. This implies that these are the most vulnerable sites, facing potential reduction of beach width and nesting area in the future.

Site	Beach slope	Trend	Beach width	IFD	BBD	Accom. space
Long Beach, AI	0.1*	Eroding	89–99	114–511	176–526	25–413
Dirk Hartog Is., AU	0.045–0.085	Eroding	45–55	>860	69–483	22–428
Busca Vida, BR	0.085–0.105	Stable	27–35	44–216	>649	17–181
Tortuguero, CR	0.1*	Accreting	37–40	>1000	>1000	>1000
Joao Barrosa, CV	0.045–0.05	Accreting	35–62	>915	603–899	567–864
Alagadi, CY	0.1*	Eroding	58–73	393–576	121–490	56–417
La Escobilla, MX	0.06–0.065	Accreting	61–85	84–682	>631	23–546
Rancho Nuevo, MX	0.1*	Eroding	21–36	>1000	>1000	>1000
Masirah Is., OM	0.065–0.085	Stable	83–136	>1000	301–634	176–498

Table 4.3: Results for all nine sea turtle nesting sites analyzed in this study. The beach slope was estimated using CoastSat and was used in the SLR term of the shoreline model. Asterisks denote a default slope of 0.1, used when the slope estimation was not reliable (i.e., do not represent a measured beach slope). The distance ranges (final four columns) are given in meters and represent the range across the three transects of each site. In the final three columns, values with a > sign are minimum values (e.g., the transects generally extended 1000 m landward from the shoreline, so if no infrastructure was within 1000 m, this is denoted as >1000).

At the remaining eroding sites, projected shoreline retreat by 2100 is below the estimated accommodation space, although close at some transects (e.g., Busca Vida T3, Long Beach T2). These findings highlight the variability in the morphological evolution and characteristics across global nesting sites and show the importance of understanding these, including the backbeach topography.

While our results provide insights into the future vulnerability of the nine sites, they present significant uncertainties, for example in the definition of the accommodation space. The IFD is particularly sensitive to building positions in sparsely-developed areas, as the position of a single building can strongly influence the available accommodation space. This is evident at La Escobilla where the accommodation space at T3 is much lower than at T1/T2 due to one building (Figure 4.6d). In general, if the accommodation space is determined by infrastructure, it is not just a question of whether the beach can migrate through, but also whether the infrastructure may be allowed to erode to provide room for the beach system (Lansu et al., 2024). Additionally, here we defined the BBD simply by an elevation of 10 m + msl, but ideally it would account for the backbeach slope, to identify cliffs, for instance. However, the horizontal resolution of DeltaDTM (1 arcsec) and other state-of-the-art global elevation models makes it difficult to identify steep slopes as the sample points along the transects are often 40–50 m apart. Local, high resolution assessments of the backbeach elevation and geology could therefore drastically improve accommodation space estimates, but are costly and time-intensive.

Our analysis assumes a fully sandy profile in which the entire beach width retreats together with the shoreline until exceeding the accommodation space and the beach starts narrowing. However, the future evolution of the beach will depend on the geomorphology of the profile. For instance, dunes behind the beach will respond more dynamically than hard substrates (Moore et al., 2025). If the beach is underlain by rocky formations, erosion may expose a rocky shoreline, potentially inaccessible to turtles (Wildermann et al., 2024). Dirk Hartog Island and Joao Barrosa both exhibit rock formations at some places along the beach. Moreover, at Dirk Hartog Island the beach is backed by a steep rocky slope. Here, this translated to zero accommodation space, but these slopes may erode and allow some

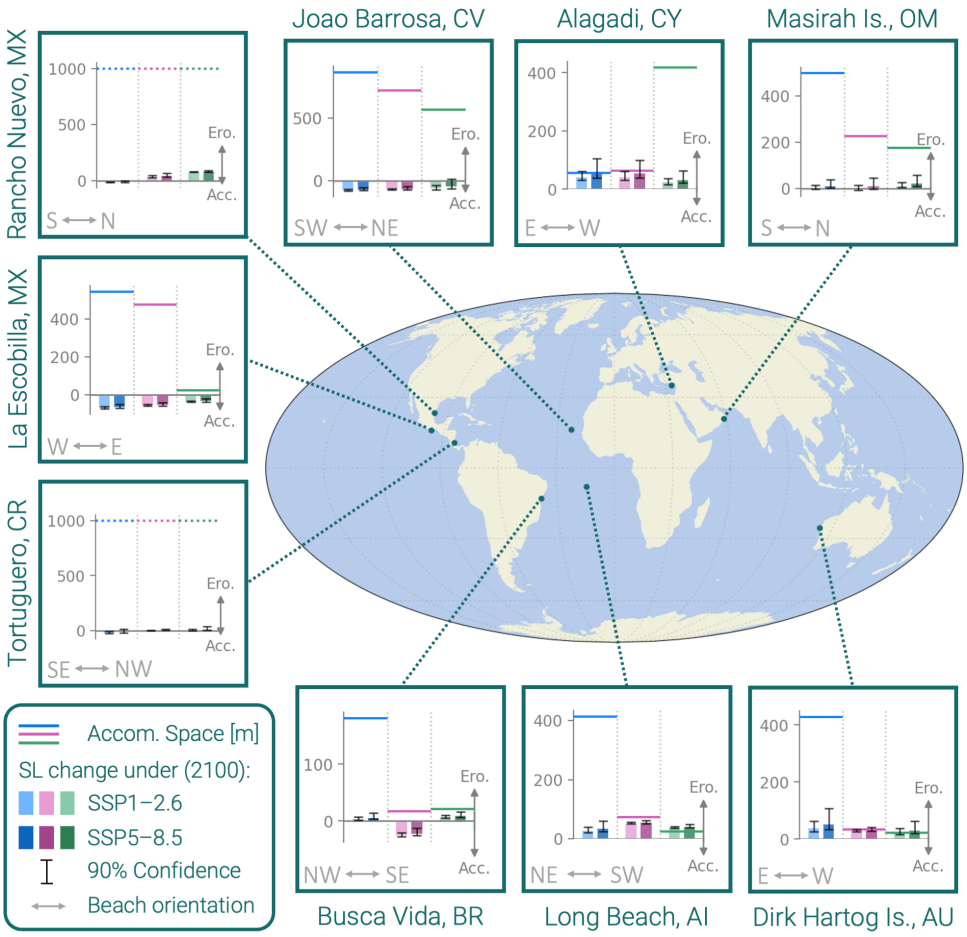

Figure 4.9: Overview map showing the accommodation space (horizontal lines) and projected shoreline change at the three transects (T1 blue, T2 pink, T3 green) of al nine nesting sites. Projected shoreline change is shown for the two SLR scenarios (SSP1–2.6 in brighter colors, SSP5–8.5 in darker colors) with the bars representing the median and the error whiskers the 90% SLR confidence interval. Erosion is positive (upward) and accretion is negative (downward) to visualize the effect on the accommodation space. The beach orientation (direction from T1 to T3) is given by the horizontal arrows. The dotted accommodation space lines at Rancho Nuevo and Tortuguero indicate that the accommodation space is at least 1 km.

beach migration (Walkden & Dickson, 2008). At Tortuguero and Rancho Nuevo, accommodation space was not limited within the first kilometer from the shoreline, suggesting they can accommodate significant shoreline retreat. But both sites are located on barrier islands, for which the response to SLR might also differ from regular sandy coastlines (Anarde et al., 2024; Moore & Murray, 2022; Thomas et al., 2024). Accounting for these different geological settings requires a more complex and integrated modeling approach. For example, shoreline models could be coupled to cliff erosion models to account for a rocky backbeach (Erikson et al., 2017; Walkden & Dickson, 2008; Wolinsky & Murray, 2009).

4.4.2. Model performance, limitations, and uncertainty

Model performance varies considerably across sites and transects (Figure 4.10) but aligns with previous shoreline modeling efforts reported in the literature, even at well-monitored sites (e.g., Gomez-de la Peña et al., 2023; Montaño et al., 2020; Repina et al., 2025). Both performance metrics show agreement in their results (i.e., locations scoring high on the Taylor diagram also score high with Mielke's index). The obtained λ indices (Figure 4.10a) are similar to those in a previous blind-testing study of shoreline models (Montaño et al., 2020). At many sites, the model captures the seasonal dynamics, but struggles to replicate inter-annual or longer-term trends not directly linked to wave conditions or sea level changes. Moreover, the Taylor diagram shows that the model generally underestimates the variability in the observations (Figure 4.10b). These are both common limitations of reduced complexity models (Bosboom et al., 2014; Hunt et al., 2023; Vitousek et al., 2023b). This results in lower performance at sites where interannual to long-term oscillations dominate the shoreline signal (e.g., Alagadi, Busca Vida, and Dirk Hartog Island), whereas the model performs better where wave-related seasonal shoreline cycles dominate (e.g., La Escobilla and Masirah Island). Notably, La Escobilla shows high performance metrics even though the model cannot replicate the interannual variation in the accretion (instead modeling it through the linear trend term, Figure 4.7). At some sites performance varies significantly across transects (e.g., Long Beach and Joao Barrosa), which is also common in shoreline modeling, especially at embayed beaches (Abdulsalam et al., 2025; Repina et al., 2025).

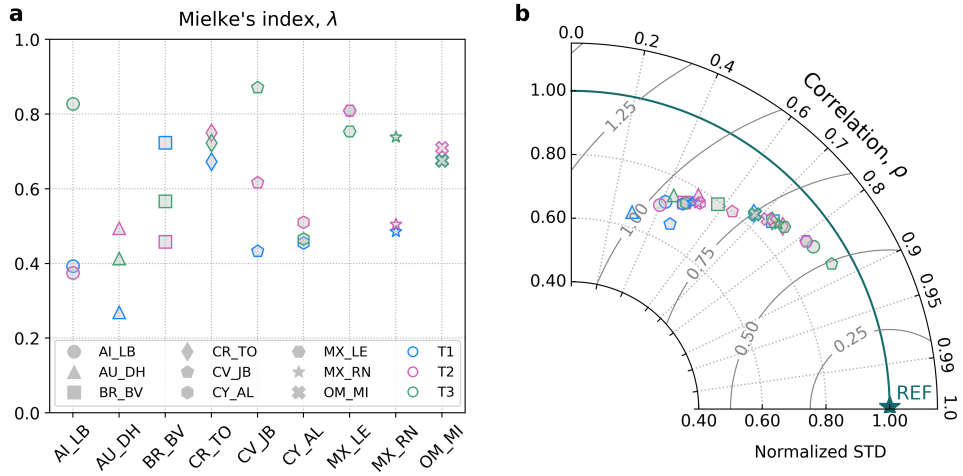

Figure 4.10: Model performance across the sites (marker shape) and transects (edge color), assessed through a) Mielke's index (λ); and b) a Taylor diagram, which shows the Pearson correlation (ρ, angle), normalized standard deviation (radial axis), and normalized RMSE (contours). The latter two are normalized by the standard deviation of the observations, hence a perfect model would have $nSTD = 1$, $\rho = 1$ and $nRMSE = 0$, corresponding to the point marked REF. Sites are abbreviated by Country_Site (e.g., AI_LB = Ascension Island, Long Beach).

The model has several limitations, which can partly explain why it struggles, for instance at Long Beach T1. First, the cross-shore term is hard-wired to erode the shoreline with increasing wave energy, and therefore cannot replicate accretion during the high-energy

season, which happens at T1 during the seasonal rotation at Long Beach. Consequently, the model minimizes the cross-shore contribution and tries to replicate the behavior with longshore transport only. Second, the CoSMoS-COAST version used here models each transect separately without enforcing a sediment balance across transects. Hence, sediment is not necessarily equally distributed during the beach rotation, as there is no mass conservation. Third, due to forcing the model with offshore wave conditions, the waves are rotated such that the mean direction is shore-normal. This is a partly valid assumption as oblique waves generally refract towards the coast (Holthuijsen, 2007), but it may not always hold. Long Beach is situated on the northwest side of the island, while the dominant wave direction is from the south-east (trade wind swells), essentially coming from behind the island and potentially not fully refracting to normal incidence.

A key limitation for this study is the uncertainty in the model's long-term components, which aligns with many previous studies (e.g., Le Cozannet et al., 2019; Vitousek et al., 2024). While seasonal fluctuations are evident in the data and may be inferred from the forcing conditions, historical SLR has been low ($\mathcal{O}$(10–15 cm) since 1980), making the morphological response hard to distinguish from shorter-term 'noise' (Vitousek et al., 2017b). Nevertheless, sea level has risen at all nine sites, which the model is hardwired to translate to shoreline retreat (Bruun rule). At eroding (accreting) transects, the model optimization generally tends to maximize (minimize) the Bruun coefficient (c), which effectively modulates the selected transgression slope. In our model runs, the optimized value for c reaches the upper or lower bound for all transects (Figure B.1), also showing the uncertainty in the applied transgression slopes. At accreting transects, the minimal SLR term combined with a positive linear trend (v_{lt}, replicating the accretion) generally projects continued accretion in the future (most obvious at La Escobilla and Joao Barrosa). While not impossible, it is uncertain whether the underlying causes will maintain accretion over time. Moreover, while the v_{lt} term allows the model to partially replicate non-wave-/sea level-driven processes, it is dependent on the accuracy and consistency of the historical observations it is derived from. Especially in the early part of the hindcast there are relatively few observations. It is therefore very sensitive to bias or extreme values in these early observations (e.g., if early observations are predominantly from the same season, this may bias v_{lt}). Moreover, it cannot account for long-term variability in sediment sinks and/or sources.

Next to uncertainty arising from the model itself, there is also intrinsic uncertainty in the natural processes. While the included uncertainty in SLR projections is not trivial, the chosen transgression slope generally has a much stronger effect on the projected shoreline change (Antolínez et al., 2019; Vitousek et al., 2024; Wolinsky & Murray, 2009). Although the Bruun coefficient (c) allows some modulation of the transgression slope during model optimization, future studies could explore a set of potential transgression slopes more rigorously (e.g., Vitousek et al., 2024). Finally, in the forecast, we opted to focus on sea level driven shoreline change and neglected expected future changes to the wave climate (Morim et al., 2023; Reguero et al., 2019) and storm intensity and frequency (Morim et al., 2025; Sobel et al., 2016). The monthly reshuffling of the historical ERA5 wave time series for the projections (Section 4.2.3) also mean that interannual variability in wave climate is removed.

4.4.3. Implications for conservation and beach management

Due to the inherent uncertainty in our long-term predictions they should be used cautiously to help inform management decisions. They serve as a first exploration of potential future shoreline change, to identify sites that may be particularly vulnerable to future erosion. Uncertainty notwithstanding, the projected erosion at Dirk Hartog Is., Alagadi, and Long Beach is concerning as these sites show shoreline erosion trends and have limited accommodation space that may lead to loss of nesting habitat. Future studies should carry out more detailed assessments of these sites, which may help inform decision-makers on beach management and/or conservation measures. Such assessments could include local, higher resolution data on beach and backbeach characteristics and more sophisticated coastal resilience indicators, beyond the shoreline position (e.g., Dong et al., 2018). They should also include more rigorous quantification of model and wave climate uncertainty (Kroon et al., 2025; Vitousek et al., 2021; Zarifsanayei et al., 2023).

Our results also reveal dominant modes of shoreline change at the different sites, which may play an important role in assessing the vulnerability to future erosion and suitability of potential beach management strategies. For instance, if, as we hypothesize, the river at La Escobilla is responsible for the observed accretion, then an effective measure protecting the beach from erosion might be to simply leave the river be—i.e., not modify its course or interrupt the sediment supply through damming. This highlights the variety of processes that may affect coastal change and the need to understand these in vulnerability assessments.

The large variability in projected shoreline change demonstrates that the *bathtub* approach, used in many previous studies (e.g., Fish et al., 2005; Fuentes et al., 2010; Rivas et al., 2023), is not suitable to assess SLR vulnerability at nesting sites. Under the bathtub assumption, any rise in sea level automatically translates to shoreline retreat, as the static morphology rules out stable or accreting profiles. The loss of nesting habitat is then purely a function of the elevation of the current nesting zone. Applying this approach to the nesting sites here would therefore have resulted in projected erosion (and likely habitat loss) at all nine sites, regardless of the historical and present shoreline evolution. We therefore strongly discourage using the bathtub approach in future SLR vulnerability assessments.

Due to the global-scale coverage of the datasets used herein, our approach is readily transferable to assess shoreline evolution and potential vulnerability at *any* other sites around the world, though it is mainly suitable for relatively open coasts and embayed beaches. Morphologically more complex sites, including river mouths, basin inlets, or migrating sand spits, may require more advanced modeling approaches to quantify beach change, as the shoreline position may not provide sufficient information (French et al., 2016; Murray et al., 2014). For instance, the olive ridley mass nesting sites in Odisha, India (Shanker et al., 2004) and the leatherback (*Dermochelys coriacea*) rookeries at Braamspunt, Suriname and Awala-Yalimapo, French Guiana (Fossette et al., 2008) are situated near large river mouths and dynamic sand spits, which can change shape rapidly, on timescales ranging from months to a few years. In such environments, shorelines determined using transect-based methods could overlap or intersect due to complex spit formation and shifting sandbanks. Moreover, shoreline recession does not necessarily indicate beach narrowing or habitat loss, but can instead reflect spit elongation or morphological reconfiguration occurring over these shorter timescales.

4.5. Conclusion

In this paper, we combined CoastSat-derived shorelines, shoreline modeling (CoSMoS-COAST), and global datasets to analyze the shoreline evolution, characteristics, and future vulnerability of nine globally important sea turtle nesting beaches. We identified seasonal and long-term trends in shoreline position and used the shoreline model CoSMoS-COAST (Vitousek et al., 2023b) to hindcast daily shoreline positions from 1980 to 2024 and forecast them from 2025 to 2100 under two SLR scenarios, including associated uncertainty. Additionally, we quantified the available accommodation space at each site using using a global digital terrain model (DeltaDTM; Pronk et al., 2024) and global infrastructure footprints (Overture maps). Long-term shoreline evolution and seasonality varied considerably across the nine sites, with four sites showing erosion trends and three sites accretion. The future shoreline projections indicated that one-third of the sites may be particularly vulnerable to SLR, due to projected shoreline retreat coupled with limited accommodation space. Our results (1) help understand the seasonal and long-term morphodynamics at these critical nesting beaches, (2) indicate which sites may be vulnerable to future erosion and SLR, and (3) provide a transferable framework to analyze shoreline evolution and vulnerability at nesting sites around the world. Given the identified uncertainties in our analysis, future work might conduct more detailed assessments at vulnerable sites, including local-scale data and robust uncertainty quantification, to support effective conservation planning and targeted management strategies.

Data availability—All data underlying the analyses presented in this chapter (including the model code) are publicly available through the 4TU.ResearchData repository at https://doi.org/10.4121/0a7cf460-e3da-4f80-aa20-f41eb7f9ef93.v1. All global datasets used in this study are also available online, for access please refer to the corresponding references mentioned in this chapter.

Acknowledgments—We would like to acknowledge the following grant, which provided the digital infrastructure to make computations with the global datasets: EINF-14436 ”Coastal Science with AI in a Changing Climate”. Further, we thank Ir. Floris Calkoen for his guidance with using GCTS and Overture Maps, Dr. Kilian Vos for his advice with using CoastSat, and Ir. Etiënne Kras for early discussions and work on this project.

Cover photo by Adhith Swaminathan ©: Olive ridley sea turtles (*Lepidochelys olivacea*) during a mass-nesting *arribada* event at Rushikulya, India.

5

New horizons for nesting sea turtles

Abstract

Climate change and human activity threaten sea turtle nesting beaches through increased flooding and erosion. Understanding the environmental characteristics that enable nesting can aid to preserve and expand these habitats. While numerous local studies exist, a comprehensive global analysis of environmental influences on the distribution of sea turtle nesting habitats remains largely unexplored. Here, we relate the distribution of global sea turtle nesting to 22 coastal indicators, spanning hydrodynamic, atmospheric, geophysical, habitat, and human processes. Using state-of-the-art global datasets and a novel 50-km-resolution hexagonal coastline grid (Coastgons), we employ machine learning to identify spatially homogeneous patterns in the indicators and correlate these to the occurrence of nesting grounds. Our findings suggest sea surface temperature, tidal range, extreme surges, and proximity to coral and seagrass habitats significantly influence global nesting distribution. Low tidal ranges and low extreme surges appear to be particularly favorable for individual species, likely due to reduced nest flooding. Other indicators, previously reported as influential (e.g., precipitation and wind speed), were not as important in our global-scale analysis. Finally, we identify new, potentially suitable nesting regions for each species. On average, 23% of global coastal regions between −39° and 48° latitude could be suitable for nesting, while only 7% is currently used by turtles, showing that the realized niche is significantly smaller than the fundamental niche, and that there is potential for sea turtles to expand their nesting habitat. Our results help identify suitable nesting conditions, quantify potential hazards to global nesting habitats, and lay a foundation for nature-based solutions to preserve and potentially expand these habitats.

This chapter is a revised version of the publication in *Scientific Reports*:

Christiaanse, J. C., Antolínez, J. A. A., Luijendijk, A. P., Athanasiou, P., Duarte, C. M., & Aarninkhof, S. (2024). Distribution of global sea turtle nesting explained from regional-scale coastal characteristics. *Scientific Reports*, 14, 752. [Link]

5.1. Introduction

Climate change and human activity pose many different challenges to sea turtles, including the flooding and erosion of their nesting habitats—sandy beaches (Hawkes et al., 2009; Patrício et al., 2021). Although sea turtles have successfully evolved and adapted to habitat changes over millions of years, their slow population growth rates mean they are unable to recover quickly from population declines (recovery rates of sea turtle populations can range from several decades to 100 years; Duarte et al., 2020). This makes them particularly vulnerable to relatively fast-paced changes to their nesting habitat (Mortimer, 1995; Pike & Stiner, 2007), such as current human and climate-induced effects on nesting beaches (e.g., rising temperatures and sea levels; Fish et al., 2005).

An imminent threat is the flooding and erosion of nesting beaches during events with high water levels and/or waves (e.g., storms and tropical cyclones). Incubating nests can get inundated or even washed away, significantly decreasing hatching success (Pike & Stiner, 2007; Van Houtan & Bass, 2007). Furthermore, storm erosion can significantly alter beach morphology, which may affect nesting over several seasons (Long et al., 2011). On longer time-scales, structural erosion and coastal squeeze may gradually diminish the amount of nesting habitat available to sea turtles (e.g., Fish et al., 2005; Fuentes et al., 2010; Katselidis et al., 2014). These threats are expected to intensify in the future, because many nesting beaches lie in (1) the tropics (Mazaris et al., 2014), the most vulnerable zone to increased future coastal flooding due to sea level rise (Vitousek et al., 2017a); (2) regions prone to tropical cyclone activity (Fuentes et al., 2019; Pike & Stiner, 2007); and (3) developing countries, where coastal areas are expected to become increasingly developed in the future (Neumann et al., 2015). Nature-based solutions—for example, through turtle-friendly design of sand nourishments or by adding coastal vegetation or reefs to provide coastal protection from flooding and erosion—may offer promising opportunities to preserve and even expand nesting habitats. However, we first need to understand the environmental characteristics that enable sea turtle nesting to design such solutions.

Many studies have attempted to identify preferential nesting conditions for sea turtles, but the results are often inconclusive or inconsistent among studies (e.g., Foley et al., 2006; Mortimer, 1990). Generally, incubating nests require certain temperature and humidity windows (Ackerman, 1997), and nesting females seemingly try to limit the exposure of their nests to conditions outside these windows. Hence, temperature (Ackerman, 1997; Mortimer, 1990; Pike, 2013; Santidrián Tomillo et al., 2015; Wood & Bjorndal, 2000), humidity (Ackerman, 1997; Mortimer, 1990; Pike, 2013; Santidrián Tomillo et al., 2015; Wood & Bjorndal, 2000), geomorphology (e.g., beach elevation and slope; Culver et al., 2020; Dunkin et al., 2016; Horrocks & Scott, 1991; Kikukawa et al., 1999; Mortimer, 1990; Provancha & Ehrhart, 1987; Yamamoto et al., 2012), hydrodynamics (e.g., waves and water levels; Foley et al., 2006; Putman et al., 2010; Santana Garcon et al., 2010), and human activity (Kikukawa et al., 1999) have all been mentioned as potentially influential factors on nesting suitability. Yet, to date there are hardly any robust ranges for the multivariate characteristics believed to enable turtle nesting. They vary significantly between nesting beaches of different species, and even populations of the same species (Pike, 2013; Yamamoto et al., 2012). The fact that all sea turtles exhibit some degree of nest site fidelity, returning to nest in the region where they hatched (Schroth et al., 1996), further complicates causation. It therefore remains uncertain how turtles select their nesting beaches (Miller et al., 2003).

Most past studies have focused on individual (and usually popular) nesting beaches, rarely comparing them to 'non-nesting' beaches, which may make it difficult to discern suitable conditions (Miller et al., 2003). Moreover, focusing on individual beaches limits the analysis to a small subset of the species' realized niche and hinders the ability to distinguish patterns on a regional level. Only few studies have tried to identify suitable characteristics for nesting on a scale that exceeds individual beaches within the same region (Almpanidou et al., 2016; Mortimer, 1990; Pike, 2013; Santana Garcon et al., 2010). Pike (2013) was the only one of these who analyzed and predicted nesting suitability over large parts of the global coastline, but his analysis was limited to variables related to temperature and precipitation, and did not include any information on hydrodynamics, geomorphology, habitat, or human activity near nesting sites.

Here, we relate sea turtle nesting activity to a broad range of environmental characteristics of global coastal regions. All five globally distributed species are considered: the loggerhead turtle (*Caretta caretta*, *Cc*), green turtle (*Chelonia mydas*, *Cm*), hawksbill turtle (*Eretmochelys imbricata*, *Ei*), leatherback turtle (*Dermochelys coriacea*, *Dc*), and olive ridley turtle (*Lepidochelys olivacea*, *Lo*). We assess the influence of 22 coastal indicators related to hydrodynamic, atmospheric, geophysical, habitat, and human processes on the global distribution of sea turtle nesting grounds, using state-of-the-art global datasets combined with tailored machine learning techniques. We then identify spatially homogeneous patterns in the most influential indicators through a global-scale cluster analysis of coastal regions. Using the clusters, we further investigate the relationship between influential coastal indicators and nesting activity and identify new, potentially suitable nesting regions (fundamental niches) for all five species. The results (1) help identify and quantify suitable nesting conditions and main hazards in each (potential) nesting region; and (2) guide research on the design of nature-based solutions to restore and preserve nesting habitats from present and future coastal impacts, and to enable the colonization of potentially suitable nesting regions (Barbanti et al., 2022).

5.2. Methods

We characterized the World's coastline using state-of-the-art global datasets on hydrodynamic, atmospheric, geophysical, habitat, and human variables (Table 5.1). These data were spatially aggregated onto a novel 50-km-resolution hexagonal coastline grid, called *Coastgons* (Christiaanse & Antolínez, 2023), to perform our analysis on a single resolution (a Coastgon being a hexagonal coastal cell). We derived 22 indicators describing temporal and spatial variability of coastal characteristics for each Coastgon (Table 5.2). Next, we assessed the importance of these indicators on the global distribution of sea turtle nesting grounds through a machine learning regression technique (random forests), and selected a subset of six influential indicators for each sea turtle species. We identified patterns in the coastal characteristics of global sea turtle nesting habitats by clustering the six indicators of each species with self-organizing maps, a machine learning clustering technique. Finally, we identified new, potentially suitable nesting regions for each species, based on the clusters, and illustrated these in nesting suitability maps. The methodology is explained in more detail in the following sections and illustrated in Figure 5.1.

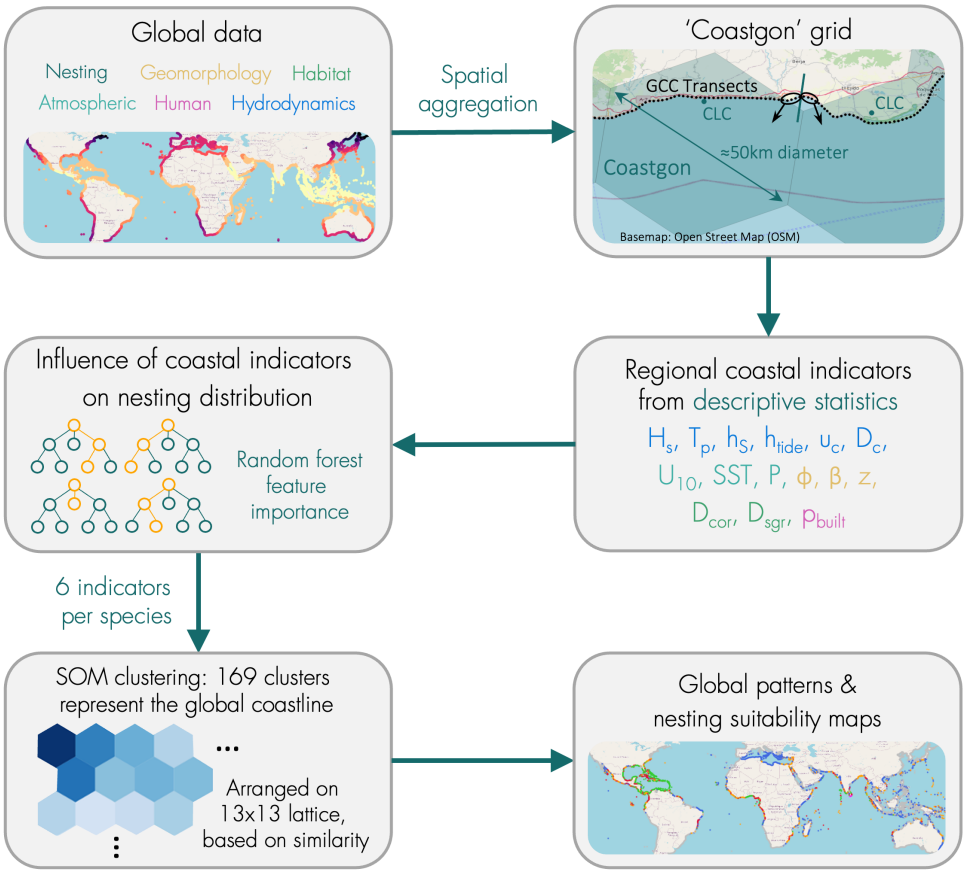

Figure 5.1: Flowchart showing the methodology of this study. First, data gathered from eight global datasets was aggregated onto the Coastgon grid. Next, we derived 22 coastal indicators for each Coastgon from these data using descriptive statistics. We then assessed the influence of each indicator on the distribution of global sea turtle nesting by fitting a random forest model. Based on the feature importance we selected a subset of six influential indicators per turtle species. Then we identified patterns in the six indicators among global sea turtle nesting regions, by clustering the Coastgons based on the six indicators selected for each species, through self-organizing maps (SOM). Finally, we identified new, potentially suitable nesting regions for each species, based on the SOM clusters.

5.2.1. Global data

We used global data describing sea turtle nesting activity from SWOT (Halpin et al., 2009; Kot et al., 2021) and WIDECAST (Eckert & Eckert, 2019), waves, wind, sea surface temperature, and precipitation (ERA5; Hersbach et al., 2018), tide and surge levels (GTSM; Muis et al., 2020), ocean currents (ORAS5; Copernicus Climate Change Service Climate Data Store, 2021), geomorphology and coastal land use (GCC; Athanasiou et al., 2024), and the distribution of coral reefs (Allan Coral Atlas; Li et al., 2020) and sea grass meadows (UNEP-WCMC; UNEP-WCMC & Short, 2021). Each dataset is briefly described below and summarized in Table 5.1.

- **SWOT**, the State of the World's Sea Turtles project, provides a database of global sea turtle nesting sites since 2004 (although including earlier data), compiled from data contributions of over 550 individuals and organizations around the World and is hosted by the OBIS-SEAMAP platform (Halpin et al., 2009; Kot et al., 2021). As such, the spatial resolution and accuracy vary significantly, ranging from different sites on the same beach, to groups of beaches (e.g., a small island with multiple beaches). Each site is labeled either as 'Quantified', 'Unquantified', or 'No-Nesting'. Since our Coastgon resolution is large enough to aggregate the different spatial resolutions of the nesting sites and we did not weight Coastgons based on the number of nesting sites, we used all quantified and unquantified nesting sites ($N = 5383$ unique sites, many with multiple species, see Figure 5.2).

- **WIDECAST**, the Wider Caribbean Sea Turtle Conservation Network, provides a nesting atlas spanning 45 Caribbean countries and territories, compiled from data provided by more than 200 contributors (Eckert & Eckert, 2019). There is significant overlap between the SWOT and WIDECAST datasets, but WIDECAST provides additional data for several regions where SWOT is incomplete (e.g., Brazil). As we aggregate all nesting sites to the Coastgon grid, the overlap is not a problem for the analysis, hence we used all available nesting sites ($N = 1336$ unique sites, many with multiple species, see Figure 5.2).

- **ERA5**, the ECMWF Reanalysis v5, is a global atmospheric reanalysis, providing hourly time series of atmospheric, land, and oceanic climate variables from 1940 to present (Hersbach et al., 2018). The model is split into two coupled structured global grids, ERA5-wave at a resolution of 0.5° for wave variables (e.g., sea and swell wave heights and periods) and ERA5-atmos at a resolution of 0.25° for atmospheric, land, and oceanic climate variables (e.g., wind, land moisture, and sea surface temperature). We used time series of significant wave height (wind sea and swell combined), peak wave period, 10 m wind speed, sea surface temperature, and total precipitation from 1980 to 2021 (42 years).

- **GTSMv3.0**, the Global Tide and Surge Model, solves tidal propagation and was forced with wind and sea level pressure fields from ERA5 to provide a 10-minute interval time series of global tide and storm surge levels (Muis et al., 2020). The spatial resolution of the output nodes varies around the globe, but is generally around 20–50 km near the coast, with higher resolution along European coastlines (< 10 km). We used tide and surge data computed for 1985 to 2014 (30 years).

- **ORAS5**, the Global Ocean ReAnalysis System, is a global, eddy-permitting ocean and sea ice ensemble reanalysis, based on five members (Copernicus Climate Change Service Climate Data Store, 2021). It provides global monthly mean values of ocean data from 1958 to present, on a structured grid with 0.25° horizontal resolution and at 75 depth levels up to 5500 m deep. We used time series of ocean current velocities at 0.5 m below the surface, from 1980 to 2021.

- **GCC**, Global Coastal Characteristics, is a dataset of hydrodynamic, geophysical, and socioeconomic indicators along the global coastline (Athanasiou et al., 2024). Data

is provided at shore-normal transects which follow the coastline at 1-km intervals. We used data on geomorphology (slopes and topography), shoreline orientation, and built environment in the coastal zone.

- The **Allan Coral Atlas** provides a global coral reef extent map, based on reef occurrence probabilities computed through a convolutional neural network (Li et al., 2020). We used geo-referenced polygons of coral reefs covering all ocean basins.

- **UNEP-WCMC** provides a global distribution of seagrass meadows (UNEP-WCMC & Short, 2021), which is regularly updated since 2003, to reflect present conditions. We used geo-referenced polygons of seagrass meadows covering all ocean basins.

Dataset	Data	Ref.	Type of data	Spatial dimensions	Temporal dimensions
SWOT	Nesting grounds	1	Observations	Geolocations, variable	n/a
WIDECAST	Nesting grounds	2	Observations	Geolocations, variable	n/a
ERA5-wave	Hydrodynamics	3	Reanalysis	Structured grid, 0.5°	1980–2021, hourly
ERA5-atmos	Meteorology	3	Reanalysis	Structured grid, 0.25°	1980–2021, hourly
GTSM	Tide and surge	4	Hindcast	Unstructured grid, variable	1980–2018, 10 min
ORAS5	Ocean currents	5	Reanalysis	Structured grid, 0.25°	1980–2021, monthly
GCC	Geomorphology	6	Mixed	Transects, 1 km	variable, single times
Allan Coral Atlas	Coral reef extent	7	Modeled	Geopolygons, variable	2020, single time
UNEP-WCMC	Seagrass locations	8	Observations	Geopolygons, variable	since 2003

Table 5.1: Summary of the global datasets used for this study. References: [1]Halpin et al. (2009) and Kot et al. (2021), [2]Eckert and Eckert (2019), [3]Hersbach et al. (2018), [4]Muis et al. (2020), [5]Copernicus Climate Change Service Climate Data Store (2021), [6]Athanasiou et al. (2024), [7]Li et al. (2020), [8]UNEP-WCMC and Short (2021).

While SWOT and WIDECAST provide invaluable sources of nesting data, we are aware that these datasets are not complete and that some developing countries in particular are underrepresented in the database (see also Section 5.4). We therefore added some additional nesting sites to our analysis—specifically in regions where we know SWOT is incomplete—based on information provided by Shimada et al. (2021, Red Sea), Shanker and Choudhury (2007, India and Pakistan), and Laloë and Hays (2023, global). An overview of all nesting sites used for this study is presented in Figure 5.2.

Moreover, the variability in accuracy and completeness of the SWOT nesting data and the use of other global datasets were one of the reasons that we chose the Coastgon approach (see next section) with a resolution (50 km) suited to regional analysis of coastal characteristics. A single nesting site in SWOT will lead to a corresponding 'nesting Coastgon', regardless of how many turtles nest there, or how many other nesting sites there are close by. This mitigates the issue of underreported and missing nesting sites.

5.2.2. Coastgons

We created a novel ≈ 50-km-resolution hexagonal coastline grid, called *Coastgons*, dividing the Earth's coastline between −39° and 48° latitude into distinct coastal regions (Christiaanse & Antolínez, 2023). The latitude limits were chosen by adding a buffer to the latitudes of the most northern and southern known sea turtle nesting sites in the SWOT database (Kot et al., 2021). We opted for a hexagonal cell grid over a point-based transect system

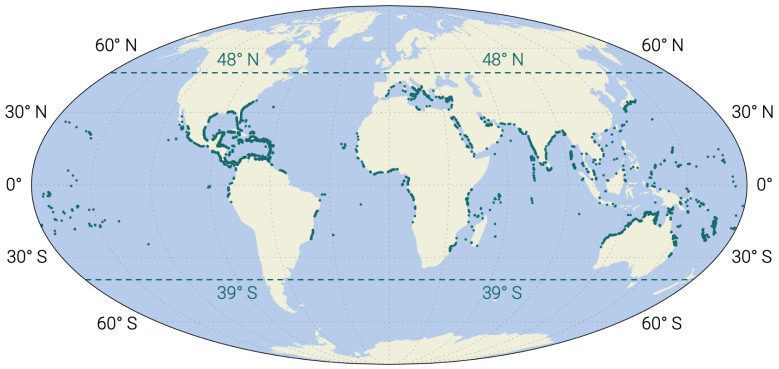

Figure 5.2: Overview of all nesting sites of all species used for this study (green dots). Dashed lines show the latitude limits applied to the Coastgon grid.

as it better represents the contiguous nature of coastal regions. Additionally, the geometric properties of hexagons, such as uniform distance between neighboring cell centers and equitable partitioning of space, make them efficient and suitable for geospatial analyses and visualization.

We used the H3 hexagonal hierarchical geospatial indexing system (Uber Technologies, 2022) as a basis for the Coastgons. H3 covers the Earth's surface with a hexagonal cell grid at 16 hierarchically leveled resolutions. The H3 grid was created by covering the 20 planar faces of an icosahedron with hexagonal cells and then projecting each face onto Earth's surface using a gnomonic projection (Uber Technologies, 2022). Each hexagon is then defined by the latitude/longitude coordinates (WGS84) of its vertices.

We created the Coastgons by overlaying the H3 grid (resolution 4) over the centroids of the coastline transects used in the GCC dataset (Athanasiou et al., 2024). The geospatial overlay selected every H3 hexagon that covered at least one GCC transect centroid, leading to many Coastgons that represented very short sections of coastline ($O(10km)$). To mitigate this issue, we refined the grid by filtering Coastgons based on their number of transects and neighboring Coastgons, while ensuring that the resulting coastline grid would not be interrupted by gaps. The GCC transects that fell into eliminated Coastgons, were subsequently matched to the nearest remaining Coastgon, up to a maximum distance of 100 km. Hence, in the final grid ($N = 5848$ Coastgons), every coastline transect within 100 km of the grid is represented by one Coastgon. Finally, we assigned a representative *coastline centroid* (CLC) to each Coastgon, given by the centroid of all transects linked to it.

The challenges of projecting a global grid over the Earth's surface mean that not all H3 hexagons are regular (equilateral and equiangular), and they can vary in size (although the size is not correlated with the latitude due to the gnomonic projection used in H3; Uber Technologies, 2022). For the Coastgon grid, this results in a mean cell area of 1775 km^2 (standard deviation 242 km^2) and a mean diameter (distance between opposing vertices) of 52 km (standard deviation 3.7 km). We accepted this property, given our analysis did not involve any indicators that are directly linked to the the Coastgon size. The chosen resolution is similar to that of the coarsest global dataset used (ERA5-wave at 0.5° $\approx$ 55 km at the equator). Hence, small-scale coastal features, like sheltered or embayed beaches, might not be resolved but regionally aggregated. We deemed this an acceptable trade-off, given our

aim to identify regional patterns of spatio-temporal characteristics of coastal systems.

5.2.3. Regional coastal indicators

We assumed that each Coastgon represents a spatially homogeneous coastal region, with a binary state regarding nesting activity: if it covered any known nesting sites, it was considered as a nesting region for the corresponding species. Each Coastgon's coastal characteristics were represented by a set of 22 indicators derived from the global data, divided into five categories: hydrodynamic, atmospheric, geophysical, habitat, and human (Table 5.2). The number of data points from which each Coastgon's indicators were computed depends on the dataset. Each GCC transect was linked to one Coastgon during the creation of the grid, so we used all transects linked to a Coastgon to compute its geophysical and human indicators. For gridded datasets (ERA5, GTSM, and ORAS5), the k nearest nodes to each CLC were used, up to a maximum of 100 km distance, where k depended on the resolution of the dataset ($k = 1$ for ERA5-wave, $k = 2$ for ERA5-atmos and ORAS5, and $k = 3$ for GTSM). Distances were computed with the Haversine formula (shortest distance between two points on the surface of a sphere). If no node was within 100 km of a Coastgon's CLC, a 'Not a Number' (NaN) was assigned to that Coastgon.

The hydrodynamic and atmospheric indicators were computed from historical time series (42 years from 1980–2021 for ERA5 and ORAS5; 30 years from 1985–2014 for GTSM), while the geophysical, habitat, and human indicators represented current or recent conditions (Table 5.1). When time series from multiple nodes were used for one Coastgon, we first computed the indicators separately from each time series, before averaging over the nodes to yield one value per indicator and Coastgon. Most indicators were derived through descriptive statistics, like the median (50^{th} percentile) as a measure of center and the 95^{th} percentile as a measure of extremes. For the peak wave period (T_p) we also included the standard deviation, as T_p is often characterized by a bimodal distribution of swell and wind waves (a larger standard deviation indicating a bimodal wave climate). We included the standard deviation of the shoreline angle as a measure of shoreline complexity—a large standard deviation indicating many different shoreline orientations, hence a more complex coastline, (e.g., islands and embayed beaches). For indicators representing distances ($D_{\text{c,03}}$, D_{cor}, and D_{sgr}), calculations were based on the CLC of each Coastgon. A detailed explanation of how each indicator was derived from the global datasets is provided in Appendix C.1. The final dataset of 5848 Coastgons, characterized by 22 coastal indicators, is available through the 4TU.ResearchData repository (Christiaanse & Antolínez, 2023).

5.2.4. Influence of coastal indicators on sea turtle nesting distribution

To assess the influence of the 22 coastal indicators on the distribution of global sea turtle nesting, we employed random forests (RF; Breiman, 2001). RF is a machine learning regression technique that constructs an ensemble of uncorrelated decision trees which predict a sample's class, and returns the majority prediction of all trees. We selected RF because it is capable of capturing complex, non-linear relationships in the data. Furthermore, the RF model computes the contribution of each variable to the predictive accuracy of the decision trees and converts these to a relative feature importance. We also tested linear discriminant analysis and logistic regression models, but these could not achieve adequate model performance, hence we only used RF.

Category	Variable	Indicator	Symbol	Unit	Dataset
Hydrodynamic	Significant waveheight	median	$H_{s,med}$	m	ERA5 Ocean
		95th percentile	$H_{s,p95}$	m	
	Peak wave period	median	$T_{p,med}$	s	
		95th percentile	$T_{p,p95}$	s	
		standard deviation	$T_{p,std}$	s	
	Surge level	median	$h_{S,med}$	m	GTSM
		95th percentile	$h_{S,p95}$	m	
	Tidal range	mean	h_{tide}	m	
	Ocean current velocity	median	$u_{c,med}$	m/s	ORAS5
	Ocean current proximity	Distance to nearest current $\geq 0.3m/s$	$D_{c,03}$	km	
Atmoshperic	10 m wind speed	median	$U_{10,med}$	m/s	ERA5 Atmos
		95th percentile	$U_{10,p95}$	m/s	
	Sea surface temperature	median	SST_{med}	$°C$	
	Total precipitation	median	P_{med}	mm/y	
Geophysical	Shoreline angle	standard deviation	ϕ_{std}	°	GCC
	Nearshore slope	median	$\beta_{ns,med}$	–	
	Backshore slope	median	$\beta_{bs,med}$	–	
	Max coastal elevation within 1km of shoreline	median	$z_{max,med}$	$m + msl$	
		standard deviation	$z_{max,std}$	$m + msl$	
Habitat	Coral reef proximity	distance to nearest coral reef habitat	D_{cor}	km	Allan Coral Atlas
	Seagrass meadow proximity	distance to nearest seagrass habitat	D_{sgr}	km	UNEP-WCMC
Human	Built env. in coastal zone	mean % built environment	p_{built}	%	GCC

Table 5.2: Overview of the 22 regional coastal indicators for each coastgon, derived from the global datasets in Table 5.1. They are divided into five categories: hydrodynamic, atmospheric, geophysical, habitat, and human.

We fitted one RF model for each species, distinguishing between nesting (1) and non-nesting (0) Coastgons. We assessed the model performance by letting the trained model predict the category of each Coastgon (nesting vs. non-nesting) and computing three performance scores: 1) precision, which quantifies the proportion of correct 'nesting' predictions out of all 'nesting' predictions; 2) recall, which quantifies the proportion of nesting Coastgons that is predicted correctly by the model; and 3) the F1 score, which is the harmonic mean of precision and recall, serving as a balanced measure of model performance. Based on the RF feature importance and our informed judgment, we then selected a subset of six influential indicators for each species for further examination in the cluster analysis.

Although RF is commonly used for predictive regression, here we used it as a dimensionality reduction technique. The aim was to identify patterns in the existing data, not to create the best generalized model to predict new, unlabeled data. Therefore, we decided to train and test the final RF models on the entire dataset. To test the robustness of our RF model we carried out a four-fold cross validation (Appendix C.3): we split the data into four equally sized partitions and trained four RF 'sub-models', each on a unique combination of three partitions (75% of the data). We then compared the RF feature importance of the five sub-models with the one trained on the full dataset. The feature importance remained consistent between the five models within each species (Figure C.2).

5.2.5. Global patterns and nesting suitability maps

To identify patterns in the coastal characteristics of global sea turtle nesting habitats, we performed a cluster analysis on the six indicators selected for each species. First, the data was normalized using a custom percentile scaler, which scales each indicator to the range $[0, 1[$, such that 0 represents the minimum and 1 represents the 99.9^{th} percentile (i.e., scaled values above the 99.9^{th} percentile were larger than 1). We applied this custom scaler instead of more conventional methods, like *MinMax* or *standard* scaling, because it is more robust to outliers and doesn't assume normally distributed data.

Next, we clustered the Coastgons based on the selected indicators, using *self-organizing maps* (SOM). SOM is a type of unsupervised neural network that groups high-dimensional data into k clusters and automatically projects these onto a two-dimensional lattice, preserving the topological properties of the data as much as possible (Kohonen, 2001). Each cluster of Coastgons is represented by one neuron, which is a point in the six-dimensional parameter space. The algorithm starts with k predefined initial neurons, and iteratively adjusts these during the learning process to yield k distinct clusters. An intuitive, metaphorical description of the method is that one throws a fishing net over the data, and then moves each node (neuron) of the net to cover the data as best as possible.

The number of clusters, k, is predefined by the user and is often determined iteratively by evaluating SOMs for different values of k. We used SOMs with $k = 169$ clusters, arranged on a 13x13 lattice. This number was determined iteratively through visual inspection of SOMs for different k, and using intra- and inter-cluster variance metrics (e.g., quantization error, silhouette score, and boxplots of each cluster). As initial neurons, we selected a subset of 169 Coastgons through a maximum dissimilarity algorithm. This algorithm ensures that the initial neurons are as dissimilar from each other as possible, meaning they span the parameter space more uniformly (i.e., the fishing net is stretched to the limits of the parameter space; Camus et al., 2011). We then computed the final 169 neurons using the MiniSom python library by Vettigli (2018).

To explain the distribution of global sea turtle nesting from the selected coastal indicators, we created a separate SOM for each species (i.e., for each subset of coastal indicators). Each cluster represented a group of coastgons with similar indicators. We then computed Spearman's rank correlation coefficient, ρ, between the cluster medians of each indicator and the percentage of nesting Coastgons in each cluster. A positive (negative) correlation coefficient therefore implies that regions with larger (lower) values for a given indicator contain a higher percentage of nesting Coastgons.

We mapped representative sea turtle nesting regions around the globe for each of the five species, by classifying the Coastgons into three categories: 'observed nesting' (O), 'potentially suitable' (S), and 'unsuitable' (U). The latter two categories encompass all Coastgons without observed nesting. These Coastgons were labeled 'potentially suitable' if they were part of a cluster containing at least 10% observed nesting Coastgons, and otherwise 'unsuitable'. To assess whether the distributions of the six indicators differed significantly across the three Coastgon categories, we applied the two-sample Kolmogorov-Smirnoff (KS) test, a non-parametric test suitable for non-normal data, to each pair-wise combination of categories. We adopted the common significance level of $\alpha = 0.05$ and adjusted the three p-values for each indicator using the Benjamini-Hochberg method, to limit inflated Type I errors due to multiple comparisons on the same indicator.

5.3. Results

5.3.1. Indicators influencing the global distribution of sea turtle nesting

We ranked the 22 coastal indicators based on their RF feature importance (see numbers of the top 10 ranks in Figure 5.3). Sea surface temperature was the only indicator with consistently high rankings across all species. Other important indicators varied more among the species but mainly consisted of hydrodynamics and distance to the nearest coral/seagrass habitats. Notably, the geophysical indicators had low importance across all species. For loggerheads (*Cc*), green turtles (*Cm*), hawksbills (*Ei*), and leatherbacks (*Dc*), extreme surge ($h_{S,p95}$) and tidal range (h_{tide}) were important (top three ranks). For olive ridleys (*Lo*), on the other hand, the wave climate (particularly the wave period) was more important than the water levels. Distance to the nearest seagrass habitat ranked in the top six for *Cc*, *Cm*, *Ei*, and *Lo*. Distance to the nearest coral reef was mainly important for *Cm* and *Ei*.

We selected a subset of six indicators for each species based on the RF feature importance and our informed judgment (circled indicators in Figure 5.3). The subset does not strictly correspond to the top six ranks, as lower ranks sometimes had similar importance values (e.g., ranks 5–8 for *Dc*). Additionally, a known characteristic of RF models is that feature importance may be spread over correlated variables, which doesn't necessarily mean that both variables together are important, but an underlying process is. For example, the median ($T_{p,med}$) and extreme wave period ($T_{p,p95}$) have the highest feature importance for *Lo*, but are strongly positively correlated (Spearman's $\rho = 0.92$, see Appendix C, Figure C.1). We therefore only selected $T_{p,med}$ to include the wave period, but leave room for other indicators in the clustering. This selection is not meant to imply that the indicators which were not selected are unimportant. However, we opted to limit the clustering to six indicators per species, to reduce the dimensionality of the analysis.

The performance scores of the random forest (RF) model were similar across the five species, with a mean F1 score of 0.9 (standard deviation 0.01). Such high scores may point to a slightly over-fitted model. We deemed this acceptable, though, given the robustness of our models in the cross-validation (Figure C.2) and our aim to understand the patterns present in the underlying data, not predict new, unlabeled Coastgons.

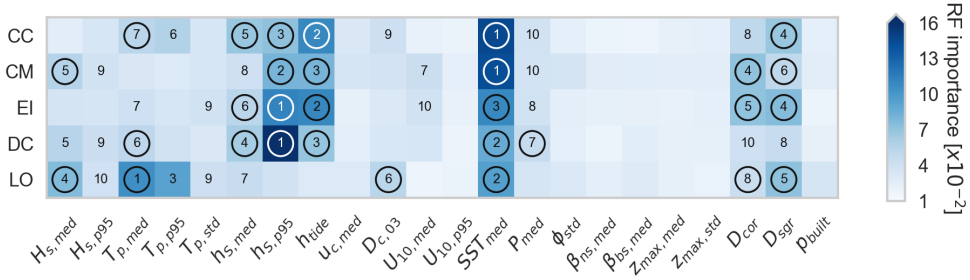

Figure 5.3: Matrix plot showing the RF feature importance of the 22 coastal indicators (Table 5.2), in separating nesting from non-nesting Coastgons. Each square represents one species/indicator pair and the blue scale indicates the magnitude of the feature importance. The numbers in the squares show the ranks of the ten most important indicators and the circles highlight the six selected indicators for each species, which are further examined in the cluster analysis.

5.3.2. Patterns in coastal indicators of global sea turtle nesting habitats

To identify patterns in the coastal indicators of global sea turtle nesting habitats, we correlated the SOM cluster medians to the proportion of nesting Coastgons in each cluster using Spearman's ρ (Figure 5.4a). For example, the correlations illustrated in Figure 5.4b–f imply that nesting Coastgons are typically found in regions with relatively low tidal ranges (*Cc*), high sea surface temperatures (*Cm*), near coral reef habitats (*Ei*), low extreme surge levels (*Dc*), and across a certain range of wave heights (*Lo*) (see Supplementary Material Section S5 for the SOM lattices of all species/indicator pairs). Although correlation magnitudes were limited to 0.56, several significant relationships emerged. To summarize these, we categorized absolute values of ρ smaller than 0.1 as insignificant, between 0.1 and 0.3 as weak, and larger or equal to 0.3 as significant, revealing the following correlations:

- **Loggerhead turtles (*Cc*)** – Nesting Coastgons significantly correlated negatively with tidal range (h_{tide}, Figure 5.4b) and extreme surge levels ($h_{S,p95}$). Weak negative correlations were observed with distance to the nearest seagrass habitat (D_{sgr}) and median surge levels ($h_{S,med}$). No significant correlations were found with the median wave period ($T_{p,med}$) and sea surface temperature (SST_{med}).

- **Green turtles (*Cm*)** – Nesting Coastgons significantly correlated negatively with extreme surge levels ($h_{S,p95}$) and distance to the nearest coral habitat (D_{cor}), while weak negative correlations were found with tidal range (h_{tide}). Significant positive correlations were observed with sea surface temperature (SST_{med}, Figure 5.4c). No significant correlation with the median wave height ($H_{s,med}$) and distance to nearest seagrass habitat (D_{sgr}).

- **Hawksbill turtles (*Ei*)** – Nesting Coastgons significantly correlated negatively with extreme surge levels ($h_{S,p95}$) and distance to the nearest coral habitat (D_{cor}, Figure 5.4d), and weak negative correlations were found with distance to the nearest seagrass habitat (D_{sgr}) and tidal range (h_{tide}). Significant positive correlations were observed with sea surface temperature (SST_{med}), and a weak positive correlation with the median surge level ($h_{S,med}$).

- **Leatherback turtles (*Dc*)** – Nesting Coastgons significantly correlated negatively with extreme surge levels ($h_{S,p95}$, Figure 5.4e) and a weak negative correlation was observed with the tidal range (h_{tide}). Significant positive correlation was found with sea surface temperature (SST_{med}) and weak positive correlations with the median wave period ($T_{p,med}$) and median total precipitation (P_{med}). No significant correlation found with median surge levels ($h_{S,med}$).

- **Olive ridley turtles (*Lo*)** – Nesting Coastgons showed a weak negative correlation with distance to the nearest coral habitat (D_{cor}). Significant positive correlation was observed with sea surface temperature (SST_{med}) and weak positive correlations with the median wave period ($T_{p,med}$), distance to ocean currents above 0.3 m/s ($D_{c,03}$), and distance to the nearest seagrass habitat (D_{sgr}). No significant correlation found with the median wave height ($H_{s,med}$, Figure 5.4f).

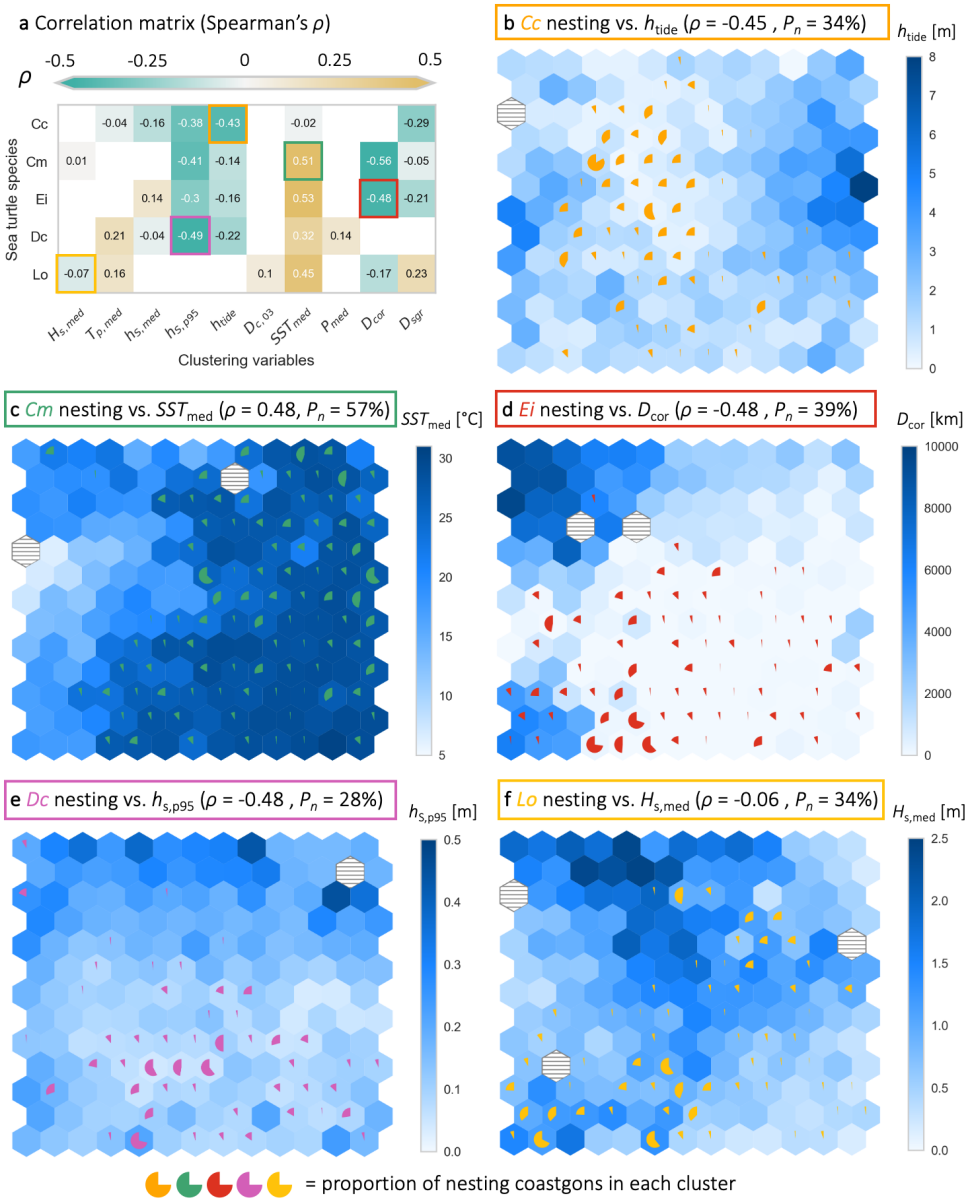

Figure 5.4: Relationship between coastal indicators and nesting distribution. a) Overview of Spearman rank correlation (ρ) between cluster medians (blue scale in panels b–f) and nesting percentages (pie charts) for each species/indicator pair. Panels b–f) visualize the correlation for five species/indicator pairs (highlighted by the colored outlines in the correlation matrix). Each 13-by-13 hexagon lattice shows a separate SOM, created for one species. Each hexagon in the lattices represents a cluster of Coastgons with similar indicators. The clusters are arranged on the lattices based on similarity. Together, the 169 clusters (hexagons) in each lattice represent the global coastline between $-39°$ and $48°$ latitude. The blue color-scale indicates the cluster medians for the given indicator, while the pie charts show the proportion of nesting Coastgons per cluster. Due to the SOM algorithm, some computed clusters may not represent any actual Coastgons (horizontally striped hexagons). Finally, P_n is the percentage of clusters containing any nesting Coastgons per species.

5.3.3. Representative sea turtle nesting regions

To map representative sea turtle nesting regions, Coastgons were categorized into three categories: observed nesting, potentially suitable (no observed nesting, but part of a cluster with at least 10% observed nesting Coastgons), and unsuitable. We zoomed into eight particular regions, inspired by the regional management units for sea turtles from Wallace et al. (2010, Figure 5.5a): Central East Pacific (CEP), North West Atlantic (NWA), South West Atlantic (SWA), Central East Atlantic (CEA), Mediterranean (MED), North West Indian (NWI), South West Indian (SWI), and North East Indian (NEI). For each region, as well as for the global coastline (all Coastgons), we created nesting suitability maps using the three categories (see examples in Figure 5.5b–f), and computed two representative statistics: (1) the percentage of observed nesting Coastgons, P_O; and (2) the percentage of observed nesting and potentially suitable Coastgons, P_S (Table 5.3). Nesting suitability maps and accompanying box-plots for all region/species pairs are provided in the Supplementary Material, Section S6.

On a global scale, the percentage of suitable Coastgons ranges from $P_S = 12.9\%$ for olive ridleys to $P_S = 36.9\%$ for green turtles (mean of all species $P_S = 23.2\%$). As expected, P_S is highest for green turtles, who have the most nesting sites of any species (Kot et al., 2021) and are known to nest across a variety of environmental conditions around the world (Mortimer, 1990). Suitability percentages are on average 3.3 times higher than observed nesting percentages (mean $P_O = 7\%$, ranging from $P_O = 4.7\%$ for *Lo* to $P_O = 10.1\%$ for *Cm*). This suggests that there are opportunities for turtles to expand their global nesting habitats.

Among individual regions, the North West Atlantic (which includes the wider Caribbean) emerged as the most suitable region, with an average observed nesting percentage of $P_O = 34\%$ and potential suitability of $P_S = 82.7\%$, across all species except olive ridleys, who do not nest there (Table 5.3). The Central East Atlantic ($P_S = 58.4\%$) and Central East Pacific ($P_S = 44\%$) also had high average suitability percentages. The Mediterranean is quite unique in that it currently only supports loggerheads (*Cc*, $P_O = 19.1\%$), and to a lesser extent green turtles (*Cm*, $P_O = 3.1\%$). The Indian Ocean regions are generally suited to all species, although with lower suitability percentages than other regions ($26.8\% < P_S < 34.1\%$). Finally, the South West Atlantic also had relatively low observed nesting and suitability percentages ($P_O = 7.1\%$ and $P_S = 35.2\%$), although a large stretch of the Brazilian coastline appears suitable for all five species (Figure 5.5a).

There were also significant differences across species. For loggerheads (*Cc*), the North West Atlantic ($P_S = 88.7\%$) and Mediterranean ($P_S = 77.8\%$) clearly emerged as the most suitable (and most used) regions. For green turtles (*Cm*), suitability percentages were high across regions, with $P_S > 35\%$ for all regions except the Mediterranean. Hawksbills (*Ei*) also had high P_S values for most regions (they do not nest in the Mediterranean), with the North West Atlantic a clear favorite ($P_S = 74.8\%$). Leatherbacks (*Dc*) appeared to be more suited to the Pacific and Atlantic regions, with consistently higher P_S values than the Indian Ocean regions. Finally, olive ridley (*Lo*) nesting suitability was highest for the Central East Pacific ($P_S = 62.3\%$) and Central East Atlantic ($P_S = 72.1\%$). Consistent with the results from the RF model, olive ridleys appeared to have more unique nesting preferences compared to the other four species.

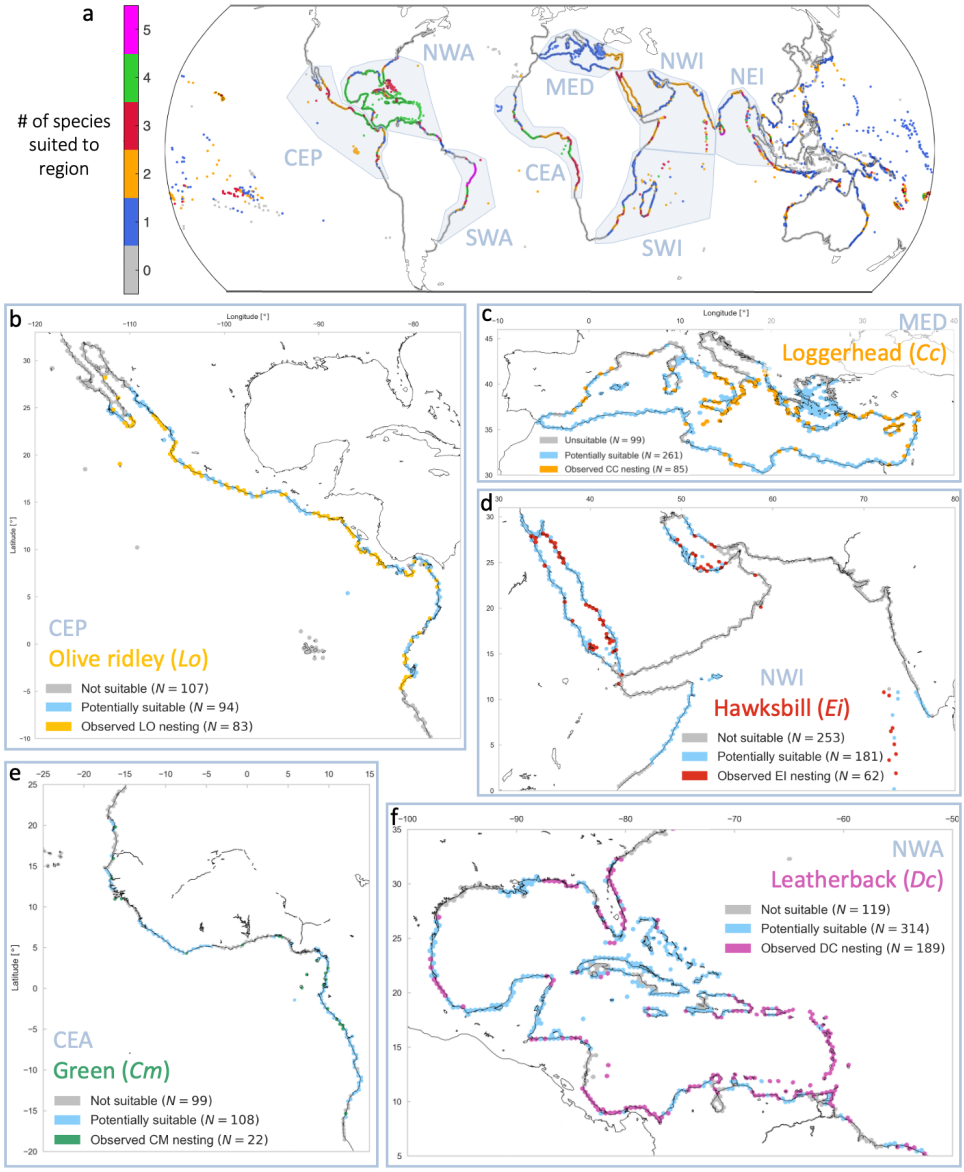

Figure 5.5: Global overview of sea turtle nesting suitability, based on the selected coastal indicators for each species. a) Global map showing the number of species for which each Coastgon is classified as either 'Observed nesting' or 'Potentially suitable'. The grey-blue polygons show the eight considered regions, inspired by the RMU's from Wallace et al. (2010). Panels b–f show nesting suitability maps for five region/species pairs: b) Olive ridley (*Lo*, yellow) in the Central East Pacific (CEP), c) Loggerheads (*Cc*, orange) in the Mediterranean (MED), d) Hawksbills (*Ei*, red) in the North West Indian (NWI), e) Green turtles (*Cm*, green) in the Central East Atlantic (CEA), and f) Leatherbacks (*Dc*, pink) in the North West Atlantic (NWA). In each map, grey indicates unsuitable Coastgons, light blue denotes potential suitability, and other colors represent observed nesting by the corresponding species.

To give an example for a regional analysis, in the Mediterranean (nesting map in Figure 5.5c), 'observed nesting' ($N = 85$) and 'potentially suitable' ($N = 261$) Coastgons for loggerhead turtles (Cc) generally exhibit higher sea surface temperatures ($17 < SST_{\text{med}} < 23.5°C$) and median wave periods ($3.5 < T_{\text{p,med}} < 6.3s$), and lower tidal ranges ($h_{\text{tide}} < 0.5m$) and extreme surge levels ($h_{\text{s,p95}} < 0.15m$) compared to 'unsuitable' ($N = 138$) Coastgons (Figure 5.6a). The p-values of the two-sample KS tests for comparisons between the 'observed nesting' and 'potentially suitable' categories ($p_{O|S}$) were above the 0.05 threshold for h_{tide}, $h_{\text{S,med}}$, $h_{\text{S,p95}}$ and D_{sgr}, and just below 0.05 for SST_{med} and $T_{\text{p,med}}$, indicating insignificant or marginal statistical differences for these indicators. In contrast, most p-values for KS-tests involving the 'unsuitable' category ($p_{O|U}$ and $p_{S|U}$) were multiple orders of magnitude smaller ($p \ll 0.001$), indicating strong statistical differences with the suitable and observed Coastgons (except for D_{sgr}). Based on these indicators, approximately 78% of Mediterranean Coastgons could potentially be suitable for nesting Loggerheads, while nesting has only been observed in 19% of Coastgons (Table 5.3). These results agree with recent reports of a loggerhead nesting range expansion towards the western Mediterranean, with most newly reported nesting sites lying within Coastgons classified as potentially suitable (Hochscheid et al., 2022).

5

	Cc		*Cm*		*Ei*		*Dc*		*Lo*		Mean	
Region	P_O	P_S	P_O	P_S	P_O	P_S	P_O	P_S	P_O	P_S	P_O	P_S
Central East Pacific	–	–	14.1	39.1	9.2	34.5	12	40.1	29.2	62.3	16.1	44
North West Atlantic	28.8	88.7	35.5	86.3	41.2	74.8	30.4	80.9	–	–	34	82.7
South West Atlantic	10.7	40.7	6	37.3	6.7	22.7	5.3	36	6.7	39.3	7.1	35.2
Central East Atlantic	–	–	9.6	56.8	7	33.2	17.5	71.6	16.6	72.1	12.7	58.4
Mediterranean	19.1	77.8	3.1	12.6	–	–	–	–	–	–	11.1	45.2
North West Indian	0.6	12.1	11.7	54.6	12.5	49	–	–	9.3	20.8	8.5	34.1
South West Indian	5.3	17.3	13.2	74.5	6.2	23.9	2.9	9.5	1.6	8.6	5.8	26.8
North East Indian	2.2	6.4	7.7	39	8.6	35.8	6.4	21.7	16.9	39	8.4	28.4
Global	6.4	21.9	10.1	36.9	8.2	23.9	5.7	20.3	4.7	12.9	7	23.2

Table 5.3: Overview of the two computed statistics for regional and global nesting suitability. Rows represent regions (see geographical overview in Figure 5.5a) and columns show the percentage of observed nesting coastgons (P_O) and the percentage of observed nesting and potentially suitable coastgons (P_S) for each species and averaged per region.

5.4. Discussion

The analysis of 22 regional coastal indicators on the distribution of global sea turtle nesting shows that, in line with previous studies (Pike, 2013; Wood & Bjorndal, 2000), sea surface temperature can be one of the most important indicators for the presence of all five species in a Coastgon. The majority of nesting grounds of all species except loggerheads are situated in regions at the upper end of the analyzed temperature range ($SST_{\text{med}} > 25°C$; Figure 5.6b). Loggerheads (Cc) also colonize cooler nesting regions ($SST_{\text{med}} > 17°C$), like the western Mediterranean and Japan, though their distribution is still influenced by temperature. In fact, had we not filtered out the World's coldest regions by limiting the Coastgon grid to latitudes between $-39°$ and $48°$, SST_{med} would have likely been more dominant in the RF model. Distance to the nearest coral reef habitat (D_{cor}) was another important indicator, although it is unclear how strongly this is biased by the negative correlation between SST_{med} and

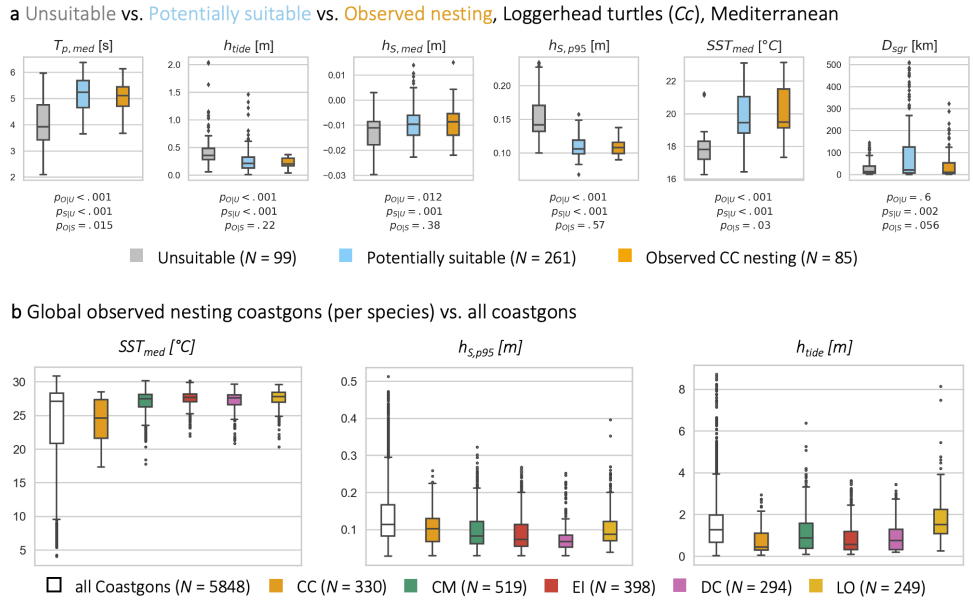

Figure 5.6: Box-plots showing the distribution of several indicators over sea turtle nesting regions. a) Box-plots for the six indicators selected for loggerhead turtles (from left to right: $T_{p,med}$, $h_{S,med}$, $h_{S,p95}$, SST_{med}, h_{tide}, D_{sgr}) for the three suitability categories along the Mediterranean coastline (Figure 5.5): unsuitable ('U', grey), potentially suitable ('S', blue), and observed nesting ('O', orange). Below each box-plot are the p-values from two-sample KS tests between the three category pairs, denoted by their subscript (e.g., $p_{O|S}$ is the p-value between the observed nesting and potentially suitable categories). b) Box-plots for SST_{med} (left), $h_{S,p95}$ (middle), and h_{tide} (right) for all Coastgons (grey) and for the observed nesting Coastgons of each individual species (colors). Boxes represent the interquartile range and whiskers extend to a maximum of 1.5 times the interquartile range. Coastgons beyond the whiskers are shown as markers.

D_{cor} ($\rho = -0.65$, Figure C.1). It would make sense for hawksbills to nest near coral reefs, which are their foraging habitats, but other species have not necessarily been linked to coral reefs in literature. Distance to seagrass (D_{sgr}) was mainly important for *Cc*, *Ei*, and *Lo*, and notably less so for green turtles, who forage in seagrass habitats (Bjorndal, 1980) (although it still ranked sixth).

It has often been hypothesized that sea turtles try to place their nests on the beach by finding a balance between a high nest elevation against flooding, and the distance to the shoreline against predation (Wood & Bjorndal, 2000). While the spatial resolution of our study precludes conclusions regarding nest placement or predation patterns, our results suggest that individual species tend to favor nesting regions with relatively low extreme surges ($h_{S,p95} < 0.25$ m for all species) and low tidal ranges ($h_{tide} < 2.5$ m for *Cc*, *Ei*, and *Dc*), possibly as a strategy to minimize the risk of nest flooding (Figure 5.6b). While areas with higher extreme surges can also support nesting—as evidenced by nesting beaches in cyclone-prone regions (Fuentes et al., 2019)—our results indicate a significant bias towards low extreme surge environments. This bias might be enhanced by the fact that GTSMv3.0, our source for surge levels, slightly underestimates tropical cyclones, though (Dullaart et al., 2021).

Our global-scale analysis also presented different findings from several relationships

previously reported in literature. For instance, Santana Garcon et al. (2010) found that nesting grounds around Australia are generally more exposed to wind and waves than non-nesting beaches. We only found a weak (though not negligible) influence of the median 10m-wind speed, for three species (*Cm*, *Dc*, and *Ei*; Figure 5.3). Moreover, despite Putman et al. (2010) reporting a strong relationship between loggerhead nesting activity and distance to the Gulf Stream along the US east coast, we only observed a weak influence from the distance of strong ocean currents. Total precipitation also had comparatively low feature importance in the RF model, contrary to findings of others (Pike, 2013; Santidrián Tomillo et al., 2015). Perhaps most notably, no geophysical indicators were identified as important in our results. This suggests that patterns resulting from local- or regional-scale analyses do not necessarily reflect large-scale patterns and may, for instance, be confounded by factors correlated with the tested predictors.

Indicators that were not identified as important in our global-scale analysis may still influence turtle nesting for individual regions and sub-populations, or on smaller spatial scales. Our study required the use of global datasets with limited resolution and accuracy. Particularly, local topographic and bathymetric indicators remain difficult to measure, hence available datasets often lack accuracy (Almar et al., 2021; Athanasiou et al., 2019). For example, although Luijendijk et al. (2018) quantified the occurrence of sandy beaches along the global coastline from satellite images, we did not include this data, as their method struggled to detect narrow beaches, particularly in tropical regions with large amounts of vegetation—where many sea turtles nest (Mazaris et al., 2014). Furthermore, aggregating the data onto the Coastgon grid effectively smoothed out local geomorphological features (e.g., embayed beaches), likely contributing to the low importance of the geophysical indicators in the RF results. Hydrodynamic indicators such as waves and water levels, on the other hand, are easier to quantify and likely more consistent over larger spatial scales, and may thus be better suited to large-scale analyses. Hence, we expect geophysical indicators to be more influential at the scale of individual beaches, in line with previous studies (e.g., Culver et al., 2020; Mortimer, 1990; Provancha & Ehrhart, 1987; Yamamoto et al., 2012). However, more regional analyses combined with high-resolution, accurate datasets are needed to prove this.

To assess the variability of the GCC transect-based data within each Coastgon, we computed the median absolute deviation from the median, normalized by the median itself ($MADm$)—a measure of variability that is more robust than the commonly used coefficient of variation (standard deviation normalized by the mean; Leys et al., 2013). For example, $MADm = 1$ implies that 50% of the samples differ from the median by more than the median itself. We did this for three geophysical indicators ($\beta_{\text{ns,med}}$, $\beta_{\text{bs,med}}$, and $z_{\text{max,med}}$) and one hydrodynamic indicator (mean higher high water from GCC, extracted from the nearest GTSMv3.0 node for every transect). It should be noted that this variability is a result of both the variability in the indicators, as well as the variable length of the coastline in each Coastgon (i.e., the number of transects linked to each Coastgon). Variability within Coastgons was significantly higher (up to $MADm = 1$) for $\beta_{\text{ns,med}}$, $\beta_{\text{bs,med}}$, and $z_{\text{max,med}}$, than for mean higher high water ($MADm < 0.1$ for 97% of Coastgons). We still included the geophysical indicators in the RF model though, because their variability was also lower for a significant number of Coastgons ($MADm < 0.4$ for 30% of Coastgons). One way to improve our analysis could be to only use sandy coastline transects to derive the geophysical

indicators, for example through an updated version of Luijendijk et al. (2018).

Some of the influential indicators selected from the RF model did not show significant correlations in the cluster analysis (Figure 5.4). This does not mean that these indicators are not influential but may be explained from the fact that Spearman's correlation coefficient is designed to detect monotonic relationships (e.g., the lower the extreme surge levels the higher the chance for nesting leatherback turtles). If nesting grounds fall within a specific range of a given indicator, however, this relationship is not readily identified through correlation. The SOM lattices and box-plots allow a quick visual inspection of the distribution of nesting grounds for each indicator, but it remains difficult to quantify such non-monotonic relationships. For example, global loggerhead (*Cc*) nesting Coastgons are limited to a median sea surface temperature range of $17 - 29°C$ (Figure 5.6b). This range is still in the upper part of the total observed SST_{med} range, but the median SST_{med} for loggerhead nesting Coastgons ($24.5°C$) is lower than for all Coastgons ($27.5°C$). Hence no significant rank correlation is observed ($\rho = -0.02$; Figure 5.4a), even though sea surface temperature clearly constrains the suitability for loggerhead nesting. Nonetheless, such relationships are still captured in the suitability maps, as the SOMs (from which the maps are derived) do identify complex, non-monotonic patterns.

Another way to show the complexity of nesting suitability and the effectiveness of our selected indicators is by examining the percentage of nesting clusters (P_n) and their distribution on the SOM lattices (Figure 5.4). Ideally, a complete set of indicators would lead to a clear division of nesting Coastgons over suitable clusters, with decreasing nesting percentages around them signaling the limits of suitability. For example, Loggerhead (*Cc*) nesting occurs in 35% of clusters, and the lattice shows one main agglomeration of high nesting percentage clusters, with decreasing percentages around it (Figure 5.4b). In contrast, green turtles (*Cm*) nest in 54% of clusters, with many low nesting percentages spread across the lattice (Figure 5.4c). A similar pattern can be seen for hawksbills (*Ei*), although the nesting cluster percentage is lower ($P_n = 40\%$; Figure 5.4d). While green turtles are particularly known to nest across a very broad range of environmental conditions (Mortimer, 1990), these findings underscore the hypothesis that nesting preferences involve a complex interplay of biotic and abiotic factors.

Our nesting suitability maps represent our best estimate of each species' *fundamental niche* (the environmental range theoretically suitable for nesting; Brown et al., 2011; Guisan & Thuiller, 2005), based on a set of abiotic environmental characteristics. The observed nesting distribution can be interpreted as an approximation of the *realized niche*, where the species actually nests. The realized niche is typically more constrained than the fundamental niche, due to complex biotic interactions (e.g., predation and recruitment limitation), which are challenging to incorporate into habitat mapping (Brown et al., 2011). Moreover, our indicator set, while comprehensive, may still miss some potentially influential abiotic factors (e.g., sandy beach occurrence and grain size characteristics; Mortimer, 1990), thereby approximating the fundamental niche.

Given our main goal was to identify characteristics that enable nesting at any scale, we chose not to weight nesting regions based on their population sizes. However, certain rookeries around the globe are hotspots of turtle nesting. For example, Raine Island, Australia for green turtles (Limpus et al., 2003), Masirah Island, Oman for loggerheads (Willson et al., 2020), or the mass nesting sites in Mesoamerica and India, where thousands of olive ridleys

nest simultaneously during so-called *arribadas* (Shanker et al., 2004; Valverde et al., 1998). Future work could benefit from incorporating such high-density nesting grounds into the analysis, which would offer a more nuanced understanding of global patterns. Additionally, we did not consider the seasonality of turtle nesting in the computation of our indicators. Sea turtles are known to venture far away from their nesting grounds outside of the nesting season, hence our analysis might benefit from filtering the time series of hydrodynamic and atmospheric data to reflect conditions during the nesting season.

A challenge for studies like this one is the availability of global sea turtle nesting data. The SWOT database is an invaluable resource for any research related to sea turtle nesting distribution, but also has limitations. Even though it contains data from over 130 countries and territories all over the globe, in some regions data availability and accuracy are limited and dependent on local programs with varying monitoring standards (Kot et al., 2021). A significant number of false non-nesting Coastgons can bias the feature importance, as characteristics supportive of nesting are erroneously associated with non-nesting. However, our chosen Coastgon resolution (50 km) helps overcome this challenge by aggregating to regional scales. The RF feature importance remained consistent through the cross-validation, showing the model is robust to relatively small changes in the input data (Figure C.2). Therefore, the results of this study can help identify currently undocumented nesting regions, to facilitate more reliable and accurate nesting data in the future. In Somalia, for example, there is currently no (public) data (van de Geer et al., 2022), but all nearby countries support nesting and our suitability maps indicate that parts of its coastline could be suitable for up to four species (Figure 5.5a).

Contrary to most previous research on sea turtle nesting characteristics, one of our main motivations behind this study is the eventual design and implementation of nature-based solutions that can help preserve and expand nesting habitats for sea turtles. Consequently, our selection of indicators was driven by a focus on abiotic indicators potentially modifiable by nature-based engineering designs, such as hydrodynamics and geomorphology. Similarly, we adopted a spatial scale that helps identify coastal regions where nature-based solutions may be suitable. Moving forward, we aim to leverage the findings of this study to identify and map coastal hazards threatening global sea turtle nesting habitats (e.g., flooding and erosion of nesting beaches) and to assess the suitability of specific nature-based solutions to mitigate these hazards.

5.5. Conclusion

We examined the relationship between regional coastal characteristics and the global nesting distribution of five sea turtle species (loggerhead, *Cc*; green, *Cm*; hawksbill, *Ei*; leatherback, *Dc*; and olive ridley, *Lo*) to identify suitable nesting conditions and lay a foundation for the design of nature-based solutions to protect and expand global nesting habitats. An initial set of 22 coastal indicators was considered—spanning hydrodynamic, atmospheric, geophysical, habitat, and human processes—on a hexagonal coastline grid (Coastgons) of $\approx$ 50 km resolution. We assessed the influence of these indicators on the global distribution of sea turtle nesting by fitting a random forest model to the data, which returns each indicator's relative importance in splitting the data into nesting and non-nesting categories. Based on this importance, a subset of six important indicators per species was examined through a SOM-based cluster analysis to reveal patterns in the coastal characteristics of global nesting

habitats, and identify new, potentially suitable nesting regions.

While there were differences between species, at the coarse, global scale considered here, important indicators consisted mainly of sea surface temperature (SST_{med}), extreme surge levels ($h_{\text{S,p95}}$), tidal range (h_{tide}), and the distance to the nearest coral reef (D_{cor}) and seagrass habitats (D_{sgr}). For example, individual species' nesting grounds tend to occur in regions with relatively low tidal ranges (*Cc*, *Ei*, and *Dc*), low extreme surge levels (*Cc*, *Cm*, *Ei*, and *Dc*), warm temperatures (*Cm*, *Ei*, *Dc*, and *Lo*), and near coral habitats (*Cm* and *Ei*). The first two observations might suggest that sea turtles select their nesting grounds in an effort to reduce the risk of (periodic) nest flooding, as has similarly been hypothesized on smaller spatial scales (e.g., Mortimer, 1990). Other indicators reported as influential in literature appeared less important according to our results, for example, precipitation (Pike, 2013) and wind (Santana Garcon et al., 2010). Notably we did not identify any important geophysical indicators at this scale, but expect these to be more influential for smaller spatial scales and more accurate data.

We identified new, potentially suitable nesting regions, mapping each species' fundamental nesting niche on global and regional nesting suitability maps. Global nesting suitability ranged from 12.9% (*Lo*) to 36.9% (*Cm*) of Coastgons (mean 23.2%). However, observed nesting currently only occurs in 4.7% to 10.1% of Coastgons (mean 7%), suggesting that the realized niche is still significantly smaller, and that there is potential for sea turtles to expand their nesting habitats. This is a particularly important finding in the face of nature-based solutions and assisted colonization of new coastal regions (Barbanti et al., 2022), as recent studies suggest that phenological shifts (earlier onset of nesting season) are unlikely to be sufficient for most sea turtle populations to stay within appropriate nesting conditions (Laloë & Hays, 2023; Monsinjon et al., 2019).

This study has revealed distinct patterns in the coastal characteristics of global sea turtle nesting habitats and has identified new, potentially suitable, nesting regions for the five globally distributed sea turtle species. Even though sea turtle nesting behavior remains difficult to predict (Miller et al., 2003), the results of this study can help identify suitable nesting conditions, quantify potential hazards to global sea turtle nesting habitats, and function as a basis for the design of nature-based solutions to preserve and potentially expand these habitats.

Data availability—The Coastgon dataset used in this study, including the 22 indicators, is publicly available through the 4TU.ResearchData repository at https://doi.org/10.4121/68377ee4-892d-40f0-a490-29f2601e6825. All global datasets used in this study are also available online, for access please refer to the corresponding references mentioned in this article. Additional data on the results (e.g., SOM clusters) can be requested from the corresponding author (J.C.).

Acknowledgments—We express our gratitude and acknowledgments to *The State of the World's Sea Turtles (SWOT)* project, and particularly the numerous contributors who have made their data available through SWOT. We also acknowledge with appreciation the more than 200 data providers in 45 Wider Caribbean nations and territories who contributed to the WIDECAST Atlas. Without the SWOT and WIDECAST data, this study would not have been possible. Finally, we would like to acknowledge the following grant, which provided us with the digital infrastructure to make large data computations: EINF-3474 "e-infra Snellius AI4NBS: Data, Statistical Learning, Machine Learning, and Numerical Models combined to design Nature Based Solutions in Coastal Waters (2022)".

Author contributions—J.C. performed the analyses and wrote the original manuscript, J.C. and J.A. conceived the study and analyzed the results, P.A. shared the GCC dataset used for the study, all authors commented on the results and reviewed the manuscript.

Cover photo by John Rodarte/Hawai'i Wildlife Fund ©: Hawksbill sea turtle (*Eretmochelys imbricata*) hatchlings crawling toward the Ocean in Hawai'i.

6

Aiding sea turtle conservation through coastal management

Abstract

Climate change and human activity pose increasing challenges to endangered sea turtles, which are key species in many marine ecosystems worldwide. Among these challenges are the flooding and erosion of nesting beaches. In this perspective, we argue that existing methods and tools from coastal science and management hold significant, yet underused, potential for sea turtle conservation. We introduce a stepwise framework for integrating sea turtle ecology and coastal management to address these coastal threats. The framework follows an Observe–Understand–Predict–Intervene cycle and links ecological thresholds, coastal processes, and management interventions across scales, from Regional Management Units (RMUs) to individual beaches. We illustrate how state-of-the-art monitoring, modeling, and nature-based solutions (NBS) can be embedded within this framework to inform when and how to intervene. Increased in-situ data collection and interdisciplinary collaboration will be critical to apply and refine this approach, thereby enhancing the long-term resilience of nesting habitats.

This chapter has been published in *Frontiers in Marine Science* as:

Christiaanse, J. C., Reniers, A. J. H. M., Aarninkhof, S. G. J., Ostertag, E. F., Nel, R., Duarte, C. M., & Antolínez, J. A. A. (2025). Aiding sea turtle conservation through coastal management. *Frontiers in Marine Science*, 12, 1669885. [Link]

6.1. Introduction

Climate change and human activity pose various challenges to endangered sea turtles, who fulfill critical ecological roles in many marine ecosystems worldwide (Christianen et al., 2023; Heithaus, 2013; Patrício et al., 2021). Sea turtles rely on sandy beaches for nesting. Successful incubation requires a relatively narrow range of sand temperature and moisture conditions, which in turn depends on various factors, including sediment characteristics, beach elevation, hydrodynamic processes, and anthropogenic disturbances (e.g., Ackerman, 1997; Culver et al., 2020; Foley et al., 2006). Consequently, the long-term survival of sea turtles directly depends on the availability of suitable nesting beaches around the world.

Among the challenges they face are the flooding and erosion of nests during the breeding season and the loss of suitable nesting habitat due to long-term beach erosion and coastal development (Figure 6.1a, b). These threats occur globally, but their expression varies regionally—for instance, Mediterranean and North West Atlantic nesting beaches face widespread coastal development (Biddiscombe et al., 2020; Hirsch et al., 2022); the Gulf of Mexico is projected to experience high relative sea level rise (Fox-Kemper et al., 2023); while Caribbean and Indo-Pacific rookeries are particularly exposed to tropical cyclones (Dewald & Pike, 2014). Although both flooding and erosion are recognized as significant threats to sea turtles (e.g., Gammon et al., 2023; Rivas et al., 2023; Van Houtan & Bass, 2007; Ware et al., 2021), they remain under-represented in conservation management and research, which are primarily focused on in-situ protection, fishery by-catch, human consumption, plastic pollution, and changing hatchling sex-ratios due to warming temperatures (Fuentes et al., 2023; Hays et al., 2025; Nel et al., 2014; Patrício et al., 2021; Wallace et al., 2025).

The driving processes behind nest flooding and beach erosion are extensively studied and understood by coastal scientists and managers. Coastal management is increasingly shifting toward nature-based solutions (NBS; e.g., de Vriend et al., 2015; Masselink & Lazarus, 2019; Spalding et al., 2014), defined by the International Union for Conservation of Nature (IUCN) as *actions to protect, sustainably manage, and restore natural or modified ecosystems, that address societal challenges effectively and adaptively, simultaneously providing human well-being and biodiversity benefits* (Cohen-Shacham et al., 2016). Examples of NBS for nesting beaches could include turtle-friendly beach nourishments (e.g., Smithers & Dawson, 2023), artificial reefs, and seagrass restoration aimed at reducing erosion and flooding (Figure 6.1c; Barbier et al., 2011). However, effectively implementing such solutions requires a comprehensive understanding of the entire beach ecosystem, including biotic (e.g., nesting characteristics) and abiotic (e.g., longshore/cross-shore processes) factors at play (Slinger & Vreugdenhil, 2020). Despite the clear need for an interdisciplinary approach (Nel et al., 2014), collaboration between the sea turtle ecology and coastal engineering communities remains limited and, as a result, nesting habitats are not commonly considered in coastal engineering projects.

In this perspective, we argue that existing methods and tools used in coastal science and management hold significant potential for sea turtle conservation and should be leveraged more effectively. To guide this integration, we propose a stepwise framework (Figure 6.2) that connects ecological thresholds, coastal threats, and management interventions from regional to local scales. We outline how state-of-the-art coastal monitoring and modeling approaches can enable us to observe, understand, and predict coastal processes at nesting

beaches, which is required to decide if and how to intervene with NBS. Finally, we call for increased interdisciplinary collaboration that bridges ecology, biology, and coastal management to enhance the future resilience of these critical habitats.

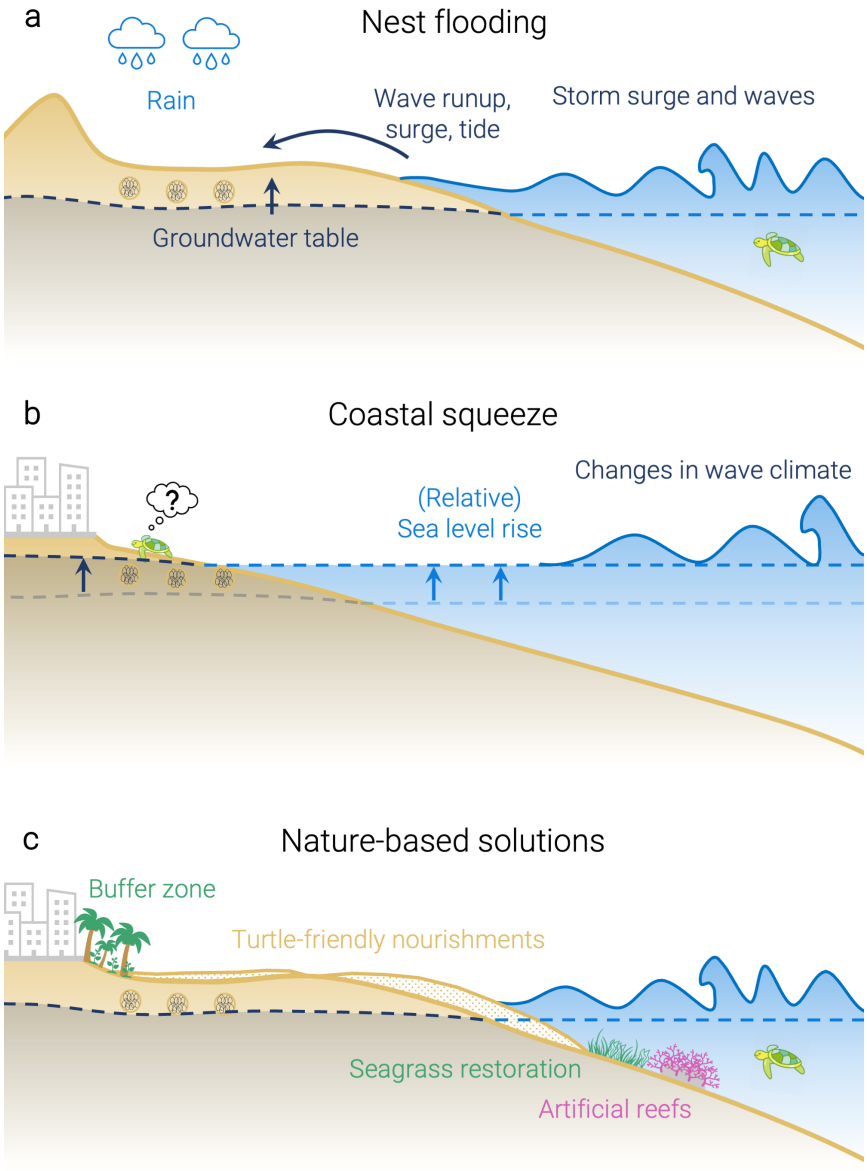

Figure 6.1: Schematic cross-shore profile of a nesting beach (not to scale), showing: a) processes related to nest flooding and erosion; b) processes related to coastal squeeze; and c) examples of potential NBS that could help mitigate flooding and erosion on nesting beaches. Although a cross-shore schematic is shown here for simplicity, these processes also have alongshore drivers and variability.

6.2. Nesting beaches under pressure

Nesting beaches are shaped by diverse coastal processes that operate across multiple temporal and spatial scales. An imminent threat is the inundation and erosion of nesting beaches during high wave and water level events (e.g., storms or tropical cyclones), which are increasing with climate change (Morim et al., 2025; Reguero et al., 2019). Such episodic events can flood or wash out incubating nests, significantly decreasing hatching success (Patrício et al., 2021; Van Houtan & Bass, 2007). Though flooding mainly occurs overland—through wave runup, storm surges, high tides, and rainfall—it effectively raises the beach groundwater table (GWT) in the nesting zone (Figure 6.1a). Since egg viability is sensitive to inundation duration (Limpus et al., 2021; Pike et al., 2015), the GWT response strongly influences the fate of individual nests (Christiaanse et al., 2025c; McGehee, 1990; Patino-Martinez et al., 2014). These flooding events are modulated by seasonal and interannual variability in storm activity (e.g., storm seasonality, El Niño/Southern Oscillation). Moreover, storm erosion can significantly alter beach morphology, which can impact nesting on a time-scale of multiple seasons (Long et al., 2011), especially after intense storms like tropical cyclones (Fuentes et al., 2019; Pike & Stiner, 2007).

Another significant threat is the long-term loss of nesting habitat due to *coastal squeeze*, which arises from the combination of structural erosion and increasing pressure from the landward side (Figure 6.1b). Structural erosion can have several causes, including sea level rise (SLR), coastal subsidence, longshore sediment transport disruption, river damming, or climate-induced shifts in sediment supply. At the same time, urban development and population growth increasingly encroach from the landward side (Neumann et al., 2015). Coastal squeeze occurs when the eroding coastline cannot migrate landward due to a fixed barrier, either human-made or natural (e.g., cliff; Pontee, 2013). Even where accommodation space exists, it remains unclear whether sediment supply and beach morphology can keep up with accelerating SLR (Rosati et al., 2013; Vitousek et al., 2017b). Erosion can also expose underlying bedrock, which may hinder nesting access or increase injury risk to turtles (Wildermann et al., 2024)

6.3. When to intervene through NBS?

The first criterion of the IUCN standard for NBS is that the NBS effectively addresses a societal challenge, which is clearly understood (IUCN, 2020). This aligns with the common approach towards NBS or *Building with Nature* (de Vriend et al., 2015) in coastal management, which we summarize here in three phases: (1) Observe and understand, (2) Predict, and (3) Intervene, if necessary (Figure 6.2). We first need to observe and understand the ecosystem, predict how the relevant natural processes might evolve, and then assess whether intervention is needed.

The goal is achieving and maintaining stable sea turtle habitats and populations rather than saving every turtle or nesting beach. Therefore, it becomes essential to identify ecological thresholds, like trigger points (when intervention becomes necessary) and tipping points (beyond which recovery is unlikely) in the sea turtle population (Figure 6.2, Step 1; Botero et al., 2015; de Bie et al., 2018; Lindenmayer et al., 2013). The widely used Regional Management Units (RMUs) in sea turtle conservation (Wallace et al., 2023) provide a practical scale for assessing such thresholds, which are likely to vary among regions and species. Thresholds should be quantified through long-term monitoring and modeling (e.g., popu-

lation viability analyses) to provide concrete decision points for managers. For example, maintaining 70% hatching success is widely accepted as a minimum threshold for population stability (Mortimer, 1999)—crossing below this value could indicate a trigger point for intervention (Figure 6.2, Step 4), while sustained declines well below it may constitute a tipping point for population collapse. Determining robust species- and region-specific thresholds will require increased interdisciplinary research and closer integration of ecological and coastal management perspectives (Hilton et al., 2023; Slinger & Vreugdenhil, 2020).

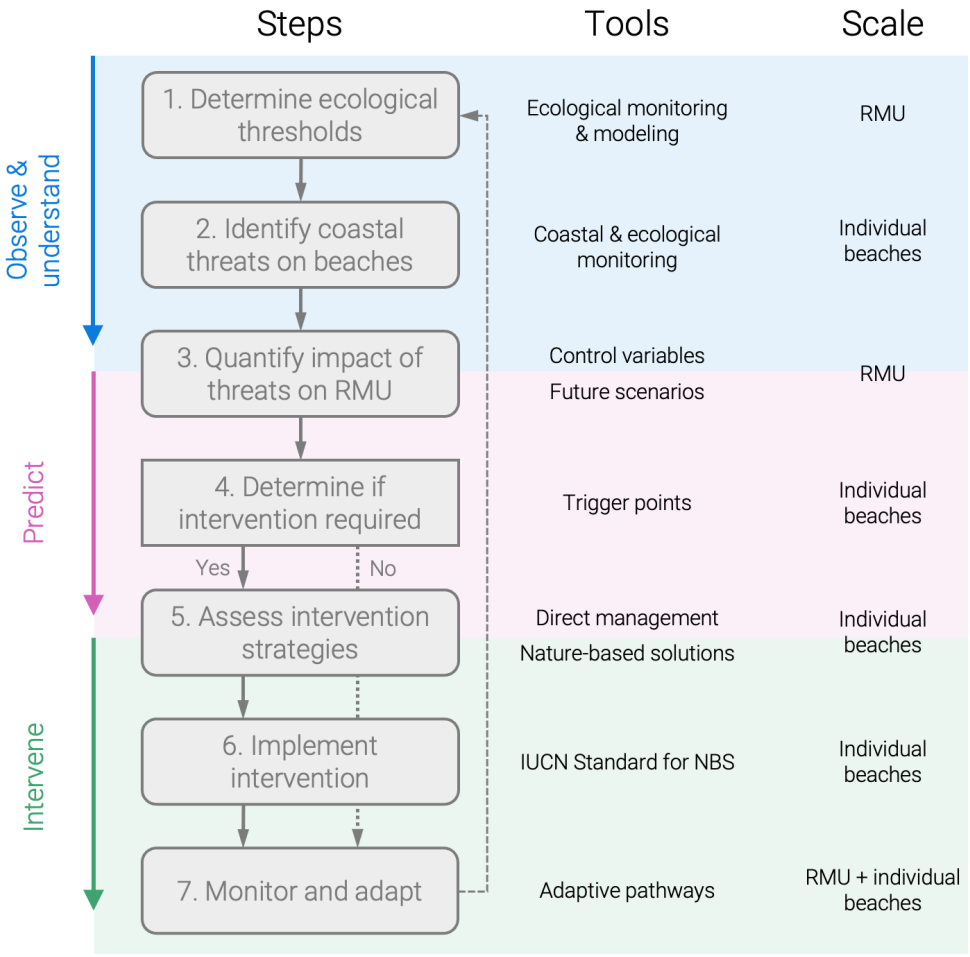

Figure 6.2: A stepwise framework for integrating sea turtle ecology and coastal management to tackle coastal threats to nesting beaches. The framework progresses through seven steps, following the Observe-Understand-Predict-Intervene phases (the first two are combined here). Each step is associated with specific tools and spatial scales, linking regional assessments (RMU) with local management of nesting beaches. Step 4 represents a key decision point on whether to intervene, while feedback loops emphasize the adaptive and iterative nature of the framework.

When ecological thresholds have been determined, the impact of coastal threats on sea turtle populations should be assessed accordingly (Figure 6.2, Steps 2 and 3). For example, if a certain percentage of nests are likely to be flooded each year, will that push the RMU-level hatching success beyond a trigger/tipping point? This can be done by defining and monitoring a set of control variables for each threat. A multitude of existing coastal tools can be leveraged to observe, understand, and predict these control variables at nesting beaches (Sections 6.4 and 6.5). Below we propose potential control variables for flooding and erosion of nesting beaches based on recent work, though these should be evaluated and refined through further interdisciplinary research.

For nest flooding, control variables should include the beach GWT (controls inundation duration) and a variable related to inundation frequency (e.g., water level exceedance). Important drivers of these control variables are the elevation of the nesting area, beach slope, sediment properties (e.g., grain size, permeability), and wave and water level climates. For example, in low-elevation, mild sloping coastal settings, the beach GWT drains slower, meaning longer inundation events negatively affect egg viability (e.g., on Galveston Island, USA and Raine Island, Australia; Christiaanse et al., 2025c; Guard et al., 2008). On steeper, coarser grained beaches, the faster drainage means egg viability may be more influenced by inundation frequency (e.g., from wave runup; Caut et al., 2010; Limpus et al., 2021; Pike et al., 2015).

Regarding beach loss, the shoreline position is a widely used indicator of coastal change (Splinter & Coco, 2021; Vitousek et al., 2023a), and may serve as a control variable to monitor nesting beach erosion (Christiaanse et al., 2025a). The advantage of using the shoreline position is that it can be monitored relatively easily at scale through remote sensing tools (e.g., CoastSat; Vos et al., 2019b). More sophisticated control variables may be required at more complex coastlines or for detailed assessments of individual nesting beaches (e.g., a beach resilience index as in Dong et al., 2018), though this requires more data and resources. Next to the shoreline position, the available accommodation space behind the beach is an important control variable, as it controls whether shoreline retreat will translate to beach loss (Christiaanse et al., 2025a). Accommodation space is determined by the geological properties of the backbeach and potential human infrastructure in the vicinity (Lansu et al., 2024; Wolinsky & Murray, 2009).

6.4. Monitoring and data

Monitoring nearshore hydrodynamics and beach groundwater can help understand the processes behind the repeated flooding of turtle nests on the beach (Christiaanse et al., 2025c; Foley et al., 2006; Ware & Fuentes, 2018). Previous studies on nest flooding have mainly focused on monitoring the high tide line and wave runup to identify flooded or exposed nests and compare their emergence success to non-flooded ones (e.g., Caut et al., 2010; Ware et al., 2019; 2021). Such approaches may provide similar accuracy in identifying at-risk nests as more time- and cost-intensive monitoring of the beach GWT (Ware & Fuentes, 2018). However, they are less useful for understanding and predicting the driving processes underlying nest flooding (Christiaanse et al., 2025c; Guard et al., 2008). Monitoring sediment characteristics (e.g., grain size) is also important, as they influence nesting suitability as well as beach morphology, slope, permeability, etc. (Botterell et al., 2025; Bujan et al., 2019; Mortimer, 1990; Yamamoto et al., 2012). Hence, we argue that more in-situ data collections

(e.g., Christiaanse et al., 2025b; Culver et al., 2020; Foley et al., 2006) will be required to understand the processes underlying coastal hazards to nesting beaches and design NBS that enable nesting.

Many nesting beaches lie in remote areas with low data availability. Moreover, most are located in the tropics and in developing countries (Mazaris et al., 2014), where access and capacity for in-situ data collection may be difficult. Nonetheless, the sea turtle community has succeeded to collect (long-term) nesting data at many (remote) beaches (e.g., Balazs & Chaloupka, 2004; Lasala et al., 2023; Restrepo et al., 2023; Willson et al., 2020). Most of these monitoring programs are ongoing and collect new data each nesting season. Including simple, cost-effective coastal monitoring in these campaigns could help fill some of the existing data gaps, without significantly increasing the workload. Key parameters would be beach elevation (e.g., weekly cross-shore GPS profiles or low-cost alternatives as in Andrade & Ferreira, 2006) and grain size. An emerging and promising way of collecting more coastal data worldwide are citizen science-based programs—e.g., *CoastSnap* for shoreline positions (Harley & Kinsela, 2022) or *SandSnap* for grain size estimation (McFall et al., 2024)—which could work particularly well on nesting beaches that are near local communities, have ongoing nest monitoring programs, and/or attract tourism.

In-situ data collection is often limited by cost and time constraints, making it difficult to scale up to large temporal and spatial scales. However, in recent years, remote sensing tools have transformed coastal monitoring by enabling the extraction of key geomorphic and environmental variables from satellite imagery. For example, satellite-derived shorelines allow for the quantification of beach width, slope, and erosion/accretion trends (e.g., Luijendijk et al., 2018; Vos et al., 2019a), which directly affect the availability of nesting habitat. While not well-established in sea turtle conservation yet, satellite imagery has previously been used to track nesting activity and distribution (Casale & Ceriani, 2019), quantify night lighting at nesting sites (Mazor et al., 2013), characterize developmental habitats (Hardy et al., 2018), and assess long-term morphological changes of nesting beaches (Christiaanse et al., 2025a; Maneja et al., 2021). We argue that the use of such tools in sea turtle conservation should be expanded, particularly to assess how nesting beaches around the world will respond to SLR in the coming decades (e.g., Christiaanse et al., 2025a). Moreover, the opportunities opening up through remote sensing are increasing at a fast pace, with new data now being collected on a near-daily scale, everywhere in the world, and may offer a much broader slate of data in the future (e.g., wave and water level climate, bathymetry, sediment characteristics; Bergsma et al., 2021; Turner et al., 2021; Vitousek et al., 2023a).

When there is no in-situ data and remote sensing tools cannot provide the required data or resolution (yet), global hindcast or reanalysis datasets offer an alternative for long-term time-series data of atmospheric and oceanic variables—e.g., ERA5 for waves, sea surface temperature, and many other variables (Hersbach et al., 2018), GTSM for water levels (Muis et al., 2020), and DeltaDTM for coastal topography (Pronk et al., 2024). Though such datasets have limited resolution and accuracy, they are often good enough for long-term statistics and exploratory modeling studies. Next to historical data, many global models and datasets offer future climate projections (e.g., the AR6 SLR projections; Garner et al., 2021). These can inform predictive models or be used to assess habitat suitability under various scenarios. For example, Christiaanse et al. (2024b) combined global datasets with machine learning to identify patterns in the coastal characteristics of nesting regions and map

new, potentially suitable nesting regions. Moreover, various types of coastal vulnerability indices have been used to provide a useful first estimate of the exposure of nesting beaches to coastal threats (de Vos et al., 2019; Gammon et al., 2023; Santana Garcon et al., 2010; Von Holle et al., 2019). These are often based on global or regional datasets making them effective at large spatial scales. Hence, they can be leveraged to identify high-risk beaches to prioritize for in-situ data collections.

Ultimately, hydromorphological monitoring should be complemented by ecological monitoring. Most existing nest monitoring programs focus on nest counts, hatching success, and nesting turtle characteristics (e.g., Balazs & Chaloupka, 2004; Margaritoulis, 2005; Restrepo et al., 2023). While these data are invaluable, measuring nest positions (GPS, ideally including elevation) and nest depth could significantly improve assessments of erosion and flooding impacts on nesting populations. While some datasets include nest coordinates (e.g., Culver et al., 2020; Ware et al., 2021), elevation is not commonly recorded. We realize this may not always be feasible, especially at high density nesting beaches. In such cases, (horizontal) coordinates of a subset of nests would already help, particularly in combination with digital elevation models of the beach.

6.5. Modeling

Collected data can be used to force, calibrate, and train models to predict the potential impact of coastal threats and NBS on nesting beaches. There are countless models available, for different purposes and scopes, generally categorized into physics/process-based models, statistical/data-driven models, and hybrid models, combining both approaches. Physics/process-based models numerically solve physical equations and empirical formulations to simulate natural processes like sediment transport or wave propagation. They range from 1D alongshore (e.g., *ShorelineS*; Roelvink et al., 2020) or cross-shore models (e.g., *Unibest-TC*; Walstra et al., 2012) over reduced-complexity shoreline models (e.g., *COCOONED*, *CoSMoS-COAST*; Antolínez et al., 2019; Vitousek et al., 2023b) to complex 2D/3D area models (e.g., *Delft3D*, *XBeach*; Lesser et al., 2004; Roelvink et al., 2009). Hybrid models use statistical tools to interpolate results from databases created from process-based models, significantly reducing computational cost (e.g., Antolínez et al., 2018; McCall et al., 2024). Finally, fully data-driven models use statistical and machine learning algorithms (e.g., neural networks) to learn from and extrapolate existing data (e.g., Gomez-de la Peña et al., 2023; Simmons & Splinter, 2025). Which model(s) to use depends on the objective (control variables), the location-specific boundary conditions, and the desired spatial/temporal scale and resolution.

To predict nest flooding, the driving hydrodynamic processes (waves and water levels) could be simulated with a 1/2-dimensional XBeach model. If the GWT is important (e.g., on mild-sloping, fine-grained beaches; Christiaanse et al., 2025c), XBeach has a groundwater module. However, this module was created for gravel beaches, and preliminary results on a mild-sloping nesting beach were poor (Galveston Island, TX; Taal, 2024). Coupling a tailored groundwater model (e.g., *PFLOTRAN*; Hammond et al., 2014) to the hydrodynamics from XBeach may provide better results. When data-availability is low, hybrid or surrogate models can be useful—for example, in many coral-lined coasts and islands, where models like *HyCReWW* (Rueda et al., 2019) or *BEWARE-2* (McCall et al., 2024; Scott et al., 2020) can provide first estimates of nest flooding from wave runup (Dédina et al., 2025).

Predicting longer-term processes, like SLR and erosion vulnerability on nesting beaches is more difficult as the larger time-scales inherently introduce more uncertainty (Vitousek et al., 2017b; 2024). Many studies have tried to quantify the loss of nesting area under various SLR scenarios, however, most use the simple *bathtub* approach—combining digital elevation models with SLR scenarios to derive inundation maps (e.g., Beber et al., 2024; Fish et al., 2005; Fuentes et al., 2010; Katselidis et al., 2014; Patrício et al., 2019; Rivas et al., 2023; Varela et al., 2019; Veelenturf et al., 2020). While time-efficient, this approach does not consider any morphological response of the system and therefore cannot provide actionable estimates of beach loss (Christiaanse et al., 2025a; Wolinsky & Murray, 2009). Others have applied the *Bruun rule* (Bruun, 1962) to estimate shoreline retreat on nesting beaches (e.g., Fish et al., 2008; Mazaris et al., 2009; Reece et al., 2013), though its validity is still debated (Cooper et al., 2020; Ranasinghe, 2020; Wolinsky & Murray, 2009). The relatively small amount of SLR over the past decades (our only dataset) means that the beach response is difficult to distinguish from more dominant modes of change, like seasonal and inter-annual signals (Vitousek et al., 2017b). Hence, beach response to SLR remains a subject of ongoing debate and corresponding model predictions come with high uncertainty. Nonetheless, reduced complexity models combined with satellite-derived shorelines at least allow us to explore potential future shoreline evolution, even in remote, data-scarce environments (Christiaanse et al., 2025a; Vitousek et al., 2024).

Ultimately, no model is perfect and any prediction comes with uncertainty. There is already intrinsic uncertainty in using future projections to force these models (e.g., SLR rates or wave climate variability; Le Cozannet et al., 2019; Ruggiero et al., 2010; Vitousek et al., 2021). Model choice is often a balancing act between achieving reasonable accuracy and minimizing uncertainty and computational cost. Simpler models are faster to run, but introduce uncertainty by missing processes and detail (Kroon et al., 2019). As more natural processes are included, the model becomes more computationally intensive, requires more input data, and uncertainty is introduced through free model parameters (Kroon et al., 2025). For robust decision-making, it is crucial to quantify these uncertainties in the predictions.

6.6. Toward nature-based solutions that enable nesting

Once we have observed the system, understand the natural processes at play, and identified a need to intervene (Figure 6.2, Step 4), we can think of solutions (Step 5). In some cases, direct conservation or management measures may suffice. For instance, nests can be relocated to mitigate inundation risk (though risky and costly; Pintus et al., 2009) and establishing Marine Protected Areas (or other area-based protection instruments) can minimize some external influences on the ecosystem (Spalding et al., 2014). Beyond direct management measures, coastal NBS offer promising ways to improve the beach system for sea turtle nesting, by altering the driving processes behind the threats (Figure 6.3; Ostertag, 2025).

Likely the most widely applied NBS for beaches is the use of nourishments to replenish/reprofile the beach with sand or even create new beaches (de Schipper et al., 2020). At nesting beaches, nourishments can elevate the nesting zone to protect it from flooding, or restore nesting area lost to erosion (Figure 6.1c; Limpus et al., 2021; Montague, 1993). The first beach re-profiling designed entirely for sea turtle nesting was implemented recently at Raine Island, Australia, which hosts the largest green turtle rookery worldwide (Smithers & Daw-

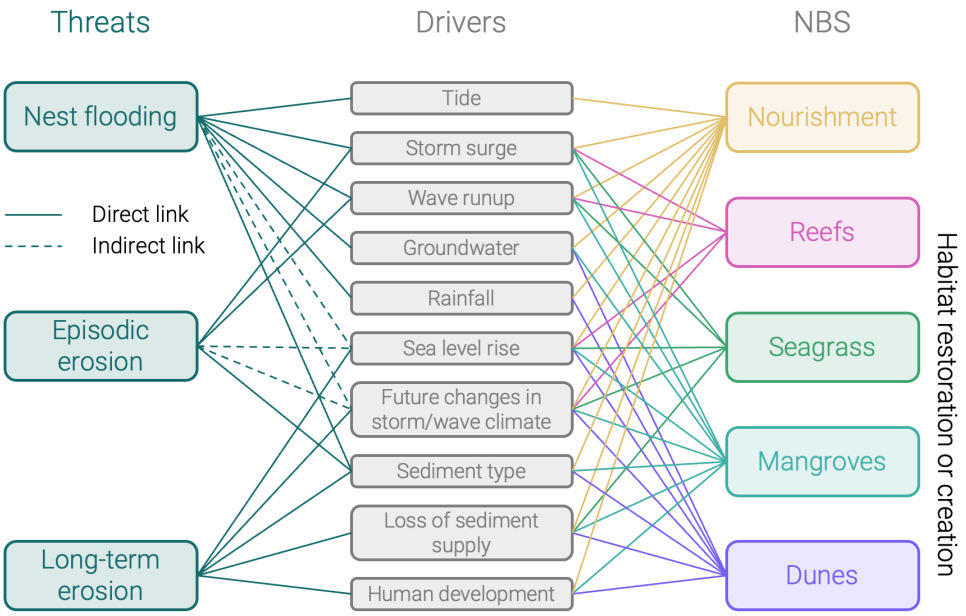

Figure 6.3: Threat-Driver-Solution matrix (non-exhaustive) showing coastal threats to sea turtle nesting beaches on the left, their driving processes in the middle, and potential NBS building blocks that could mitigate some of these threats. The lines show links between the three: NBS solutions affect one or more of the driving processes, through which they can mitigate threats.

6

son, 2023). Early results indicate that it has successfully boosted hatchling production. However, several studies have also reported negative effects of nourishments on turtle nesting, especially shortly after implementation and when specific characteristics like grain size, beach slope, or compaction changed (e.g., Brock et al., 2009; Grain et al., 1995; Rumbold et al., 2001; Steinitz et al., 1998). Fortunately, nourishment designs increasingly include societal and ecosystem services (de Schipper et al., 2020). As a NBS for sea turtle nesting beaches, nourishments must be carefully designed to effectively enhance nesting, ideally over multiple years. Further research should therefore focus on specific design requirements for nourishments that generate positive outcomes for sea turtles.

Additional NBS building blocks may include the restoration or creation of ecosystem services that mitigate flooding and erosion (Figure 6.3; Spalding et al., 2014). For example, (coral) reefs are known to dissipate wave and surge energy and can therefore reduce flooding of the nesting area (Borsje et al., 2011; Lowe et al., 2005). Similarly, seagrass beds can attenuate waves and currents, provide erosion control by stabilizing the foreshore, and stimulate accretion through sediment trapping (Bradley & Houser, 2009; Gacia et al., 1999; James et al., 2019). Moreover, they function as foraging habitats for green turtles (Christianen et al., 2023) and provide an added climate benefit through carbon sequestration (Duarte et al., 2013). Mangroves also have similar benefits of reducing flooding and erosion (Gedan et al., 2011; Thampanya et al., 2006). Although their presence near the shoreline may reduce beach access for turtles, eastern-pacific hawksbill turtles are known to nest in mangrove estuaries (Gaos et al., 2016; Mast et al., 2025). Dunes may also offer

benefits for sea turtle nesting, by providing sediment reserves, storage capacity for groundwater, and a buffer from human development (Barbier et al., 2011; Spalding et al., 2014). These ecosystem services can be leveraged through NBS by either restoring degraded habitats or creating new ones (e.g., through artificial reefs; Duarte et al., 2020; Reguero et al., 2018).

What type of NBS to implement (Figure 6.2, Step 6) depends on the environmental and societal challenges and the existing ecosystem (e.g., developed vs. undeveloped coastline), and design should follow a standardized design framework (e.g., the IUCN Global Standard for NBS; IUCN, 2020). Specific NBS that enable sea turtle nesting have not yet been tested at scale, thus to better understand their effect on sea turtles and the ecosystem as a whole, they need to be implemented and evaluated in the field. The above listed ecosystem services (non-exhaustive) may function as building blocks to design tailored solutions, depending on the identified threats and their driving processes (Figure 6.3). These building blocks can be combined, which may generate positive synergies. For instance, coral or shellfish reefs can create favorable conditions for seagrass and mangroves to develop (Barbier et al., 2011; Smith et al., 2009). There can also be drawbacks to these solutions—for example, while reefs, seagrass, and mangroves can locally trap sediment and reduce erosion, this can potentially disrupt longshore transport, causing erosion downstream. Ultimately, the effectiveness of any NBS is dependent on a healthy and stable ecosystem (Spalding et al., 2014). Potential side-effects and maintenance costs should, therefore, also be taken into account: are there detrimental effects on other ecosystem services? How long will the NBS last without intervening again (e.g., re-nourishment period)? In that regard, NBS should be managed adaptively and based on evidence (criterion 7 of the IUCN Standard; IUCN, 2020)—i.e., the ecosystem should be continuously monitored after implementation, to evaluate if the NBS has the desired effects and, if not, plan adjustment strategies (Figure 6.2, Step 7).

6.7. Conclusion & outlook

In this perspective, we argue that a stronger connection between coastal management and sea turtle conservation is needed to advance the research, design, and implementation of NBS that enable sea turtle nesting on sandy beaches. We support this perspective through a stepwise framework (Figure 6.2), which provides a conceptual roadmap for linking ecological thresholds, coastal processes, and management interventions across scales, from RMUs to individual beaches. We highlight how monitoring and modeling tools can be used to observe and understand coastal threats to nesting beaches, predict their impacts on sea turtle populations, and, where appropriate, intervene through adaptive NBS.

Each element of the framework points to concrete priorities for research and practice. Defining robust ecological thresholds and control variables requires increased collaboration between coastal scientists, managers, and sea turtle eco-/biologists. Improved in-situ monitoring and integration of cost-effective coastal measurements into ongoing nest monitoring programs will be essential for understanding flooding and erosion dynamics at nesting beaches. Combined with recent advances in remote sensing and machine learning, these data can feed into a growing suite of coastal models to simulate nesting beach evolution under various climate and management scenarios. Finally, interventions should be tested and implemented adaptively, guided by the IUCN Global Standard for NBS (IUCN, 2020)

and evaluated through continuous monitoring and refinement.

Acknowledgments—We would like to thank Prof. dr. Brendan Godley from the University of Exeter for the many inspiring conversations and Dr. Vanesa Chalastani for early discussions leading up to this paper.

Cover photo by Sean Williamson ©: Flatback sea turtle (*Natator depressus*) nesting at Mundabullangana, Australia.

7 Conclusion

This thesis aimed to *identify coastal processes that govern the vulnerability of sea turtle nesting beaches, and assess their implications for global habitat suitability and conservation*. In Chapter 1, this overarching aim was reformulated into three specific research questions. This concluding chapter provides an answer to each research question (Section 7.1), along with several specific recommendations for follow-up research (Section 7.2).

7.1. Conclusions

RQ1: What are the driving processes behind sea turtle nest flooding on sandy beaches?

This research question was addressed in detail in Chapters 2 and 3. We investigated the beach GWT response to ocean processes and rain in a fine-grained, mild-sloping beach system by analyzing field data gathered on Galveston Island, Texas in the fall of 2023. We quantified the influence of IG waves, tide, surge, and rainfall on short-term GWT fluctuations between the high tide line and the dune toe by performing tailored spectral analyses on $\pm$30-day time series of water level observations.

We observed significant short-term variability in the beach GWT across the nesting zone ($\mathcal{O}$(1 m)), and our results showed that these were mainly driven by the surge and rainfall. The tidal signal was increasingly damped and asymmetric towards the dune, whereas IG waves were only relevant near the swash zone. A flooding threshold based on a representative Kemp's ridley nest depth of 30 cm below the surface revealed multiple prolonged nest inundation events (exceeding 12 hours). Kemp's ridleys generally have the shallowest nests, so other species' nests in the same area would have been flooded for even longer durations. Our results imply that Galveston Island is currently not a suitable nesting habitat for sea turtles as nests are likely to get flooded frequently and for prolonged periods.

On fine-grained, mild-sloping beach systems, like Galveston Island, the low permeability and slow drainage means that flooding events (e.g., by a storm surge) are likely to elevate the beach GWT for prolonged periods of time. This is likely also the case on low-lying islands, including the largest existing green turtle rookery on Raine Island, Australia (Guard et al., 2008; Limpus et al., 2021). At such nesting sites, the GWT is therefore a critical variable in assessments of nest flooding. However, given the interdependence between groundwater dynamics and beach slope, elevation, and sediment size, the importance of GWT fluctuations for nest flooding may vary significantly among global sea turtle nesting beaches. Specifically, steeper, higher elevation beaches with coarser sediments typically have greater permeability and drainage (Turner et al., 1997), meaning that the mean GWT is likely deeper below the surface and the capillary fringe is narrower (Turner & Nielsen,

1997). In such environments, we do not expect such extended periods of elevated groundwater and egg viability may depend more on flooding frequency. This in turn can change the dominant drivers of nest flooding, with wave runup and tidal inundation potentially being more important.

RQ2: How vulnerable are key global nesting beaches to erosion and sea level rise?

This research question was addressed in detail in Chapter 4, where we combined satellite-derived shorelines, shoreline modeling, and global datasets to analyze the shoreline evolution, characteristics, and future vulnerability of nine globally important sea turtle nesting beaches. We identified seasonal and long-term trends in shoreline position and used the shoreline model CoSMoS-COAST (Mao et al., 2025; Vitousek et al., 2023b) to hindcast daily shoreline positions from 1980 to 2024 and forecast them from 2025 to 2100 under two SLR scenarios, including associated uncertainty. Additionally, we quantified the available accommodation space at each site using a global digital terrain model (DeltaDTM; Pronk et al., 2024) and global infrastructure footprints (Overture maps).

Long-term shoreline evolution and seasonality varied considerably across the nine sites, with four sites showing erosion trends and three sites accretion. As a result, future vulnerability also varied significantly. The projections indicated that three sites may be particularly vulnerable to SLR, due to future shoreline retreat coupled with limited accommodation space: Alagadi on Cyprus, Dirk Hartog Island in Western Australia, and Long Beach on Ascension Island. The applied framework can be readily applied to other nesting beaches around the world. While the analysis in Chapter 4 provides a first exploration of potential future shoreline change at these critical nesting beaches, the results come in tandem with high uncertainty. What is clear is that the *bathub* approach, widely applied in previous studies, cannot provide useful estimates of nesting area loss.

7

RQ3: How do regional coastal characteristics influence global habitat suitability for sea turtle nesting?

This research question was addressed in detail in Chapter 5. We examined the relationship between regional coastal characteristics and the global nesting distribution of five sea turtle species (loggerhead, *Cc*; green, *Cm*; hawksbill, *Ei*; leatherback, *Dc*; and olive ridley, *Lo*). An initial set of 22 coastal indicators was considered—spanning hydrodynamic, atmospheric, geophysical, habitat, and human processes—on a hexagonal coastline grid (Coastgons) of $\approx$ 50 km-resolution. We assessed the influence of these indicators on the global distribution of sea turtle nesting by computing each indicator's relative importance in splitting the data into nesting and non-nesting categories, through a random forest model. Based on this importance, a subset of six influential indicators per species was examined through a cluster analysis (self-organizing maps) to reveal patterns in the coastal characteristics of global nesting habitats, and identify new, potentially suitable nesting regions.

While there were differences between species, at the coarse, global scale considered here, important indicators consisted mainly of sea surface temperature, extreme surge levels, tidal range, and the distance to the nearest coral reef and seagrass habitats. For example, individual species' nesting grounds tended to occur in regions with relatively low tidal ranges (*Cc*, *Ei*, and *Dc*), low extreme surge levels (*Cc*, *Cm*, *Ei*, and *Dc*), warm temperatures (*Cm*, *Ei*, *Dc*, and *Lo*), and near coral habitats (*Cm* and *Ei*). The first two observations might suggest that sea turtles select their nesting grounds in an effort to reduce the risk of (periodic)

nest flooding, as has similarly been hypothesized on smaller spatial scales (e.g., Mortimer, 1990). Other indicators reported as influential in literature appeared less important according to our results, for example, precipitation (Pike, 2013) and wind (Santana Garcon et al., 2010). Notably we did not identify any important geophysical indicators (e.g., beach slope, elevation) at this scale, but expect these to be more influential for smaller spatial scales and more accurate data. For example, geophysical indicators significantly influence the beach groundwater table characteristics (see Chapter 3).

We identified new, potentially suitable nesting regions, mapping each species' fundamental nesting niche on global and regional nesting suitability maps. Global nesting suitability ranged from 12.9% (*Lo*) to 36.9% (*Cm*) of Coastgons (mean 23.2%). However, observed nesting currently only occurs in 4.7% to 10.1% of Coastgons (mean 7%), suggesting that the realized niche is still significantly smaller, and that there is potential for sea turtles to expand their nesting habitats. This is a particularly important finding in the face of nature-based solutions and assisted colonization of new coastal regions (Barbanti et al., 2022), as recent studies suggest that phenological shifts (earlier onset of nesting season) are unlikely to be sufficient for most sea turtle populations to stay within appropriate nesting conditions (Laloë & Hays, 2023; Monsinjon et al., 2019).

It should be noted that the analyses presented in Chapters 3–5 were conducted at different temporal and spatial scales—i.e., individual beaches in Chapters 3 and 4 versus regional grid cells in Chapter 5. Consequently, some of the conclusions presented above may appear contradictory. For instance, the relatively low importance of geophysical indicators in Chapter 5 contrasts with the strong influence of beach slope and grain size on nest flooding, identified in Chapter 3. The framework developed in Chapter 6 aims to bridge these scale differences by providing an integrated approach to incorporating coastal science and management considerations into sea turtle conservation. Moreover, through this framework, local, beach scale flooding and erosion threats are linked back to the impact at regional management unit-level. This is important as the ultimate goal is not to save every nest, but to maintain stable sea turtle populations.

7.2. Future research

Chapter 6 already presented the author's perspective on the future of coastal science and management in sea turtle conservation, along with a call for increased interdisciplinary collaboration, and some recommendations for potential research and management directions. While that perspective represents a broad outlook across disciplines, there are also several specific research opportunities arising from the results discussed in Chapters 2–5. Here, recommendations for future research emerging from this thesis are summarized along with a brief description of how they could be tackled.

1. *Assess long-term groundwater variability and inland processes at Galveston Island.* While the analysis in Chapter 3 excluded inland groundwater processes, these could play a role in longer-term fluctuations of the beach groundwater table and may therefore also affect the risk of nest flooding. Moreover, our field observations were too short to assess potential seasonal fluctuations in the groundwater table. Installing a few groundwater wells at larger spatial intervals (covering the backbeach, potentially all the way to the bay side of the island) to monitor the groundwater table long-term

(6+ months, at lower sampling frequencies) could therefore improve future assessments.

2. *Assess the influence of the capillary fringe on egg viability.*
   Unfortunately, the moisture sensors used during the field experiment were not calibrated correctly (see Chapter 2) which prevented us from quantifying the capillary fringe width on Galveston Island. However, on fine-grained, mild-sloping beaches it can generally be quite wide (0.5–1 m). Given this could significantly increase nest exposure, future research should assess egg viability of nests situated in the capillary fringe, which has not been tested before. This could be done through lab experiments, similar to Limpus et al. (2021) and Pike et al. (2015).

3. *Assess sea turtle nest flooding for different beach profiles and nourishment strategies on Galveston Island.*
   Given that Galveston Island is currently not suitable for nesting due to the high risk of nest flooding, a logical next step could be to assess nest flooding for different beach profile shapes and nourishment strategies. A possible approach could be to couple a hydrodynamic model (e.g., XBeach) to a groundwater model (e.g., PFLOTRAN; Taal, 2024). This is particularly relevant for Galveston Island as large coastal protection measures are planned to better protect the region from flooding (USACE, 2021). Hence, such a modeling study could inform nourishment strategies to improve the suitability for turtle nesting.

4. *Develop a generic framework to assess sea turtle nest flooding across different coastal environments.*
   Although Chapter 3 provided new insights into the drivers and impact of nest flooding on Galveston Island, the results cannot be directly translated to nesting sites in different coastal environments (e.g., with lower surges, higher wave impacts, steeper slopes, etc.). Therefore, future research should try to develop a framework to assess the dominant drivers of nest flooding across varying coastal environments. A starting point could be to identify important environmental characteristics (e.g., beach slope, wave climate) that determine which processes are most likely to drive nest flooding.

5. *Use local data and advanced coastal resilience indicators to assess nesting sites vulnerable to erosion.*
   The vulnerability assessments in Chapter 4 have relied on the use of global datasets and a relatively simple coastal change indicator (shoreline position). These assessments could be significantly improved by using local, higher resolution data on the beach slope and backbeach topography and geology. Such data are often not readily available, however, so future research could seek to collect such data and use them to make more robust coastal vulnerability assessments, especially at sites that are likely to be vulnerable. Local data could also facilitate the use of more sophisticated coastal resilience indicators (e.g., Dong et al., 2018).

6. *Quantify wave climate variability and model uncertainty in shoreline predictions.*
   Uncertainty is important in every modeling exercise, but particularly in long-term climate-change related projections, like the shoreline modeling exercise in Chapter 4.

While we quantified uncertainty due to unknown sea level rise rates, future research should address the uncertainties owing to wave climate variability and the optimized model parameters (in particular the Bruun transgression slope).

7. *Investigate sediment characteristics across global nesting beaches.*
Many of the driving processes behind flooding and erosion are influenced by sediment characteristics of the beach, most notably the grain size. However, these data are hard to come by and a global database of grain sizes does not (yet) exist. Recently, a set of about 200 sediment samples from turtle beaches around the world has been collected to measure microplastics (Botterell et al., 2025). These samples provide an excellent opportunity to gain new insights on sea turtle beach sediment characteristics (Heijl, 2025).

8. *Include seasonality and population size in global distribution analysis.*
The global analysis of nesting site distribution in Chapter 5 treated all nesting sites equally. In reality, these sites differ significantly in the size of the nesting populations they support, ranging from a few individuals to tens of thousands. Moreover, we did not constrain the coastal characteristics by the local nesting seasons. Future studies could improve this analysis by including seasonality in the coastal characteristics and taking the relative size of nesting populations into account.

9. *Map potential nesting suitability based on future climate projections.*
The analysis in Chapter 5 used historical and current data to identify potentially suitable nesting regions. However, many of the important variables are projected to change in the coming decades (e.g., sea surface temperature, surge heights). Thus, regions that were suitable in the past or are suitable today may not necessarily be suitable in the future (and vice versa). Although accompanied by uncertainties, climate change projections exist for many of these variables, so future research could map potentially suitable nesting regions under different climate scenarios (e.g., Duquesne & Fournier, 2025; Patel et al., 2021).

10. *Evaluate ecological thresholds (trigger and tipping points) for intervention.*
Chapter 6 emphasized the importance of determining ecological thresholds for deciding when intervention is necessary (trigger points) or when irreversible changes occur (tipping points). Future research should focus on identifying and quantifying these ecological thresholds, ideally at the level of Regional Management Units (RMUs; Wallace et al., 2023). This would require integrated ecological and coastal data collection to inform robust decision-making frameworks.

11. *Implement long-term, joint hydromorphological and ecological monitoring strategies at nesting beaches.*
In Chapter 6, we argued that interdisciplinary research is required to move sea turtle conservation through coastal management forward. Such research requires joint data collection on hydropmorphological (e.g., water levels, sediment characteristics) and ecological (e.g. nest counts, hatching success) parameters in an integrated monitoring strategy. These could, for example, be implemented into existing long-term nest monitoring programs.

12. *Develop coupled hydromorphological and ecological modeling frameworks.*
Chapter 6 highlighted the critical need for combining ecological knowledge with coastal modeling to effectively assess and predict the impacts of flooding and erosion on nesting populations. Current coastal models primarily simulate hydrodynamic and morphological processes independently from ecological responses, limiting their ability to accurately represent interactions between these components. Future research should focus on developing coupled modeling frameworks that integrate hydrodynamics, beach morphology, groundwater dynamics, and ecological factors (e.g., nest suitability, hatching success, and species-specific nesting behaviors). Such integrative approaches could significantly improve predictions of sea turtle population responses to coastal threats and enhance the design of targeted nature-based solutions to enable nesting on current nesting beaches, as well as potentially new ones.

13. *Test and evaluate specific nature-based solutions at nesting beaches.*
While several promising nature-based solutions (e.g., turtle-friendly sand nourishments, artificial reefs, seagrass restoration, dune restoration) are mentioned in Chapter 6, their effectiveness for turtle nesting remains largely untested at scale. Future research should therefore involve field testing and systematically evaluating the effectiveness, ecological impacts, maintenance requirements, and potential side effects of these nature-based solutions. This knowledge will support adaptive coastal management and the effective implementation of nature-based solutions tailored specifically to nesting beach environments

References

Abdulsalam, M. B., Jaramillo, C., de Freitas, L., González, M., & Antolínez, J. A. (2025). Assessing shoreline orientation variation across diverse coastal environments. *Coastal Engineering*, *200*, 104770. https://doi.org/10.1016/j.coastaleng.2025.104770 (cit. on pp. 72, 91).

Ackerman, R. A. (1997). The nest environment and the embryonic development of sea turtles. In P. L. Lutz & J. A. Musick (Eds.), *The biology of sea turtles* (pp. 83–106, Vol. 1). CRC Press. (Cit. on pp. 2, 12, 42, 63, 72, 100, 124).

Almar, R., Ranasinghe, R., Bergsma, E. W. J., Diaz, H., Melet, A., Papa, F., Vousdoukas, M., Athanasiou, P., Dada, O., Almeida, L. P., & Kestenare, E. (2021). A global analysis of extreme coastal water levels with implications for potential coastal overtopping. *Nature Communications*, *12*(1), 3775. https://doi.org/10.1038/s41467-021-24008-9 (cit. on p. 116).

Almpanidou, V., Schofield, G., Kallimanis, A. S., Türkozan, O., Hays, G. C., & Mazaris, A. D. (2016). Using climatic suitability thresholds to identify past, present and future population viability. *Ecological Indicators*, *71*, 551–556. https://doi.org/10.1016/j.ecolind.2016.07.038 (cit. on p. 101).

Anarde, K. A., Moore, L. J., Murray, A. B., & Reeves, I. R. B. (2024). The Future of Developed Barrier Systems: 1. Pathways Toward Uninhabitability, Drowning, and Rebound. *Earth's Future*, *12*(4), e2023EF003672. https://doi.org/10.1029/2023EF003672 (cit. on p. 90).

Anarde, K., Figlus, J., Sous, D., & Tissier, M. (2020). Transformation of Infragravity Waves during Hurricane Overwash. *Journal of Marine Science and Engineering*, *8*(8), 545. https://doi.org/10.3390/jmse8080545 (cit. on pp. 48, 61).

Andrade, F., & Ferreira, M. A. (2006). A Simple Method of Measuring Beach Profiles. *Journal of Coastal Research*, *22*(4 (224)), 995–999. https://doi.org/10.2112/04-0387.1 (cit. on p. 129).

Antolínez, J. A. A., Méndez, F. J., Anderson, D., Ruggiero, P., & Kaminsky, G. M. (2019). Predicting Climate-Driven Coastlines With a Simple and Efficient Multiscale Model. *Journal of Geophysical Research: Earth Surface*, *124*(6), 1596–1624. https://doi.org/10.1029/2018JF004790 (cit. on pp. 82, 92, 130).

Antolínez, J. A. A., Murray, A. B., Méndez, F. J., Moore, L. J., Farley, G., & Wood, J. (2018). Downscaling Changing Coastlines in a Changing Climate: The Hybrid Approach. *Journal of Geophysical Research: Earth Surface*, *123*(2), 229–251. https://doi.org/10.1002/2017JF004367 (cit. on pp. 72, 130).

Ashton, A., Murray, A. B., & Arnoult, O. (2001). Formation of coastline features by large-scale instabilities induced by high-angle waves. *Nature*, *414*(6861), 296–300. https://doi.org/10.1038/35104541 (cit. on p. 72).

Athanasiou, P., van Dongeren, A., Giardino, A., Vousdoukas, M., Gaytan-Aguilar, S., & Ranasinghe, R. (2019). Global distribution of nearshore slopes with implications for coastal retreat. *Earth System Science Data*, *11*(4), 1515–1529. https://doi.org/10.5194/essd-11-1515-2019 (cit. on p. 116).

Athanasiou, P., van Dongeren, A., Pronk, M., Giardino, A., Vousdoukas, M., & Ranasinghe, R. (2024). Global Coastal Characteristics (GCC): a global dataset of geophysical, hydrodynamic, and socioeconomic coastal indicators. *Earth System Science Data*, *16*(7), 3433–3452. https://doi.org/10.5194/essd-16-3433-2024 (cit. on pp. 102–105, 190).

Atkins, J. E., & McBride, E. F. (1992). Porosity and Packing of Holocene River, Dune, and Beach Sands. *AAPG Bulletin*, *76*(3), 339–355. https://doi.org/10.1306/BDFF87F4-1718-11D7-8645000102C1865D (cit. on p. 33).

Babadi, B., & Brown, E. N. (2014). A Review of Multitaper Spectral Analysis. *IEEE Transactions on Biomedical Engineering*, *61*(5), 1555–1564. https://doi.org/10.1109/TBME.2014.2311996 (cit. on p. 49).

Baker, J. D., Harting, A. L., Johanos, T. C., London, J. M., Barbieri, M. M., & Littnan, C. L. (2020). *Terrestrial Habitat Loss and the Long-term Viability of the French Frigate Shoals Hawaiian Monk Seal Subpopulation* (tech. rep.). NOAA technical memorandum NMFS-PIFSC. https://doi.org/10.25923/76vx-ve75 (cit. on p. 4).

Balazs, G. H., & Chaloupka, M. (2004). Thirty-year recovery trend in the once depleted Hawaiian green sea turtle stock. *Biological Conservation*, *117*(5), 491–498. https://doi.org/10.1016/j.biocon.2003.08.008 (cit. on pp. 129, 130).

Barbanti, A., Blumenthal, J. M., Broderick, A. C., Godley, B. J., Prat-Varela, A., Turmo, M., Pascual, M., & Carreras, C. (2022). The architecture of assisted colonisation in sea turtles: building new populations in a biodiversity crisis. *Nature Communica-*

tions, *13*(1), 1580. https://doi.org/10.1038/s41467-022-29232-5 (cit. on pp. 5, 101, 119, 141).

Barbier, E. B., Hacker, S. D., Kennedy, C., Koch, E. W., Stier, A. C., & Silliman, B. R. (2011). The value of estuarine and coastal ecosystem services. *Ecological Monographs*, *81*(2), 169–193. https://doi.org/10.1890/10-1510.1 (cit. on pp. 1, 72, 124, 133).

Barnard, P. L., Short, A. D., Harley, M. D., Splinter, K. D., Vitousek, S., Turner, I. L., Allan, J., Banno, M., Bryan, K. R., Doria, A., Hansen, J. E., Kato, S., Kuriyama, Y., Randall-Goodwin, E., Ruggiero, P., Walker, I. J., & Heathfield, D. K. (2015). Coastal vulnerability across the Pacific dominated by El Niño/Southern Oscillation. *Nature Geoscience*, *8*(10), 801–807. https://doi.org/10.1038/ngeo2539 (cit. on pp. 4, 72).

Battjes, J. A., Bakkenes, H. J., Janssen, T. T., & van Dongeren, A. R. (2004). Shoaling of subharmonic gravity waves. *Journal of Geophysical Research: Oceans*, *109*(C2). https://doi.org/10.1029/2003JC001863 (cit. on p. 53).

Bauer, B., Davidson-Arnott, R., Hesp, P., Namikas, S., Ollerhead, J., & Walker, I. (2009). Aeolian sediment transport on a beach: Surface moisture, wind fetch, and mean transport. *Geomorphology*, *105*(1-2), 106–116. https://doi.org/10.1016/j.geomorph.2008.02.016 (cit. on pp. 12, 42).

Bear, J., Cheng, A. H.-D., Sorek, S., Ouazar, D., & Herrera, I. (Eds.). (1999). *Seawater Intrusion in Coastal Aquifers — Concepts, Methods and Practices* (Vol. 14). Springer Netherlands. https://doi.org/10.1007/978-94-017-2969-7 (cit. on pp. 12, 42).

Beber, I., Sellés-Ríos, B., & Whitworth, A. (2024). Future sea-level rise impacts to Olive Ridley (Lepidochelys olivacea) and Green Sea Turtle (Chelonia mydas) nesting habitat on the Osa Peninsula, Costa Rica. *Climate Change Ecology*, *7*, 100085. https://doi.org/10.1016/j.ecochg.2024.100085 (cit. on p. 131).

Beckman, J. N., & Long, J. W. (2022). Quantifying errors in wind and wave measurements from a compact, low-cost wave buoy. *Frontiers in Marine Science*, *9*, 966855. https://doi.org/10.3389/fmars.2022.966855 (cit. on p. 34).

Befus, K. M., Barnard, P. L., Hoover, D. J., Finzi Hart, J. A., & Voss, C. I. (2020). Increasing threat of coastal groundwater hazards from sea-level rise in California. *Nature Climate Change*, *10*(10), 946–952. https://doi.org/10.1038/s41558-020-0874-1 (cit. on pp. 12, 44).

Bergsma, E. W., Almar, R., Rolland, A., Binet, R., Brodie, K. L., & Bak, A. S. (2021). Coastal morphology from space: A showcase of monitoring the topography-bathymetry continuum. *Remote Sensing of Environment*, *261*, 112469. https://doi.org/10.1016/j.rse.2021.112469 (cit. on pp. 73, 129).

Bertin, X., de Bakker, A., van Dongeren, A., Coco, G., André, G., Ardhuin, F., Bonneton, P., Bouchette, F., Castelle, B., Crawford, W. C., Davidson, M., Deen, M., Dodet, G., Guérin, T., Inch, K., Leckler, F., McCall, R., Muller, H., Olabarrieta, M., … Tissier, M. (2018). Infragravity waves: From driving mechanisms to impacts. *Earth-Science Reviews*, *177*, 774–799. https://doi.org/10.1016/j.earscirev.2018.01.002 (cit. on p. 48).

Bevan, E., Wibbels, T., Najera, B. M. Z., Martinez, M. A. C., Martinez, L. A. S., Reyes, D. J. L., Hernandez, M. H., Gamez, D. G., Pena, L. J., & Burchfield, P. M. (2014). In situ nest and hatchling survival at Rancho Nuevo, the primary nesting beach of the Kemp's ridley sea turtle, Lepidochelys Kempii. *Herpetological Conservation and Biology*, *9*(3), 563–577. https://www.herpconbio.org/Volume_9/Issue_3/Bevan_etal_2014.pdf (cit. on p. 172).

Biddiscombe, S. J., Smith, E. A., & Hawkes, L. A. (2020). A Global Analysis of Anthropogenic Development of Marine Turtle Nesting Beaches. *Remote Sensing*, *12*(9), 1492. https://doi.org/10.3390/rs12091492 (cit. on p. 124).

de Bie, K., Addison, P. F. E., & Cook, C. N. (2018). Integrating decision triggers into conservation management practice. *Journal of Applied Ecology*, *55*(2), 494–502. https://doi.org/10.1111/1365-2664.13042 (cit. on p. 126).

Bjerklie, D. M., Mullaney, J. R., Stone, J. R., Skinner, B. J., & Ramlow, M. A. (2012). *Preliminary investigation of the effects of sea-level rise on groundwater levels in New Haven, Connecticut* (tech. rep.). U.S. Geological Survey Open-File Report 2012-1025. https://doi.org/10.3133/OFR20121025 (cit. on pp. 12, 43, 65).

Bjorndal, K. A. (1980). Nutrition and grazing behavior of the green turtle Chelonia mydas. *Marine Biology*, *56*(2), 147–154. https://doi.org/10.1007/BF00397131 (cit. on p. 115).

Bjorndal, K. A., Wetherall, J. A., Bolten, A. B., & Mortimer, J. A. (1999). Twenty-Six Years of Green Turtle Nesting at Tortuguero, Costa Rica: An Encouraging Trend. *Conservation Biology*, *13*(1), 126–134. https://doi.org/10.1046/j.1523-1739.1999.97329.x (cit. on p. 171).

Borsje, B. W., van Wesenbeeck, B. K., Dekker, F., Paalvast, P., Bouma, T. J., van Katwijk, M. M., & de Vries, M. B. (2011). How ecological engineering can serve in coastal protection. *Ecological Engineering*, *37*(2), 113–122. https://doi.org/10.1016/j.ecoleng.2010.11.027 (cit. on p. 132).

Bosboom, J., Reniers, A. J. H. M., & Luijendijk, A. P. (2014). On the perception of morphodynamic model skill. *Coastal Engineering*, *94*, 112–125. https://doi.org/10.1016/j.coastaleng.2014.08.008 (cit. on p. 91).

Botero, C. A., Weissing, F. J., Wright, J., & Rubenstein, D. R. (2015). Evolutionary tipping points in the ca-

pacity to adapt to environmental change. *Proceedings of the National Academy of Sciences*, *112*(1), 184–189. https://doi.org/10.1073/pnas.1408589111 (cit. on p. 126).

Botterell, Z. L., Ardren, J., Dove, E., McArthur, E., Addison, D. S., Adegbile, O. M., Agamboue, P. D., Agyekumhene, A., Allman, P., Alterman, A., Anderson, A., Arenholz, T., Ariano-Sánchez, D., Arnold, Z., Báez, J. C., Bahar, A., Barbosa, C., Barrios-Garrido, H., Başkale, E., … Godley, B. J. (2025). A global assessment of microplastic abundance and characteristics on marine turtle nesting beaches. *Marine Pollution Bulletin*, *215*, 117768. https://doi.org/10.1016/j.marpolbul.2025.117768 (cit. on pp. 128, 143).

Bradley, K., & Houser, C. (2009). Relative velocity of seagrass blades: Implications for wave attenuation in low□energy environments. *Journal of Geophysical Research: Earth Surface*, *114*(F01004). https://doi.org/10.1029/2007JF000951 (cit. on p. 132).

Bradski, G. (2000). The OpenCV Library. *Dr. Dobb's Journal: Software Tools for the Professional Programmer*, *25*(11), 120–123 (cit. on p. 21).

Breiman, L. (2001). Random forests. *Machine Learning*, *45*(1), 5–32. https://doi.org/10.1023/A:1010933404324 (cit. on p. 106).

Brock, K. A., Reece, J. S., & Ehrhart, L. M. (2009). The Effects of Artificial Beach Nourishment on Marine Turtles: Differences between Loggerhead and Green Turtles. *Restoration Ecology*, *17*(2), 297–307. https://doi.org/10.1111/j.1526-100X.2007.00337.x (cit. on pp. 64, 132).

Broderick, A. C., Glen, F., Godley, B. J., & Hays, G. C. (2002). Estimating the number of green and loggerhead turtles nesting annually in the Mediterranean. *Oryx*, *36*(3), 227–235. https://doi.org/10.1017/S0030605302000431 (cit. on p. 172).

Bronez, T. (1992). On the performance advantage of multitaper spectral analysis. *IEEE Transactions on Signal Processing*, *40*(12), 2941–2946. https://doi.org/10.1109/78.175738 (cit. on p. 49).

Brown, C. J., Smith, S. J., Lawton, P., & Anderson, J. T. (2011). Benthic habitat mapping: A review of progress towards improved understanding of the spatial ecology of the seafloor using acoustic techniques. *Estuarine, Coastal and Shelf Science*, *92*(3), 502–520. https://doi.org/10.1016/j.ecss.2011.02.007 (cit. on p. 117).

Bruder, B. L., & Brodie, K. L. (2020). CIRN Quantitative Coastal Imaging Toolbox. *SoftwareX*, *12*, 100582. https://doi.org/10.1016/j.softx.2020.100582 (cit. on p. 21).

Bruun, P. (1962). Sea-Level Rise as a Cause of Shore Erosion. *Journal of the Waterways and Harbors Division*, *88*(1), 117–130. https://doi.org/10.1061/JWHEAU.0000252 (cit. on p. 131).

Bujan, N., Cox, R., & Masselink, G. (2019). From fine sand to boulders: Examining the relationship between beach-face slope and sediment size. *Marine Geology*, *417*, 106012. https://doi.org/10.1016/j.margeo.2019.106012 (cit. on pp. 65, 128).

Cai, W., Borlace, S., Lengaigne, M., van Rensch, P., Collins, M., Vecchi, G., Timmermann, A., Santoso, A., McPhaden, M. J., Wu, L., England, M. H., Wang, G., Guilyardi, E., & Jin, F.-F. (2014). Increasing frequency of extreme El Niño events due to greenhouse warming. *Nature Climate Change*, *4*(2), 111–116. https://doi.org/10.1038/nclimate2100 (cit. on p. 4).

Calkoen, F. R., Luijendijk, A. P., Barli, P., Hemmes, J., Ranasinghe, R., & Nicholls, R. J. (2025a). Global Coastal Erosion: present-day exposure and future risk due to shoreline retreat (in prep.) (cit. on p. 76).

Calkoen, F. R., Luijendijk, A. P., Vos, K., Kras, E., & Baart, F. (2025b). Enabling coastal analytics at planetary scale. *Environmental Modelling & Software*, *183*, 106257. https://doi.org/10.1016/j.envsoft.2024.106257 (cit. on p. 75).

Camus, P., Mendez, F. J., Medina, R., & Cofiño, A. S. (2011). Analysis of clustering and selection algorithms for the study of multivariate wave climate. *Coastal Engineering*, *58*(6), 453–462. https://doi.org/10.1016/j.coastaleng.2011.02.003 (cit. on p. 108).

Cappellari, M., McDermid, R. M., Alatalo, K., Blitz, L., Bois, M., Bournaud, F., Bureau, M., Crocker, A. F., Davies, R. L., Davis, T. A., de Zeeuw, P. T., Duc, P.-A., Emsellem, E., Khochfar, S., Krajnović, D., Kuntschner, H., Morganti, R., Naab, T., Oosterloo, T., … Young, L. M. (2013). The ATLAS3D project – XX. Mass–size and mass–σ distributions of early-type galaxies: bulge fraction drives kinematics, mass-to-light ratio, molecular gas fraction and stellar initial mass function. *Monthly Notices of the Royal Astronomical Society*, *432*(3), 1862–1893. https://doi.org/10.1093/mnras/stt644 (cit. on p. 82).

Capuano, R. M., & Jones, C. R. (2022). Clay-cation composition of river sediments as evidence of wet versus dry paleoclimate. *Applied Geochemistry*, *146*, 105421. https://doi.org/10.1016/j.apgeochem.2022.105421 (cit. on p. 44).

Carpio Camargo, A. J., Álvarez Gutiérrez, Y., Jaramillo Véliz, J., & Sánchez Tortosa, F. (2020). Nesting failure of sea turtles in Ecuador - causes of the loss of sea turtle nests: the role of the tide. *Journal of Coastal Conservation*, *24*(5), 55. https://doi.org/10.1007/s11852-020-00775-3 (cit. on p. 42).

Cartwright, N., Nielsen, P., & Li, L. (2004). Experimental observations of watertable waves in an unconfined aquifer with a sloping boundary. *Advances in Water Resources*, *27*(10), 991–1004. https://doi.org/10.1016/j.advwatres.2004.08.006 (cit. on pp. 42, 60).

Casale, P., & Tucker, A. D. (2017, August). Caretta caretta (amended version of 2015 assessment). https:

//doi.org/10.2305/IUCN.UK.2017-2.RLTS.T3897A119333622.en (cit. on p. 172).

Casale, P., & Ceriani, S. A. (2019). Satellite surveys: a novel approach for assessing sea turtle nesting activity and distribution. *Marine Biology*, *166*(4), 47. https://doi.org/10.1007/s00227-019-3494-4 (cit. on p. 129).

Castelle, B., Bujan, S., Ferreira, S., & Dodet, G. (2017). Foredune morphological changes and beach recovery from the extreme 2013/2014 winter at a high-energy sandy coast. *Marine Geology*, *385*, 41–55. https://doi.org/10.1016/j.margeo.2016.12.006 (cit. on p. 2).

Castelle, B., Kras, E., Masselink, G., Scott, T., Konstantinou, A., & Luijendijk, A. (2024). Satellite-derived sandy shoreline trends and interannual variability along the Atlantic coast of Europe. *Scientific Reports*, *14*(1), 13002. https://doi.org/10.1038/s41598-024-63849-4 (cit. on p. 4).

Castelle, B., Marieu, V., Bujan, S., Splinter, K. D., Robinet, A., Sénéchal, N., & Ferreira, S. (2015). Impact of the winter 2013–2014 series of severe Western Europe storms on a double-barred sandy coast: Beach and dune erosion and megacusp embayments. *Geomorphology*, *238*, 135–148. https://doi.org/10.1016/j.geomorph.2015.03.006 (cit. on p. 72).

Castelle, B., Masselink, G., Scott, T., Stokes, C., Konstantinou, A., Marieu, V., & Bujan, S. (2021). Satellite-derived shoreline detection at a high-energy meso-macrotidal beach. *Geomorphology*, *383*, 107707. https://doi.org/10.1016/j.geomorph.2021.107707 (cit. on p. 76).

Castelle, B., Ritz, A., Marieu, V., Nicolae Lerma, A., & Vandenhove, M. (2022). Primary drivers of multidecadal spatial and temporal patterns of shoreline change derived from optical satellite imagery. *Geomorphology*, *413*, 108360. https://doi.org/10.1016/j.geomorph.2022.108360 (cit. on p. 76).

Caut, S., Guirlet, E., & Girondot, M. (2010). Effect of tidal overwash on the embryonic development of leatherback turtles in French Guiana. *Marine Environmental Research*, *69*(4), 254–261. https://doi.org/10.1016/j.marenvres.2009.11.004 (cit. on pp. 2, 42, 128).

Cayan, D. R., Bromirski, P. D., Hayhoe, K., Tyree, M., Dettinger, M. D., & Flick, R. E. (2008). Climate change projections of sea level extremes along the California coast. *Climatic Change*, *87*(S1), 57–73. https://doi.org/10.1007/s10584-007-9376-7 (cit. on p. 12).

Christiaanse, J. C., Vitousek, S., Reniers, A. J. H. M., & Antolínez, J. A. A. (2025a). Vulnerability of key sea turtle nesting beaches to future erosion and sea level rise (submitted for publication) (cit. on pp. 128, 129, 131).

Christiaanse, J. C., Antolínez, J. A. A., van der Grinten, M. J., Taal, F., Figlus, J., Dellapenna, T. M., Ritt, B., Marshall, C. D., Tereszkiewicz, P., Cohn, N., Majzlik, E. J., & Reniers, A. J. H. M. (2024a). TURTLE: Measurements of groundwater, hydrodynamics, sand temperature, and sediment characteristics at two beach transects on Galveston Island, Texas, USA. https://doi.org/10.4121/93256801-ed01-4627-9e49-8607967a0853 (cit. on p. 25).

Christiaanse, J. C., & Antolínez, J. A. A. (2023). Coastgons: regional coastal characteristics along a global hexagonal coastline grid. https://doi.org/10.4121/68377ee4-892d-40f0-a490-29f2601e6825 (cit. on pp. 101, 104, 106).

Christiaanse, J. C., Antolínez, J. A. A., van der Grinten, M. J., Taal, F., Figlus, J., Dellapenna, T. M., Ritt, B., Marshall, C. D., Tereszkiewicz, P. A., Cohn, N., Majzlik, E. J., & Reniers, A. J. H. M. (2025b). Measurements of groundwater, hydrodynamics, and sand characteristics at a dissipative sea turtle nesting beach. *Scientific Data*, *12*(1), 123. https://doi.org/10.1038/s41597-025-04455-5 (cit. on pp. 43–47, 63, 64, 67, 129, 165, 166).

Christiaanse, J. C., Antolínez, J. A. A., Luijendijk, A. P., Athanasiou, P., Duarte, C. M., & Aarninkhof, S. (2024b). Distribution of global sea turtle nesting explained from regional-scale coastal characteristics. *Scientific Reports*, *14*, 752. https://doi.org/10.1038/s41598-023-50239-5 (cit. on pp. 65, 72, 129).

Christiaanse, J. C., Antolínez, J. A., Marshall, C. D., Figlus, J., Dellapenna, T. M., & Reniers, A. J. (2025c). Beach groundwater response to ocean processes and rain on a mild-sloping barrier island: Implications for sea turtle nest flooding. *Coastal Engineering*, *201*, 104795. https://doi.org/10.1016/j.coastaleng.2025.104795 (cit. on pp. 126, 128, 130).

Christiaanse, J. C., Reniers, A. J. H. M., Aarninkhof, S. G. J., Ostertag, E. F., Nel, R., Duarte, C. M., & Antolínez, J. A. A. (2025d). Aiding sea turtle conservation through coastal management. *Frontiers in Marine Science*, *12*, 1669885. https://doi.org/10.3389/fmars.2025.1669885 (cit. on p. 72).

Christianen, M. J. A., Smulders, F. O. H., Vonk, J. A., Becking, L. E., Bouma, T. J., Engel, S. M., James, R. K., Nava, M. I., de Smit, J. C., van der Zee, J. P., Palsbøll, P. J., & Bakker, E. S. (2023). Seagrass ecosystem multifunctionality under the rise of a flagship marine megaherbivore. *Global Change Biology*, *29*(1), 215–230. https://doi.org/10.1111/gcb.16464 (cit. on pp. 1, 42, 72, 124, 132).

Cleveland, R. B., Cleveland, W. S., McRae, J. E., & Terpenning, I. (1990). STL: A Seasonal-Trend Decomposition Procedure Based on Loess. *Journal of Official Statistics*, *6*(1), 3–73 (cit. on p. 81).

Cleveland, W. S. (1979). Robust Locally Weighted Regression and Smoothing Scatterplots. *Journal of the American Statistical Association*, *74*(368), 829–836. https://doi.org/10.1080/01621459.1979.10481038 (cit. on p. 81).

CNES. (2024). FES2022 (Finite Element Solution) Ocean Tide (Version 2022) [Data set]. https://doi.org/10.24400/527896/A01-2024.004 (cit. on p. 76).

Coco, G., Senechal, N., Rejas, A., Bryan, K., Capo, S., Parisot, J., Brown, J., & MacMahan, J. (2014). Beach response to a sequence of extreme storms. *Geomorphology*, *204*, 493–501. https://doi.org/10.1016/j.geomorph.2013.08.028 (cit. on p. 2).

Cohen-Shacham, E., Walters, G., Janzen, C., & Maginnis, S. (Eds.). (2016). *Nature-based solutions to address global societal challenges*. IUCN. https://doi.org/10.2305/IUCN.CH.2016.13.en (cit. on p. 124).

Colomina, I., & Molina, P. (2014). Unmanned aerial systems for photogrammetry and remote sensing: A review. *ISPRS Journal of Photogrammetry and Remote Sensing*, *92*, 79–97. https://doi.org/10.1016/j.isprsjprs.2014.02.013 (cit. on p. 16).

Cooper, J. A. G., Masselink, G., Coco, G., Short, A. D., Castelle, B., Rogers, K., Anthony, E., Green, A. N., Kelley, J. T., Pilkey, O. H., & Jackson, D. W. T. (2020). Sandy beaches can survive sea-level rise. *Nature Climate Change*, *10*(11), 993–995. https://doi.org/10.1038/s41558-020-00934-2 (cit. on pp. 72, 131).

Copernicus Climate Change Service Climate Data Store. (2021). ORAS5 global ocean reanalysis monthly data from 1958 to present. https://doi.org/10.24381/cds.67e8eeb7 (cit. on pp. 102–104, 190).

Culver, M., Gibeaut, J. C., Shaver, D. J., Tissot, P., & Starek, M. (2020). Using Lidar Data to Assess the Relationship Between Beach Geomorphology and Kemp's Ridley (Lepidochelys kempii) Nest Site Selection Along Padre Island, TX, United States. *Frontiers in Marine Science*, *7*, 214. https://doi.org/10.3389/fmars.2020.00214 (cit. on pp. 51, 65, 100, 116, 124, 129, 130).

Davidson, M., Lewis, R., & Turner, I. (2010). Forecasting seasonal to multi-year shoreline change. *Coastal Engineering*, *57*(6), 620–629. https://doi.org/10.1016/j.coastaleng.2010.02.001 (cit. on p. 80).

Davis, A. B., Jr. (1951). HISTORY OF THE GALVESTON SEA WALL. *Coastal Engineering Proceedings*, *1*(2), 24. https://doi.org/10.9753/icce.v2.24 (cit. on p. 14).

Dédina, D., Christiaanse, J. C., Roelvink, F., Elshinnawy, A. I. A., Mccall, R., Reniers, A., Duarte, C., & Antolínez, J. A. A. (2025). RUNUP MODELING IN LOW-DATA CORAL REEF ENVIRONMENTS: IMPLICATIONS FOR NESTING SEA TURTLES. *Proceedings of the 10th International Coastal Dynamics Conference* (cit. on p. 130).

Defeo, O., McLachlan, A., Schoeman, D. S., Schlacher, T. A., Dugan, J., Jones, A., Lastra, M., & Scapini, F. (2009). Threats to sandy beach ecosystems: A review. *Estuarine, Coastal and Shelf Science*, *81*(1), 1–12. https://doi.org/10.1016/j.ecss.2008.09.022 (cit. on pp. 1, 72).

Delisle, M.-P. C., Kim, Y., & Gallien, T. W. (2023). A Numerical Study of Dam-Break Driven Swash and Beach Groundwater Interactions. *Journal of Geophysical Research: Oceans*, *128*(9). https://doi.org/10.1029/2022JC019615 (cit. on pp. 12, 42, 43).

Dewald, J. R., & Pike, D. A. (2014). Geographical variation in hurricane impacts among sea turtle populations. *Journal of Biogeography*, *41*(2), 307–316. https://doi.org/10.1111/jbi.12197 (cit. on pp. 2, 124).

DJI. (2023). *Phantom 4 RTK User Manual v2.6* (tech. rep.). https://enterprise.dji.com/phantom-4-rtk (cit. on p. 16).

Dong, Z., Elko, N., Robertson, Q., & Rosati, J. (2018). QUANTIFYING BEACH AND DUNE RESILIENCE USING THE COASTAL RESILIENCE INDEX. *Coastal Engineering Proceedings*, *1*(36), 30. https://doi.org/10.9753/icce.v36.papers.30 (cit. on pp. 93, 128, 142).

van Dongeren, A., Battjes, J., Janssen, T., van Noorloos, J., Steenhauer, K., Steenbergen, G., & Reniers, A. (2007). Shoaling and shoreline dissipation of low-frequency waves. *Journal of Geophysical Research: Oceans*, *112*(C2). https://doi.org/10.1029/2006JC003701 (cit. on pp. 53, 60).

Duarte, C. M., Agusti, S., Barbier, E., Britten, G. L., Castilla, J. C., Gattuso, J.-P., Fulweiler, R. W., Hughes, T. P., Knowlton, N., Lovelock, C. E., Lotze, H. K., Predragovic, M., Poloczanska, E., Roberts, C., & Worm, B. (2020). Rebuilding marine life. *Nature*, *580*(7801), 39–51. https://doi.org/10.1038/s41586-020-2146-7 (cit. on pp. 2, 72, 100, 133).

Duarte, C. M., Losada, I. J., Hendriks, I. E., Mazarrasa, I., & Marbà, N. (2013). The role of coastal plant communities for climate change mitigation and adaptation. *Nature Climate Change*, *3*(11), 961–968. https://doi.org/10.1038/nclimate1970 (cit. on p. 132).

Dullaart, J. C. M., Muis, S., Bloemendaal, N., Chertova, M. V., Couasnon, A., & Aerts, J. C. J. H. (2021). Accounting for tropical cyclones more than doubles the global population exposed to low-probability coastal flooding. *Communications Earth & Environment*, *2*(1), 135. https://doi.org/10.1038/s43247-021-00204-9 (cit. on p. 115).

Dunkin, L., Reif, M., Altman, S., & Swannack, T. (2016). A Spatially Explicit, Multi-Criteria Decision Support Model for Loggerhead Sea Turtle Nesting Habitat Suitability: A Remote Sensing-Based Approach. *Remote Sensing*, *8*(7), 573. https://doi.org/10.3390/rs8070573 (cit. on p. 100).

Duquesne, E., & Fournier, D. (2025). Climate change redefines sea turtle hotspots: Vessel strike risks and gaps in protected areas. *Science Advances*, *11*(26), 4495. https://doi.org/10.1126/sciadv.adw4495 (cit. on p. 143).

Duveiller, G., Fasbender, D., & Meroni, M. (2016). Revisiting the concept of a symmetric index of agree-

ment for continuous datasets. *Scientific Reports*, *6*, 19401. https://doi.org/10.1038/srep19401 (cit. on p. 80).

Eckert, K. L., & Eckert, A. E. (2019). *An Atlas of Sea Turtle Nesting Habitat for the Wider Caribbean Region. Revised Edition*. WIDECAST Technical Report No. 19. (Cit. on pp. 4, 102–104).

Elko, N., Briggs, T. R., Benedet, L., Robertson, Q., Thomson, G., Webb, B. M., & Garvey, K. (2021). A century of U.S. beach nourishment. *Ocean & Coastal Management*, *199*. https://doi.org/10.1016/j.ocecoaman.2020.105406 (cit. on p. 14).

Erikson, L. H., O'Neill, A. C., Barnard, P. L., Vitousek, S., & Limber, P. W. (2017). Climate change-driven cliff and beach evolution at decadal to centennial time scales. In T. Aagaard, R. Deigaard, & D. Fuhrman (Eds.), *Proceedings of coastal dynamics 2017* (pp. 125–136). (Cit. on p. 90).

ESRI. (2024). World Imagery Basemap. https://services.arcgisonline.com/ArcGIS/rest/services/World_Imagery/MapServer (cit. on pp. 13, 74).

Feagin, R. A., Sherman, D. J., & Grant, W. E. (2005). Coastal erosion, global sea-level rise, and the loss of sand dune plant habitats. *Frontiers in Ecology and the Environment*, *3*(7), 359–365. https://doi.org/10.1890/1540-9295(2005)003[0359:CEGSRA]2.0.CO;2 (cit. on p. 14).

Fish, M. R., Côte, I. M., Gill, J. A., Jones, A. P., Renshoff, S., & Watkinson, A. R. (2005). Predicting the Impact of Sea-Level Rise on Caribbean Sea Turtle Nesting Habitat. *Conservation Biology*, *19*(2), 482–491. https://doi.org/10.1111/j.1523-1739.2005.00146.x (cit. on pp. 4, 5, 73, 93, 100, 131).

Fish, M. R., Côté, I. M., Horrocks, J. A., Mulligan, B., Watkinson, A. R., & Jones, A. P. (2008). Construction setback regulations and sea-level rise: Mitigating sea turtle nesting beach loss. *Ocean & Coastal Management*, *51*(4), 330–341. https://doi.org/10.1016/j.ocecoaman.2007.09.002 (cit. on p. 131).

Foley, A. M., Peck, S. A., & Harman, G. R. (2006). Effects of Sand Characteristics and Inundation on the Hatching Success of Loggerhead Sea Turtle (Caretta caretta) Clutches on Low-Relief Mangrove Islands in Southwest Florida. *Chelonian Research Foundation and Turtle Conservancy*, *5*(1), 32–41. https://doi.org/10.2744/1071-8443(2006)5[32:EOSCAI]2.0.CO;2 (cit. on pp. 2, 42, 65, 100, 124, 128, 129).

Fossette, S., Kelle, L., Girondot, M., Goverse, E., Hilterman, M. L., Verhage, B., de Thoisy, B., & Georges, J.-Y. (2008). The world's largest leatherback rookeries: A review of conservation-oriented research in French Guiana/Suriname and Gabon. *Journal of Experimental Marine Biology and Ecology*, *356*(1-2), 69–82. https://doi.org/10.1016/j.jembe.2007.12.024 (cit. on p. 93).

Fox-Kemper, B., Hewitt, H. T., Xiao, C., Adalgeirsdóttir, G., Drijfhout, S. S., Edwards, T. L., Golledge, N. R., Hemer, M., Kopp, R. E., Krinner, G., Mix, A., Notz, D., Nowicki, S., Nurhati, I. S., Ruiz, L., Sallée, J. B., Slangen, A. B. A., & Yu, Y. (2023, July). Ocean, Cryosphere and Sea Level Change. In V. Masson-Delmotte, P. Zhai, A. Pirani, S. L. Connors, C. Péan, S. Berger, N. Caud, Y. Chen, L. Goldfarb, M. I. Gomis, M. Huang, K. Leitzell, E. Lonnoy, J. B. R. Matthews, T. K. Maycock, T. Waterfield, O. Yelekçi, R. Yu, & B. Zhou (Eds.), *Climate change 2021 – the physical science basis* (pp. 1211–1362). Cambridge University Press. https://doi.org/10.1017/9781009157896.011 (cit. on pp. 80, 124).

French, J., Payo, A., Murray, B., Orford, J., Eliot, M., & Cowell, P. (2016). Appropriate complexity for the prediction of coastal and estuarine geomorphic behaviour at decadal to centennial scales. *Geomorphology*, *256*, 3–16. https://doi.org/10.1016/j.geomorph.2015.10.005 (cit. on p. 93).

Fuentes, M. M. P. B., Limpus, C. J., Hamann, M., & Dawson, J. (2010). Potential impacts of projected sea-level rise on sea turtle rookeries. *Aquatic Conservation: Marine and Freshwater Ecosystems*, *20*(2), 132–139. https://doi.org/10.1002/aqc.1088 (cit. on pp. 4, 5, 73, 93, 100, 131).

Fuentes, M. M. P. B., Santos, A. J. B., Abreu-Grobois, A., Briseño-Dueñas, R., Al-Khayat, J., Hamza, S., Saliba, S., Anderson, D., Rusenko, K. W., Mitchell, N. J., Gammon, M., Bentley, B. P., Beton, D., Booth, D. T. B., Broderick, A. C., Colman, L. P., Snape, R. T. E., Calderon-Campuzano, M. F., Cuevas, E., … Monsinjon, J. R. (2024). Adaptation of sea turtles to climate warming: Will phenological responses be sufficient to counteract changes in reproductive output? *Global Change Biology*, *30*(1). https://doi.org/10.1111/gcb.16991 (cit. on p. 5).

Fuentes, M. M. P. B., Bateman, B. L., & Hamann, M. (2011). Relationship between tropical cyclones and the distribution of sea turtle nesting grounds. *Journal of Biogeography*, *38*(10), 1886–1896. https://doi.org/10.1111/j.1365-2699.2011.02541.x (cit. on p. 2).

Fuentes, M. M. P. B., Godfrey, M. H., Shaver, D., Ceriani, S., Gredzens, C., Boettcher, R., Ingram, D., Ware, M., & Wildermann, N. (2019). Exposure of Marine Turtle Nesting Grounds to Named Storms Along the Continental USA. *Remote Sensing*, *11*(24), 2996. https://doi.org/10.3390/rs11242996 (cit. on pp. 2, 100, 115, 126).

Fuentes, M., McMichael, E., Kot, C., Silver-Gorges, I., Wallace, B., Godley, B., Brooks, A., Ceriani, S., Cortés-Gómez, A., Dawson, T., Dodge, K., Flint, M., Jensen, M., Komoroske, L., Kophamel, S., Lettrich, M., Long, C., Nelms, S., Patrício, A., … Hays, G. (2023). Key issues in assessing threats to sea turtles: knowledge gaps and future directions. *Endangered Species Research*, *52*, 303–341. https://doi.org/10.3354/esr01278 (cit. on p. 124).

Gacia, E., Granata, T. C., & Duarte, C. M. (1999). An approach to measurement of particle flux and sediment retention within seagrass (Posidonia oceanica) meadows. *Aquatic Botany*, *65*(1-4), 255–268. https://doi.org/10.1016/S0304-3770(99)00044-3 (cit. on p. 132).

Gammon, M., Whiting, S., & Fossette, S. (2023). Vulnerability of sea turtle nesting sites to erosion and inundation: A decision support framework to maximize conservation. *Ecosphere*, *14*(6), e4529. https://doi.org/10.1002/ecs2.4529 (cit. on pp. 2, 42, 124, 130).

Gaos, A. R., Lewison, R. L., Liles, M. J., Gadea, V., Altamirano, E., Henríquez, A. V., Torres, P., Urteaga, J., Vallejo, F., Baquero, A., LeMarie, C., Muñoz, J. P., Chaves, J. A., Hart, C. E., Peña de Niz, A., Chácon, D., Fonseca, L., Otterstrom, S., Yañez, I. L., … Dutton, P. H. (2016). Hawksbill turtle terra incognita: conservation genetics of eastern Pacific rookeries. *Ecology and Evolution*, *6*(4), 1251–1264. https://doi.org/10.1002/ece3.1897 (cit. on p. 132).

Garcia, D. (2010). Robust smoothing of gridded data in one and higher dimensions with missing values. *Computational Statistics & Data Analysis*, *54*(4), 1167–1178. https://doi.org/10.1016/j.csda.2009.09.020 (cit. on p. 80).

Garner, G. G., Hermans, T., Kopp, R. E., Slangen, A. B. A., Edwards, T. L., Levermann, A., Nowikci, S., Palmer, M. D., Smith, C., Fox-Kemper, B., Hewitt, H. T., Xiao, C., Adalgeirsdóttir, G., Drijfhout, S. S., Golledge, N. R., Hemer, M., Krinner, G., Mix, A., Notz, D., … Pearson, B. (2021). [Dataset] IPCC AR6 Sea Level Projections. Version 20210809. https://doi.org/10.5281/zenodo.5914709 (cit. on pp. 80, 129).

Garner, L. E. (1997). *Geologic History, Depositional Environment, Processes, and Hydrology of Galveston Island, Texas* (tech. rep.). Bureau of Economic Geology, University of Texas at Austin. https://doi.org/https://doi.org/10.26153/tsw/51702 (cit. on p. 44).

Gedan, K. B., Kirwan, M. L., Wolanski, E., Barbier, E. B., & Silliman, B. R. (2011). The present and future role of coastal wetland vegetation in protecting shorelines: answering recent challenges to the paradigm. *Climatic Change*, *106*(1), 7–29. https://doi.org/10.1007/s10584-010-0003-7 (cit. on p. 132).

van de Geer, C. H., Bourjea, J., Broderick, A., Dalleau, M., Fernandes, R., Harris, L., Inteca, G., Kiponda, F., Louro, C., Mortimer, J., Msangameno, D., Mwasi, L., Nel, R., Okemwa, G., Olendo, M., Pereira, M., Rees, A., Silva, I., Singh, S., … Godley, B. (2022). Marine turtles of the African east coast: current knowledge and priorities for conservation and research. *Endangered Species Research*, *47*, 297–331. https://doi.org/10.3354/esr01180 (cit. on p. 118).

Geotek. (2021). *Multi-Sensor Core Logger – Standard Manual* (tech. rep.). (Cit. on pp. 22, 28).

Gillham, R. (1984). The capillary fringe and its effect on water-table response. *Journal of Hydrology*, *67*(1-4), 307–324. https://doi.org/10.1016/0022-1694(84)90248-8 (cit. on p. 43).

Godley, B. J., Broderick, A. C., & Hays, G. C. (2001). Nesting of green turtles (Chelonia mydas) at Ascension Island, South Atlantic. *Biological Conservation*, *97*(2), 151–158. https://doi.org/10.1016/S0006-3207(00)00107-5 (cit. on p. 74).

Gomes da Silva, P., Coco, G., Garnier, R., & Klein, A. H. (2020). On the prediction of runup, setup and swash on beaches. *Earth-Science Reviews*, *204*, 103148. https://doi.org/10.1016/j.earscirev.2020.103148 (cit. on p. 2).

Gomez-de la Peña, E., Coco, G., Whittaker, C., & Montaño, J. (2023). On the use of convolutional deep learning to predict shoreline change. *Earth Surface Dynamics*, *11*(6), 1145–1160. https://doi.org/10.5194/esurf-11-1145-2023 (cit. on pp. 80, 91, 130).

GoPro Inc. (2021). *HERO10 Black Product Manual* (tech. rep.). (Cit. on p. 20).

Gourlay, M. (1992). Wave set-up, wave run-up and beach water table: Interaction between surf zone hydraulics and groundwater hydraulics. *Coastal Engineering*, *17*(1-2), 93–144. https://doi.org/10.1016/0378-3839(92)90015-M (cit. on pp. 12, 43).

Grain, D. A., Bolten, A. B., & Bjorndal, K. A. (1995). Effects of Beach Nourishment on Sea Turtles: Review and Research Initiatives. *Restoration Ecology*, *3*(2), 95–104. https://doi.org/10.1111/j.1526-100X.1995.tb00082.x (cit. on pp. 64, 66, 132).

van der Grinten, M. J., Christiaanse, J. C., Reniers, A. J., Taal, F., Figlus, J., & Antolínez, J. A. (2025). Wave runup extraction on dissipative beaches: New video-based methods. *Coastal Engineering*, *200*, 104757. https://doi.org/10.1016/j.coastaleng.2025.104757 (cit. on pp. 47, 167).

Guard, P., McPherson, K., & Mohoupt, J. (2008, February). *A Field Investigation into the Groundwater Dynamics of Raine Island* (tech. rep.). The University of Queensland. https://doi.org/10.14264/131499 (cit. on pp. 42, 128, 139).

Guisan, A., & Thuiller, W. (2005). Predicting species distribution: offering more than simple habitat models. *Ecology Letters*, *8*(9), 993–1009. https://doi.org/10.1111/j.1461-0248.2005.00792.x (cit. on p. 117).

Haberer, C. M., Cirpka, O. A., Rolle, M., & Grathwohl, P. (2014). Experimental Sensitivity Analysis of Oxygen Transfer in the Capillary Fringe. *Groundwater*, *52*(1), 37–49. https://doi.org/10.1111/gwat.12028 (cit. on p. 63).

Halpin, P. N., Read, A. J., Fujioka, E., Best, B. D., Donnelly, B., Hazen, L. J., Kot, C., Urian, K., Labrecque, E., Dimatteo, A., Cleary, J., Good, C., Crowder, L. B., & Hyrenbach, K. D. (2009). OBIS-SEAMAP: The world data center for marine mammal, sea bird, and sea turtle distributions. *Oceanography*, *22*(SPL.ISS.

2), 104–115. https://doi.org/10.5670/OCEANOG.2009.42 (cit. on pp. 4, 102–104).

Hammond, G. E., Lichtner, P. C., & Mills, R. T. (2014). Evaluating the performance of parallel subsurface simulators: An illustrative example with PFLOTRAN. *Water Resources Research*, *50*(1), 208–228. https://doi.org/10.1002/2012WR013483 (cit. on p. 130).

Hannides, A., Elko, N., & Humiston, K. (2019). The state of understanding of the effects of beach nourishment activities on coastal biogeochemical processes and conditions. *Shore & Beach*, 46–57. https://doi.org/10.34237/1008734 (cit. on pp. 64, 66).

Hardy, R. F., Hu, C., Witherington, B., Lapointe, B., Meylan, A., Peebles, E., Meirose, L., & Hirama, S. (2018). Characterizing a Sea Turtle Developmental Habitat Using Landsat Observations of Surface-Pelagic Drift Communities in the Eastern Gulf of Mexico. *IEEE Journal of Selected Topics in Applied Earth Observations and Remote Sensing*, *11*(10), 3646–3659. https://doi.org/10.1109/JSTARS.2018.2863194 (cit. on p. 129).

Harley, M. D., Turner, I. L., & Short, A. D. (2015). New insights into embayed beach rotation: The importance of wave exposure and cross-shore processes. *Journal of Geophysical Research: Earth Surface*, *120*(8), 1470–1484. https://doi.org/10.1002/2014JF003390 (cit. on p. 72).

Harley, M. D., & Kinsela, M. A. (2022). CoastSnap: A global citizen science program to monitor changing coastlines. *Continental Shelf Research*, *245*, 104796. https://doi.org/10.1016/j.csr.2022.104796 (cit. on p. 129).

Hawkes, L., Broderick, A., Godfrey, M., & Godley, B. (2009). Climate change and marine turtles. *Endangered Species Research*, *7*(2), 137–154. https://doi.org/10.3354/esr00198 (cit. on pp. 1, 72, 100).

Hays, G. C., Laloë, J.-O., & Seminoff, J. A. (2025). Status, trends and conservation of global sea turtle populations. *Nature Reviews Biodiversity*, *1*(2), 119–133. https://doi.org/10.1038/s44358-024-00011-y (cit. on p. 124).

Hegge, B. J., & Masselink, G. (1991). Groundwater-Table Responses to Wave Run-up: An Experimental Study from Western Australia. *Journal of Coastal Research*, *7*(3), 623–634. https://www.jstor.org/stable/4297881 (cit. on p. 60).

Heijl, M. E. (2025). *Characterizing sediments of sea turtle nesting beaches (MSc Thesis)* (tech. rep.). Delft University of Technology. https://resolver.tudelft.nl/uuid:b9d7dafa-f03a-4be2-973c-124c74db4ca5 (cit. on p. 143).

Heithaus, M. R. (2013). Chapter 10: Predators, Prey, and the Ecological Roles of Sea Turtles. In *The biology of sea turtles* (pp. 249–273, Vol. 3). CRC Press. (Cit. on pp. 1, 124).

Henderson, S. M., & Bowen, A. J. (2002). Observations of surf beat forcing and dissipation. *Journal of Geophysical Research: Oceans*, *107*(C11). https://doi.org/10.1029/2000JC000498 (cit. on pp. 53, 60).

Hersbach, H., Bell, B., Berrisford, P., Biavati, G., Horányi, A., Muñoz Sabater, J., Nicolas, J., Peuby, C., Radu, R., Rozum, I., Schepers, D., Simmons, A., Soci, C., Dee, D., & Thépaut, J.-N. (2018). ERA5 hourly data on single levels from 1979 to present. https://doi.org/10.24381/cds.adbb2d47 (cit. on pp. 79, 102–104, 129, 189).

Hilton, M., Walsh, J. C., Maloney, R. F., Hansen, N. A., & Cook, C. N. (2023). The value of capturing diverse perspectives when setting decision triggers for threatened species management. *Journal of Applied Ecology*, *60*(10), 2267–2281. https://doi.org/10.1111/1365-2664.14477 (cit. on p. 127).

Hirsch, S. E., Toonder, M., Reilly, J. D., Hoover, S. R., & Perrault, J. R. (2022). Responses of three nesting sea turtle species to hard-armoring structures. *Frontiers in Marine Science*, *9*, 980715. https://doi.org/10.3389/fmars.2022.980715 (cit. on p. 124).

HOBO Data Loggers. (2022). *HOBO® TidbiT® MX Temp 400 (MX2203) and Temp 5000 (MX2204) Logger Manual* (tech. rep.). HOBO Data Loggers. (Cit. on p. 19).

HOBO Data Loggers. (2024). *HOBO® U20L Water Level Logger (U20L-0x) Manual* (tech. rep.). https://www.onsetcomp.com/products/data-loggers/u20l-0x#documents (cit. on p. 17).

Hochscheid, S., Maffucci, F., Abella, E., Bradai, M. N., Camedda, A., Carreras, C., Claro, F., de Lucia, G. A., Jribi, I., Mancusi, C., Marco, A., Marrone, N., Papetti, L., Revuelta, O., Urso, S., & Tomás, J. (2022). Nesting range expansion of loggerhead turtles in the Mediterranean: Phenology, spatial distribution, and conservation implications. *Global Ecology and Conservation*, *38*, e02194. https://doi.org/10.1016/j.gecco.2022.e02194 (cit. on pp. 5, 114).

Hofland, B., Chen, X., Altomare, C., & Oosterlo, P. (2017). Prediction formula for the spectral wave period T m-1,0 on mildly sloping shallow foreshores. *Coastal Engineering*, *123*, 21–28. https://doi.org/10.1016/j.coastaleng.2017.02.005 (cit. on p. 48).

Holding, S., Allen, D. M., Foster, S., Hsieh, A., Larocque, I., Klassen, J., & Van Pelt, S. C. (2016). Groundwater vulnerability on small islands. *Nature Climate Change*, *6*(12), 1100–1103. https://doi.org/10.1038/nclimate3128 (cit. on pp. 42, 43).

Holthuijsen, L. H. (2007, January). *Waves in Oceanic and Coastal Waters*. Cambridge University Press. https://doi.org/10.1017/CBO9780511618536 (cit. on pp. 47, 48, 92, 166).

Horn, D. P. (2006). Measurements and modelling of beach groundwater flow in the swash-zone: a review. *Continental Shelf Research*, *26*(5), 622–652. https:

//doi.org/10.1016/j.csr.2006.02.001 (cit. on pp. 12, 43).

Horrocks, J. A., & Scott, N. M. (1991). Nest site location and nest success in the hawksbill turtle Eretmochelys imbricata in Barbados, West Indies. *Marine Ecology Progress Series*, *69*, 1–8. https://www.jstor.org/stable/44634759 (cit. on pp. 65, 100).

Housego, R., Raubenheimer, B., Elgar, S., Cross, S., Legner, C., & Ryan, D. (2021). Coastal flooding generated by ocean wave- and surge-driven groundwater fluctuations on a sandy barrier island. *Journal of Hydrology*, *603*, 126920. https://doi.org/10.1016/j.jhydrol.2021.126920 (cit. on pp. 12, 42–44, 60).

Huff, T., Feagin, R., & Figlus, J. (2020). Enhanced tide model: Improving tidal predictions with integration of wind data. *Shore & Beach*, *88*(2), 40–45. https://doi.org/10.34237/1008824 (cit. on pp. 14, 44).

Hulskamp, R., Luijendijk, A., van Maren, B., Moreno-Rodenas, A., Calkoen, F., Kras, E., Lhermitte, S., & Aarninkhof, S. (2023). Global distribution and dynamics of muddy coasts. *Nature Communications*, *14*(1), 8259. https://doi.org/10.1038/s41467-023-43819-6 (cit. on p. 1).

Humber, F., Godley, B. J., & Broderick, A. C. (2014). So excellent a fishe: a global overview of legal marine turtle fisheries (O. Defeo, Ed.). *Diversity and Distributions*, *20*(5), 579–590. https://doi.org/10.1111/ddi.12183 (cit. on p. 1).

Hunt, E., Davidson, M., Steele, E. C. C., Amies, J. D., Scott, T., & Russell, P. (2023). Shoreline modelling on timescales of days to decades. *Cambridge Prisms: Coastal Futures*, *1*, e16. https://doi.org/10.1017/CFT.2023.5 (cit. on p. 91).

Iribarren, C. R., & Nogales, C. (1949). Protection des ports. *Proceedings XVIIth International Navigation Congress, Section II, Communication, vol. 4*, 31–80 (cit. on p. 47).

IUCN. (2020). *Global Standard for Nature-based Solutions. A user-friendly framework for the verification, design and scaling up of NbS.* (1st ed.). https://doi.org/10.2305/IUCN.CH.2020.08.en (cit. on pp. 126, 133).

IUCN. (2022). The IUCN Red List of Threatened Species. Version 2022-2. https://www.iucnredlist.org (cit. on p. 1).

James, R. K., Silva, R., van Tussenbroek, B. I., Escudero-Castillo, M., Mariño-Tapia, I., Dijkstra, H. A., van Westen, R. M., Pietrzak, J. D., Candy, A. S., Katsman, C. A., van der Boog, C. G., Riva, R. E. M., Slobbe, C., Klees, R., Stapel, J., van der Heide, T., van Katwijk, M. M., Herman, P. M. J., & Bouma, T. J. (2019). Maintaining Tropical Beaches with Seagrass and Algae: A Promising Alternative to Engineering Solutions. *BioScience*, *69*(2), 136–142. https://doi.org/10.1093/biosci/biy154 (cit. on p. 132).

Jeyaseelan, A., & Balaji, R. (2015). Spectral analysis of wave elevation time histories using multi-taper method. *Ocean Engineering*, *105*, 242–246. https://doi.org/10.1016/j.oceaneng.2015.06.051 (cit. on p. 48).

Jost, D., Winter, J., & Gallert, C. (2011). Water and Oxygen Dependence of Pseudomonas putida Growing in Silica Sand Capillary Fringes. *Vadose Zone Journal*, *10*(2), 532–540. https://doi.org/10.2136/vzj2010.0092 (cit. on p. 63).

Katselidis, K. A., Schofield, G., Stamou, G., Dimopoulos, P., & Pantis, J. D. (2014). Employing sea-level rise scenarios to strategically select sea turtle nesting habitat important for long-term management at a temperate breeding area. *Journal of Experimental Marine Biology and Ecology*, *450*, 47–54. https://doi.org/10.1016/j.jembe.2013.10.017 (cit. on pp. 4, 100, 131).

Kikukawa, A., Kamezaki, N., & Ota, H. (1999). Factors affecting nesting beach selection by loggerhead turtles (Caretta caretta): a multiple regression approach. *Journal of Zoology*, *249*(4), 447–454. https://doi.org/10.1111/j.1469-7998.1999.tb01214.x (cit. on pp. 65, 100).

Kinsela, M. A., Morris, B. D., Ingleton, T. C., Doyle, T. B., Sutherland, M. D., Doszpot, N. E., Miller, J. J., Holtznagel, S. F., Harley, M. D., & Hanslow, D. J. (2024). Nearshore wave buoy data from southeastern Australia for coastal research and management. *Scientific Data*, *11*(1), 190. https://doi.org/10.1038/s41597-023-02865-x (cit. on p. 34).

Knutson, T. R., Chung, M. V., Vecchi, G., Sun, J., Hsieh, T.-L., & Smith, A. J. P. (2021). ScienceBrief Review: Climate change is probably increasing the intensity of tropical cyclones. In C. Le Quéré, P. Liss, & P. Forster (Eds.), *Critical issues in climate change science*. https://doi.org/10.5281/zenodo.4570334 (cit. on p. 4).

Kohonen, T. (2001). *Self-Organizing Maps* (3rd ed., Vol. 30). Springer Berlin Heidelberg. https://doi.org/10.1007/978-3-642-56927-2 (cit. on p. 108).

Kopp, R. E., Garner, G. G., Hermans, T. H. J., Jha, S., Kumar, P., Reedy, A., Slangen, A. B. A., Turilli, M., Edwards, T. L., Gregory, J. M., Koubbe, G., Levermann, A., Merzky, A., Nowicki, S., Palmer, M. D., & Smith, C. (2023). The Framework for Assessing Changes To Sea-level (FACTS) v1.0: a platform for characterizing parametric and structural uncertainty in future global, relative, and extreme sea-level change. *Geoscientific Model Development*, *16*(24), 7461–7489. https://doi.org/10.5194/gmd-16-7461-2023 (cit. on p. 80).

Kot, C. Y., Fujioka, E., DiMatteo, A. D., Wallace, B. P., Hutchinson, B. J., Cleary, J., Halpin, P. N., & Mast, R. B. (2021). The State of the World's Sea Turtles Online Database: Data provided by the SWOT Team and hosted on OBIS-SEAMAP. http://seamap.env.duke.edu/swot (cit. on pp. 4, 102–104, 112, 118).

Kreitler, C. W., Guevera, E., Granata, G., & Mckalips, D. (1977). Hydrogeology of Gulf Coast aquifers, Houston-Galveston, Texas. *Gulf Coast Association of Geological Societies, Transactions*, *27*, 72–89 (cit. on p. 44).

Kroon, A., Christiaanse, J. C., Luijendijk, A. P., Schipper, M. A. d., & Ranasinghe, R. (2025). Parameter uncertainty in medium-term coastal morphodynamic modeling. *Scientific Reports*, *15*, 18471. https://doi.org/10.1038/s41598-025-02300-8 (cit. on pp. 93, 131).

Kroon, A., De Schipper, M., Van Gelder, P., & Aarninkhof, S. (2019, May). Quantification of Model Uncertainty in Lifetime Predictions of Nourishments. In P. Wang, J. D. Rosati, & M. Vallee (Eds.), *Coastal sediments 2019* (pp. 338–346). World Scientific. https://doi.org/10.1142/9789811204487_0032 (cit. on p. 131).

Laloë, J.-O., & Hays, G. C. (2023). Can a present-day thermal niche be preserved in a warming climate by a shift in phenology? A case study with sea turtles. *Royal Society Open Science*, *10*(2). https://doi.org/10.1098/rsos.221002 (cit. on pp. 5, 104, 119, 141).

Lansu, E. M., Reijers, V. C., Höfer, S., Luijendijk, A., Rietkerk, M., Wassen, M. J., Lammerts, E. J., & van der Heide, T. (2024). A global analysis of how human infrastructure squeezes sandy coasts. *Nature Communications*, *15*(1), 432. https://doi.org/10.1038/s41467-023-44659-0 (cit. on pp. 77, 89, 128).

Lasala, J. A., Macksey, M. C., Mazzarella, K. T., Main, K. L., Foote, J. J., & Tucker, A. D. (2023). Forty years of monitoring increasing sea turtle relative abundance in the Gulf of Mexico. *Scientific Reports*, *13*(1), 17213. https://doi.org/10.1038/s41598-023-43651-4 (cit. on p. 129).

Le Cozannet, G., Bulteau, T., Castelle, B., Ranasinghe, R., Wöppelmann, G., Rohmer, J., Bernon, N., Idier, D., Louisor, J., & Salas-y-Mélia, D. (2019). Quantifying uncertainties of sandy shoreline change projections as sea level rises. *Scientific Reports*, *9*, 42. https://doi.org/10.1038/s41598-018-37017-4 (cit. on pp. 92, 131).

Leaman, C. K., Harley, M. D., Splinter, K. D., Thran, M. C., Kinsela, M. A., & Turner, I. L. (2021). A storm hazard matrix combining coastal flooding and beach erosion. *Coastal Engineering*, *170*, 104001. https://doi.org/10.1016/j.coastaleng.2021.104001 (cit. on pp. 1, 72).

Leica Geosystems AG. (2016a). *Leica Viva CS10 & CS15 Data sheet* (tech. rep.). https://leica-geosystems.com/-/media/files/leicageosystems/products/datasheets/leica_viva_controller_cs10_cs15_ds.pdf?sc_lang=en&hash=58BBD766248EBAACC7535BF516C58AAA (cit. on p. 16).

Leica Geosystems AG. (2016b). *Leica Viva GS08plus Data sheet* (tech. rep.). https://leica-geosystems.com/-/media/files/leicageosystems/products/datasheets/leica_viva_gs08plus_ds.ashx?la=es-es (cit. on p. 16).

Lesser, G. R., Roelvink, J. A., van Kester, J. A., & Stelling, G. S. (2004). Development and validation of a three-dimensional morphological model. *Coastal Engineering*, *51*(8-9), 883–915. https://doi.org/10.1016/j.coastaleng.2004.07.014 (cit. on p. 130).

Leys, C., Ley, C., Klein, O., Bernard, P., & Licata, L. (2013). Detecting outliers: Do not use standard deviation around the mean, use absolute deviation around the median. *Journal of Experimental Social Psychology*, *49*(4), 764–766. https://doi.org/10.1016/j.jesp.2013.03.013 (cit. on p. 116).

Li, J., Knapp, D. E., Fabina, N. S., Kennedy, E. V., Larsen, K., Lyons, M. B., Murray, N. J., Phinn, S. R., Roelfsema, C. M., & Asner, G. P. (2020). A global coral reef probability map generated using convolutional neural networks. *Coral Reefs*, *39*(6), 1805–1815. https://doi.org/10.1007/s00338-020-02005-6 (cit. on pp. 102, 104, 190).

Li, L., Cartwright, N., Nielsen, P., & Lockington, D. (2004). Response of coastal groundwater table to offshore storms. *China Ocean Engineering*, *18*(3), 423–431 (cit. on pp. 42, 60).

Limpus, C. J., Miller, J. D., John, C., & Limpus, D. J. (2003). The green turtle, Chelonia mydas, population of Raine Island and the northern Great Barrier Reef: 1843-2001. *Memoirs of the Queensland Museum*, *49*(1), 349–440. https://georgehbalazs.com/wp-content/uploads/2020/03/Cm_RaineIs_2003QMmemoirs.pdf (cit. on p. 117).

Limpus, C. J., Miller, J. D., & Pfaller, J. B. (2021). Flooding-induced mortality of loggerhead sea turtle eggs. *Wildlife Research*, *48*(2), 142. https://doi.org/10.1071/WR20080 (cit. on pp. 2, 42, 62, 63, 65, 66, 126, 128, 131, 139, 142).

Lindenmayer, D. B., Piggott, M. P., & Wintle, B. A. (2013). Counting the books while the library burns: why conservation monitoring programs need a plan for action. *Frontiers in Ecology and the Environment*, *11*(10), 549–555. https://doi.org/10.1890/120220 (cit. on p. 126).

Long, T. M., Angelo, J., & Weishampel, J. F. (2011). LiDAR-derived measures of hurricane- and restoration-generated beach morphodynamics in relation to sea turtle nesting behaviour. *International Journal of Remote Sensing*, *32*(1), 231–241. https://doi.org/10.1080/01431160903439973 (cit. on pp. 2, 100, 126).

Lowe, R. J., Falter, J. L., Bandet, M. D., Pawlak, G., Atkinson, M. J., Monismith, S. G., & Koseff, J. R. (2005). Spectral wave dissipation over a barrier reef. *Journal of Geophysical Research: Oceans*, *110*(C4), 1–16. https://doi.org/10.1029/2004JC002711 (cit. on p. 132).

Luijendijk, A., Hagenaars, G., Ranasinghe, R., Baart, F., Donchyts, G., & Aarninkhof, S. (2018). The State of the World's Beaches. *Scientific Reports*, *8*(1), 6641. https://doi.org/10.1038/s41598-018-24630-6 (cit. on pp. 1, 72, 116, 117, 129).

Lyons, M. P., von Holle, B., & Weishampel, J. F. (2022). Why do sea turtle nests fail? Modeling clutch loss across the southeastern United States. *Ecosphere*, *13*(3), e3988. https://doi.org/10.1002/ecs2.3988 (cit. on p. 42).

Maglio, C., Das, H., & Fenner, F. (2020). MODAL GRAIN SIZE EVOLUTION AS IT RELATES TO THE DREDGING AND PLACEMENT PROCESS - GALVESTON ISLAND, TEXAS. *Coastal Engineering Proceedings*, (36v), 7. https://doi.org/10.9753/icce.v36v.papers.7 (cit. on pp. 14, 35, 44).

Malvern Instruments Ltd. (2007). *Mastersizer 2000 User Manual* (tech. rep.). (Cit. on p. 22).

Mancino, C., Hochscheid, S., & Maiorano, L. (2023). Increase of nesting habitat suitability for green turtles in a warming Mediterranean Sea. *Scientific Reports*, *13*(1), 19906. https://doi.org/10.1038/s41598-023-46958-4 (cit. on p. 5).

Maneja, R. H., Miller, J. D., Li, W., Thomas, R., El-Askary, H., Perera, S., Flandez, A. V. B., Basali, A. U., Alcaria, J. F. A., Gopalan, J., Tiwari, S., Al-Jedani, M., Prihartato, P. K., Loughland, R. A., Qasem, A., Qurban, M. A., Falath, W., & Struppa, D. (2021). Multidecadal analysis of beach loss at the major offshore sea turtle nesting islands in the northern Arabian Gulf. *Ecological Indicators*, *121*, 107146. https://doi.org/10.1016/j.ecolind.2020.107146 (cit. on p. 129).

Mao, Y., Coco, G., Vitousek, S., Antolinez, J. A. A., Azorakos, G., Banno, M., Bouvier, C., Bryan, K. R., Cagigal, L., Calcraft, K., Castelle, B., Chen, X., D'Anna, M., de Freitas Pereira, L., de Santiago, I., Deshmukh, A. N., Dong, B., Elghandour, A., Gohari, A., … Splinter, K. D. (2025). Benchmarking shoreline prediction models over multi-decadal timescales. *Communications Earth & Environment*, *6*(1), 581. https://doi.org/10.1038/s43247-025-02550-4 (cit. on pp. 78, 140).

Marco, A., Abella, E., Liria-Loza, A., Martins, S., López, O., Jiménez-Bordón, S., Medina, M., Oujo, C., Gaona, P., Godley, B. J., & López-Jurado, L. F. (2012). Abundance and exploitation of loggerhead turtles nesting in Boa vista island, Cape Verde: the only substantial rookery in the eastern Atlantic (T. Garner & R. Williams, Eds.). *Animal Conservation*, *15*(4), 351–360. https://doi.org/10.1111/j.1469-1795.2012.00547.x (cit. on p. 172).

Marcovaldi, M. A., Lopez, G. G., Soares, L. S., Santos, A. J., Bellini, C., & Barata, P. C. (2007). Fifteen years of Hawksbill Sea Turtle (Eretmochelys imbricata) nesting in Northern Brazil. *Chelonian Conservation and Biology*, *6*(2), 223–228. https://doi.org/10.2744/1071-8443(2007)6[223:FYOHST]2.0.CO;2 (cit. on p. 171).

Marcovaldi, M. A., Vieitas, C. F., & Godfrey, M. H. (1999). Nesting and Conservation Management of Hawksbill Turtles (Eretmochelys imbricata) in Northern Bahia, Brazil. *Chelonian Conservation and Biology*, *3*(2), 301–307 (cit. on p. 171).

Margaritoulis, D. (2005). Nesting Activity and Reproductive Output of Loggerhead Sea Turtles, Caretta caretta, Over 19 Seasons (1984-2002) at Laganas Bay, Zakynthos, Greece: The Largest Rookery in the Mediterranean. *Chelonian Conservation and Biology*, *4*(4), 916–929. https://archelon.gr/files/bibliography/%5B86%5DMargaritoulis05_Nesting19YearsZak.pdf (cit. on p. 130).

Marquez, M. (1994). *Synopsis of biological data on the Kemp's ridley turtle, Lepidochelys kempi (Garman, 1880)* (tech. rep.). NOAA. Silver Spring, MD. https://repository.library.noaa.gov/view/noaa/6184/noaa_6184_DS1.pdf (cit. on pp. 45, 51, 62).

Marquez, R., Carrasco, M. A., Jimenez, M. C., Peñaflores, C., & Bravo, R. (2005). Kemp's and Olive Ridley Sea Turtles Populations Status. In M. S. Coyne & R. D. Clark (Eds.), *Proceedings of the twenty-first annual symposium on sea turtle biology and conservation. noaa technical memorandum nmfs-sefsc-528* (pp. 237–239). (Cit. on p. 45).

Martins, S., Patrício, R., Clarke, L. J., de Santos Loureiro, N., & Marco, A. (2022). High variability in nest site selection in a loggerhead turtle rookery, in Boa Vista Island, Cabo Verde. *Journal of Experimental Marine Biology and Ecology*, *556*, 151798. https://doi.org/10.1016/J.JEMBE.2022.151798 (cit. on p. 2).

Masselink, G., Turner, I. L., & Williams, J. (2009). Large-Scale Laboratory Investigation into the Effect of the Beach Groundwater Table on Gravel Beach Morphology. *Journal of Coastal Research*, (56), 93–97. https://www.jstor.org/stable/25737544 (cit. on pp. 12, 42).

Masselink, G., & Lazarus, E. (2019). Defining Coastal Resilience. *Water*, *11*(12), 2587. https://doi.org/10.3390/w11122587 (cit. on p. 124).

Mast, R. B., Hutchinson, B. J., Villegas, P. E., & Bandimere, A. (2025). *SWOT Report Volume 20* (tech. rep.). SWOT: The State of the World's Sea Turtles. https://www.seaturtlestatus.org/swot-report-vol-20 (cit. on pp. 75, 132).

Masterson, J. P., Fienen, M. N., Thieler, E. R., Gesch, D. B., Gutierrez, B. T., & Plant, N. G. (2014). Effects of sea-level rise on barrier island groundwater system dynamics – ecohydrological implications. *Ecohydrology*, *7*(3), 1064–1071. https://doi.org/10.1002/eco.1442 (cit. on pp. 12, 42).

Maurer, A. S., & Johnson, M. W. (2017). Loggerhead Nesting in the Northern Gulf of Mexico: Importance of Beach Slope to Nest Site Selection in the Mis-

sissippi Barrier Islands. *Chelonian Conservation and Biology*, *16*(2), 250–254. https://doi.org/10.2744/CCB-1256.1 (cit. on p. 65).

Mazaris, A. D., Almpanidou, V., Wallace, B. P., Pantis, J. D., & Schofield, G. (2014). A global gap analysis of sea turtle protection coverage. *Biological Conservation*, *173*, 17–23. https://doi.org/10.1016/j.biocon.2014.03.005 (cit. on pp. 4, 73, 100, 116, 129).

Mazaris, A. D., Matsinos, G., & Pantis, J. D. (2009). Evaluating the impacts of coastal squeeze on sea turtle nesting. *Ocean & Coastal Management*, *52*(2), 139–145. https://doi.org/10.1016/j.ocecoaman.2008.10.005 (cit. on p. 131).

Mazor, T., Levin, N., Possingham, H. P., Levy, Y., Rocchini, D., Richardson, A. J., & Kark, S. (2013). Can satellite-based night lights be used for conservation? The case of nesting sea turtles in the Mediterranean. *Biological Conservation*, *159*, 63–72. https://doi.org/10.1016/j.biocon.2012.11.004 (cit. on p. 129).

McCall, R., Storlazzi, C., Roelvink, F., Pearson, S. G., de Goede, R., & Antolínez, J. A. Á. (2024). Rapid simulation of wave runup on morphologically diverse, reef-lined coasts with the BEWARE-2 (Broad-range Estimator of Wave Attack in Reef Environments) meta-process model. *Natural Hazards and Earth System Sciences*, *24*(10), 3597–3625. https://doi.org/10.5194/nhess-24-3597-2024 (cit. on p. 130).

McClenachan, L., Jackson, J. B., & Newman, M. J. (2006). Conservation implications of historic sea turtle nesting beach loss. *Frontiers in Ecology and the Environment*, *4*(6), 290–296. https://doi.org/10.1890/1540-9295(2006)4%5B290:CIOHST%5D2.0.CO;2 (cit. on pp. 1, 72).

McFall, B. C., Young, D. L., Whitmeyer, S. J., Buscombe, D., Cohn, N., Stasiewicz, J. B., Skaden, J. E., Walker, B. M., & Stever, S. N. (2024). SandSnap: Measuring and mapping beach grain size using crowd-sourced smartphone images. *Coastal Engineering*, *192*, 104554. https://doi.org/10.1016/j.coastaleng.2024.104554 (cit. on p. 129).

McGehee, A. M. (1990). Effects of Moisture on Eggs and Hatchlings of Loggerhead Sea Turtles (Caretta caretta). *Herpetologica*, *46*(3), 251–258. https://www.jstor.org/stable/3892967 (cit. on pp. 42, 126).

McLachlan, A., Defeo, O., Jaramillo, E., & Short, A. D. (2013). Sandy beach conservation and recreation: Guidelines for optimising management strategies for multi-purpose use. *Ocean & Coastal Management*, *71*, 256–268. https://doi.org/10.1016/j.ocecoaman.2012.10.005 (cit. on p. 1).

METER Group Inc. (2023). *ZL6* (tech. rep.). https://publications.metergroup.com/Manuals/20789_ZL6_Manual_Web.pdf (cit. on p. 19).

METER Group Inc. (2024). *TEROS 11/12* (tech. rep.). https://publications.metergroup.com/Manuals/20587_TEROS11-12_Manual_Web.pdf (cit. on pp. 19, 33).

Meylan, A. (1988). Spongivory in Hawksbill Turtles: A Diet of Glass. *Science*, *239*(4838), 393–395. https://doi.org/10.1126/science.239.4838.393 (cit. on pp. 1, 42, 72).

Michael, H. A., Russoniello, C. J., & Byron, L. A. (2013). Global assessment of vulnerability to sea-level rise in topography-limited and recharge-limited coastal groundwater systems. *Water Resources Research*, *49*(4), 2228–2240. https://doi.org/10.1002/wrcr.20213 (cit. on pp. 12, 43, 65).

Miller, J. D., Limpus, C. J., & Godfrey, M. (2003). Chapter 8: Nest Site Selection, Oviposition, Eggs, Development, Hatching, and Emergence of Loggerhead Turtles. In A. B. Bolten & B. E. Witherington (Eds.), *Loggerhead sea turtles* (pp. 125–143). Smithsonian Press. (Cit. on pp. 65, 100, 101, 119).

Miller, J. K., & Dean, R. G. (2007a). Shoreline variability via empirical orthogonal function analysis: Part I temporal and spatial characteristics. *Coastal Engineering*, *54*(2), 111–131. https://doi.org/10.1016/j.coastaleng.2006.08.013 (cit. on p. 82).

Miller, J. K., & Dean, R. G. (2007b). Shoreline variability via empirical orthogonal function analysis: Part II relationship to nearshore conditions. *Coastal Engineering*, *54*(2), 133–150. https://doi.org/10.1016/j.coastaleng.2006.08.014 (cit. on p. 82).

Milton, S. L., Leone-Kabler, S., Schulman, A. A., & Lutz, P. L. (1994). Effects of Hurricane Andrew on the Sea Turtle Nesting Beaches of South Florida. *Bulletin of Marine Science*, *54*(3), 974–981. https://www.ingentaconnect.com/content/umrsmas/bullmar/1994/00000054/00000003/art00030 (cit. on p. 2).

Monsinjon, J. R., Wyneken, J., Rusenko, K., López-Mendilaharsu, M., Lara, P., Santos, A., dei Marcovaldi, M. A., Fuentes, M. M., Kaska, Y., Tucek, J., Nel, R., Williams, K. L., LeBlanc, A. M., Rostal, D., Guillon, J. M., & Girondot, M. (2019). The climatic debt of loggerhead sea turtle populations in a warming world. *Ecological Indicators*, *107*, 105657. https://doi.org/10.1016/J.ECOLIND.2019.105657 (cit. on pp. 119, 141).

Montague, C. L. (1993). Ecological Engineering of Inlets in Southeastern Florida: Design Criteria for Sea Turtle Nesting Beaches. *Journal of Coastal Research*, *18*, 267–276. https://www.jstor.org/stable/25735685 (cit. on pp. 66, 131).

Montaño, J., Coco, G., Antolínez, J. A. A., Beuzen, T., Bryan, K. R., Cagigal, L., Castelle, B., Davidson, M. A., Goldstein, E. B., Ibaceta, R., Idier, D., Ludka, B. C., Masoud-Ansari, S., Méndez, F. J., Murray, A. B., Plant, N. G., Ratliff, K. M., Robinet, A., Rueda, A., … Vos, K. (2020). Blind testing of shoreline evolution models. *Scientific Reports*, *10*, 2137.

https://doi.org/10.1038/s41598-020-59018-y (cit. on pp. 80, 91).

Moore, L. J., Hacker, S. D., Breithaupt, J., de Vries, S., Miller, T., Ruggiero, P., & Zinnert, J. C. (2025). Ecomorphodynamics of coastal foredune evolution. *Nature Reviews Earth & Environment*, *6*(6), 417–432. https://doi.org/10.1038/s43017-025-00672-z (cit. on p. 89).

Moore, L. J., & Murray, A. B. (2022). Islands on the move. *Nature Geoscience*, *15*(8), 602–603. https://doi.org/10.1038/s41561-022-01000-6 (cit. on p. 90).

Morim, J., Wahl, T., Rasmussen, D. J., Calafat, F. M., Vitousek, S., Dangendorf, S., Kopp, R. E., & Oppenheimer, M. (2025). Observations reveal changing coastal storm extremes around the United States. *Nature Climate Change*, *15*(5), 538–545. https://doi.org/10.1038/s41558-025-02315-z (cit. on pp. 80, 92, 126).

Morim, J., Wahl, T., Vitousek, S., Santamaria-Aguilar, S., Young, I., & Hemer, M. (2023). Understanding uncertainties in contemporary and future extreme wave events for broad-scale impact and adaptation planning. *Science Advances*, *9*(2). https://doi.org/10.1126/sciadv.ade3170 (cit. on p. 92).

Mortimer, J. (1999). Reducing Threats to Eggs and Hatchlings: Hatcheries. In K. L. Eckert, K. A. Bjorndal, F. A. Abreu-Grobois, & M. Donnelly (Eds.), *Research and management techniques for the conservation of sea turtles*. IUCN/SSC Marine Turtle Specialist Group Publication no. 4. (Cit. on p. 127).

Mortimer, J. A. (1995). Teaching critical concepts for the conservation of sea turtles. *Marine Turtle Newsletter*, *71*(4). http://seaturtle.org/mtn/archives/mtn71/mtn71p1.shtml (cit. on pp. 2, 72, 100).

Mortimer, J. A. (1990). The Influence of Beach Sand Characteristics on the Nesting Behavior and Clutch Survival of Green Turtles (Chelonia mydas). *Copeia*, *1990*(3), 802. https://doi.org/10.2307/1446446 (cit. on pp. 2, 42, 63, 65, 100, 101, 112, 116, 117, 119, 128, 141).

Muis, S., Irazoqui Apecechea, M., Dullaart, J., de Lima Rego, J., Madsen, K. S., Su, J., Yan, K., & Verlaan, M. (2020). A High-Resolution Global Dataset of Extreme Sea Levels, Tides, and Storm Surges, Including Future Projections. *Frontiers in Marine Science*, *7*, 512955. https://doi.org/10.3389/fmars.2020.00263 (cit. on pp. 79, 102–104, 129, 189).

Murray, A. B., Coco, G., & Goldstein, E. B. (2014). Cause and effect in geomorphic systems: Complex systems perspectives. *Geomorphology*, *214*, 1–9. https://doi.org/10.1016/j.geomorph.2014.03.001 (cit. on p. 93).

NCEI. (2023). U.S. Climate Normals v1.0.1. https://www.ncei.noaa.gov/products/land-based-station/us-climate-normals (cit. on p. 46).

Nel, R., Campbell, E. E., Harris, L., Hauser, L., Schoeman, D. S., McLachlan, A., du Preez, D. R., Bezuidenhout, K., & Schlacher, T. A. (2014). The status of sandy beach science: Past trends, progress, and possible futures. *Estuarine, Coastal and Shelf Science*, *150*(PA), 1–10. https://doi.org/10.1016/j.ecss.2014.07.016 (cit. on pp. 1, 5, 12, 42, 72, 124).

Neumann, B., Vafeidis, A. T., Zimmermann, J., & Nicholls, R. J. (2015). Future Coastal Population Growth and Exposure to Sea-Level Rise and Coastal Flooding - A Global Assessment. *PLOS ONE*, *10*(3), e0118571. https://doi.org/10.1371/journal.pone.0118571 (cit. on pp. 1, 4, 100, 126).

Nielsen, P. (1999). Groundwater Dynamics and Salinity in Coastal Barriers. *Journal of Coastal Research*, *15*(3), 732–740. https://www.jstor.org/stable/4298987 (cit. on p. 60).

Nielsen, P. (1989). Measurements of Wave Setup and the Coastal Water Table. *Ninth Australasian Conference on Coastal and Ocean Engineering, 1989: Preprints of Papers*, 276–280. https://search.informit.org/doi/10.3316/informit.919586751063314 (cit. on p. 43).

Nielsen, P. (1990). Tidal dynamics of the water table in beaches. *Water Resources Research*, *26*(9), 2127–2134. https://doi.org/10.1029/WR026i009p02127 (cit. on pp. 12, 42, 53, 60).

Nitime. (2019). Nitime: time-series analysis for neuroscience, v0.9. https://nipy.org/nitime/documentation.html (cit. on p. 49).

NOAA. (2024a). National Data Buoy Centre. https://www.ndbc.noaa.gov (cit. on pp. 14, 34).

NOAA. (2024b). National Oceanic and Atmospheric Administration (NOAA) Tides and Currents. https://tidesandcurrents.noaa.gov (cit. on pp. 14, 26, 29, 44, 46, 50).

NWS. (2024). Galveston, Scholes Field. https://www.weather.gov/wrh/timeseries?site=KGLS (cit. on p. 46).

Ocana, M., Harfush-Melendez, M., & Heppell, S. S. (2012). Mass nesting of olive ridley sea turtles Lepidochelys olivacea at La Escobilla, Mexico: linking nest density and rates of destruction. *Endangered Species Research*, *16*(1), 45–54. https://doi.org/10.3354/ESR00388 (cit. on p. 75).

Ostertag, E. F. (2025). *Exploring Nature-based Solutions to Mitigate Climate Change Impacts on Sea Turtle Nesting Beaches (MSc Thesis)* (tech. rep.). RWTH Aachen University & Delft University of Technology. (Cit. on p. 131).

Paine, J. G., Caudle, T., & Andrews, J. R. (2021). *Shoreline Movement and Beach and Dune Volumetrics along the Texas Gulf Coast,1930s to 2019* (tech. rep.). Bureau of Economic Geology. Austin, TX. https://coastal.beg.utexas.edu/shorelinechange2019/assets/glo_gsu_2019_r02_d4.pdf (cit. on pp. 14, 44).

Patel, S. H., Winton, M. V., Hatch, J. M., Haas, H. L., Saba, V. S., Fay, G., & Smolowitz, R. J. (2021). Projected shifts in loggerhead sea turtle thermal habitat in

the Northwest Atlantic Ocean due to climate change. *Scientific Reports*, *11*, 8850. https://doi.org/10.1038/s41598-021-88290-9 (cit. on pp. 5, 143).

Patino-Martinez, J., Marco, A., Quiñones, L., & Hawkes, L. A. (2014). The potential future influence of sea level rise on leatherback turtle nests. *Journal of Experimental Marine Biology and Ecology*, *461*, 116–123. https://doi.org/10.1016/j.jembe.2014.07.021 (cit. on pp. 42, 126).

Patrício, A. R., Hawkes, L. A., Monsinjon, J. R., Godley, B. J., & Fuentes, M. M. P. B. (2021). Climate change and marine turtles: recent advances and future directions. *Endangered Species Research*, *44*, 363–395. https://doi.org/10.3354/esr01110 (cit. on pp. 1, 2, 12, 42, 72, 100, 124, 126).

Patrício, A. R., Varela, M. R., Barbosa, C., Broderick, A. C., Catry, P., Hawkes, L. A., Regalla, A., & Godley, B. J. (2019). Climate change resilience of a globally important sea turtle nesting population. *Global Change Biology*, *25*(2), 522–535. https://doi.org/10.1111/gcb.14520 (cit. on p. 131).

Percival, D. B., & Walden, A. T. (1993, June). Multitaper Spectral Estimation. In *Spectral analysis for physical applications* (pp. 331–377). Cambridge University Press. https://doi.org/10.1017/CBO9780511622762.010 (cit. on pp. 48, 49).

Petitt, B. M., & Winslow, A. G. (1957). *Geology and ground-water resources of Galveston County, Texas* (tech. rep.). USGS Water Supply Paper 1416. https://doi.org/10.3133/wsp1416 (cit. on p. 44).

Pianca, C., Holman, R., & Siegle, E. (2015). Shoreline variability from days to decades: Results of long-term video imaging. *Journal of Geophysical Research: Oceans*, *120*(3), 2159–2178. https://doi.org/10.1002/2014JC010329 (cit. on p. 72).

Pike, D. A. (2013). Climate influences the global distribution of sea turtle nesting. *Global Ecology and Biogeography*, *22*(5), 555–566. https://doi.org/10.1111/geb.12025 (cit. on pp. 100, 101, 114, 116, 119, 141).

Pike, D. A., Roznik, E. A., & Bell, I. (2015). Nest inundation from sea-level rise threatens sea turtle population viability. *Royal Society Open Science*, *2*(7), 150127. https://doi.org/10.1098/rsos.150127 (cit. on pp. 2, 42, 62, 63, 126, 128, 142).

Pike, D. A., & Stiner, J. C. (2007). Sea turtle species vary in their susceptibility to tropical cyclones. *Oecologia*, *153*(2), 471–478. https://doi.org/10.1007/s00442-007-0732-0 (cit. on pp. 2, 72, 100, 126).

Pintus, K. J., Godley, B. J., McGowan, A., & Broderick, A. C. (2009). Impact of Clutch Relocation on Green Turtle Offspring. *The Journal of Wildlife Management*, *73*(7), 1151–1157. https://doi.org/10.2193/2008-103 (cit. on pp. 2, 42, 131).

Pontee, N. (2013). Defining coastal squeeze: A discussion. *Ocean & Coastal Management*, *84*, 204–207. https://doi.org/10.1016/j.ocecoaman.2013.07.010 (cit. on pp. 4, 72, 126).

Prince, R. I. T. (1994). Shark Bay World Heritage Area: An Important Loggerhead Nesting Site. *Marine Turtle Newsletter*, *67*, 5–6. http://www.seaturtle.org/mtn/archives/mtn67/mtn67p5.shtml (cit. on p. 171).

Pronk, M., Hooijer, A., Eilander, D., Haag, A., de Jong, T., Vousdoukas, M., Vernimmen, R., Ledoux, H., & Eleveld, M. (2024). DeltaDTM: A global coastal digital terrain model. *Scientific Data*, *11*(1), 273. https://doi.org/10.1038/s41597-024-03091-9 (cit. on pp. 73, 76, 94, 129, 140).

Provancha, J. A., & Ehrhart, L. M. (1987). Sea Turtle Nesting Trends at Kennedy Space Center and Cape Canaveral Air Force Station, Florida, and Relationships with Factors Influencing Nest Site Selection. In W. N. Witzell (Ed.), *Ecology of east florida sea turtles* (pp. 33–44). NOAA Tech. Rep. NMFS 53. https://www.researchgate.net/publication/24320682 (cit. on pp. 100, 116).

Putman, N. F., Bane, J. M., & Lohmann, K. J. (2010). Sea turtle nesting distributions and oceanographic constraints on hatchling migration. *Proceedings of the Royal Society B: Biological Sciences*, *277*, 3631–3637. https://doi.org/10.1098/rspb.2010.1088 (cit. on pp. 100, 116).

Raghukumar, K., Chang, G., Spada, F., Jones, C., Janssen, T., & Gans, A. (2019). Performance Characteristics of "Spotter," a Newly Developed Real-Time Wave Measurement Buoy. *Journal of Atmospheric and Oceanic Technology*, *36*(6), 1127–1141. https://doi.org/10.1175/JTECH-D-18-0151.1 (cit. on p. 34).

Ranasinghe, R. (2016). Assessing climate change impacts on open sandy coasts: A review. *Earth-Science Reviews*, *160*, 320–332. https://doi.org/10.1016/j.earscirev.2016.07.011 (cit. on p. 12).

Ranasinghe, R. (2020). On the need for a new generation of coastal change models for the 21st century. *Scientific Reports*, *10*(2010). https://doi.org/10.1038/s41598-020-58376-x (cit. on p. 131).

Raubenheimer, B., Guza, R. T., & Elgar, S. (1999). Tidal water table fluctuations in a sandy ocean beach. *Water Resources Research*, *35*(8), 2313–2320. https://doi.org/10.1029/1999WR900105 (cit. on pp. 12, 42, 43, 60).

RBR Global. (2022). *RBR Solo3 & RBR Duet3 Instrument Guide* (tech. rep.). RBR Global. https://rbr-global.com/products/compact-loggers/rbrsolo-d/ (cit. on p. 17).

Reece, J., Passeri, D., Ehrhart, L., Hagen, S., Hays, A., Long, C., Noss, R., Bilskie, M., Sanchez, C., Schwoerer, M., Von Holle, B., Weishampel, J., & Wolf, S. (2013). Sea level rise, land use, and climate change influence the distribution of loggerhead turtle nests at the largest USA rookery (Melbourne Beach, Florida). *Marine Ecology Progress Series*, *493*, 259–274. https://doi.org/10.3354/meps10531 (cit. on p. 131).

Reguero, B. G., Beck, M. W., Agostini, V. N., Kramer, P., & Hancock, B. (2018). Coral reefs for coastal protection: A new methodological approach and engineering case study in Grenada. *Journal of Environmental Management*, *210*, 146–161. https://doi.org/10.1016/j.jenvman.2018.01.024 (cit. on p. 133).

Reguero, B. G., Losada, I. J., & Méndez, F. J. (2019). A recent increase in global wave power as a consequence of oceanic warming. *Nature Communications*, *10*(1), 205. https://doi.org/10.1038/s41467-018-08066-0 (cit. on pp. 4, 80, 92, 126).

Reinhold, L., & Whiting, A. (2014). High-density Loggerhead Sea Turtle Nesting on Dirk Hartog Island, Western Australia. *Marine Turtle Newsletter*, *141*, 7–10. http://www.seaturtle.org/mtn/archives/mtn141/mtn141-3.shtml (cit. on p. 171).

Repina, O., Carvalho, R. C., Coco, G., Antolínez, J. A., de Santiago, I., Harley, M. D., Jaramillo, C., Splinter, K. D., Vitousek, S., & Woodroffe, C. D. (2025). Evaluating five shoreline change models against 40 years of field survey data at an embayed sandy beach. *Coastal Engineering*, *199*, 104738. https://doi.org/10.1016/j.coastaleng.2025.104738 (cit. on pp. 80, 91).

Restrepo, J., Webster, E., Ramos, I., & Valverde, R. (2023). Recent decline of green turtle Chelonia mydas nesting trend at Tortuguero, Costa Rica. *Endangered Species Research*, *51*, 59–72. https://doi.org/10.3354/esr01237 (cit. on pp. 129, 130, 171).

Richardson, C. M., Davis, K. L., Ruiz-González, C., Guimond, J. A., Michael, H. A., Paldor, A., Moosdorf, N., & Paytan, A. (2024). The impacts of climate change on coastal groundwater. *Nature Reviews Earth & Environment*, *5*(2), 100–119. https://doi.org/10.1038/s43017-023-00500-2 (cit. on p. 42).

Rivas, M. L., Rodríguez-Caballero, E., Esteban, N., Carpio, A. J., Barrera-Vilarmau, B., Fuentes, M. M. P. B., Robertson, K., Azanza, J., León, Y., & Ortega, Z. (2023). Uncertain future for global sea turtle populations in face of sea level rise. *Scientific Reports*, *13*(1), 5277. https://doi.org/10.1038/s41598-023-31467-1 (cit. on pp. 5, 72, 73, 93, 124, 131).

Roelvink, D., Reniers, A., van Dongeren, A., van Thiel de Vries, J., McCall, R., & Lescinski, J. (2009). Modelling storm impacts on beaches, dunes and barrier islands. *Coastal Engineering*, *56*(11-12), 1133–1152. https://doi.org/10.1016/j.coastaleng.2009.08.006 (cit. on p. 130).

Roelvink, J. A., Huisman, B., Elghandour, A., Ghonim, M., & Reyns, J. (2020). Efficient Modeling of Complex Sandy Coastal Evolution at Monthly to Century Time Scales. *Frontiers in Marine Science*, *7*, 535. https://doi.org/10.3389/fmars.2020.00535 (cit. on p. 130).

Román-Sierra, J., Muñoz-Perez, J., & Navarro-Pons, M. (2014). Beach nourishment effects on sand porosity variability. *Coastal Engineering*, *83*, 221–232. https://doi.org/10.1016/j.coastaleng.2013.10.009 (cit. on p. 33).

Rosati, J., Dean, R., & Walton, T. (2013). The modified Bruun Rule extended for landward transport. *Marine Geology*, *340*, 71–81. https://doi.org/10.1016/j.margeo.2013.04.018 (cit. on pp. 4, 72, 126).

Rotzoll, K., & Fletcher, C. H. (2013). Assessment of groundwater inundation as a consequence of sea-level rise. *Nature Climate Change*, *3*(5), 477–481. https://doi.org/10.1038/nclimate1725 (cit. on pp. 4, 12, 42, 44).

Rueda, A., Cagigal, L., Pearson, S., Antolínez, J. A., Storlazzi, C., van Dongeren, A., Camus, P., & Mendez, F. J. (2019). HyCReWW: A Hybrid Coral Reef Wave and Water level metamodel. *Computers & Geosciences*, *127*, 85–90. https://doi.org/10.1016/j.cageo.2019.03.004 (cit. on p. 130).

Ruggiero, P., Buijsman, M., Kaminsky, G. M., & Gelfenbaum, G. (2010). Modeling the effects of wave climate and sediment supply variability on large-scale shoreline change. *Marine Geology*, *273*(1-4), 127–140. https://doi.org/10.1016/j.margeo.2010.02.008 (cit. on p. 131).

Rumbold, D. G., Davis, P. W., & Perretta, C. (2001). Estimating the Effect of Beach Nourishment on Caretta caretta (Loggerhead Sea Turtle) Nesting. *Restoration Ecology*, *9*(3), 304–310. https://doi.org/10.1046/j.1526-100x.2001.009003304.x (cit. on p. 132).

Santana Garcon, J., Grech, A., Moloney, J., & Hamann, M. (2010). Relative Exposure Index: an important factor in sea turtle nesting distribution. *Aquatic Conservation: Marine and Freshwater Ecosystems*, *20*(2), 140–149. https://doi.org/10.1002/aqc.1057 (cit. on pp. 100, 101, 116, 119, 130, 141).

Santidrián Tomillo, P., Saba, V. S., Lombard, C. D., Valiulis, J. M., Robinson, N. J., Paladino, F. V., Spotila, J. R., Fernández, C., Rivas, M. L., Tucek, J., Nel, R., & Oro, D. (2015). Global analysis of the effect of local climate on the hatchling output of leatherback turtles. *Scientific Reports*, *5*(1), 16789. https://doi.org/10.1038/srep16789 (cit. on pp. 100, 116).

SBG Systems. (2016). *Ekinox Surface Series Hardware Manual v1.4* (tech. rep.). (Cit. on p. 17).

de Schipper, M. A., Ludka, B. C., Raubenheimer, B., Luijendijk, A. P., & Schlacher, T. A. (2020). Beach nourishment has complex implications for the future of sandy shores. *Nature Reviews Earth & Environment*, *2*, 70–84. https://doi.org/10.1038/s43017-020-00109-9 (cit. on pp. 131, 132).

Schroth, W., Streit, B., & Schierwater, B. (1996). Evolutionary handicap for turtles. *Nature*, *384*(6609), 521–522. https://doi.org/10.1038/384521a0 (cit. on p. 100).

Scott, F., Antolinez, J. A. A., McCall, R., Storlazzi, C., Reniers, A., & Pearson, S. (2020). Hydro-Morphological Characterization of Coral Reefs for Wave Runup Prediction. *Frontiers in Marine Science*,

7. https://doi.org/10.3389/fmars.2020.00361 (cit. on p. 130).

Seney, E., & Landry, A. (2008). Movements of Kemp's ridley sea turtles nesting on the upper Texas coast: implications for management. *Endangered Species Research*, *4*(1-2), 73–84. https://doi.org/10.3354/esr00077 (cit. on pp. 14, 44).

Shanker, K., & Choudhury, B. C. (Eds.). (2007). *Marine turtles of the Indian subcontinent* (1st ed.). CRC Press. https://www.seaturtlesofindia.org/marine-turtles-of-the-indian-subcontinent/ (cit. on p. 104).

Shanker, K., Pandav, B., & Choudhury, B. (2004). An assessment of the olive ridley turtle (Lepidochelys olivacea) nesting population in Orissa, India. *Biological Conservation*, *115*(1), 149–160. https://doi.org/10.1016/S0006-3207(03)00104-6 (cit. on pp. 93, 118).

Shaver, D. J., & Caillouet Jr., C. W. (2015). Reintroduction of Kemp's ridley (Lepidochelys kempii) sea turtle to Padre Island National Seashore, Texas and its connection to head-starting. *Herpetological Conservation and Biology*, *10*(1), 378–435. https://www.herpconbio.org/Volume_10/Symposium/Caillouet_etal_2015.pdf (cit. on pp. 5, 45, 172).

Shimada, T., Meekan, M. G., Baldwin, R., Al-Suwailem, A. M., Clarke, C., Santillan, A. S., & Duarte, C. M. (2021). Distribution and temporal trends in the abundance of nesting sea turtles in the Red Sea. *Biological Conservation*, *261*, 109235. https://doi.org/10.1016/j.biocon.2021.109235 (cit. on p. 104).

Simmons, J. A., & Splinter, K. D. (2025). Data-driven shoreline modelling at timescales of days to years. *Coastal Engineering*, *197*, 104685. https://doi.org/10.1016/j.coastaleng.2024.104685 (cit. on p. 130).

Slepian, D. (1978). Prolate Spheroidal Wave Functions, Fourier Analysis, and Uncertainty-V: The Discrete Case. *Bell System Technical Journal*, *57*(5), 1371–1430. https://doi.org/10.1002/j.1538-7305.1978.tb02104.x (cit. on p. 48).

Slinger, J. H., & Vreugdenhil, H. S. I. (2020). Coastal Engineers Embrace Nature: Characterizing the Metamorphosis in Hydraulic Engineering in Terms of Four Continua. *Water*, *12*(9), 2504. https://doi.org/10.3390/w12092504 (cit. on pp. 5, 124, 127).

Smit, P. B. (2021). Spotter SD Card Parser (GitHub Repository). https://github.com/sofarocean/spotter-sd-parser (cit. on p. 27).

Smith, K. A., North, E. W., Shi, F., Chen, S.-N., Hood, R. R., Koch, E. W., & Newell, R. I. E. (2009). Modeling the Effects of Oyster Reefs and Breakwaters on Seagrass Growth. *Estuaries and Coasts*, *32*(4), 748–757. https://doi.org/10.1007/s12237-009-9170-z (cit. on p. 133).

Smithers, S. G., & Dawson, J. L. (2023). Beach reprofiling to improve reproductive output at the world's largest remaining green turtle rookery: Raine Island, northern Great Barrier Reef. *Ocean & Coastal Management*, *231*, 106385. https://doi.org/10.1016/j.ocecoaman.2022.106385 (cit. on pp. 66, 72, 124, 131).

Sobel, A. H., Camargo, S. J., Hall, T. M., Lee, C.-Y., Tippett, M. K., & Wing, A. A. (2016). Human influence on tropical cyclone intensity. *Science*, *353*(6296), 242–246. https://doi.org/10.1126/science.aaf6574 (cit. on p. 92).

Sofar Ocean Technologies Inc. (n.d.). *Spotter Technical Reference Manual* (tech. rep.). https://sofarocean.notion.site/Spotter-Documentation-Onboarding-935a67d619f84f828e77b3a1d77fdc28 (cit. on p. 19).

Sofar Ocean Technologies Inc. (2023). *SOFAR SPOTTER User Guide* (tech. rep.). (Cit. on p. 19).

Sous, D., Lambert, A., Rey, V., & Michallet, H. (2013). Swash–groundwater dynamics in a sandy beach laboratory experiment. *Coastal Engineering*, *80*, 122–136. https://doi.org/10.1016/j.coastaleng.2013.05.006 (cit. on pp. 12, 43).

Spalding, M. D., Ruffo, S., Lacambra, C., Meliane, I., Hale, L. Z., Shepard, C. C., & Beck, M. W. (2014). The role of ecosystems in coastal protection: Adapting to climate change and coastal hazards. *Ocean & Coastal Management*, *90*, 50–57. https://doi.org/10.1016/j.ocecoaman.2013.09.007 (cit. on pp. 124, 131–133).

Splinter, K. D., & Coco, G. (2021). Challenges and Opportunities in Coastal Shoreline Prediction. *Frontiers in Marine Science*, *8*. https://doi.org/10.3389/fmars.2021.788657 (cit. on pp. 73, 128).

Steinitz, M. J., Salmon, M., & Wyneken, J. (1998). Beach Renourishment and Loggerhead Turtle Reproduction: A Seven Year Study at Jupiter Island. *Journal of Coastal Research*, *14*(3), 1000–1013. http://www.jstor.org/stable/4298852 (cit. on pp. 64, 132).

Stockdon, H. F., Holman, R. A., Howd, P. A., & Sallenger, A. H. (2006). Empirical parameterization of setup, swash, and runup. *Coastal Engineering*, *53*(7), 573–588. https://doi.org/10.1016/j.coastaleng.2005.12.005 (cit. on pp. 46, 166, 167).

Taal, F. (2024). *Modelling Hydrodynamic and Groundwater Processes on a Sea Turtle Nesting Beach (MSc Thesis)* (tech. rep.). Delft University of Technology. https://resolver.tudelft.nl/uuid:20642828-b587-43cd-b82e-bfc30751ed49 (cit. on pp. 130, 142).

Taherkhani, M., Vitousek, S., Barnard, P. L., Frazer, N., Anderson, T. R., & Fletcher, C. H. (2020). Sea-level rise exponentially increases coastal flood frequency. *Scientific Reports*, *10*(1), 6466. https://doi.org/10.1038/s41598-020-62188-4 (cit. on p. 4).

Taylor, K. E. (2001). Summarizing multiple aspects of model performance in a single diagram. *Journal of Geophysical Research: Atmospheres*, *106*(D7), 7183–7192. https://doi.org/10.1029/2000JD900719 (cit. on p. 80).

Teledyne Odom Hydrographic. (2015). *Echotrac CV100 Single or Dual Channel Echo Sounder* (tech. rep.). www.odomhydrographic.com (cit. on p. 17).

Thampanya, U., Vermaat, J., Sinsakul, S., & Panapitukkul, N. (2006). Coastal erosion and mangrove progradation of Southern Thailand. *Estuarine, Coastal and Shelf Science*, *68*(1-2), 75–85. https://doi.org/10.1016/j.ecss.2006.01.011 (cit. on p. 132).

Thomas, J. A., Barnard, P. L., Vitousek, S., Erikson, L. H., Parker, K., Nederhoff, K., Befus, K. M., & Shirzaei, M. (2024). The projected exposure and response of a natural barrier island system to climate-driven coastal hazards. *Scientific Reports*, *14*, 25814. https://doi.org/10.1038/s41598-024-76749-4 (cit. on p. 90).

Thomson, D. (2007). Jackknifing Multitaper Spectrum Estimates. *IEEE Signal Processing Magazine*, *24*(4), 20–30. https://doi.org/10.1109/MSP.2007.4286561 (cit. on pp. 49, 168).

Thomson, D. (1982). Spectrum estimation and harmonic analysis. *Proceedings of the IEEE*, *70*(9), 1055–1096. https://doi.org/10.1109/PROC.1982.12433 (cit. on p. 48).

Thomson, J., Elgar, S., Raubenheimer, B., Herbers, T. H. C., & Guza, R. T. (2006). Tidal modulation of infragravity waves via nonlinear energy losses in the surfzone. *Geophysical Research Letters*, *33*(5). https://doi.org/10.1029/2005GL025514 (cit. on pp. 53, 60).

Trimble Marine Construction. (2021). *Trimble MPS865 Marine Positioning System GNSS Receiver* (tech. rep.). (Cit. on p. 17).

Turner, I. L. (1993). The Total Water Content of Sandy Beaches. *Journal of Coastal Research*, (15), 11–26. https://www.jstor.org/stable/25735720 (cit. on p. 43).

Turner, I. L. (1998). Monitoring groundwater dynamics in the littoral zone at seasonal, storm, tide and swash frequencies. *Coastal Engineering*, *35*(1-2), 1–16. https://doi.org/10.1016/S0378-3839(98)00023-4 (cit. on p. 12).

Turner, I. L., Coates, B. P., & Acworth, R. I. (1997). Tides, Waves and the Super-elevation of Groundwater at the Coast. *Journal of Coastal Research*, *13*(1), 46–60. http://www.jstor.org/stable/4298589 (cit. on pp. 12, 42, 43, 53, 60, 64, 65, 139).

Turner, I. L., Harley, M. D., Almar, R., & Bergsma, E. W. (2021). Satellite optical imagery in Coastal Engineering. *Coastal Engineering*, *167*, 103919. https://doi.org/10.1016/j.coastaleng.2021.103919 (cit. on p. 129).

Turner, I. L., & Nielsen, P. (1997). Rapid water table fluctuations within the beach face: Implications for swash zone sediment mobility? *Coastal Engineering*, *32*(1), 45–59. https://doi.org/10.1016/S0378-3839(97)00015-X (cit. on pp. 43, 60, 63, 65, 139).

Uber Technologies. (2022). H3: A Hexagonal Hierarchical Geospatial Indexing System. https://h3geo.org/%20https://github.com/uber/h3 (cit. on p. 105).

UNEP-WCMC & Short, F. T. (2021). Global distribution of seagrasses (version 7.1). Seventh update to the data layer used in Green and Short (2003). https://doi.org/10.34892/x6r3-d211 (cit. on pp. 102, 104, 190).

USACE. (2021). *Coastal Texas protection and restoration feasibility study. Final Report* (tech. rep.). U.S. Army Corps of Engineers. Galveston District and Texas General Land Office. https://www.swg.usace.army.mil/Portals/26/Coastal%20TX%20Protection%20and%20Restoration%20FINAL%20Feasibility%20Report_20210827.pdf (cit. on pp. 43, 66, 142).

USACE. (2022). *Galveston 204 CAP – Beach Nourishment, Engineering Appendix, Hydrology and Hydraulics* (tech. rep.). US Army Corps of Engineers, Galveston District. Galveston, TX. https://www.swg.usace.army.mil/Portals/26/HHGalv204AppxA5may22%20-%20DRAFT_1.pdf (cit. on pp. 14, 35, 44).

Valeport Limited. (2023). *SWiFT SVP Sound Velocity Profiler* (tech. rep.). www.valeport.co.uk (cit. on p. 17).

Valverde, R. A., Cornelius, S. E., & Mo, C. L. (1998). Decline of the olive ridley sea turtle (Lepidochelys olivacea) nesting assemblage at Nancite beach, Santa Rosa National Park, Costa Rica. *Chelonian Conservation and Biology*, *3*, 58–63 (cit. on p. 118).

Valverde, R. A., & Holzwart, K. R. (2017, June). Sea Turtles of the Gulf of Mexico. In C. H. Ward (Ed.), *Habitats and biota of the gulf of mexico: Before the deepwater horizon oil spill* (pp. 1189–1351). Springer New York. https://doi.org/10.1007/978-1-4939-3456-0_3 (cit. on pp. 12, 14, 45).

Van Hoek, M., Jia, L., Zhou, J., Zheng, C., & Menenti, M. (2016). Early Drought Detection by Spectral Analysis of Satellite Time Series of Precipitation and Normalized Difference Vegetation Index (NDVI). *Remote Sensing*, *8*(5), 422. https://doi.org/10.3390/rs8050422 (cit. on p. 48).

Van Houtan, K. S., & Bass, O. L. (2007). Stormy oceans are associated with declines in sea turtle hatching. *Current Biology*, *17*(15), R590–R591. https://doi.org/10.1016/j.cub.2007.06.021 (cit. on pp. 2, 12, 42, 100, 124, 126).

Varela, M. R., Patrício, A. R., Anderson, K., Broderick, A. C., DeBell, L., Hawkes, L. A., Tilley, D., Snape, R. T. E., Westoby, M. J., & Godley, B. J. (2019). Assessing climate change associated sea-level rise impacts on sea turtle nesting beaches using drones, photogrammetry and a novel GPS system. *Global Change Biology*, *25*(2), 753–762. https://doi.org/10.1111/gcb.14526 (cit. on p. 131).

Veelenturf, C. A., Sinclair, E. M., Paladino, F. V., & Honarvar, S. (2020). Predicting the impacts of sea

level rise in sea turtle nesting habitat on Bioko Island, Equatorial Guinea (G. Hays, Ed.). *PLOS ONE*, *15*(7), e0222251. https://doi.org/10.1371/journal.pone.0222251 (cit. on p. 131).

Vettigli, G. (2018). MiniSom: minimalistic and NumPy-based implementation of the Self Organizing Map. https://github.com/JustGlowing/minisom/ (cit. on p. 108).

Vitousek, S., Barnard, P. L., Fletcher, C. H., Frazer, N., Erikson, L., & Storlazzi, C. D. (2017a). Doubling of coastal flooding frequency within decades due to sea-level rise. *Scientific Reports*, *7*(1), 1399. https://doi.org/10.1038/s41598-017-01362-7 (cit. on pp. 4, 12, 100).

Vitousek, S., Barnard, P. L., & Limber, P. (2017b). Can beaches survive climate change? *Journal of Geophysical Research: Earth Surface*, *122*(4), 1060–1067. https://doi.org/10.1002/2017JF004308 (cit. on pp. 4, 72, 92, 126, 131).

Vitousek, S., Barnard, P. L., Limber, P., Erikson, L., & Cole, B. (2017c). A model integrating longshore and cross-shore processes for predicting long-term shoreline response to climate change. *Journal of Geophysical Research: Earth Surface*, *122*(4), 782–806. https://doi.org/10.1002/2016JF004065 (cit. on pp. 77, 78).

Vitousek, S., Buscombe, D., Gomez-de la Peña, E., Calcraft, K., Lundine, M., Splinter, K. D., Coco, G., & Barnard, P. L. (2025). Are Equilibrium Shoreline Models Just Convolutions? *Journal of Geophysical Research: Earth Surface*, *130*(6), e2025JF008452. https://doi.org/10.1029/2025JF008452 (cit. on pp. 73, 78).

Vitousek, S., Buscombe, D., Vos, K., Barnard, P. L., Ritchie, A. C., & Warrick, J. A. (2023a). The future of coastal monitoring through satellite remote sensing. *Cambridge Prisms: Coastal Futures*, *1*, e10. https://doi.org/10.1017/cft.2022.4 (cit. on pp. 73, 80, 128, 129).

Vitousek, S., Cagigal, L., Montaño, J., Rueda, A., Mendez, F., Coco, G., & Barnard, P. L. (2021). The Application of Ensemble Wave Forcing to Quantify Uncertainty of Shoreline Change Predictions. *Journal of Geophysical Research: Earth Surface*, *126*(7), e2019JF005506. https://doi.org/10.1029/2019JF005506 (cit. on pp. 77, 78, 93, 131).

Vitousek, S., Vos, K., Splinter, K. D., Erikson, L., & Barnard, P. L. (2023b). A Model Integrating Satellite-Derived Shoreline Observations for Predicting Fine-Scale Shoreline Response to Waves and Sea-Level Rise Across Large Coastal Regions. *Journal of Geophysical Research: Earth Surface*, *128*(7). https://doi.org/10.1029/2022JF006936 (cit. on pp. 73, 77–79, 91, 94, 130, 140).

Vitousek, S., Vos, K., Splinter, K. D., Parker, K., O'Neill, A., Foxgrover, A. C., Hayden, M. K., Thomas, J. A., Erikson, L., & Barnard, P. L. (2024). Scalable, data-assimilated models predict large-scale shoreline response to waves and sea-level rise. *Scientific Reports*, *14*, 28029. https://doi.org/10.1038/s41598-024-77030-4 (cit. on pp. 92, 131).

Voermans, J. J., Smit, P. B., Janssen, T. T., & Babanin, A. V. (2020). Estimating Wind Speed and Direction Using Wave Spectra. *Journal of Geophysical Research: Oceans*, *125*(2), e2019JC015717. https://doi.org/10.1029/2019JC015717 (cit. on pp. 19, 34).

Von Holle, B., Irish, J. L., Spivy, A., Weishampel, J. F., Meylan, A., Godfrey, M. H., Dodd, M., Schweitzer, S. H., Keyes, T., Sanders, F., Chaplin, M. K., & Taylor, N. R. (2019). Effects of future sea level rise on coastal habitat. *The Journal of Wildlife Management*, *83*(3), 694–704. https://doi.org/10.1002/jwmg.21633 (cit. on p. 130).

de Vos, D., Nel, R., Schoeman, D., Harris, L. R., & du Preez, D. (2019). Effect of introduced Casuarina trees on the vulnerability of sea turtle nesting beaches to erosion. *Estuarine, Coastal and Shelf Science*, *223*, 147–158. https://doi.org/10.1016/j.ecss.2019.03.015 (cit. on p. 130).

Vos, K., Splinter, K. D., Palomar-Vázquez, J., Pardo-Pascual, J. E., Almonacid-Caballer, J., Cabezas-Rabadán, C., Kras, E. C., Luijendijk, A. P., Calkoen, F., Almeida, L. P., Pais, D., Klein, A. H. F., Mao, Y., Harris, D., Castelle, B., Buscombe, D., & Vitousek, S. (2023a). Benchmarking satellite-derived shoreline mapping algorithms. *Communications Earth & Environment*, *4*(1), 345. https://doi.org/10.1038/s43247-023-01001-2 (cit. on p. 76).

Vos, K., Harley, M. D., Splinter, K. D., Simmons, J. A., & Turner, I. L. (2019a). Sub-annual to multi-decadal shoreline variability from publicly available satellite imagery. *Coastal Engineering*, *150*, 160–174. https://doi.org/10.1016/j.coastaleng.2019.04.004 (cit. on pp. 73, 76, 80, 129).

Vos, K., Harley, M. D., Splinter, K. D., Walker, A., & Turner, I. L. (2020). Beach Slopes From Satellite-Derived Shorelines. *Geophysical Research Letters*, *47*(14). https://doi.org/10.1029/2020GL088365 (cit. on p. 76).

Vos, K., Harley, M. D., Turner, I. L., & Splinter, K. D. (2023b). Pacific shoreline erosion and accretion patterns controlled by El Niño/Southern Oscillation. *Nature Geoscience*, *16*(2), 140–146. https://doi.org/10.1038/s41561-022-01117-8 (cit. on pp. 4, 72, 76).

Vos, K., Splinter, K. D., Harley, M. D., Simmons, J. A., & Turner, I. L. (2019b). CoastSat: A Google Earth Engine-enabled Python toolkit to extract shorelines from publicly available satellite imagery. *Environmental Modelling & Software*, *122*, 104528. https://doi.org/10.1016/j.envsoft.2019.104528 (cit. on pp. 75, 128, 172, 173).

Vousdoukas, M. I., Ranasinghe, R., Mentaschi, L., Plomaritis, T. A., Athanasiou, P., Luijendijk, A., & Feyen, L. (2020). Sandy coastlines under threat of erosion. *Nature Climate Change*, *10*(3), 260–263.

https://doi.org/10.1038/s41558-020-0697-0 (cit. on p. 72).

de Vriend, H. J., van Koningsveld, M., Aarninkhof, S. G., de Vries, M. B., & Baptist, M. J. (2015). Sustainable hydraulic engineering through building with nature. *Journal of Hydro-Environment Research*, *9*(2), 159–171. https://doi.org/10.1016/j.jher.2014.06.004 (cit. on pp. 5, 42, 124, 126).

Walkden, M., & Dickson, M. (2008). Equilibrium erosion of soft rock shores with a shallow or absent beach under increased sea level rise. *Marine Geology*, *251*(1-2), 75–84. https://doi.org/10.1016/j.margeo.2008.02.003 (cit. on p. 90).

Wallace, B. P., Bandimere, A. N., Abreu-Grobois, F., Acosta, H., Akiti, J., Akomedi, M., Alfaro-Shigueto, J., Allen, C., Angenda, D., Ayissi, I., Azanza Ricardo, J., Barrientos-Muñoz, K., Barrios-Garrido, H., Bjorndal, K., Bretón Vargas, E., Broderick, A., Calderón Peña, R., Carreras, C., Ceriani, S., … Mast, R. (2025). Updated global conservation status and priorities for marine turtles. *Endangered Species Research*, *56*, 247–276. https://doi.org/10.3354/esr01385 (cit. on p. 124).

Wallace, B. P., Posnik, Z. A., Hurley, B. J., DiMatteo, A. D., Bandimere, A., Rodriguez, I., Maxwell, S. M., Meyer, L., Brenner, H., Jensen, M. P., LaCasella, E., Shamblin, B. M., Abreu Abreu-Grobois, F. A., Stewart, K. R., Dutton, P. H., Barrios-Garrido, H., Dalleau, M., Dell'amico, F., Eckert, K. L., … Mast, R. B. (2023). Marine turtle regional management units 2.0: an updated framework for conservation and research of wide-ranging megafauna species. *Endangered Species Research*, *52*, 209–223. https://doi.org/10.3354/esr01243 (cit. on pp. 126, 143).

Wallace, B. P., DiMatteo, A. D., Hurley, B. J., Finkbeiner, E. M., Bolten, A. B., Chaloupka, M. Y., Hutchinson, B. J., Abreu-Grobois, F. A., Amorocho, D., Bjorndal, K. A., Bourjea, J., Bowen, B. W., Dueñas, R. B., Casale, P., Choudhury, B. C., Costa, A., Dutton, P. H., Fallabrino, A., Girard, A., … Mast, R. B. (2010). Regional Management Units for Marine Turtles: A Novel Framework for Prioritizing Conservation and Research across Multiple Scales. *PLOS ONE*, *5*(12), e15465. https://doi.org/10.1371/JOURNAL.PONE.0015465 (cit. on pp. 112, 113).

Walstra, D., Reniers, A., Ranasinghe, R., Roelvink, J., & Ruessink, B. (2012). On bar growth and decay during interannual net offshore migration. *Coastal Engineering*, *60*(1), 190–200. https://doi.org/10.1016/j.coastaleng.2011.10.002 (cit. on p. 130).

Ware, M., Ceriani, S., Long, J., & Fuentes, M. M. P. B. (2021). Exposure of Loggerhead Sea Turtle Nests to Waves in the Florida Panhandle. *Remote Sensing*, *13*(14), 2654. https://doi.org/10.3390/rs13142654 (cit. on pp. 2, 42, 124, 128, 130).

Ware, M., & Fuentes, M. M. (2018). A comparison of methods used to monitor groundwater inundation of sea turtle nests. *Journal of Experimental Marine Biology and Ecology*, *503*, 1–7. https://doi.org/10.1016/j.jembe.2018.02.001 (cit. on pp. 2, 42, 128).

Ware, M., Long, J. W., & Fuentes, M. M. P. B. (2019). Using wave runup modeling to inform coastal species management: An example application for sea turtle nest relocation. *Ocean & Coastal Management*, *173*, 17–25. https://doi.org/10.1016/j.ocecoaman.2019.02.011 (cit. on p. 128).

Warrick, J. A., Buscombe, D., Vos, K., Kenyon, H., Ritchie, A. C., Harley, M. D., Janda, C., L'Heureux, J., & Vitousek, S. (2025). Shoreline Seasonality of California's Beaches. *Journal of Geophysical Research: Earth Surface*, *130*(2), e2024JF007836. https://doi.org/10.1029/2024JF007836 (cit. on pp. 76, 82).

Waycott, M., Duarte, C. M., Carruthers, T. J. B., Orth, R. J., Dennison, W. C., Olyarnik, S., Calladine, A., Fourqurean, J. W., Heck, K. L., Hughes, A. R., Kendrick, G. A., Kenworthy, W. J., Short, F. T., & Williams, S. L. (2009). Accelerating loss of seagrasses across the globe threatens coastal ecosystems. *Proceedings of the National Academy of Sciences*, *106*(30), 12377–12381. https://doi.org/10.1073/pnas.0905620106 (cit. on p. 1).

Weber, S. B., Weber, N., Ellick, J., Avery, A., Frauenstein, R., Godley, B. J., Sim, J., Williams, N., & Broderick, A. C. (2014). Recovery of the South Atlantic's largest green turtle nesting population. *Biodiversity and Conservation*, *23*(12), 3005–3018. https://doi.org/10.1007/s10531-014-0759-6 (cit. on p. 74).

Welch, P. (1967). The use of fast Fourier transform for the estimation of power spectra: A method based on time averaging over short, modified periodograms. *IEEE Transactions on Audio and Electroacoustics*, *15*(2), 70–73. https://doi.org/10.1109/TAU.1967.1161901 (cit. on p. 48).

Wildermann, N. E., Barrios-Garrido, H., Jabby, K., Hardenstine, R. S., Shimada, T., Williams, I. D., & Duarte, C. M. (2024). An emerging hazard to nesting sea turtles in the face of sea-level rise. *Global Ecology and Conservation*, *56*, e03334. https://doi.org/10.1016/j.gecco.2024.e03334 (cit. on pp. 89, 126).

Willson, A., Witherington, B., Baldwin, R., Tiwari, M., Al Sariri, T., Al Kiyumi, A., Al Harthi, S., Willson, M. S., Al Bulushi, A., Al Farsi, G., Al Humaidy, J., Al Araimi, J., Daar, L. A., Schroeder, B., Ross, J. P., & Possardt, E. (2020). Evaluating the Long-Term Trend and Management of a Globally Important Loggerhead Population Nesting on Masirah Island, Sultanate of Oman. *Frontiers in Marine Science*, *7*, 548395. https://doi.org/10.3389/fmars.2020.00666 (cit. on pp. 117, 129, 172).

Wolinsky, M. A., & Murray, A. B. (2009). A unifying framework for shoreline migration: 2. Application to wave-dominated coasts. *Journal of Geophysical Re-*

search: Earth Surface, *114*(F1). https://doi.org/10.1029/2007JF000856 (cit. on pp. 73, 90, 92, 128, 131).

Wood, D. W., & Bjorndal, K. A. (2000). Relation of Temperature, Moisture, Salinity, and Slope to Nest Site Selection in Loggerhead Sea Turtles. *Copeia*, *2000*(1), 119–128. https://doi.org/10.1643/0045-8511(2000)2000[0119:ROTMSA]2.0.CO;2 (cit. on pp. 100, 114, 115).

Wright, L., & Short, A. (1984). Morphodynamic variability of surf zones and beaches: A synthesis. *Marine Geology*, *56*(1-4), 93–118. https://doi.org/10.1016/0025-3227(84)90008-2 (cit. on pp. 12, 72).

Xu, H. (2006). Modification of normalised difference water index (NDWI) to enhance open water features in remotely sensed imagery. *International Journal of Remote Sensing*, *27*(14), 3025–3033. https://doi.org/10.1080/01431160600589179 (cit. on p. 76).

Yamamoto, K. H., Powell, R. L., Anderson, S., & Sutton, P. C. (2012). Using LiDAR to quantify topographic and bathymetric details for sea turtle nesting beaches in Florida. *Remote Sensing of Environment*, *125*, 125–133. https://doi.org/10.1016/j.rse.2012.07.016 (cit. on pp. 65, 100, 116, 128).

Yates, M. L., Guza, R. T., & O'Reilly, W. C. (2009). Equilibrium shoreline response: Observations and modeling. *Journal of Geophysical Research: Oceans*, *114*(C9), 9014. https://doi.org/10.1029/2009JC005359 (cit. on p. 78).

Zarifsanayei, A. R., Antolínez, J. A. A., Cartwright, N., Etemad-Shahidi, A., Strauss, D., Lemos, G., Semedo, A., Kumar, R., Dobrynin, M., & Akpinar, A. (2023). Uncertainties in wave-driven longshore sediment transport projections presented by a dynamic CMIP6-based ensemble. *Frontiers in Marine Science*, *10*, 1188136. https://doi.org/10.3389/fmars.2023.1188136 (cit. on p. 93).

Zavala Hidalgo, J., Morey, S. L., & O'Brien, J. J. (2003). Seasonal circulation on the western shelf of the Gulf of Mexico using a high-resolution numerical model. *Journal of Geophysical Research: Oceans*, *108*(C12), 3389. https://doi.org/10.1029/2003JC001879 (cit. on p. 14).

Zheng, F., Westra, S., & Sisson, S. A. (2013). Quantifying the dependence between extreme rainfall and storm surge in the coastal zone. *Journal of Hydrology*, *505*, 172–187. https://doi.org/10.1016/j.jhydrol.2013.09.054 (cit. on p. 60).

A

Supporting information for Chapter 3

A.1. Data gaps

Below we briefly explain the data gaps in the time series and how they were filled for this study. For a detailed description of the incidents behind these gaps and how they were handled, we refer to Christiaanse et al. (2025b).

- The loggers at TT2, SW1, and SW2 (foreshore) emerged during several low tides, therefore missing observations of the lowest water levels, which could not be linearly interpolated. Since the foreshore water levels at TT and SW compared well and the logger at TT1 recorded all low water levels, we filled the gaps at TT2 and SW1 with the data from TT1. The gaps at SW2 were subsequently filled with the corrected data from SW1.

- Because of the berm, the logger in the well at TT6 was installed slightly higher than the rest and emerged during the lowest water levels on 28 and 29 November (for about four and six hours respectively). However, these gaps could not be filled with data from another station. Given that the difference was within a few cm, we used a quadratic interpolation to reproduce the minima.

- The logger at TT8 malfunctioned after a data offload on 21 November, 16:25 CST, and was replaced on 27 November, 9:03 CST. No data was recorded during this period, leading to the largest gap in any of the time series (six days). There was no way to interpolate or fill the data gap adequately.

- The loggers at SW5 and SW8 did not record the full length of the first storm on 13 November. At SW5 the well and logger were removed on 13 November 13:15 CST, after being hit by a truck earlier, and reinstalled on 14 November 10:30 CST. At SW8 the bottom plug of the well was not weighted correctly and was pushed upward during the storm around 13:20 CST, also pushing the installed logger upwards by an unknown amount. The logger was in the correct position again on 13 November 20:35 CST. Given the gaps included a significant part of the storm we could not interpolate or replace the data appropriately.

A

A.2. Wave runup estimation ($R_{2\%}$)

A.2.1. Deepwater wave conditions

The 2% exceedance elevation of the runup was derived from four estimates based on Stockdon et al. (2006), as explained in the main text. For these estimates, the offshore wave conditions were needed. These were derived from the wave conditions (significant wave height, H_s, and peak period, T_p) measured by a Spotter wave buoy at station TT0, roughly 1.5km offshore off field site TT at a water depth of 8 m (Christiaanse et al., 2025b).

The relatively shallow water depth means that the measured waves cannot be assumed to be in deep water conditions, which are needed for the Stockdon formulations. Hence, they were transformed to deepwater conditions through linear wave theory (Holthuijsen, 2007). Hereby, we only included linear shoaling, neglecting refraction under the assumption of alongshore uniformity and normally incident waves.

The Stockdon formulations require the deepwater wavelength (L_0) and significant wave height (H_0). L_0 can be readily computed from the peak period as $L_0 = gT_p^2/2\pi$. To obtain H_0, we first iteratively solve the dispersion relationship for the wave number k:

$$\omega^2 = gk \tanh kd \tag{A.1}$$

where $\omega = 2\pi/T_p$ is the angular frequency, $d = 8$ m is the water depth, and $g = 9.81$ m/s is the gravitational acceleration. Using k, the linear shoaling coefficient K_s can be computed as:

$$K_s = \sqrt{\frac{1}{\tanh kd}\left(1 + \frac{2kd}{\sinh 2kd}\right)^{-1}} \tag{A.2}$$

and from there follows:

$$H_0 = \frac{H_s}{K_s} \tag{A.3}$$

A.2.2. Interpolation for missing wave data

The wave buoy at TT0 recorded data between 3 and 26 November 2023, whereas the water level data spans from 2 November to 4 December 2023 (Christiaanse et al., 2025b). Given the closest NOAA buoy (*ID 42035*) was also down during the entire fieldwork period, there were no alternative options for in situ wave data. We therefore used linear regression to fill the gaps in the $R_{2\%}$ and setup (S) time series.

For this, we tested several correlations. The best correlation was found with $\sqrt{H_s L_0}$ derived from the measured water level at TT1/SW1. The correlation was $r = 0.88$ at TT and $r = 0.86$ at SW (Figure A.1). The wave conditions (H_s, T_p, and, by extension, L_0) were obtained from a spectral analysis of 30-min time windows from the observed water level time series at TT1/SW1. The power spectra and parameters were derived in the same fashion as the infragravity (IG) spectra (see Section 3.2.5) with the following differences:

- We used eight blocks of 3.25 minutes instead of four blocks of 7.5 minutes.
- The spectral parameters were computed over the entire frequency range (not only the IG band).
- Instead of T_{m-10} we computed the peak period T_p as f_p^{-1} where f_p is the peak frequency.

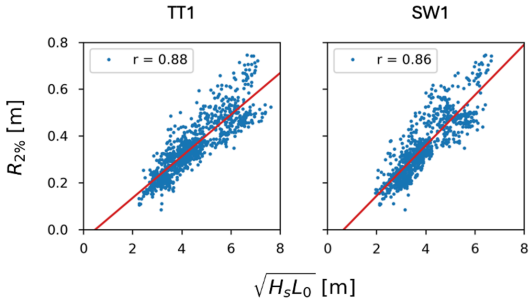

Figure A.1: Correlation between $\sqrt{H_s L_0}$ at TT1 (left) and SW1 (right) and $R_{2\%}$ computed with the dissipative formulation from Stockdon et al. (2006). The red line indicates the linear fit used to fill the gaps in the time series.

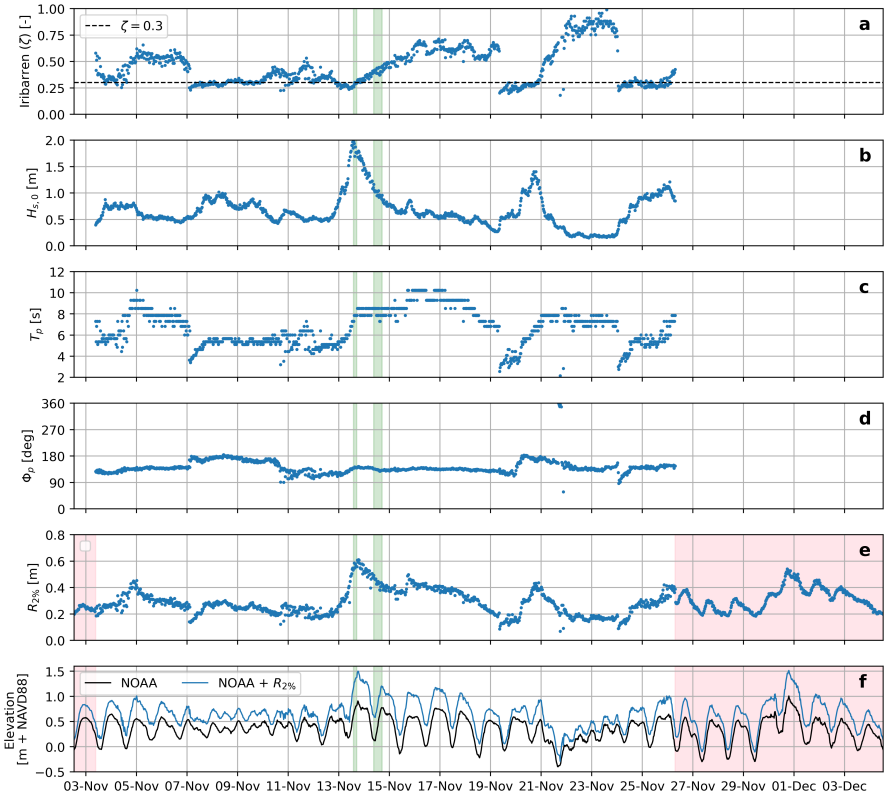

Figure A.2: Offshore wave conditions and estimation of the wave runup ($R_{2\%}$) based on the dissipative formulation by Stockdon et al. (2006). a) Surf similarity parameter (Iribarren number) based on a beach slope of $\beta = 0.04$; b) Significant wave height (deepwater, see derivation in Section A.2.1), c) peak wave period; d) mean wave direction; e) $R_{2\%}$ estimates (unreferenced) based on equations 1 (blue) and 2 (orange) in the main text (without the referenced water level); f) 30-min averaged observed water level at the NOAA Jetty station (black) and the water level plus $R_{2\%}$ (blue). The red shaded areas in panels e and f represent the time frame for which the $R_{2\%}$ estimates were interpolated due to missing wave data (see Section A.2.2). The green shaded areas represent the time frames over which the observed wave runup was compared to various Stockdon formulations in van der Grinten et al. (2025).

A.3. Tidal multitaper analysis

A.3.1. Multitaper uncertainty estimation for coherence and phase

We quantified an uncertainty estimate for the coherence and the phase difference using a jackknifing technique, as outlined in Thomson (2007). Suppose our spectral estimate (in this case the coherence or phase) is denoted by θ. The estimate made using all tapers is denoted by $\hat{\theta}$. We now create K estimates of θ, by leaving out one of the K tapers each time:

$$\theta_{\setminus i} = \theta\{x_1, \ldots x_{i-1}, x_{i+1}, \ldots x_K\} \tag{A.4}$$

The average of these K estimates is given as:

$$\bar{\theta}_{\setminus} = \frac{1}{K}\sum_{i=1}^{K}\theta_{\setminus i} \tag{A.5}$$

And the jackknife variance of the full estimator $\hat{\theta}$ is then computed as:

$$\mathrm{Var}[\hat{\theta}] = \frac{K-1}{K}\sum_{i=1}^{K}\left(\theta_{\setminus i} - \bar{\theta}_{\setminus}\right)^2 \tag{A.6}$$

Where the scale factor is added to account for the fact that the $\theta_{\setminus i}$ estimates are not independent. The estimator is assumed to be distributed around the true parameter θ approximately as a student's t distribution with degrees of freedom equal to the number of tapers used. The 90% percent confidence interval can then be computed from the jackknife variance using the student's t distribution. This method is implemented in the *Nitime* library that we used to estimate the multitapers, and we applied it to the coherence using the *jackknifed_coh_variance()* function (see further details in the *Nitime* documentation: https://nipy.org/nitime/examples/multi_taper_coh.html).

For the phase difference, this approach is not directly applicable because it is a circular variable (it wraps around its maximum and minimum values, when the signal is completely out-of-phase). We therefore based our uncertainty estimate of the phase difference on the range given by the maximum and minimum estimate obtained from the K leave-one-out estimates ($\theta_{\setminus i}$). So, the green-shaded area in Figures 3.5 and A.3 represent this min-max range.

A.3.2. Figure for SW

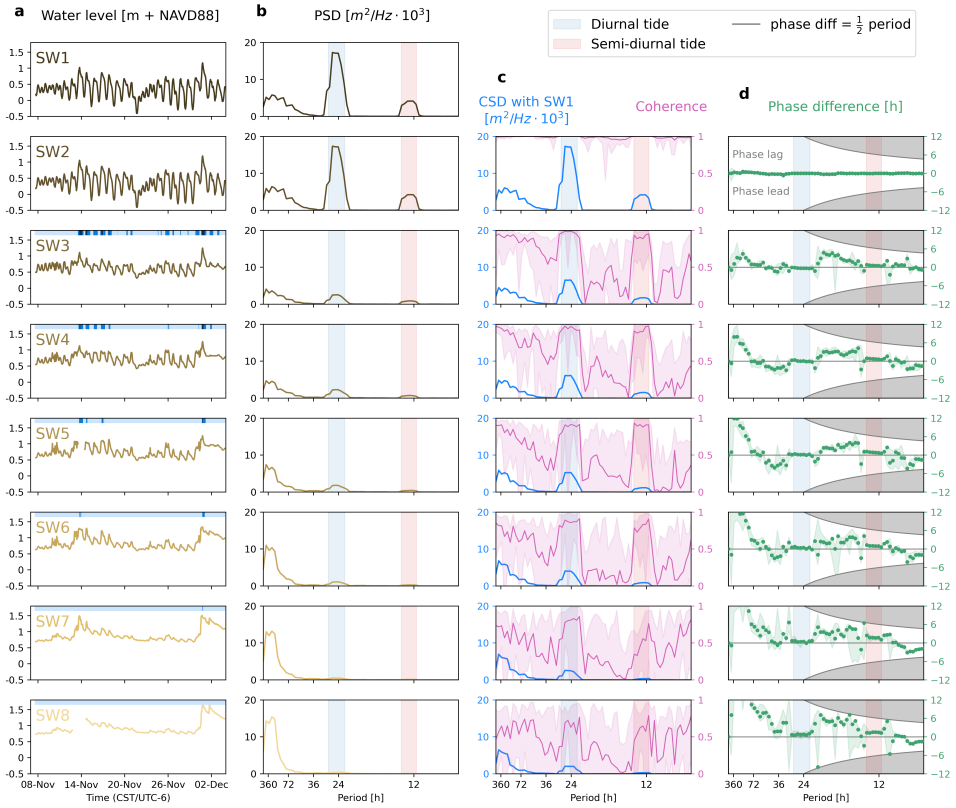

Figure A.3: Multitaper spectral analysis of the tidal propagation along the stations at SW. a) Observed water level time series at each station, with the blue shaded bar representing the inundation regime over time (see Figure 3.3 in Chapter 3); b) Power spectral density (PSD) computed from the detrended time series; c) cross-spectral density (CSD, blue) and coherence (pink, 90% confidence interval given by shaded area) between station 1 and stations 2–8; d) estimated phase difference (green) between station 1 and stations 2–8 in hours (uncertainty given as green shaded area). A positive (negative) phase difference denotes a lag (lead) in the signal at stations 2–8. The maximum phase difference ($1/2$ period) is denoted by the grey borders. In columns b–d, the tidal bandwidths are shaded in blue (diurnal) and red (semidiurnal). Figure 3.5 presents the same figure for TT.

B

Supporting information for Chapter 4

B.1. Description of remaining study sites

Below a description of the seven study sites that were not described in detail in Chapter 4:

Dirk Hartog Island, Australia (AU_DH)

Dirk Hartog Island is a large, remote island on the central West Australian coastline, which hosts an important regional loggerhead turtle (*Caretta caretta, Cc*) rookery (Prince, 1994). Nesting occurs from November to April and is concentrated at Turtle Bay on the northern tip of the island, spanning five relatively narrow beaches (2.1 km total length, about 30 m wide) interspersed with rocky sections and backed by steep rocky slopes (Reinhold & Whiting, 2014). Though the island is exposed to high wave energy ($\overline{H}_s \approx 2$ m), Turtle Bay is partly sheltered from the predominantly south-westerly swell. Nonetheless, during cyclones, entire nesting beaches have been stripped of sand (Reinhold & Whiting, 2014). The tidal range is relatively small (0.9 m).

Busca Vida, Brazil (BR_BV)

Busca Vida is situated on the northern outskirts of the city of Salvador in Bahia, Brazil. Bahia's northern coastline (covering a stretch of about 200 km) is Brazil's primary nesting area of Hawksbill turtles (*Eretmochelys imbricata, Ei*; Marcovaldi et al., 1999), while also supporting nesting by green, loggerhead, olive ridley, and leatherback (*Dermochelys coriacea, Dc*) turtles. The shoreline is mostly sandy with interspersed rock and reef formations along the coast (Marcovaldi et al., 2007). The beach at Busca Vida is backed by residential homes and coconut plantations, while there is a river mouth at the southern end. The tidal range (1.7 m) and wave energy ($\overline{H}_s \approx 1.1$ m) are moderate.

Tortuguero, Costa Rica (CR_TO)

Tortuguero national park covers a 30-km stretch of open beach on the northern Caribbean coast of Costa Rica. This barrier island hosts the largest green turtle rookery in the Atlantic Ocean, holding enormous conservation value for the species (Bjorndal et al., 1999). Nesting occurs between June and November (Restrepo et al., 2023). The relatively narrow beach ($\approx$ 30 m) consists of dark sand and is backed by dense vegetation. The tidal range is very small (0.3 m) and wave energy is moderate ($\overline{H}_s \approx 0.9$ m).

Joao Barrosa, Cape Verde (CV_JB)

Joao Barrosa covers a roughly 8 km-long stretch of sandy coast on the southeastern part of Boa Vista island, Cape Verde. The island hosts the largest loggerhead turtle rookery of

the endangered eastern Atlantic population, most of which nest near Joao Barrosa (Marco et al., 2012). The area has a mixed setting of open and embayed beaches backed by sparse vegetation and virtually no human infrastructure. The tidal range is relatively small (0.7 m) but the beaches are exposed to moderate to high wave energy ($\overline{H}_s \approx 1.4$ m).

Alagadi, Cyprus, (CY_AL)

Alagadi covers two pocket beaches on the north coast of Cyprus in the eastern Mediterranean. The two beaches (total length 1.7 km) serve as important nesting habitat for the Mediterranean loggerhead and green turtle populations, which both nest between May and October (Broderick et al., 2002). The region is characterized by a very small tidal range (0.3 m) and relatively low wave energy ($\overline{H}_s \approx 0.8$ m).

Rancho Nuevo, Mexico (MX_RN)

Rancho Nuevo, a stretch of undeveloped open sandy beach along Mexico's northern Gulf of Mexico coast, is the single most important nesting site for the critically endangered Kemp's ridley sea turtle (*Lepidochelys kempii, Lk;* Bevan et al., 2014; Shaver & Caillouet Jr., 2015). Kemp's ridleys nest here in mass-nesting events (*arribadas*) from April through July. The beach is relatively narrow (20–30 m) and interspersed by several small rivers and lagoons. The tidal range is very small (0.4 m) and wave energy is moderate ($\overline{H}_s \approx 1$ m).

Masirah Island, Oman (OM_MI)

Masirah Island is a large island off the eastern coast of Oman, which hosts the second-largest loggerhead nesting population in the world (after the south-eastern US; Willson et al., 2020). It holds huge conservation value for the species, as the North-West Indian Ocean population is classified as *critically endangered* by the IUCN (Casale & Tucker, 2017). The island also hosts smaller nesting populations of green, hawksbill, and olive ridley turtles. The region is strongly influenced by the seasonal Monsoon climate, which overlaps with the nesting season from May through September, bringing high waves. Outside the Monsoon, waves are small leading to a moderate mean wave climate ($\overline{H}_s \approx 1.1$ m). The tide range is relatively high (2 m).

B.2. CoastSat settings

Table B.1 gives the full manual settings used for the CoastSat analysis. For a complete explanation of all settings we refer to Vos et al. (2019b). Briefly, *output_epsg* is the EPSG code of the coordinate reference system to be used at each site; *max_dist_ref* is the maximum distance (m) to the user-defined reference shoreline for a detected shoreline to be valid; *dist_clouds* is the distance (m) around identified clouds, where no shoreline can be mapped; *sand_color* denotes which classifier should be used, based on the beach sand color; *cloud_mask_issue* is a flag that can be activated in case sand pixels are wrongly identified as clouds on S2 images; and *s2cloudless_prob* denotes the threshold to identify cloudy pixels in the *s2cloudless* algorithm for S2 images.

Site	*output_epsg*	*max_dist_ref*	*dist_clouds*	*sand_color*	*cloud_mask_issue*	*s2cloudless_prob*
AI_LB	32728	50	100	default*	False*	40
AU_DH	7849	75	30	default*	True	60
BR_BV	31984	100*	90	default*	False*	30*
CR_TO	5456	100*	90	default*	True	40
CV_JB	4826	75	90	default*	True	30*
CY_AL	6312	50	90	default*	False*	30*
MX_LE	6372	100*	90	default*	True	30*
MX_RN	6372	75	90	default*	True	50
OM_MI	32640	100*	90	bright	True	60

Table B.1: Overview of manually adjusted CoastSat settings. All settings not represented in the columns were left at the default values (see Vos et al., 2019b). Values in the table marked with an asterisk also denote default values.

B.3. Model parameters and optimization

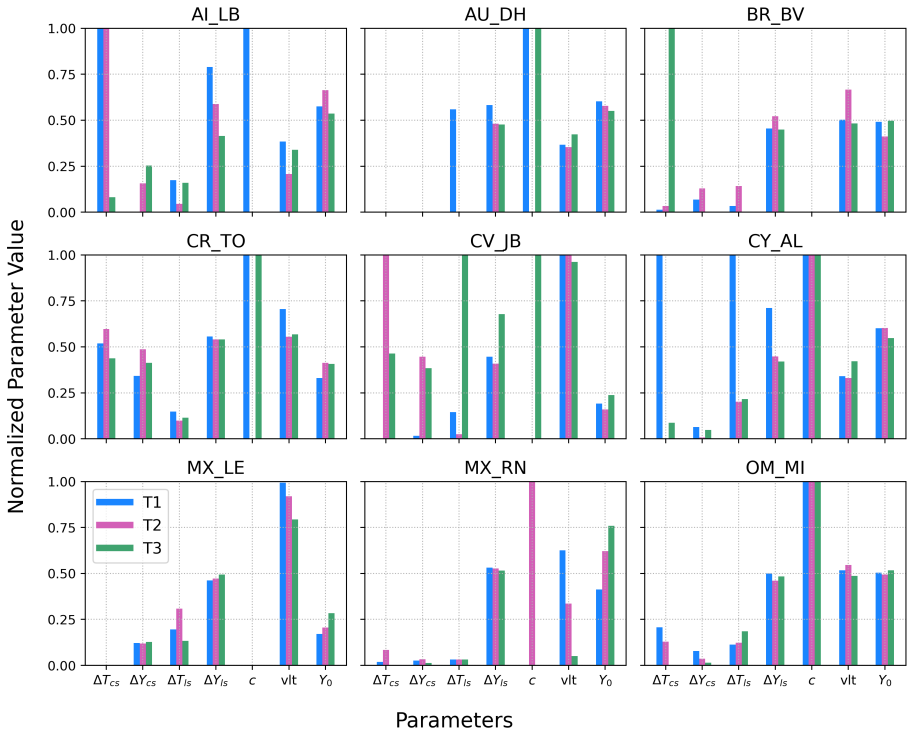

Figure B.1: Optimized model parameters for each location and transect. The parameter values are normalized, so the minimum/maximum values in the possible range are represented by 0 and 1 (see Table 4.2 for the ranges). The ranges of ΔY_{ls}, v_{lt}, and Y_0 are centered around 0, meaning that a value of 0.5 in the bar plots corresponds to 0, higher is positive, and lower is negative.

B.4. Observation and model results for remaining study sites

Here we present the equivalent to Figures 4.4–4.7 for the seven remaining study sites.

Dirk Hartog Island, Australia (AU_DH)

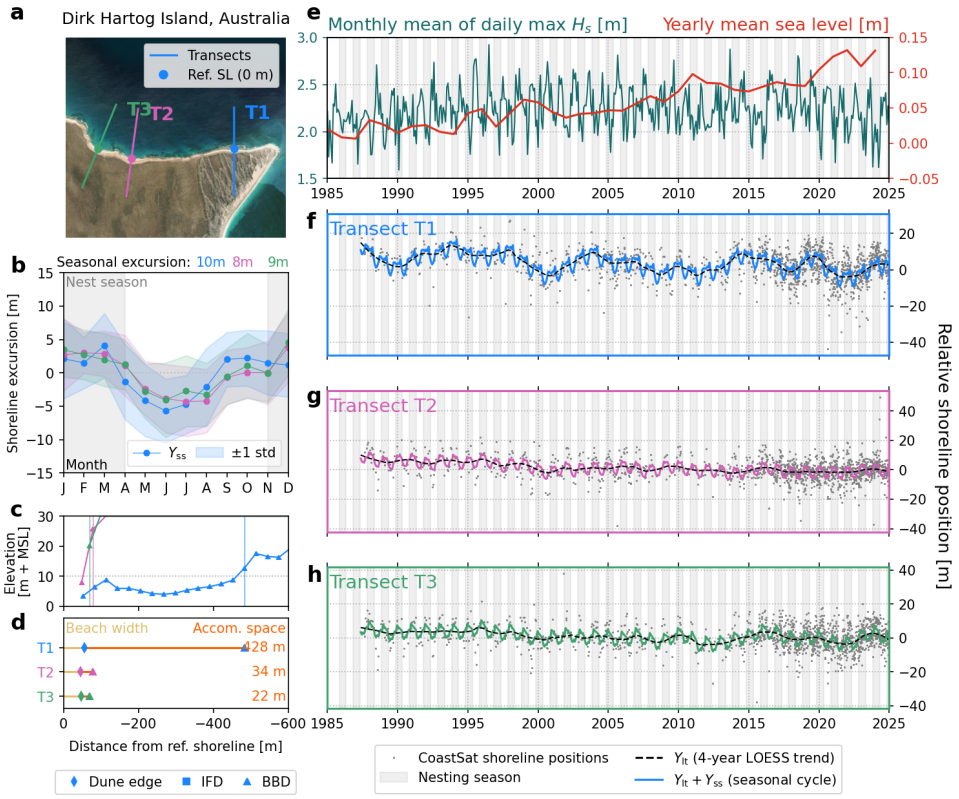

Figure B.2: Shoreline and accommodation space analysis for Dirk Hartog Island, Australia: a) Satellite image showing the transects and reference shoreline position; b) Seasonal shoreline component, SL_{ss}, at each transect; c) Backbeach elevation profiles, with vertical lines denoting the first point above 10 m + MSL; d) Beach width and accommodation space at each transect; e) Historical wave and water level time series; f-g) Observed and decomposed (long-term and seasonal) shoreline position time series at each transect.

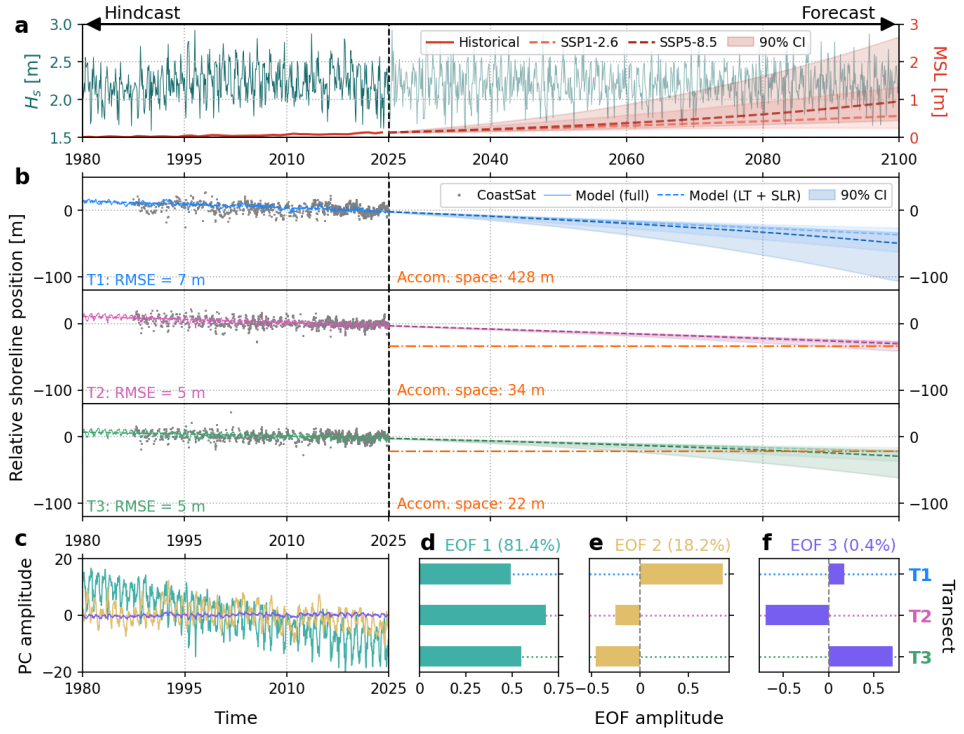

Figure B.3: Shoreline modeling results at Dirk Hartog Island, Australia. a) Wave and sea level time series used to force the model; b) Modeled shoreline position at each transect for the hindcast (1980–2025) and forecast (2025–2100) periods. Grey dots are the CoastSat shorelines, solid lines represent the full model results, and dashed lines only include the long-term trend (υ_{lt}) and SLR components. In the forecasts, the two dashed lines represent the median SSP1–2.6 (lighter color) and SSP5–8.5 (darker color) SLR projections, while the shading indicates the area between the 5th and 95th percentile; c) Amplitude of the three PCs over the hindcast period; d–f) Amplitudes of the three EOFs at each transect and percentage of explained variance.

Busca Vida, Brazil (BR_BV)

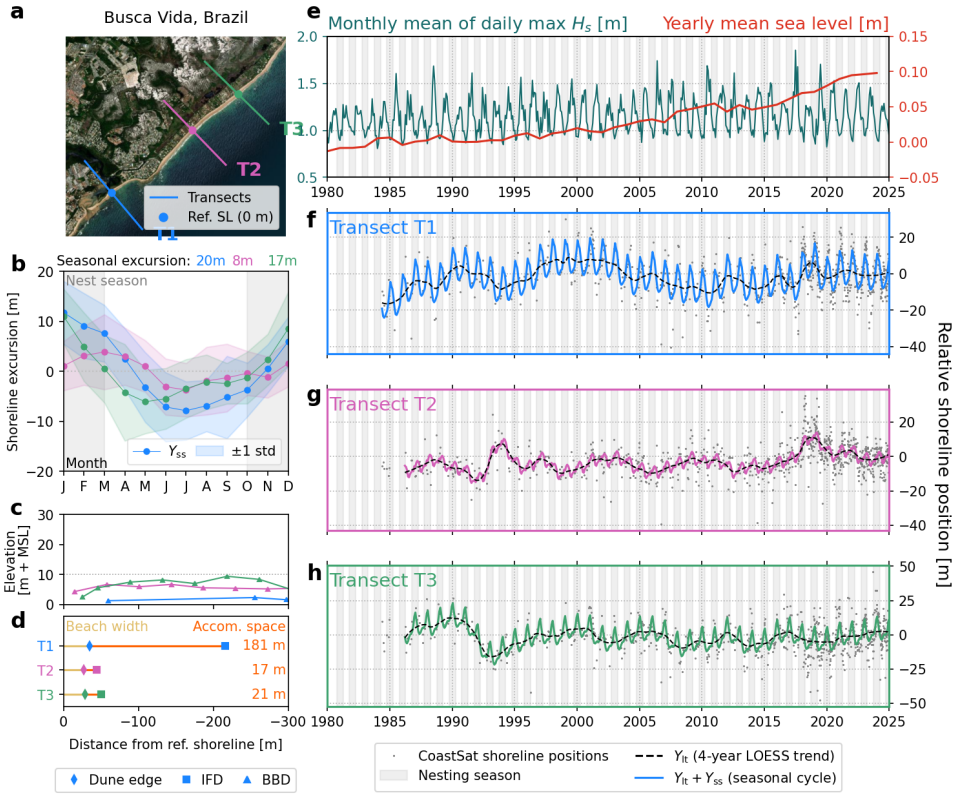

Figure B.4: Shoreline and accommodation space analysis for Busca Vida, Brazil: a) Satellite image showing the transects and reference shoreline position; b) Seasonal shoreline component, SL_{ss}, at each transect; c) Backbeach elevation profiles, with vertical lines denoting the first point above 10 m + MSL; d) Beach width and accommodation space at each transect; e) Historical wave and water level time series; f-g) Observed and decomposed (long-term and seasonal) shoreline position time series at each transect.

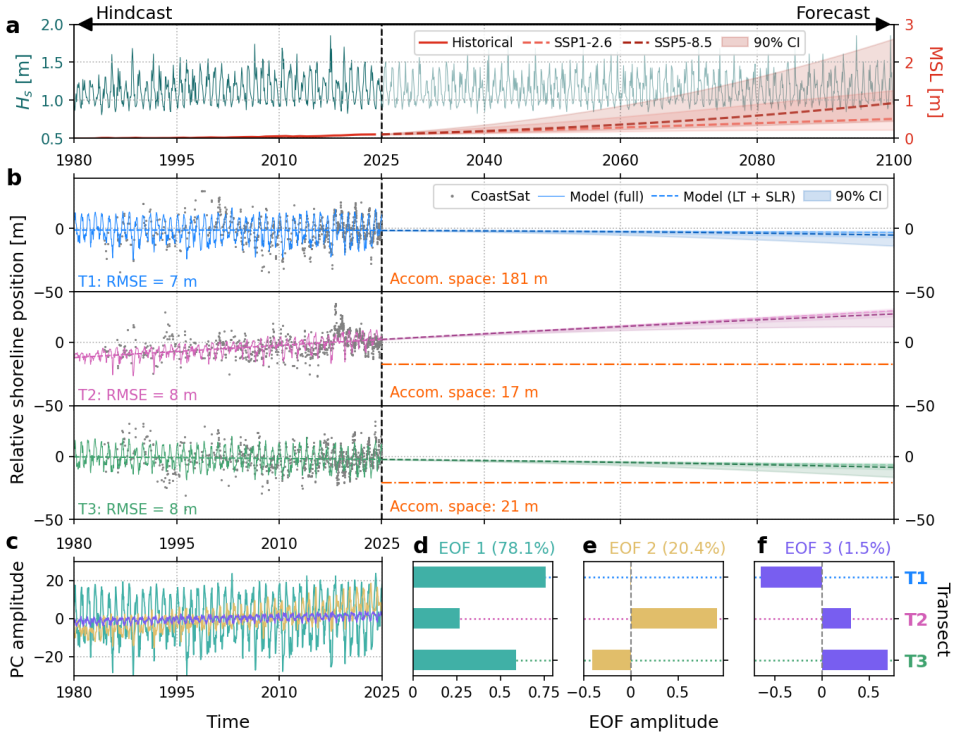

Figure B.5: Shoreline modeling results at Busca Vida, Brazil. a) Wave and sea level time series used to force the model; b) Modeled shoreline position at each transect for the hindcast (1980–2025) and forecast (2025–2100) periods. Grey dots are the CoastSat shorelines, solid lines represent the full model results, and dashed lines only include the long-term trend (v_{lt}) and SLR components. In the forecasts, the two dashed lines represent the median SSP1–2.6 (lighter color) and SSP5–8.5 (darker color) SLR projections, while the shading indicates the area between the 5th and 95th percentile; c) Amplitude of the three PCs over the hindcast period; d–f) Amplitudes of the three EOFs at each transect and percentage of explained variance.

Tortuguero, Costa Rica (CR_TO)

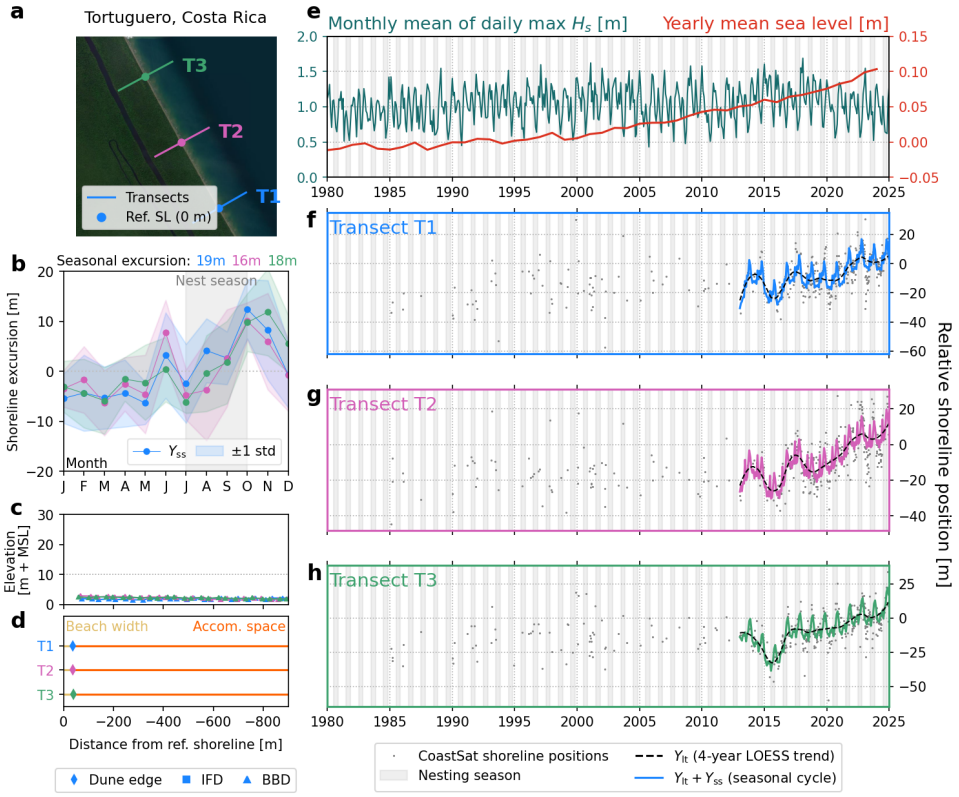

Figure B.6: Shoreline and accommodation space analysis for Tortuguero, Costa Rica: a) Satellite image showing the transects and reference shoreline position; b) Seasonal shoreline component, SL_{ss}, at each transect; c) Backbeach elevation profiles, with vertical lines denoting the first point above 10 m + MSL; d) Beach width and accommodation space at each transect; e) Historical wave and water level time series; f-g) Observed and decomposed (long-term and seasonal) shoreline position time series at each transect.

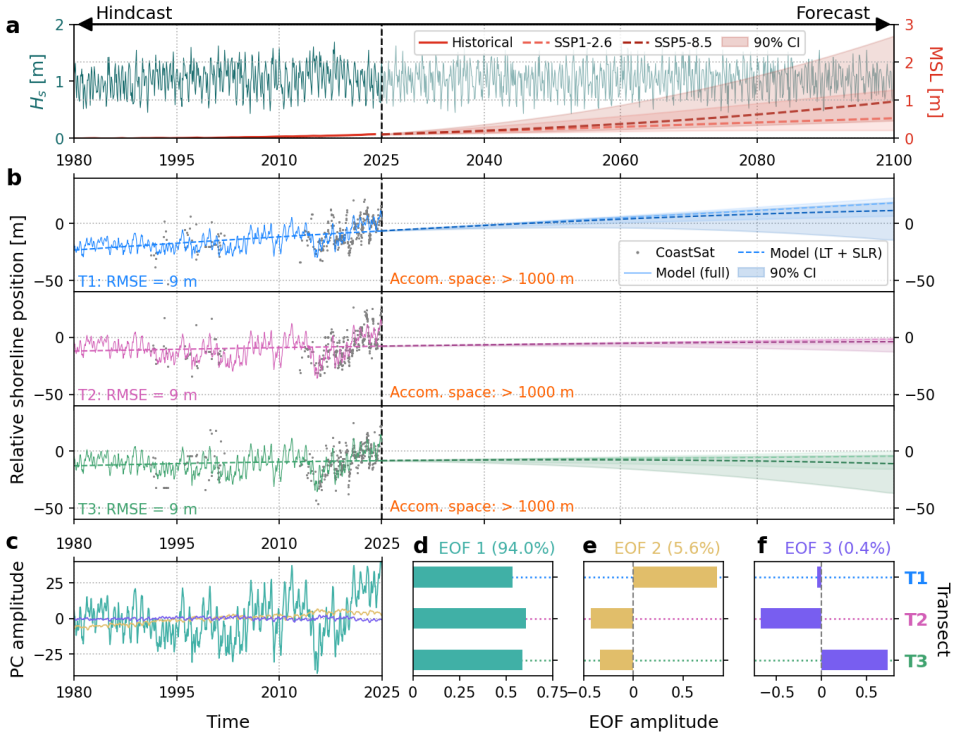

Figure B.7: Shoreline modeling results at Tortuguero, Costa Rica. a) Wave and sea level time series used to force the model; b) Modeled shoreline position at each transect for the hindcast (1980–2025) and forecast (2025–2100) periods. Grey dots are the CoastSat shorelines, solid lines represent the full model results, and dashed lines only include the long-term trend (v_{lt}) and SLR components. In the forecasts, the two dashed lines represent the median SSP1–2.6 (lighter color) and SSP5–8.5 (darker color) SLR projections, while the shading indicates the area between the 5th and 95th percentile; c) Amplitude of the three PCs over the hindcast period; d–f) Amplitudes of the three EOFs at each transect and percentage of explained variance.

B

Joao Barrosa, Cape Verde (CV_JB)

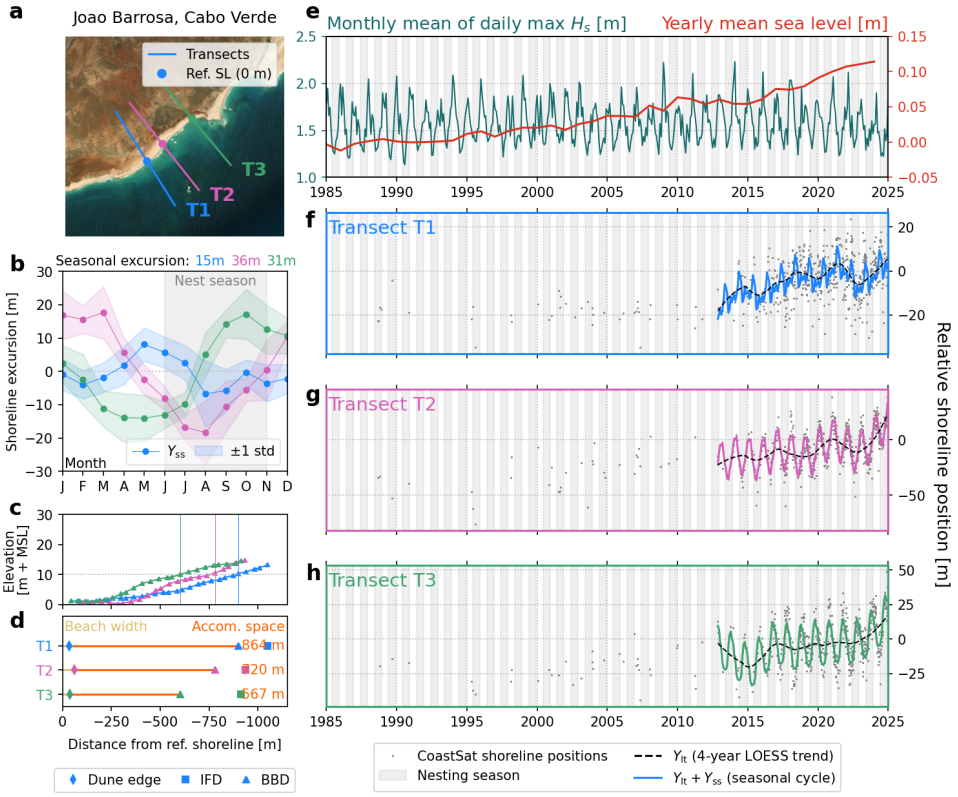

Figure B.8: Shoreline and accommodation space analysis for Joao Barrosa, Cape Verde: a) Satellite image showing the transects and reference shoreline position; b) Seasonal shoreline component, SL_{ss}, at each transect; c) Backbeach elevation profiles, with vertical lines denoting the first point above 10 m + MSL; d) Beach width and accommodation space at each transect; e) Historical wave and water level time series; f-g) Observed and decomposed (long-term and seasonal) shoreline position time series at each transect.

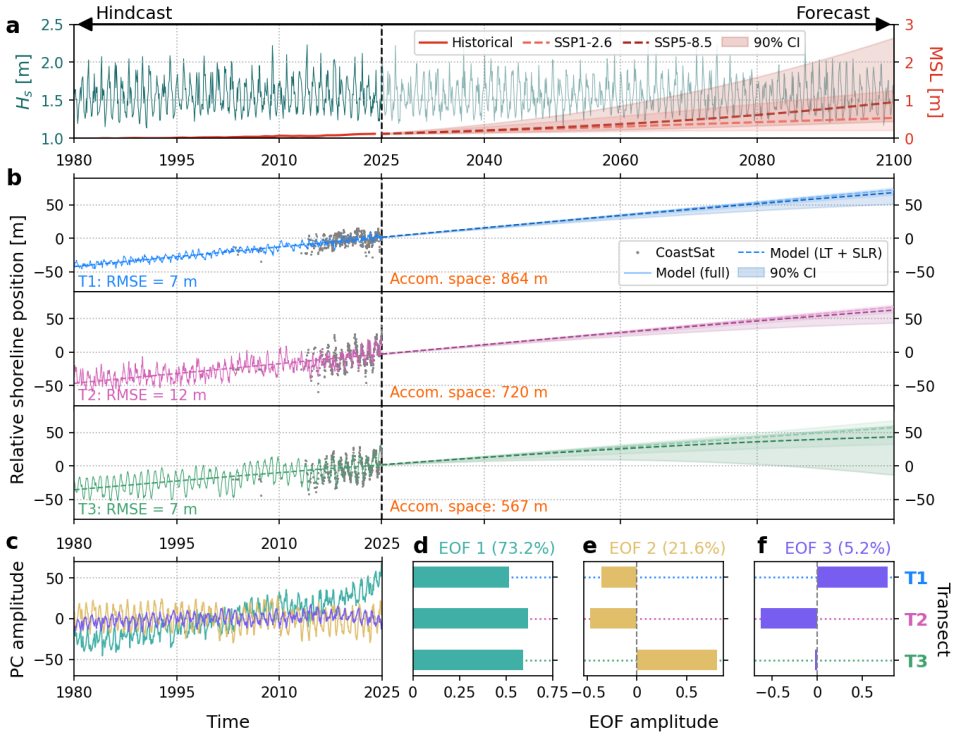

Figure B.9: Shoreline modeling results at Joao Barrosa, Cape Verde. a) Wave and sea level time series used to force the model; b) Modeled shoreline position at each transect for the hindcast (1980–2025) and forecast (2025–2100) periods. Grey dots are the CoastSat shorelines, solid lines represent the full model results, and dashed lines only include the long-term trend (v_{lt}) and SLR components. In the forecasts, the two dashed lines represent the median SSP1–2.6 (lighter color) and SSP5–8.5 (darker color) SLR projections, while the shading indicates the area between the 5th and 95th percentile; c) Amplitude of the three PCs over the hindcast period; d–f) Amplitudes of the three EOFs at each transect and percentage of explained variance.

Alagadi, Cyprus, (CY_AL)

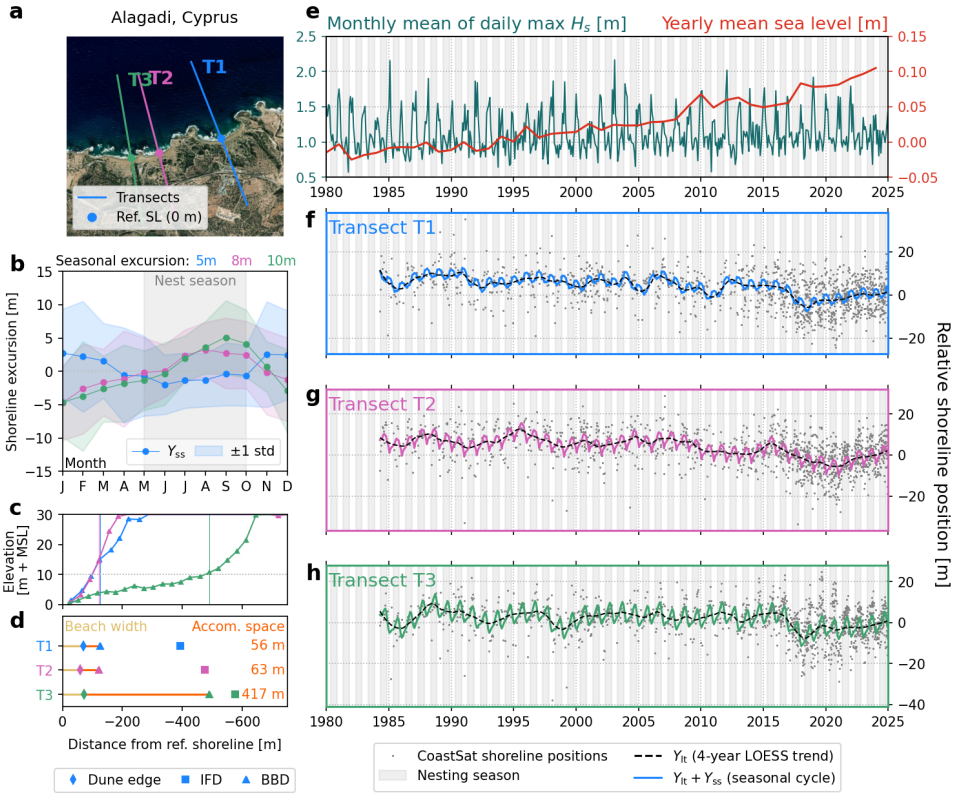

Figure B.10: Shoreline and accommodation space analysis for Alagadi, Cyprus: a) Satellite image showing the transects and reference shoreline position; b) Seasonal shoreline component, SL_{ss}, at each transect; c) Backbeach elevation profiles, with vertical lines denoting the first point above 10 m + MSL; d) Beach width and accommodation space at each transect; e) Historical wave and water level time series; f-g) Observed and decomposed (long-term and seasonal) shoreline position time series at each transect.

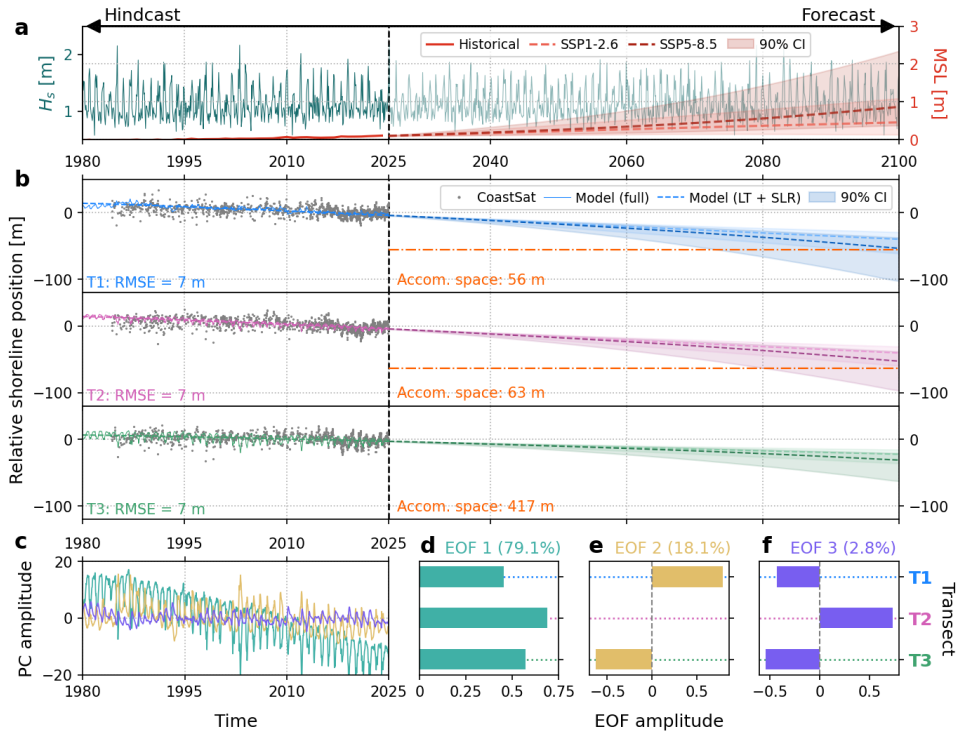

Figure B.11: Shoreline modeling results at Alagadi, Cyprus. a) Wave and sea level time series used to force the model; b) Modeled shoreline position at each transect for the hindcast (1980–2025) and forecast (2025–2100) periods. Grey dots are the CoastSat shorelines, solid lines represent the full model results, and dashed lines only include the long-term trend (v_{lt}) and SLR components. In the forecasts, the two dashed lines represent the median SSP1–2.6 (lighter color) and SSP5–8.5 (darker color) SLR projections, while the shading indicates the area between the 5th and 95th percentile; c) Amplitude of the three PCs over the hindcast period; d–f) Amplitudes of the three EOFs at each transect and percentage of explained variance.

Rancho Nuevo, Mexico (MX_RN)

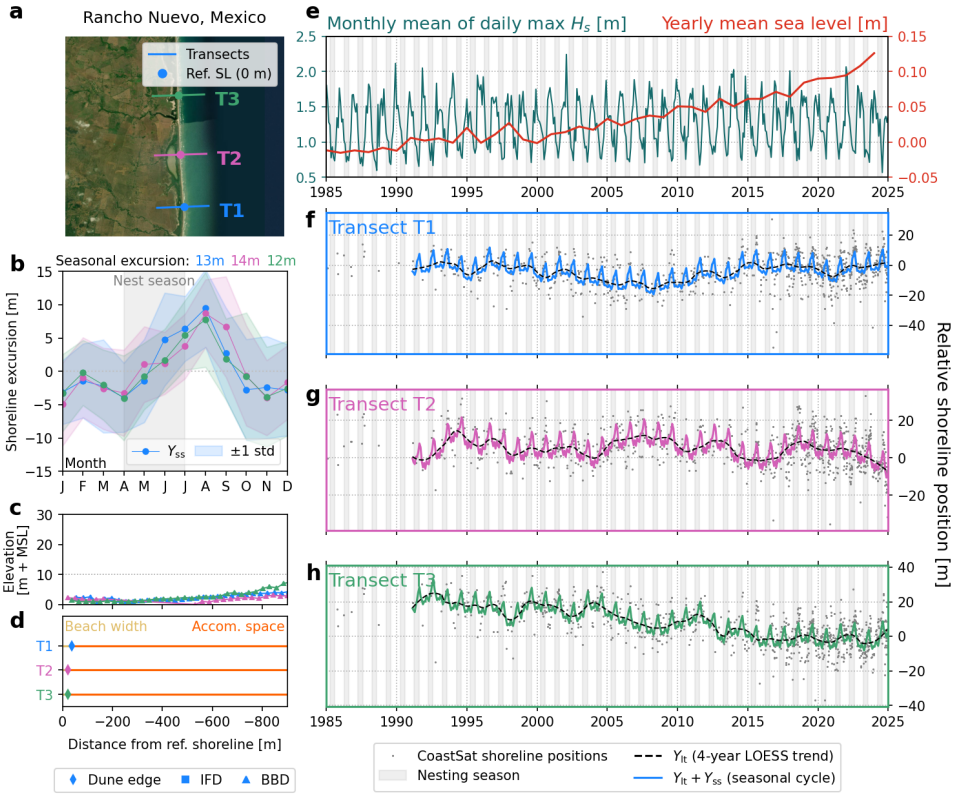

Figure B.12: Shoreline and accommodation space analysis for Rancho Nuevo, Mexico: a) Satellite image showing the transects and reference shoreline position; b) Seasonal shoreline component, SL_{ss}, at each transect; c) Backbeach elevation profiles, with vertical lines denoting the first point above 10 m + MSL; d) Beach width and accommodation space at each transect; e) Historical wave and water level time series; f-g) Observed and decomposed (long-term and seasonal) shoreline position time series at each transect.

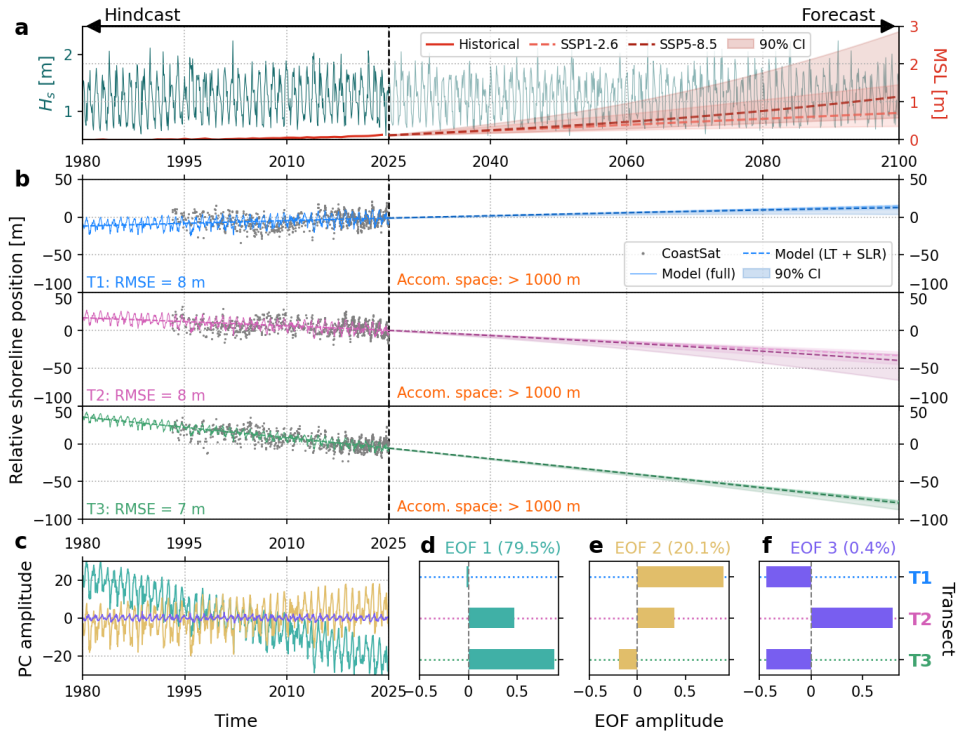

Figure B.13: Shoreline modeling results at Rancho Nuevo, Mexico. a) Wave and sea level time series used to force the model; b) Modeled shoreline position at each transect for the hindcast (1980–2025) and forecast (2025–2100) periods. Grey dots are the CoastSat shorelines, solid lines represent the full model results, and dashed lines only include the long-term trend (v_{lt}) and SLR components. In the forecasts, the two dashed lines represent the median SSP1–2.6 (lighter color) and SSP5–8.5 (darker color) SLR projections, while the shading indicates the area between the 5th and 95th percentile; c) Amplitude of the three PCs over the hindcast period; d–f) Amplitudes of the three EOFs at each transect and percentage of explained variance.

Masirah Island, Oman (OM_MI)

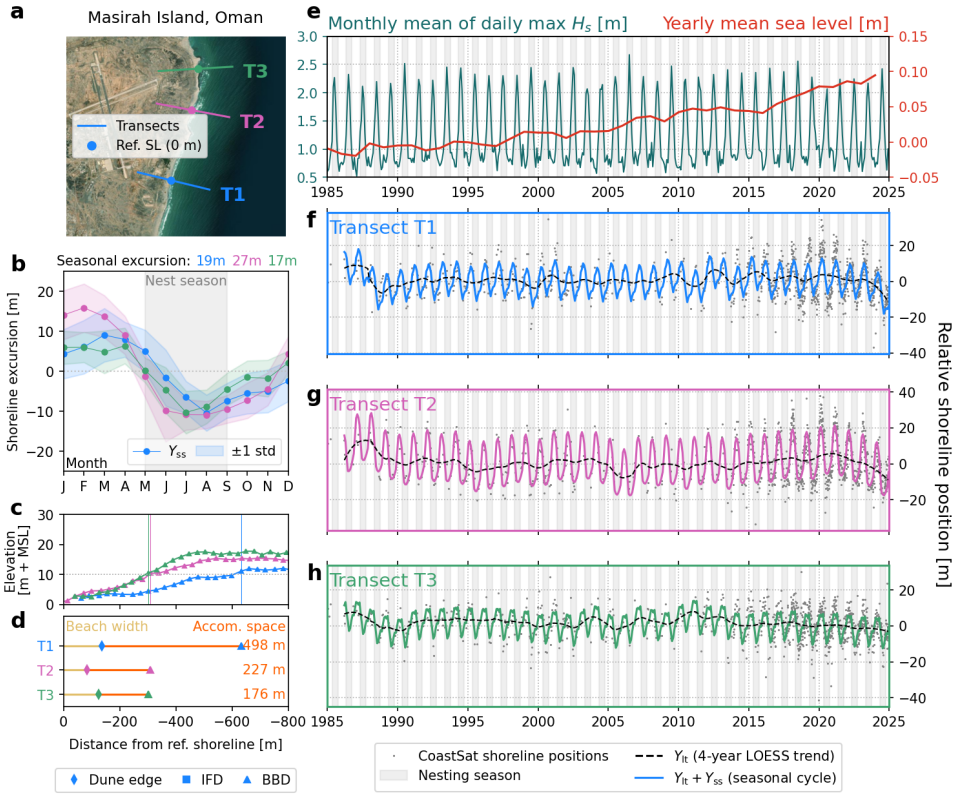

Figure B.14: Shoreline and accommodation space analysis for Masirah Island, Oman: a) Satellite image showing the transects and reference shoreline position; b) Seasonal shoreline component, SL_{ss}, at each transect; c) Backbeach elevation profiles, with vertical lines denoting the first point above 10 m + MSL; d) Beach width and accommodation space at each transect; e) Historical wave and water level time series; f-g) Observed and decomposed (long-term and seasonal) shoreline position time series at each transect.

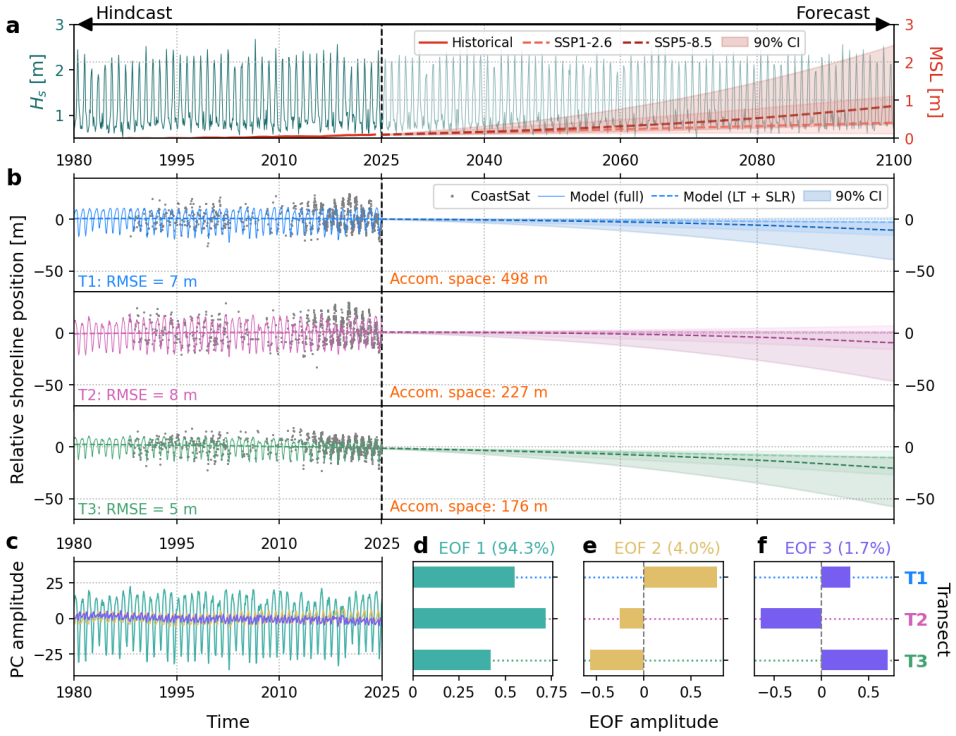

Figure B.15: Shoreline modeling results at Masirah Island, Oman. a) Wave and sea level time series used to force the model; b) Modeled shoreline position at each transect for the hindcast (1980–2025) and forecast (2025–2100) periods. Grey dots are the CoastSat shorelines, solid lines represent the full model results, and dashed lines only include the long-term trend (v_{lt}) and SLR components. In the forecasts, the two dashed lines represent the median SSP1–2.6 (lighter color) and SSP5–8.5 (darker color) SLR projections, while the shading indicates the area between the 5th and 95th percentile; c) Amplitude of the three PCs over the hindcast period; d–f) Amplitudes of the three EOFs at each transect and percentage of explained variance.

C

Supporting information for Chapter 5

C.1. Derivation of coastal indicators

As explained in Chapter 5, 22 coastal indicators were used in the analysis, divided in five categories: hydrodynamic, atmospheric, geophysical, habitat, and human. Here, we explain the derivation of the indicators for each global dataset we used.

For all indicators, we had to compute a distance metric at some stage, either when selecting the nodes from which to extract data for each Coastgon, or directly for the three distance indicators ($D_{c,03}$, D_{cor}, D_{sgr}). For all distances, we used the Haversine distance, which is the shortest distance between two points on the surface of a sphere, given their longitudes and latitudes.

ERA5 Ocean ($H_{s,med}$, $H_{s,p95}$, $T_{p,med}$, $T_{p,p95}$, $T_{p,std}$)

The wave climate indicators were derived from ERA5-wave (Hersbach et al., 2018), which has a structured grid at a spatial resolution of 0.5° ($\approx$ 55 km at the equator). Since this resolution is similar to the Coastgon resolution ($\approx$ 50 km diameter), we extracted the hourly time series (42 years, 1980–2021) of the significant wave height (H_s) and peak wave period (T_p) from the closest ERA5 Ocean node to each Coastgon (i.e., we extracted a single time series for H_s and T_p for each Coastgon). We then simply used descriptive statistics (median, standard deviation, and 95th percentile) to derive the five indicators from the time series.

ERA5 Atmos ($U_{10,med}$, $U_{10,p95}$, SST_{med}, P_{med})

All four atmospheric indicators were derived from ERA5-atmos (Hersbach et al., 2018), in similar fashion to the wave indicators. However, since the ERA5 Atmos grid has a higher spatial resolution (0.25° or $\approx$ 27.5 km at the equator), we extracted hourly time series (42 years, 1980–2021) from the two closest nodes to each Coastgon, instead of only the closest. We again used descriptive statistics (median and 95th percentile) to compute the indicators for each node, and then took the average of the two nodes associated to each Coastgon.

ERA5 provides the wind speed (and direction) as U/V components, so we first transformed the time series of each node from Cartesian to polar coordinates to derive the full wind speed. For precipitation, we used the annual total precipitation as base indicator, so we first computed the sum of the total precipitation for each year, and then took the median of all years to determine P_{med}, which has unit mm/year.

GTSM ($h_{S,med}$, $h_{S,p95}$, h_{tide})

The GTSMv3.0 grid has a spatial resolution that varies geographically (Muis et al., 2020). Along most of the global coastline, the resolution of the output nodes is between 10–50 km,

but for European coastlines it is higher (< 10 km). We decided to use one consistent way of selecting nodes for data extraction, so we used the three closest nodes to each Coastgon.

GTSM provides 10-minute interval time series of various water level components and also computed indicators for the period between 1985–2014 (30 years). We extracted the mean tidal range and the median/95th percentile of the storm surge for each GTSM node. For each Coastgon, we again averaged the obtained values of the three assigned nodes to yield one value per Coastgon.

ORAS5 ($u_{c,med}$, $D_{c,03}$)

ORAS5 provides monthly mean values of current velocities over a 0.25° resolution grid, at varying depth intervals (Copernicus Climate Change Service Climate Data Store, 2021). We extracted time series (42 years, 1980–2021) of the current velocity at 0.5 m depth. Velocities are provided in zonal and meridional components, so, as for the wind speeds in ERA5, we transformed the time series from Cartesian to polar notation to obtain the full current velocity. We then computed $u_{c,med}$ as the average of the median monthly current velocities of the three nodes assigned to each Coastgon. As a metric for the proximity of strong ocean currents, we computed the distance (Haversine) of each Coastgon to the nearest ORAS5 node where the median monthly current velocity was larger than 0.3 m/s.

GCC (ϕ_{std}, $\beta_{ns,med}$, $\beta_{bs,med}$, $z_{max,med}$, $z_{max,std}$, p_{built})

The coastline transects of the GCC dataset (Athanasiou et al., 2024) were already used to create the Coastgon grid (see Chapter 5), so each GCC transect was associated with one Coastgon (transects further than 100 km from any Coastgon were ignored in the analysis). So, for each of geophysical indicators we used descriptive statistics to compute the median/standard deviation over all transects linked to each Coastgon. For the percentage of built environment, we used the mean instead of the median, to obtain the total percentage of built environment for each Coastgon.

Allan Coral Atlas and UNEP-WCMC (D_{cor}, D_{sgr})

The Allan Coral Atlas (Li et al., 2020) and the UNEP-WCMC seagrass dataset (UNEP-WCMC & Short, 2021) provide geo-referenced locations of coral reefs and seagrass meadows respectively. We computed the distance (Haversine) from each Coastgon to the nearest coral reef or seagrass meadow from the two datasets.

We first overlaid the H3 global hexagonal grid resolution 5 over the coral reef / seagrass polygons. The resolution 5 H3 hexagons have a diameter of ≈ 15 km, which is one level higher than resolution 4 (used to create the Coastgon grid). We did this because our algorithm computes the distances between the coastline centroids of the Coastgons and the centroids of the coral reef / seagrass polygons. Since some of these polygons cover large spatial areas, their centroids can sometimes be several hundred kilometers away from the border of the polygon, giving a wrong representation of the actual distance between a Coastgon and the nearest coral reef / polygon. By overlaying the resolution 5 H3 grid over the polygons, we create a layer of approximately equal size hexagons that cover the same areas as the original polygons (up to the ≈ 15-km-resolution of the H3 grid). Therefore, the distance between the Coastgon and the nearest coral reef / seagrass hexagon is never further away than the hexagon radius (≈ 6–10 km). Additionally, the computational cost of this

approach is less, as very small coral reef / seagrass polygons are grouped together in the H3 hexagons, leading to a smaller total number of polygons.

Challenges with distance indicators

We had to constrain the three distance indicators ($D_{c,03}$, D_{cor}, D_{sgr}) to certain ocean basins to avoid distances that cross continents and are therefore much shorter than they would be through the Ocean. For relatively short island crossings ($O(10\ km)$) this is negligible, given the scale and resolution of our analysis, but it becomes problematic in regions like the Mediterranean, for example. When simply using a closest distance approach, the eastern Mediterranean would be closest to the coral reefs of the Red Sea. Similarly, the nearest coral reefs to some parts of the Pacific Central American coast would be in the Caribbean. Assuming that sea turtles do not actively cross the Suez or Panama Canals to change ocean basins, however, these distances are not appropriate for our analysis. We therefore computed distances within two main basins: an Atlantic basin (including the Mediterranean, Gulf of Mexico, and Caribbean) and an Indo-Pacific basin, covering the rest of the World's oceans. This way, the closest coral reefs to the Mediterranean, for example, are in the Caribbean. This approach has worked well for $D_{c,03}$ and D_{sgr}. However, for D_{cor} some relatively large land crossings remained in the South West Atlantic (Argentina, Uruguay, Brazil) and Southern Australia. Furthermore, at the border of the Atlantic and Indo-Pacific basins (near Capetown), the closest coral reefs are in southern Mozambique (Indo-Pacific basin), approximately 2.000 km northwest of Capetown. The Coastgons in the Atlantic basin, however, were linked to the coral reefs in the Caribbean, some 9.500 km away. We mitigated these challenges by recomputing D_{cor} using the Searoute python package, which computes the shortest maritime distance between two points (i.e., only crossing through the sea):

- For the southern west coast of Africa (Ivory Coast to South Africa), we computed D_{cor} as the minimum out of the Haversine distance to the nearest Caribbean corals and the Searoute distance to the nearest coral in southern Mozambique.
- For the East coast of South America (Brazil, Uruguay, Argentina), we used the Searoute distance to the nearest Caribbean coral reef.
- For the South coast of Australia, we used the smaller of the two Searoute distances to the nearest corals off of the east and west coasts of Australia.

C

C.2. Correlation matrix coastal indicators

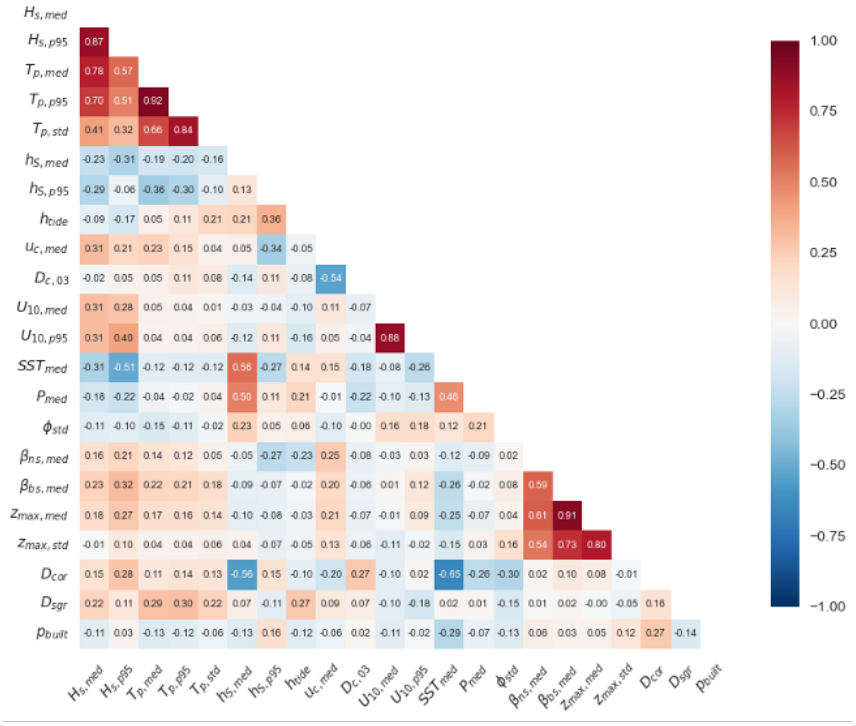

Figure C.1: Matrix plot showing Spearman's rank correlation (ρ) between each pair of the 22 coastal indicators (see Table 5.2 in Chapter 5). Red (blue) colors indicate positive (negative) correlations.

C.3. Random Forest cross-validation

To test the robustness of the RF model used to select the indicators for the clustering, we carried out a four-fold cross validation: we split the data into four equally sized partitions (each containing 25% of the original data) and trained four RF 'sub-models', each on a unique combination of three out of the four partitions (75% of the data). Since the dataset has imbalanced classes (i.e., there are much less nesting Coastgons than non-nesting), we used a stratified split, meaning each individual partition had approximately the same percentage of nesting and non-nesting Coastgons as the full dataset.

As we are not doing prediction with the RF model, it would make little sense to test each sub-model's predictive capability on the 'unseen' 25% (as would be the conventional cross-validation procedure for predictive regression). Rather we compared the RF feature importance of the four sub-models with the one trained on the full dataset. As can be seen in Figure C.2, both the feature importance values and the ranks are very consistent between the five models within each species (four trained on the subsets and one on the entire dataset), and the same dominant variables stand out. This shows that the RF model is robust to (relatively small) changes in the input data.

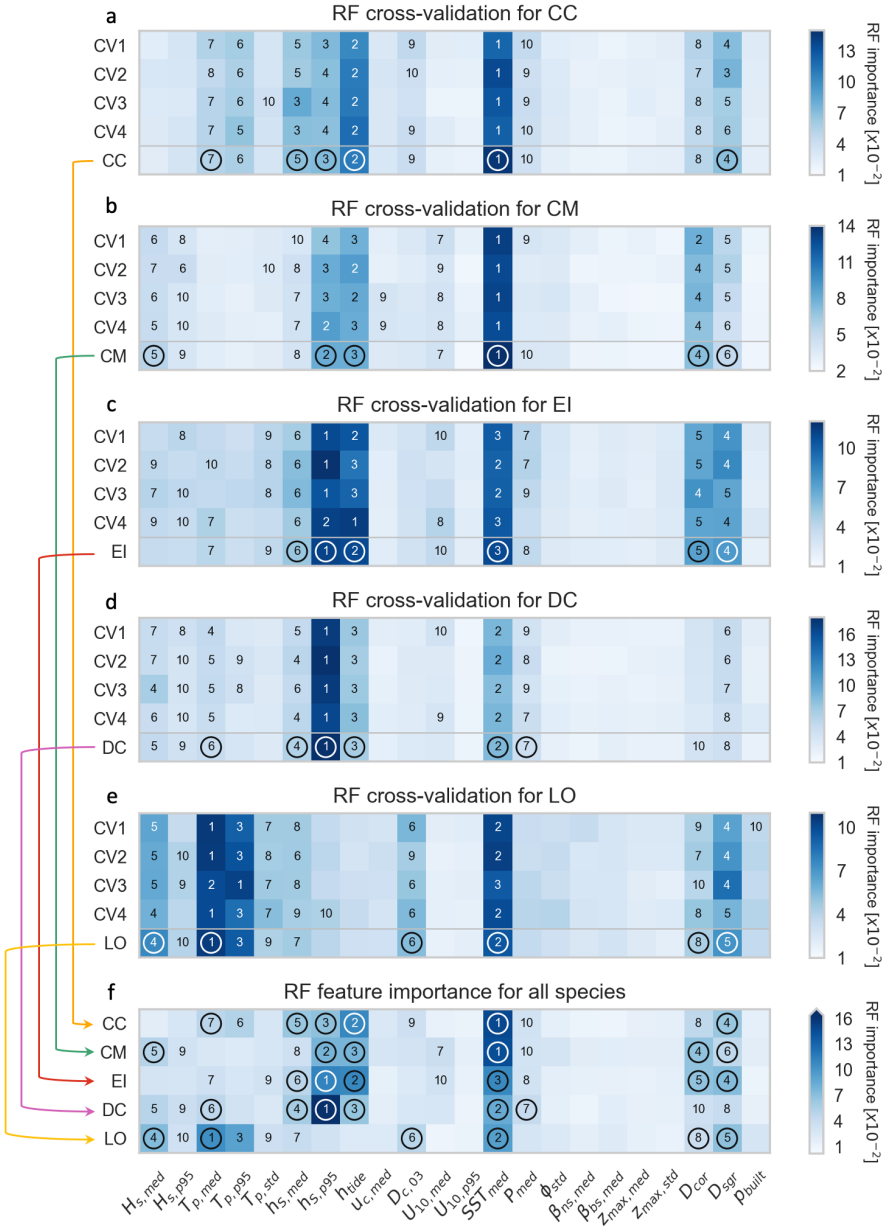

Figure C.2: Cross-validation of the RF model for each species. For each species, we split the data into four equal-size partitions and trained four 'sub-models', each on a unique 75% of the original data. The full model was trained on the full dataset. Panels a-e show the cross-validation results for each species: feature importance (blue scale) of the four sub-models on the first four rows (CV1 to CV4) and of the main model on the last row (denoted by species abbreviation). Panel f is identical to Figure 5.3 in Chapter 5—it summarizes the full RF models for the five species, so its rows are equivalent to the last row of each panel a-e (marked by the colored arrows). The numbers show the ranks of the ten most important indicators and the circles show the selected indicators for each species, based on the full RF models.

Acknowledgments

The last four years have been a challenging but also incredibly fun and rewarding journey. Of course, this was in large part due to the amazing people I've been surrounded with, many of whom have contributed to this work in some way or another. Here, I would like to take a moment to acknowledge all these people.

First of all, I would like to thank my three supervisors. José, I could not have asked for a better supervisor over these past years. Your positivity and enthusiasm have kept me going many times, particularly during the paper reviews (luckily every revision is minor to you). We had a great click from day one and that has made my work so much easier (even though it took me a while to get used to your perception of time...). In the end we never managed to visit a conference together, but we've had so many great moments and fun memories in these four years that will stay forever: the research (surf) trip to Cornwall, our Red Sea sailing adventure on the White Shadow, and sharing some Alligator nuggets in the Tipsy Turtle in Galveston, just to name a few. Gracias por los buenos momentos. Estoy orgulloso y feliz de haberte tenido como supervisor en el pasado y como amigo por la vida.

Ad, you were first involved as the external member in the Go/No Go but quickly became a cornerstone for me in the final 1.5 years after Galveston (when I wrote 80% of this thesis). You're calm and constructive way of giving feedback—never too much and always on point—is something I admire and that has helped me to stay focused during difficult moments, like the groundwater paper review. Thank you for putting so much time and effort into the most important stretch of my PhD, and also for sharing your career experiences and advice with me. I always enjoy our conversations.

Last but not least, Stefan, thank you for sticking with us till the end! I know how busy you were already before becoming dean and it means a lot that you continued to be involved afterward. You continuously managed to see the bigger picture in my research and helped me see it too, through your feedback. But most importantly, in every progress meeting I felt comfortable to say what's on my mind and that is in large part to the friendly atmosphere and safe environment you create. Your first concern was always my well-being and then the performance, I'll never forget that.

To the members of my independent committee, Jill Slinger, Tundi Agardy, Bas Jonkman, and Ian Turner: thank you for taking the time to review my thesis and joining the defense to discuss your thoughts and remarks. Bas, thank you for connecting us to the team in Galveston, which facilitated the field experiments on which the first two chapters are built. Ian, I fondly remember our whiteboard groundwater session in Delft a few years back—thank you for your enthusiasm and for teaching me the basics of coastal groundwater theory.

Apart from my supervisors and external committee, I've had the pleasure of collaborating with many other great colleagues and people, all of whom have contributed to shaping the past four years.

To the team at Texas A&M University, Jens Figlus, Tim Dellapenna, and Chris Marshall: thank you for hosting us in Galveston, facilitating the field experiments, and inviting us to

field trips, turtle collections, and the Gumbo dinner at Tim's house. You've made the stay in Galveston so much nicer for all four of us and without your help we could have never completed the field work. Jens, thank you in particular for putting so much time and effort into our collaboration. It was amazing to see your enthusiasm out in the field with us, and I'll never forget all your help. I also want to thank Nick Cohn and Peter Tereskiewicz from ERDC and Matthieu de Schipper and Pieter van der Gaag from TU Delft for helping us out with additional instruments and manpower. Finally, thanks to all the other people in Galveston who have helped us, showed us around, or simply did some fun activities with us, making it an unforgettable research stay: Josh, Nick, Miranda, Fangzhou, Jaclynn, Ben, Eddie, Thomas D., Thomas M., Justin, and Avery. Josh, thanks for showing us the many culinary treats Texas has to offer and for watching NFL with me. Miranda and Nick, thanks for the many fun evenings and especially the rodeo/line-dance lessons, all the best to you two in the future!

To the MSc students I've had the pleasure of supervising, Daniel, Meye, Falco, Merel, and Elias: thank you all for your hard work and interest—you have all inspired me and made meaningful contributions to the project. I hope you've learned as much from me as I have from you. Meye and Falco, thank you two in particular for your amazing support and contributions to the Galvetson project. Without you we'd have never been able to collect so much data and this thesis would have looked very different. Most importantly, thank you for all the fun we had in Galvy—BBQ'ing in the garden, spotting alligators, or cheering on the Texas A&M Aggies!

Sean, thank you for hosting me (and Floris) in Santa Cruz and showing us the USGS office as well as Santa Cruz's many surf spots. Spending time with you, Sylvia, Meri, and Vinnie inbetween the surf sessions was a lot of fun and very relaxing after a busy week at AGU. Of course, thank you also for the cool collaboration in Chapter 4 of this thesis—running and sharing your model, discussing the results (for hours), and helping me put it all together in a paper just before my PhD deadline.

Arjen and Panos, thank you for sharing your data and for your contributions to Chapter 5 of this thesis. Arjen, thank you also for taking up a supervisory role and continuing to mentor me during the first year of my PhD.

Carlos, thank you for showing so much interest in my research from the very beginning and staying involved till the end. Thanks also for inviting José and me to visit KAUST and join the research vessel on the Red Sea. Thanks Nayra, Hugo, Christopher, and Hector for showing us around at KAUST and making us feel at home. The slightly dangerous Red Sea research trip on the White Shadow was a rollercoaster, but definitely one with many positive memories!

Ronel, thank you for your enthusiasm and interest in our project and for representing the "beach perspective" in the turtle community. Thanks also for your contribution to Chapter 6 and for supporting me from the sidelines.

To Brendan Godley and Zara Botterell: thank you for inviting José and me to come to Penryn and pick up the turtle beach sediments. We've had an amazing week in Cornwall, not least due to your warm welcome. Though I haven't managed to include the sediment data in this thesis, it's a super valuable dataset and I'm sure we will continue collaborating on it in the future. Brendan, thank you in particular for all the discussions we've had and staying involved in our project. It feels a bit incomplete that we haven't published anything

together yet, but I hope that will come soon. Thanks also for introducing me to the turtle community when I finally made it to an ISTS in Ghana this year.

To Felipe Calleja and the IMARES team at Universidad de Costa Rica: thank you for hosting and supervising our MDP student groups in Costa Rica and facilitating the measurements at Ostional. I hope I can make it there myself one day and visit IMARES and the Ostional research station. Thanks also to Roldán Valverde and Camilo Jaramillo for your help and collaboration with the student projects. And, of course, thanks a lot to all the MDP students, you've managed to collect and analyse valuable data.

Judith and Stuart, thanks for giving me the opportunity to explore the educational part of working at the university and sparking my passion for teaching. Coastal Systems (Dynamics) was always one of the most interesting and well-organized courses of the curriculum and it was a pleasure to experience and contribute to this behind the scenes. Thanks also for giving me the chance to give some of the course lectures, that was a very nice experience and I always felt supported by both of you.

A big thank you goes to all the amazing colleagues at the HE department: Alessandro, Ana, Anna Kroon, Anna Enge, Anne, Bas, Bram, Bregje, Camilo, Christa, Daan Hulskemper, Daan Poppema, Dimitris, Floor, Hassan, Jill, Jos, Judith, Ligaya, Lisa, Marion, Marcel, Mark, Marlein, Marlies, Mats, Matthieu, Matthijs, Menno, Mia, Natascia, Paul Bayle, Paulina, Ponni, Robert, Romy, Roy, Sander, Sierd, Stuart, Tess, Tom, Tosca, Valentina, Valeria, Wouter, Yu Kuai. Thank you for all the nice moments over the past four years, whether during lunch, in PSOR, or at a department outing. A special shout-out to my 3.62 roommates: Bart, Dorette (undercover), Floris, Gijs, Kevin, Mario, Marthe, Paul, Su, and Vincent: thank you for all the music hours, snicker breaks, conferences, drinking nights, and all the other fun memories—you've made the past four years unforgettable!

A special thanks to the secretaries: Eefke, Inge, Marlene, Otti, and Sandra, thank you very much for always smiling and helping out! And thank you Pieter and Chantal for all your help (and patience) with the lab and instruments.

To all my friends, thank you for being around and for all the fun times that have kept my mind off work when needed. Bart and Els, thanks for being my paranymphs at the defense. Els, Paul, Chris, and the rest, thanks for all the surf-work trips, which have made these four years so much more fun. Els here it finally is: thanks for recommending random forests to me for Chapter 5. Tuna, thanks for being my buddy since moving to Delft 11 years ago. Don't forget to pick up your wand. To my Waterbouwdispuut friends, thanks for the amazing MSc years, you laid the foundation for me staying another four years on the 3rd floor. To everyone I've lived with in the past four years, thanks for being great roommates! To the crew in Züri, thanks for all the dinners, game nights, and tüfi afternoons, I'm really happy we still see each other so regularly, especially with more and more kids joining the family. Alex thanks for an amazing time in California before I went to Galveston.

A huge thank you to my Family: Mami, Kees, Chris, and Simon, I love you all. Though we don't see each other so much in person, our reunions in Feldis and Belle Ile were always highlights and helped me stay motivated and energized during the PhD. Mami, Kees, thank you so much for always supporting and never doubting. Who would have thought we'd reach this day when I walked away from the Aufnahmeprüfung... Without you I would have never made it this far and I'll be forever grateful for all the energy and support you've given me—not just these four years, but my whole life.

Last but certainly not least, thank you Annekee for always loving and supporting me. Incidentally, September 2021 was not only the start of my PhD but also of our relationship. Now, four years later, I finished my PhD and we're engaged. What a ride! Thank you so much for all the memories we've created over the past years and the many that are still to come. Thank you for being my travel companion, my hiking partner, my surf buddy, my tryout student, my personal designer, my girl—thank you for being my everything. I love you and I can't wait for our next adventures, wherever they may be!

About the author

Jakob Christiaanse was born in Rotterdam, the Netherlands, on 10 April 1995. He lived there until 2002, when he moved with his family to Berlin, Germany, and subsequently to Zürich, Switzerland, in 2003. There he completed the Swiss Gymnasium education (Matura) at Kantonsschule Hohe Promenade in 2013. After a gap year in which he interned at Swiss engineering firm Basler & Hoffman and traveled through the United States, he moved back to the Netherlands in 2014 to pursue his Bachelor's degree in Civil Engineering at TU Delft. During his BSc, Jakob followed a minor in Environmental Engineering at UNSW in Sydney, Australia, and completed his BSc thesis on plastic river pollution in Bandung, Indonesia.

After graduating from his BSc in 2018, Jakob continued with a MSc in Hydraulic Engineering at TU Delft, specializing in Coastal Engineering. In his first Master's year he was vice-president of the Hydraulic Engineering Student Association "Het Waterbouwdispuut", where he managed the financial acquisition and organized student activities with engineering firms. In 2019 he went to Buenos Aires, Argentina, for a six-month internship at engineering firm Serman & Asociados, learning Spanish, and traveling around South America. Returning home when Covid hit, he completed his MSc thesis on quantifying parameter uncertainty in coastal numerical modeling with Deltares, graduating *cum laude* from his Master's degree in January 2021. The MSc thesis work sparked his growing interest in research, which further increased when he presented his findings at the 9th International Coastal Dynamics Conference in Delft a few months later. As a result, he started his PhD on coastal science for sea turtle conservation at TU Delft in September 2021.

Jakob lives in The Hague with his fiancée Annekee. Outside of work he likes to spend his time with friends and in nature—often surfing, hiking, and back-country skiing. He also plays tennis and basketball, and enjoys reading and watching movies and sports.

List of publications

Journal papers

First author

6. **Christiaanse, J. C.**, Vitousek, S., Reniers, A. J. H. M., & Antolínez, J. A. A. (in review). Vulnerability of key sea turtle nesting beaches to future erosion and sea level rise. *Earth's Future*. [Chapter 4]

5. **Christiaanse, J. C.**, Reniers, A. J. H. M., Aarninkhof, S. G. J., Ostertag, E. F., Nel, R., Duarte, C. M., & Antolínez, J. A. A. (2025). Aiding sea turtle conservation through coastal management. *Frontiers in Marine Science*, 12, 1669885. https://doi.org/10.3389/fmars.2025.1669885 [Chapter 6]

4. Kroon, A.*, **Christiaanse, J. C.***, Luijendijk, A. P., de Schipper, M. A., & Ranasinghe, R. (2025). Parameter uncertainty in medium-term coastal morphodynamic modeling. *Scientific Reports*, 15, 18471. https://doi.org/10.1038/s41598-025-02300-8. *Equal first author contribution

3. **Christiaanse, J. C.**, Antolínez, J. A. A., Marshall, C. D., Figlus, J., Dellapenna, T. M., & Reniers, A. J. H. M. (2025). Beach groundwater response to ocean processes and rain on a mild-sloping barrier island: implications for sea turtle nest flooding. *Coastal Engineering*, 201, 104795. https://doi.org/10.1016/j.coastaleng.2025.104795 [Chapter 3]

2. **Christiaanse, J. C.**, Antolínez, J. A. A., van der Grinten, M. J., Taal, F., Figlus, J., Dellapenna, T. M., Ritt, B., Marshall, C. D., Tereszkiewicz, P. A., Cohn, N., Majzlik, E. J., & Reniers, A. J. H. M. (2025). Measurements of groundwater, hydrodynamics, and sand characteristics at a dissipative sea turtle nesting beach. *Scientific Data*, 12, 123. https://doi.org/10.1038/s41597-025-04455-5 [Chapter 2]

1. **Christiaanse, J. C.**, Antolínez, J. A. A., Luijendijk, A. P., Athanasiou, P., Duarte, C. M., & Aarninkhof, S. (2024). Distribution of global sea turtle nesting explained from regional-scale coastal characteristics. *Scientific Reports*, 14, 752. https://doi.org/10.1038/s41598-023-50239-5 [Chapter 5]

    - Awarded *Best Climate Change Adaptation Paper 2023* by TU Delft.

Co-author

1. van der Grinten, M. J., **Christiaanse, J. C.**, Reniers, A., Figlus, J., Taal, F., & Antolínez, J. A. A. (2025). Wave runup extraction on dissipative beaches: new video-based methods. *Coastal Engineering*, 200, 104757. https://doi.org/10.1016/j.coastaleng.2025.104757

Conference proceedings and talks

First author

7. **Christiaanse, J. C.** & Antolínez, J. A. A. (2025). Aiding sea turtle conservation through coastal monitoring and modeling. *43rd International Sea Turtle Society Symposium, Accra, Ghana, 2025*. Oral presentation.

6. **Christiaanse, J. C.**, Antolínez, J. A. A., Reniers, A. J. H. M., Figlus, J., Marshall, C. D., Dellapenna, T. M., Calleja, F., & Jaramillo, C. (2025). Assessing the risk of sea turtle nest flooding: the role of beach groundwater dynamics. *43rd International Sea Turtle Society Symposium, Accra, Ghana, 2025*. Poster presentation.

5. **Christiaanse, J. C.**, Antolínez, J. A. A., van der Grinten, M., Taal, F., Figlus, J., Dellapenna, T. M., & Marshal, C. D. (2024). Predicting sea turtle nest flooding on sandy beaches. *38th International Conference on Coastal Engineering, Rome, Italy, 2024*. Oral presentation. https://doi.org/10.9753/icce.v38.management.141

4. **Christiaanse, J. C.**, Antolínez, J. A. A., van der Grinten, M., Taal, F., Figlus, J., Dellapenna, T. M., Marshal, C. D., Tereszkiewicz, P., & Cohn, N. (2023). Assessing the Risk of Sea Turtle Nest Inundation on Sandy Beaches: A Field Experiment on Galveston Island, Texas. *AGU Fall Meeting, San Francisco, CA, USA, 2023*. Poster presentation. https://doi.org/10.22541/essoar.170421431.13722834/v1

3. **Christiaanse, J. C.**, Antolínez, J. A. A., Aarninkhof, S., Luijendijk, A., & Duarte, C. (2022). A global characterization of coastal regions to guide nature-based solutions to sea turtle nesting beaches. *37th International Conference on Coastal Engineering, Sydney, Australia, 2022*. Oral presentation. https://doi.org/10.9753/icce.v37.management.81

2. **Christiaanse, J. C.**, Antolínez, J. A. A., Aarninkhof, S., Luijendijk, A. P., & Duarte, C. (2022). Towards nature-based solutions to sea turtle nesting beaches: A global hydro-morphological characterisation of nesting sites. *Ocean Sciences Meeting, virtual conference, 2022*. Oral presentation.

1. **Christiaanse, J. C.**, Kroon, A., Luijendijk, A. P., de Schipper, M. A. (2021) Quantifying parameter uncertainty in coastal area predictions. *9th International Coastal Dynamics Conference, Delft, Netherlands, 2021*. Oral presentation.

Co-author

5. Antolínez, J. A. A., **Christiaanse, J. C.**, Reniers, A. J. H. M., Aarninkhof, S. G. J., Godley, B. J., Nel, R., Duarte, C. M. (2025). Managing Coasts and Conserving Sea Turtle Habitats. *Ocean Sciences Meeting, Glasgow, Scotland, 2026*.

4. Antolínez, J. A. A., **Christiaanse, J. C.**, van der Grinten, M. J., Heijl, M., Taal, F. Dédina, D., Ostertag, E. F., Reniers, A. J. H. M., Aarninkhof, S. G. J., Figlus, J., Dellapenna, T. M., Marshall, C. M., Calleja, F., Valverde, R., Godley, B. J., Duarte, C. M. (2025). Coastal science for flood and erosion proof sea turtle nesting beaches. *4th International Workshop on Waves, Storm Surges, and Coastal Hazards, Santander, Spain, 2025*. Poster presentation.

3. Dédina, D., **Christiaanse, J. C.**, Roelvink, F., Elshinnawy, A. I. A., McCall, R., Reniers, A., Duarte, C., &, Antolínez, J. A. A. (2025). Runup modeling in low-data coral reef environments: implications for nesting sea turtles. *10th International Coastal Dynamics Conference, Aveiro, Portugal, 2025*. Oral presentation and conference paper.

2. van der Grinten, M. J., **Christiaanse, J. C.**, Reniers, A. J. H. M, Figlus, J., Taal, F., & Antolínez, J. A. A. (2025). Wave runup extraction on dissipative beaches: new video-based methods. *NCK Days, Zeeland, Netherlands, 2025*. Oral presentation.

1. Figlus, J., **Christiaanse, J. C.**, Antolínez, J. A. A., van der Grinten, M., Taal, F., Dellapenna, T. M., & Marshal, C. D. (2024). Turtles and Engineered Beaches: A Galveston Island Field Study. *ASBPA National Coastal Conference, Galveston, TX, USA, 2024*. Oral presentation.

Data & Code

3. **Christiaanse, J. C.**, Antolínez, J. A. A., van der Grinten, M. J., Taal, F., Figlus, J., Dellapenna, T. M., Ritt, B., Marshall, C. D., Tereszkiewicz, P. A., Cohn, N., Majzlik, E. J., & Reniers, A. J. H. M. (2024). TURTLE: Measurements of groundwater, hydrodynamics, sand temperature, and sediment characteristics at two beach transects on Galveston Island, Texas, USA. 4TU.ResearchData. https://doi.org/10.4121/93256801-ed01-4627-9e49-8607967a0853

2. **Christiaanse, J. C.** (2024). Coastal Fieldwork: Python-based readout and processing of coastal fieldwork data. GitHub repository. https://github.com/jakobchristiaanse/coastal-fieldwork.git

1. **Christiaanse, J. C.**, & Antolínez, J. A. A. (2024). Coastgons: regional coastal characteristics along a global hexagonal coastline grid. 4TU.ResearchData. https://doi.org/10.4121/68377ee4-892d-40f0-a490-29f2601e6825